

**Damaged Collagen Detection and A Novel Approach to 1,3-Dipolar Cycloaddition  
Reactivity: Research at the Interface of Chemistry and Biology**

By

Jesús M. Dones Monroig

B.S. Chemistry  
University of Puerto Rico at Rio Piedras, 2014

M.S. Chemical Biology  
University of Wisconsin – Madison, 2017

Submitted to the Department of Chemistry  
in Partial Fulfillment of the Requirements for the Degree of

Doctor of Philosophy in Chemical Biology

at the

Massachusetts Institute of Technology

June 2021

Signature of Author: \_\_\_\_\_  
Department of Chemistry  
May 14, 2021

Certified by: \_\_\_\_\_  
Ronald T. Raines  
Firmenich Professor of Chemistry  
Thesis Supervisor

Accepted by: \_\_\_\_\_  
Adam Willard  
Associate Professor of Chemistry  
Chair, Department Committee on Graduate Students

This doctoral thesis has been examined by a Committee of the Department of Chemistry as follows:

---

Laura L. Kiessling  
Novartis Professor of Chemistry  
Committee Chairman

---

Ronald T. Raines  
Firmenich Professor of Chemistry  
Thesis Supervisor

---

Bradley L. Pentelute  
MIT Associate Professor of Chemistry  
Committee Member

Damaged Collagen Detection and A Novel Approach to 1,3-Dipolar Cycloaddition Reactivity:  
Research at the Interface of Chemistry and Biology

by

Jesús M. Dones

Submitted to the Department of Chemistry on May 14, 2021  
in Partial Fulfillment of the Requirements for the Degree of  
Doctor of Philosophy in Chemistry

**Abstract**

**Part I**

**Chapter 1. Collagen Mimetic Peptides as a Selective Binder for Damaged Collagen.** “Collagen diseases” were first introduced by Klemperer and coworkers in the 1950s. This type of disease can cause fibrinoid degeneration or changes in the collagen fibers that denature the collagen triple helix. Collagen mimetic peptides (CMPs), variants that are monomeric in solution but have high ability to anneal with damaged collagen, are a growing tool in the biomedical field for the detection and treatment of collagen-related diseases. This chapter provides a review of recent developments in the field of damaged collagen targeting for studying collagen-related diseases and injuries.

**Chapter 2. Optimization of interstrand interactions enables burn detection with a collagen-mimetic peptide.** In this chapter, through a computational screen, we identify (flpHypGly)<sub>7</sub> as an optimal monomeric CMP for heterotrimer formation. We find that (flpHypGly)<sub>7</sub> forms stable triple helices with (ProProGly)<sub>7</sub> but not with itself. The nonnatural amino acid HflpOH, which is (2*S*,4*S*)-4-fluoroproline, is not toxic to human fibroblasts or keratinocytes. Conjugation of (flpHypGly)<sub>7</sub> to a fluorescent dye enables the facile detection of burned collagenous tissue with high specificity. The ubiquity of collagen and the prevalence of injuries and diseases that disrupt endogenous collagen suggests widespread utility for this approach.

**Chapter 3. A Cyclic Peptide Mimetic of Damaged Collagen.** In this chapter, a duplex of CMPs was envisioned as a macromolecular mimic for damaged collagen. The duplex was synthesized on a solid support from the amino groups of a lysine residue and by using olefin metathesis to link the N termini. The resulting cyclic peptide, which is a monomer in solution, binds to CMPs to form a triple helix. Among these, CMPs that are engineered to avoid the formation of homotrimers but preorganized to adopt the conformation of a collagen strand exhibit enhanced association. Thus, this cyclic peptide enables the assessment of CMPs for utility in annealing to damaged collagen. Such CMPs have potential use in the diagnosis and treatment of fibrotic diseases and wounds.

**Chapter 4. Optical imaging of collagen fiber damage to assess thermally injured human skin.** In this chapter, we present two complementary candidate methods for visualization of collagen structure in three dimensions. Second harmonic generation imaging offers a label-free, high-resolution method to identify intact collagen. Simultaneously, a fluorophore-tagged collagen-mimetic peptide can detect damaged collagen. Together, these methods enable the characterization of collagen damage in human skin biopsies from burn patients, as well as *ex vivo* thermally injured

human skin samples. These combined methods could enhance the understanding of the role of collagen in human wound healing after thermal injury and potentially assist in clinical decision-making.

**Chapter 5: Hox genes maintain critical roles in the adult skeleton.** Recently, it has been demonstrated that *Hox* expression continues from embryonic stages through postnatal and adult stages exclusively in a skeletal stem cell population. However, whether *Hox* genes continue to function after development has not been rigorously investigated. In this chapter we discuss *Hox11* critical roles in skeletal homeostasis of the forelimb zeugopod (radius and ulna). We generated a *Hoxd11* conditional allele and induced genetic deletion at adult stages. Together, our studies show that *Hox11* genes continuously function in the adult skeleton in a region-specific manner by regulating differentiation of *Hox*-expressing skeletal stem cells into the osteolineage.

## Part II

**Chapter 1. Acceleration of 1,3-Dipolar Cycloadditions by Integration of Strain and Electronic-Tuning.** The 1,3-dipolar cycloaddition between azides and alkynes is enabling new means to probe and control biological processes. A major challenge is to achieve high reaction rates with stable reagents. The optimization of alkynyl reagents has relied on two strategies: increasing strain and tuning electronics. In this chapter we report on the integration of these strategies through both computational and experimental analysis. A computational analysis suggested that a CH→N aryl substitution in dibenzocyclooctyne (DIBO) could be beneficial. In transition states, the nitrogen of 2-azabenzobenzocyclooctyne (ABC) engages in an  $n \rightarrow \pi^*$  interaction with the C=O of  $\alpha$ -azidoacetamides and forms a hydrogen bond with the N-H of  $\alpha$ -diazoacetamides. These interactions act cooperatively with electronic activation of the strained  $\pi$ -bond to increase reactivity. Both ABC and DIBO are accessible in three steps by the alkylidene carbene-mediated ring expansion of commercial cycloheptanones. Our findings enhance the accessibility and utility of 1,3-dipolar cycloadditions and encourage further innovation.

Thesis Supervisor: Ronald T. Raines  
Title: Firmenich Professor of Chemistry

## Acknowledgments

First and foremost, I am grateful to Professor Ronald Raines, who allowed me to work with his group on these projects. His contagious enthusiasm has kept the motivation on high throughout my graduate studies, and his mentorship and support have been pivotal for my success. The outstanding environment that Professor Raines has created and the scientific independence that he promotes has helped me evolve into a confident, independent scientist and thinker.

Much of my research benefited greatly from close collaboration with fellow Raines lab members, for whom I am truly grateful. Thanks to Professor Brian Gold and Dr. I. Caglar Tanrikulu for their guidance and mentorship during my time as a graduate student. Thanks to Dr. Aubrey Ellison, Nile S. Abularrage, and Dr. Trish T. Hoang for their insightful contributions and hard work that helped drive these projects forward. I also would like to thank Kalie, Brian Graham, Emily, Ian, Leland, Lindsey, Matt, Lucas, Robert, Valerie, Jinyi, JoLynn, Jess, Sonja, Yana, Kenton, Vicky, Aniekan, and Thom for making the Raines lab such a fantastic place to work.

I have been fortunate to work with many talented scientists, without whom many of the projects detailed in this thesis would not have been possible. Special thanks to my collaborators Professor Angela L. F. Gibson, Professor Kevin W. Eliceiri, Dr. Jenu V. Chacko, and Dr. Alexandra B. Schroeder.

The impact of my parents, Maribel Monroig and Pedro Dones, on my education and upbringing is impossible to overstate. I can never appreciate enough their constant love and support and being such terrific role models throughout my life. To my brother and sister, Pedro Dones and Adriana Dones, although our age differences created a gap in our joint experiences I look back fondly on the fun times and lessons we have had over the years.

I first discovered my love for chemistry at the University of Puerto Rico, Rio Piedras campus. I'm forever in debt to Professor Ingrid Montes for not only showing me how to love chemistry but also for allowing me to develop myself as an organic chemist in her lab. Prof. Montes inspiring passion for outreach and mentorship were contagious and were instrumental for my development and my current goals. Since I met her, she has been my inspiration for pursuing a higher purpose and recognizing the importance of always taking time to serve the community. I'm also grateful to Sara Delgado and Juan C. Apontes for their mentorship and guidance throughout my undergraduate career. Your presence throughout my last years in college was instrumental to my success as a student and young scientist.

The move to the Massachusetts Institute of Technology was monumental and helped along by many people. Thanks to everyone who made the process better including the Kiessling lab members that have been a great source of advice, encouragement, and laughter as we adapted to the new MIT space. I am particularly grateful to Professor Laura Kiessling and Professor Bradley L. Pentelute for their support and flexibility in acting as my thesis committee at MIT. I appreciate their time and helpful suggestions throughout my time here.

My journey through graduate school also allowed me to seek passions outside of the lab. As a member of an underrepresented community, I felt responsible for fostering a safe, inclusive, and supportive environment in both UW-Madison and MIT. During my time at MIT, I was able to start and developed a new student group with the purpose of providing a space that encourages the success of all underrepresented communities in the Chemistry Department and beyond. The Chemistry Alliance for Diversity and Inclusion (CADI) wouldn't be possible without the help and support from MIT staff, faculty, and students. I want to give special thanks to Professor Tim Jamison for believing in the idea and supporting me to start the group. In addition, to all CADI members, especially Francesca, Diomedes, Charlotte, and Tony, for believing in the idea from day one and being instrumental to the success of the student group. Also, I would like to thank Prof.

Steven Buchwald, Liz McGrath, Jennifer Weisman, Rebecca Teixeira and Danielle Randall for their dedication and incredible support to CADI's success.

In addition, I would like to acknowledge the extended family that I have acquired through my educational journey. To my high school friends that have consistently been present in my life and have shown support since day one. To my chemistry undergraduate friends, Ivan, Luis, Giovanni, Angel, Nelson, and William, you guys kept me motivated and made me a better student allowing me to seek success to a higher level than I ever intended. Finally, to my graduate school family, your love and support throughout this journey have helped to keep me sane and I am very grateful to have made some great friendships while at UW-Madison and MIT. Last but not least, I want to thank Shana for her immense support, encouragement, and patience through my stressful times at MIT, I'm forever grateful.

Finally, I would like to express my deep and sincere gratitude to everyone who has provided me with assistance throughout my graduate career.

## Table of Contents

<b>TITLE PAGE</b> .....	<b>1</b>
<b>ABSTRACT</b> .....	<b>3</b>
<b>ACKNOWLEDGMENTS</b> .....	<b>5</b>
<b>LIST OF FIGURES</b> .....	<b>11</b>
<b>LIST OF TABLES</b> .....	<b>26</b>
<b>TABLE OF SCHEME</b> .....	<b>28</b>
<b>LIST OF ABBREVIATIONS</b> .....	<b>29</b>
<b>PART I</b> .....	<b>32</b>
<b>CHAPTER 1 INTRODUCTION: COLLAGEN MIMETIC PEPTIDES AS A SELECTIVE BINDER FOR DAMAGED COLLAGEN</b> .....	<b>32</b>
<b>1.1.1 ABSTRACT</b> .....	<b>33</b>
<b>1.1.2 INTRODUCTION</b> .....	<b>33</b>
<b>1.1.3 COLLAGEN STABILITY</b> .....	<b>35</b>
<b>1.1.4 CMPS AS INVADING STRANDS</b> .....	<b>38</b>
<b>1.1.5 DAMAGED COLLAGEN</b> .....	<b>41</b>
<b>CHAPTER 2 OPTIMIZATION OF INTERSTRAND INTERACTIONS ENABLES BURN DETECTION WITH A COLLAGEN-MIMETIC PEPTIDE</b> .....	<b>44</b>
<b>1.2.1 ABSTRACT</b> .....	<b>45</b>
<b>1.2.2 INTRODUCTION</b> .....	<b>45</b>
<b>1.2.3 RESULTS AND DISCUSSION</b> .....	<b>48</b>

1.2.4 CONCLUSIONS.....	58
1.2.5 ACKNOWLEDGEMENTS .....	58
1.2.6 NOTES AND REFERENCES .....	58
1.2.7 EXPERIMENTAL.....	59
1.2.8 ANALYTICAL HPLC TRACES .....	65
1.2.9 MALDI-TOF MASS SPECTRA .....	69
<b>CHAPTER 3 A CYCLIC PEPTIDE MIMETIC OF DAMAGED COLLAGEN .....</b>	<b>71</b>
1.3.1 ABSTRACT .....	72
1.3.2 INTRODUCTION .....	72
1.3.3 RESULTS .....	73
1.3.4 DISCUSSION.....	82
1.3.5 CONCLUSION .....	85
1.3.6 ACKNOWLEDGMENT .....	85
1.3.7 EXPERIMENTAL.....	86
1.3.8 NMR SPECTRA .....	97
1.3.9 UPLC TRACES OF CMPS .....	102
<b>CHAPTER 4 OPTICAL IMAGING OF COLLAGEN FIBER DAMAGE TO ASSESS</b>	
<b>THERMALLY INJURED HUMAN SKIN.....</b>	<b>105</b>
1.4.1 ABSTRACT .....	106
1.4.2 INTRODUCTION .....	106
1.4.3 RESULTS.....	110



1.4.4 DISCUSSION.....	116
1.4.5 CONCLUSION .....	118
1.4.6 ACKNOWLEDGMENTS.....	118
1.4.7 METHODS.....	118
<b>CHAPTER 5 HOX GENES MAINTAIN CRITICAL ROLES IN THE ADULT</b>	
<b>SKELETON .....</b>	<b>123</b>
1.5.1 ABSTRACT .....	124
1.5.2 INTRODUCTION .....	124
1.5.3 RESULTS.....	126
5.4 DISCUSSION.....	149
1.5.5 CONCLUSION .....	153
1.5.6 ACKNOWLEDGMENTS.....	154
1.5.7 MATERIALS AND METHODS.....	154
<b>PART II.....</b>	<b>161</b>
<b>CHAPTER 1 ACCELERATION OF 1,3-DIPOLAR CYCLOADDITIONS BY</b>	
<b>INTEGRATION OF STRAIN AND ELECTRONIC-TUNING.....</b>	<b>161</b>
2.1.1 ABSTRACT: .....	162
2.1.2 INTRODUCTION .....	162
2.1.3 DESIGN OF AN OPTIMAL DIPOLAROPHILE .....	164
2.1.4 SYNTHESIS OF ABC.....	170
2.1.5 REACTIVITY OF ABC.....	172

<b>2.1.6 STABILITY OF ABC .....</b>	<b>175</b>
<b>2.1.7 CONCLUSION .....</b>	<b>175</b>
<b>2.1.8 COMPUTATIONAL DETAILS .....</b>	<b>176</b>
<b>2.1.9 ACKNOWLEDGMENTS.....</b>	<b>177</b>
<b>2.1.10 EXPERIMENTAL PROCEDURE .....</b>	<b>178</b>
<b>2.1.11 KINETIC ANALYSES.....</b>	<b>186</b>
<b>2.1.12 KINETIC TRACES.....</b>	<b>189</b>
<b>2.1.13 SUPPORTING INFORMATION FIGURES: .....</b>	<b>192</b>
<b>2.1.14 NMR SPECTRA .....</b>	<b>202</b>
<b>REFERENCES .....</b>	<b>217</b>

## List of Figures

**Figure 1.1.1.** Collagen depiction from fibrils to individual amino acids within each  $\alpha$  chains.

**Figure 1.1.2.** Collagen Mimetic Peptides that have been chemically modify to prevent the formation of homotrimeric collagen binding selectively to damaged collagen.

**Figure 1.1.3.** Structure of triple-helical collagen. Hydrogen bonds, blue dashed lines;  $n \rightarrow \pi^*$  interactions, red dashed lines. Image adapted from Chattopadhyay et al. 2014.

**Figure 1.1.4.** Cartoon depiction of CMPs selectively annealing to the heavily collagen damage site. Upon delivery, “click to release” chemistry can allow drug release specifically at the targeted site.

**Figure 1.2.1.** Molecular models of neighboring Xaa and Yaa positions on strands of a collagen triple helix. (A) When Xaa and Yaa are Pro, there is not a steric clash between the neighboring side chains (cyan). (B) When flp and Flp are placed similarly, clashing fluoro groups (cyan spheres) deter strand-association.

**Figure 1.2.2.** Representation of a collagen-mimetic peptide with a pendant moiety ( $^X$ CMP) annealing selectively to a damaged site within the collagen triple helix but not forming a homotrimeric triple helix.

**Figure 1.2.3.** Analyses of CMPs (0.8 mM) in 50 mM acetic acid by circular dichroism spectroscopy. (A) Spectra of (flpHypGly)<sub>7</sub>, (ProProGly)<sub>7</sub>, and a 1:2 mixture at 4 °C. (B) Graph showing the effect of temperature on the molar ellipticity at 225 nm of (flpHypGly)<sub>7</sub>, (ProProGly)<sub>7</sub>, and a 1:2 mixture. The mixture had  $T_m = 28$  °C. (C) Spectra of (HypflpGly)<sub>7</sub>, (ProProGly)<sub>7</sub>, and a 1:2 mixture at 4 °C. and its mixture at 4 °C. (D) Graph showing the effect of temperature on the molar ellipticity at 225 nm of (HypflpGly)<sub>7</sub>, (ProProGly)<sub>7</sub>, and a 1:2 mixture.

**Figure 1.2.4.** Transformed circular dichroism data for the thermal denaturation of CMP mixtures based on two-state model for triple-helix unfolding. (A) Transformed data of 1:2

(flpHypGly)<sub>7</sub>/(ProProGly)<sub>7</sub> (Figure 1.2.3 B);  $T_m = 28\text{ }^\circ\text{C}$  (B) Transformed data of 2:1 (flpHypGly)<sub>7</sub>/(ProProGly)<sub>7</sub> (Figure 1.2.5 B);  $T_m = 28\text{ }^\circ\text{C}$ .

**Figure 1.2.5.** Analyses of CMPs with circular dichroism spectroscopy. Each solution contained 0.8 mM CMP (or a mixture) in 50 mM acetic acid. Data for (flpHypGly)<sub>7</sub>, (HypflpGly)<sub>7</sub>, and (ProProGly)<sub>7</sub>, but not the 2:1 mixtures, are identical to those in Figure 3. (A) Spectra of (flpHypGly)<sub>7</sub>, (ProProGly)<sub>7</sub>, and a 2:1 mixture at 4 °C. (B) Graph showing the effect of temperature on the molar ellipticity at 225 nm of (flpHypGly)<sub>7</sub>, (ProProGly)<sub>7</sub>, and a 2:1 mixture. The mixture had  $T_m = 28\text{ }^\circ\text{C}$ . (C) Spectra of (HypflpGly)<sub>7</sub>, (ProProGly)<sub>7</sub>, and a 2:1 mixture at 4 °C.

**Figure 1.2.6.** Graph showing the effect of HflpOH on the viability of human fibroblasts (A) and primary human epidermal keratinocytes (B). Data were obtained with a tetrazolium dye-based assay for metabolic activity. Values are the mean  $\pm$  SEM ( $n = 3$ , biological replicates).

**Figure 1.2.7.** Second Harmonic Generation (SHG) channel of collagen fibrils. Scale bar, 500  $\mu\text{m}$ .

**Figure 1.2.8.** Multiphoton microscopy images of the annealing of fluorescently labeled CMP and its compositional isomer to collagen fibers from rat tails. (A) Amino acid sequences of the <sup>Cy5</sup>CMP and <sup>Cy5</sup>CI peptides. (B) Method for probing for damaged collagen in a rat-tail tendon. (C) Superimposed images of a damaged rat-tail tendon using second harmonic generation (SHG) in the green channel and the fluorescence from <sup>Cy5</sup>CMP in the red channel. (D) Superimposed images of the SHG channel of a damaged rat-tail tendon and the fluorescence from the compositional isomer, <sup>Cy5</sup>CI. (E) Bar graph of the mean fluorescence intensity in the indicated regions of interest (ROIs) as determined with ImageJ software.

**Figure 1.3.1.** Scheme showing the molecular mimicry of damaged collagen by a cyclic “host” of two parallel collagen strands. A collagen mimetic peptide with a conjugated pendant “X” (purple) is shown annealing to the damaged collagen.

**Figure 1.3.2.** Chemical structures of the open host (host-o), closed host (host-c), and closed, reduced host (host-r). The macrocyclic rings of host-c and host-r contain 221 atoms.

**Figure 1.3.3.** MALDI–TOF mass spectra of host-o (5757.07), host-c (5728.55), and host-r (5731.67).

**Figure 1.3.4.** Sedimentation equilibrium analysis. Equilibrium gradients (gray circles) for host-o and host-r are shown at four different speeds (20, 26, 34, and 42 k rpm) with models that provide optimal fits (red lines). The host-o data are modeled best as a mixture of monomers and pentamers, whereas the host-r data are modeled best as a mixture of monomers and trimers. The gradients for host-r are mostly linear, due to a near-uniform composition dominated by monomers. In contrast, non-linear behavior seen in host-o gradients indicate appreciable levels of high-molecular weight species present in solution. These trends are apparent at all speeds.

**Figure 1.3.5.** Graphs of analytical ultracentrifugation data obtained at 34,000 rpm for host-o and host-r. (A) Data for host-o fitted to a monomer + pentamer mode. (B) Data for host-r fitted to a monomer + trimer mode.

**Figure 1.3.6.** Binding of immobilized host-o and host-r to a fluorescent CMP. (A) Scheme showing the experimental design. (B) Representative confocal microscopy images. Streptavidin-coated fluorescent beads (red) were treated with biotin-conjugated host-o or host-r and then incubated with fluorescein–CMP (green), which is Ac-Lys(flourescein)-(Ser-Gly)<sub>3</sub>-(Pro-Pro-Gly)<sub>7</sub>. Also shown are images from a negative control of untreated beads and a positive control of beads treated with a biotin–fluorescein conjugate (green), which is biotin-(Gly-Ser)<sub>3</sub>-Lys(flourescein)-NH<sub>2</sub>. Scale bar: 10 μm.

**Figure 1.3.7.** Binding of immobilized host-o and host-r to a fluorescent D-CMP, which is (D-Pro-D-Pro-Gly)<sub>7</sub>. Representative confocal microscopy images are shown. Streptavidin-coated fluorescent beads (red) were treated with host-o or host-r and then incubated with D-CMP–fluorescein (green), as in Figure 1.3.6. Scale bar: 10 μm.

**Figure 1.3.8.** Quantification of binding of immobilized host-o and host-r to a CMP. Streptavidin-coated fluorescent beads were treated with host-o–biotin or host-r–biotin, and then with

fluorescein–CMP, which is Ac-Lys(fluorescein)-(Ser-Gly)<sub>3</sub>-(Pro-Pro-Gly)<sub>7</sub>. Beads were also treated with biotin–fluorescein conjugate (which is biotin-(Gly-Ser)<sub>3</sub>-Lys(fluorescein)-NH<sub>2</sub>), host-o alone, or host-r alone. Values represent the percent of the sample population with fluorescein-labeling relative to that from treatment with biotin–fluorescein.

**Figure 1.3.9.** Circular dichroism spectra of hosts (A), guest CMPs (B) and host·CMP complexes (C). Calculated spectra for noninteracting mixtures of host-r and CMPs are shown (dashed gray lines) together with acquired spectra for host-r·CMP complexes (red lines). Spectra were obtained in 50 mM HOAc at 4 °C.

**Figure 1.3.10.** Circular dichroism spectra of host-o·CMP complexes. Calculated spectra for non-interacting mixtures of host-o and CMPs are shown (dashed gray lines) together with acquired spectra for host-o·CMP complexes (red lines). Spectra were obtained in 50 mM HOAc at 4 °C.

**Figure 1.3.11.** Circular dichroism temperature-denaturation experiments for all three hosts alone (A) and host-r·CMP complexes (B).

**Figure 1.3.12.** Circular dichroism spectra of host-r and (Pro-Hyp-Gly)<sub>7</sub> alone (A), and their complex (B). A spectrum calculated assuming a mixture of non-interacting species is shown as a comparison (dashed gray line). Spectra were obtained in 50 mM HOAc at 4 °C.

**Figure 1.4.1.** The specificity of Cy5-CMP to denatured collagen in patient burn tissue. Stitched z-projections of multiphoton micrographs of (A) Cy5 fluorescence image with regions of interest (ROIs) (yellow circles) showing Cy5-CMP labeling on the deep surface (en face view) of 6 mm biopsies of tangentially excised deep partial-thickness burn tissue, and (B) absence of SHG signal in the same ROIs (yellow circles). (C) Composite image of Cy5 fluorescence and SHG. The region of brighter Cy5 fluorescence near the right side of the image corresponds to a portion of the cut edge of the biopsy where we see some fluorescence signal from the superficial side of the biopsy penetrating through the z stacked images. (D) Burn tissue sample labeled with Cy5-Cl (negative control) imaged with Cy5 parameters and (E) SHG parameters. Yellow ROIs and (F) the composite

image of tissue labeled with Cy5-CI indicating that the dark regions in panel E are not fluorescent in panel D. The Cy5 fluorescence on the circumference of the biopsy corresponds to non-specific binding around the superficial cut edge of the biopsy. Scale bars = 1 mm.

**Figure 1.4.2.** Cy5 excitation of Cy5-CMP reveals collagen damage with depth on cross-sectional views. Shown are the side profiles of a 6 mm biopsy of (A-D) normal non-burned skin and (E-H) skin burned for 3 seconds at 150°C with a custom burn device. (A) Multiphoton excitation of Cy5-CMP shows little fluorescence, while (B) SHG image reveals intact collagen throughout the normal biopsy. In contrast, (E) Cy5-CMP extensively labels the burned sample while the (F) SHG signal is minimal. SHG signal exhibits an inversion of signal intensity to the Cy5 channel, highlighted by the composite images of (C) Cy5-CMP + SHG for normal skin and (G) 3 seconds burned skin. LDH images show that viable cells (blue) are present throughout the (D) non-burned skin and in the (H) deep portion in the 3 seconds burned skin, correlating with intact collagen. Scale bar = 1 mm.

**Figure 1.4.3.** Assessment of Cy5-CMP labeling using widefield fluorescence microscopy. Fluorescence of an ex vivo 6 mm biopsy from (A) normal non-burned skin and (B) burned skin relative to the same samples imaged with multiphoton microscopy in (C) non-burned and (D) burned skin. Scale bar = 1 mm.

**Figure 1.4.4.** Cy5 multiphoton excitation fluorescence images of 6 mm biopsy punches from (A,B) normal non-burned skin and (C,D) burned skin excised from a patient treated with (A,C) Cy5-CMP or (B,D) Cy5-CI. Cy5-CMP shows enhanced binding with greater contrast on the superficial surface of these clinical biopsies. (E) Cy5-CMP and (F) Cy5-CI on non-burned skin compared to (G) Cy5-CMP and (H) Cy5-CI on burned skin, displaying what a wound treated with Cy5-CMP would look like vs normal skin after washing. Cy5-CMP and Cy5-CI appear blue to the naked eye under white light. Note: in images (C) and (D) a liquid droplet from the dye application is visible as an artifact surrounding the punch. Scale bars = 1 mm.

**Figure 1.5.1.** Adult *Hox11*-expressing skeletal stem cells continuously give rise to osteoblasts and osteocytes. (A) *Hoxa11*-eGFP real-time reporter allele demonstrates continuous expression of *Hoxa11* (green) at 12 wk of age. The panel was created by stitching 17 individual 10× images. t, tendon. DAPI, gray. (Scale bar: 200 μm.) Shown is a higher magnification image of the boxed area in A showing localization of *Hoxa11* expression (green) in the periosteum, endosteum, and bone marrow compartment. BM, bone marrow; CB, cortical bone; endo, endosteum; PO, periosteum. DAPI, blue. (Scale bar: 75 μm.) Animals of the indicated genotype were fed on tamoxifen (Tam) chow at 8 to 10 wk of age for a duration of 3 wk to induce deletion and collected at 8 mo of age. Boxes marked “B” and “C” in A represent the approximate locations of magnified images shown in B and C. (B) *Hoxa11*-lineage marked cells (red) are found in the trabecular bone coexpressing osterix (*Osx*) (white). The yellow dashed line outlines the cortical bone, and the white dashed line demarcates the growth plate border. gp, growth plate. DAPI, blue. (Scale bar: 75 μm.) (C) *Hoxa11*-lineage marked cells (red) are also found as osteocytes embedded within the cortical bone coexpressing *SOST* (green). *Hoxa11*-lineage marked cells and DAPI (gray) in the far-left, *SOST* (green) and DAPI (gray) in the middle, and the merged image is shown in the far-right. (Scale bar: 60 μm.) All images: BM, bone marrow; CB, cortical bone; endo, endosteum; PO, periosteum.

**Figure 1.5.2.** Adult *Hox11*-expressing skeletal stem cells continuously contribute to endosteal osteoblasts. Animals harboring the *Hoxa11-CreER<sup>T2</sup>* allele (genotype indicated) were fed on tamoxifen chow for 3 weeks starting at 8- 10 weeks of age and collected at 8-months of age. (A, B) High magnification images of *Hoxa11*-lineage marked osteoblasts (red) co-expressing *Osx* (white) on the endosteal surface. White dashed line demarcates the endosteal surface. DAPI: blue. All images are from the ulna, endo = endosteum, CB = cortical bone. Scale bar, 25μm.

**Figure 1.5.3.** Conditional deletion of *Hox11* function recapitulates the germline null mutation. (A) Schematic illustrating the *Hoxd11* locus. Yellow arrowheads illustrate the inserted loxP sites. Two guide RNAs with the indicated sequences (underlined) along with their corresponding PAM



(highlighted blue) were used to flank exon 2 of *Hoxd11* in order to insert loxP sites. Homology sequences used in the donor sequences are highlighted with thick dark blue line (5' loxP) and thick light blue line (3' loxP). Red arrows marked with P1, P2, and P3 mark the location of the PCR primers used to confirm recombination. Corresponding PCR product sizes are indicated as well. The PCR elongation time was adjusted so that a 300-bp PCR product would appear only if recombination had occurred between the loxP sites. Pregnant dams were fed on tamoxifen chow for 1 wk to induce recombination, and the resulting embryos were collected at E17.5. (B) PCR analysis using the PCR primers produces a robust 600-bp control band only present in the controls and a 300-bp recombined band only present in the conditional mutants. cKO denotes *Hox11* conditional mutants. Skeletal preparations of limbs from (C) WT, (D) littermate control for *Hox11* conditional mutant, (E) *Hox11*<sup>ROSACreERT2</sup> conditional mutant, and (F) *Hox11* germline-null mutant. The red box highlights the zeugopod skeleton.

**Figure 1.5.4.** CRISPR/Cas9 generation of the *Hoxd11* conditional allele. LoxP sites were sequentially targeted both 5' and 3' of *Hoxd11* exon2. Homology sequence used in the donor sequences are highlighted with thick dark blue line (5' loxP) and thick light blue line (3' loxP). Orange arrows mark the approximate location of the PCR primers used to confirm correct targeting. (A) PCR genotyping of founder (F0) animals for insertion of the 5' loxP site. Animals #377, 387, and 394 were sequence verified and male F1 animals were used as stud males for second round of targeting. (B) PCR genotyping of F0 animals for insertion at the 5' loxP (top panel) and 3' loxP (bottom panel). Animals # 742, 743, 745, 750, 763 and 767 were heterozygous for 5' loxP and sequence verified to harbor correctly targeted 3' loxP. Animals #742 and 745 were found to be chimeric. Animal #763 contained the loxP sites in *trans*. Animals # 743, 750 and 767 contained the loxP sites in *cis* and #743 was selected to be the final founder. (C) 8-week old adult with the genotype *ROSA*<sup>CreERT2/LSL-tdTomato</sup>; *Hoxd11*<sup>loxP/loxP</sup> without tamoxifen administration shows minimal recombination visualized by ROSA-lineage marked cells (red). DAPI: blue. Scale bar: 200µm. (D)

PCR analysis shows that the minimal recombination seen in the zeugopod bones do not result in detectable recombined bands (bottom panel) and robust control band (top panel). Three samples are biological replicates of the same genotype. (E) Equally strong detection of the recombined PCR band between zeugopod skeleton and tail sample taken from  $Hox11^{ROSACreERT2}$  conditional mutants collected at 6 months of age.

**Figure 1.5.5.** Deletion of *Hox11* function at adult stages results in the regional disruption in cortical bone homeostasis. *Hox11* conditional mutants with the *ROSA-CreERT<sup>2</sup>* (genotype indicated) allele along with control animals were fed on tamoxifen chow beginning at 8 to 10 wk of age for a total of 3 wk to delete *Hox11* function. Animals were evaluated at 4 mo of age, 6 mo of age, and 1 y of age. (A) Tail samples from all animals collected were analyzed via PCR to assess recombination. A robust 300-bp band in the conditional mutants demonstrates strong recombination. (B) qRT-PCR of *Hoxa11eGFP*-expressing zeugopod skeletal cells from the conditional mutants show robust deletion of *Hoxd11* in the conditional mutants. Data are presented relative to mouse GAPDH using the  $\Delta\Delta C_t$  method. ND, none detected. Error is represented as mean  $\pm$  SEM. (C–H) H&E stains of paraffin bone sections (ulna) of control and  $Hox11^{ROSACreERT2}$  conditional mutant animals. The dashed line demarcates the border between lamellar (above) and abnormal (below) bone. Green brackets demarcate the abnormal matrix. Boxed areas in D and G represent high-magnification images of an individual matrix-embedded cell highlighting the morphological differences between control and *Hox11* conditional mutant osteocyte-like cells. (I) Quantification of cells embedded within the abnormal matrix at 4 mo, 6 mo, and 1 y of age shows a significant increase in cell number in  $Hox11^{ROSACreERT2}$  conditional mutant bone. Error is represented as mean  $\pm$  SEM. Statistics by Student's *t* test. (J) Percentage of osteocytes or osteocyte-like cells in *Hox11* conditional mutant bones that exhibit an ellipsoid shape within lamellar (above dotted line in F–H) and abnormal (below dotted line, green bracket in F–H) bony matrix. Error is represented as mean  $\pm$  SEM. Statistics by Student's *t* test. (K and L) H&E

stains of bones from the humerus of control (*K*) and *Hox11* conditional mutant (*L*) show no differences in morphology at 1 y of age. All images: BM, bone marrow; CB, cortical bone; PO, periosteum. (Scale bar in all images: 100  $\mu\text{m}$ .)

**Figure 1.5.6.** *Hox11*-expressing skeletal stem cells are maintained in the *Hox11* conditional mutants. *Hox11*<sup>ROSACreERT2</sup> conditional mutants were fed on tamoxifen chow for 3 weeks starting at 8-10 weeks of age and collected at 1-year of age. **(A, B)** *Hox11*eGFP-expressing skeletal stem cells (green) are present in the expected locations at 1-year of age in both the control (*A*) and *Hox11* conditional mutants (*B*). All images are from the ulna, PO = periosteum, CB = cortical bone, endo = endosteum, BM = bone marrow. DAPI: blue. Scale bar, 75 $\mu\text{m}$ .

**Figure 1.5.7.** Long-term deletion of *Hox11* function at adult stages do not lead to noticeable gross morphological differences. *Hox11* conditional mutants with the *ROSA-CreERT2* (genotype indicated) allele along with control animals were fed on tamoxifen chow for 3 weeks beginning at 8-10 weeks of age to delete *Hox11* function and evaluated at 4-months, 6-months, and 1 year of age. **(A)** Top panel: 3D rendering from microCT scans of the zeugopod skeleton (radius/ulna) from control and *Hox11*<sup>ROSACreERT2</sup> conditional mutants. Bottom panel: Cross section of the zeugopod skeleton through the distal end at 10% of the entire length of the ulna. **(B)** Table outlining the morphological measurements generated from microCT scans. Statistics by Student's t test; \**p* < 0.05.

**Figure 1.5.8.** Woven bone-like region in the *Hox11* conditional mutant bones has a disorganized collagen matrix. *Hox11* conditional mutants with the *ROSA-CreERT2* (genotype indicated) allele along with control animals were fed on tamoxifen chow for 3 wk beginning at 8 to 10 wk of age to induce deletion, and animals were examined at 6 mo of age. *(A and B)* H&E stains of paraffin-processed bone sections of control and *Hox11*<sup>ROSACreERT2</sup> conditional mutant animals. *(C and D)* Brightfield images of picosirius red stain of consecutive bone sections from *A* and *B*. *(E and F)* Polarized light images of picosirius red stain of bone sections from *C* and *D*. *(G and H)* H&E

stains of paraffin-processed bone sections of control and  $Hox11^{ROSACreERT2}$  conditional mutant animals. (I and J) Consecutive bone sections from G and H stained with  $Cy5CMP$  (red). White dashed line marks border of cortical bone. (K and L) Control (K) and  $Hox11^{ROSACreERT2}$  conditional mutant (L) bone sections stained with TRAP. Note the distinct distribution of TRAP stain in conditional mutant. (M) Quantification of osteoclast number (N. Oc) on bone surface (BS) using the Bioquant Osteo software. Statistics by Student's *t* test. Error is represented as mean  $\pm$  SEM. All images are from the ulna. BM, bone marrow; CB, cortical bone; PO, periosteum. The yellow dashed line demarcates border between lamellar (above) and abnormal (below) bone. ns, not significant. (Scale bar in all images: 100  $\mu$ m.)

**Figure 1.5.9. Adult conditional deletion of Hox11 function lead abnormal matrix at all times points examined.**  $Hox11$  conditional mutants with the *ROSA-CreER<sup>T2</sup>* (genotype indicated) allele along with control animals were fed on tamoxifen chow at 8-10 weeks of age for 3 weeks to delete *Hox11* function and evaluated at 4-months of age, 6-months of age, and 1 year of age. (A-D) H&E stains of control (A, C) and  $Hox11^{ROSACreERT2}$  conditional mutant (B, D) at 4- months and 1-year of age. (E-H) Brightfield images of picosirius red stain of consecutive bone sections from A-D. (I-L) Polarized light images of picosirius red stain of bone sections from E-H. Yellow (B), black (F) white (J) arrows highlight the abnormal matrix in the 4-month old conditional mutant bone. (M, N) Bone sections from control (M) and  $Hox11^{ROSACreERT2}$  conditional mutant (N, 4- months following deletion) were stained with  $Cy5CI$ . Both bone sections do not show staining. White dashed line marks border of cortical bone. All images are from the ulna, PO = periosteum, CB = cortical bone, BM = bone marrow. Scale bar in all images: 100 $\mu$ m.

**Figure 1.5.10. Distribution of TRAP staining, but not number of osteoclasts is distinct in Hox11 conditional mutant bones.**  $Hox11$  conditional mutants with the *ROSA-CreER<sup>T2</sup>* (genotype indicated) allele along with control animals were fed on tamoxifen chow at 8-10 weeks of age for 3 weeks to induce deletion of *Hox11* function and collected at 6-months of age. (A-B) Higher

magnification of osteoclasts to show apparent TRAP stain leakage into cortical bone matrix. Yellow dashed line demarcates the endosteal bone surface. TRAP enzyme leaked into the bone matrix in mutants (blue arrow). Scale bar: 25 $\mu$ m (C, D) TRAP stain with hematoxylin for visualization of nuclei. No cells were associated with TRAP stain in cortical bone (yellow arrow).

**Figure 1.5.11.** Osteoblast differentiation is perturbed in Hox11 conditional mutant bone. Hox11 conditional mutants with the *Hoxa11-CreER<sup>T2</sup>* allele (genotype indicated) along with control animals were fed on tamoxifen chow for 3 wk starting at 8 to 10 wk of age and collected at 4 mo of age. (A) Brightfield image of a bone section from a control animal overlaid with Hox11-lineage marked cells (red) shows contribution to osteocytes. (B) Brightfield image of bone section from a Hox11<sup>Hoxa11CreERT2</sup> conditional mutant overlaid with Hox11-lineage-positive cells (red) shows contribution to abnormal bone matrix. (C and D) Control (C) and Hox11<sup>Hoxa11CreERT2</sup> conditional mutant (D) bone stained with RUNX2 (magenta). DAPI, gray. White arrows in C and D mark the endosteal bone surfaces. (E and F) Control (E) and Hox11<sup>Hoxa11CreERT2</sup> conditional mutant (F) bone stained with osteopontin (Opn, green). (G and H) Control (G) and Hox11<sup>Hoxa11CreERT2</sup> conditional mutant (H) bone sections stained with osteocalcin (Ocn, green). (I–J'') Hoxa11eGFP (green) and DAPI (blue) in I and J, Hoxa11-lineage marked cells (red) and DAPI (blue) in I' and J', and merged images in I'' and J''. Control (I–I'') and Hox11<sup>Hoxa11CreERT2</sup> conditional mutant (J–J'') bone sections show Hoxa11-lineage marked (red), non-Hoxa11eGFP endosteal surface osteoblasts (yellow arrowhead). Notice stark difference in morphology. All images are from the ulna. DAPI, blue (unless noted otherwise); Hox11-lineage marked cells, red. CB, cortical bone; endo, endosteum. The white dashed line demarcates the endosteal surface. (Scale bars in all images: 50  $\mu$ m.)

**Figure 1.5.12.** Hox11 conditional mutant osteocytes fail to form dendrites or express SOST. Hox11 conditional mutants with the *ROSA-CreER<sup>T2</sup>* (genotype indicated) allele along with control animals were fed on tamoxifen chow beginning at 8 to 10 wk of age for 3 wk to

delete *Hox11* function, and animals were evaluated at 4 mo of age, 6 mo of age, and 1 y of age for *C–E*. (*A–C*) Control (*Left*) and  $\text{Hox11}^{\text{ROSACreERT2}}$  conditional mutants (*Right*) were treated with silver nitrate. Green dashed lines demarcate the lamellar (above) and abnormal (below) bone. Brackets outline abnormal bone matrix. (*D*) High magnification of osteocytes from the white-boxed area in *B*. *Hox11* conditional mutants with the *Hoxa11-CreERT2* allele (genotype indicated) along with control animals were fed on tamoxifen chow for 3 wk starting at 8 to 10 wk of age and collected at 4 mo of age for *E–M*. (*E* and *F*) Control (*E*) and  $\text{Hox11}^{\text{Hoxa11CreERT2}}$  conditional mutant (*F*) bone sections showing *Hox11*-lineage marked cells (red) that contributed to osteocytes. (*G* and *H*) Control (*G*) and  $\text{Hox11}^{\text{Hoxa11CreERT2}}$  conditional mutant (*H*) bone sections stained with SOST (green). (*I* and *J*) Merged images of *E* and *G* in *I* or *F* and *H* in *J* showing overlap or the lack thereof of *Hox11*-lineage marked cells (red) and SOST (green). The yellow dashed line in *E–J* outline the cortical bone. (*K* and *L*) Close-up of osteocytes in white-boxed region in *I* and *J*. (*M*) Quantification of *Hox11*-lineage marked cells (red) that also express SOST (green). Error is represented as mean  $\pm$  SEM. Statistics by Student's *t* test. All images are from the ulna. DAPI, gray. BM, bone marrow; CB, cortical bone; PO, periosteum. (Scale bar: 25  $\mu\text{m}$  [*A–C*], 10  $\mu\text{m}$  [*D*], 100  $\mu\text{m}$  [*E–J*], 10  $\mu\text{m}$  [*K* and *L*].)

**Figure 2.1.1.** Optimization strategies employed to accelerate the strain-promoted cycloaddition reactivity of cyclooctynes. (A) Heteroatom-incorporation tunes alkyne electronics; benzannulation increases strain. (B) Cyclooctyne substitutions can engender steric repulsion or electrostatic attraction. (C) Strategic heteroatom placement in azabenzocyclooctyne (ABC) combines electronic-tuning with increasing strain while replacing steric repulsion with a potentially dipole-specific hydrogen bond. Second-order rate constants ( $\text{M}^{-1}\text{s}^{-1}$ ) are for the reaction with benzyl azide, *N*-benzylazidoacetamide,<sup>a</sup> or *N*-benzyl diazoacetamide<sup>b</sup> (this work).

**Figure 2.1.2.** Combining increased strain with electronic activation. (A) Optimized geometries and NBO charge on the alkynyl carbons of DIBO, DIBAC, 2-ABC, and 6-ABC calculated at the

M06-2X/6-311++G(d,p) employing the IEFPCM solvation model (water). (B) Interactions of the distorted alkyne with the syn-periplanar C–N bond in 2-ABC and the anti-periplanar C–N bond in 6-ABC. Shown are natural bonding orbitals depicting  $\pi_{CC} \rightarrow \sigma^*_{CN}$  interactions, second-order perturbations energies, and PNBO overlap integrals ( $S$ ). Strain energies ( $SE$ ) were calculated with the isodesmic equation in Figure 2.1.S3.

**Figure 2.1.3.** Computational analysis of cycloadditions with *N*-methylazidoacetamide (1) and *N*-methyldiazoacetamide (2). (A,B) Optimized transition state geometries and free energies of activation (kcal/mol) calculated at the M06-2X/6-311++G(d,p) level employing the IEFPCM solvation model (water). (C) Distortion/Interaction (Strain–Activation) analysis.

Comparison of hydrogen bonding interactions in 2-ABC cycloadditions with *N*-methylazidoacetamide (1) and *N*-methyldiazoacetamide (2). Second-order perturbations (black) and steric repulsion (red) obtained from the NBO analysis provide a measure of relative hydrogen bond strengths.

**Figure 2.1.4.** Comparison of interactions in 2-ABC cycloadditions with *N*-methylazidoacetamide (1) and *N*-methyldiazoacetamide (2). (A) Second-order perturbations (black) and steric repulsion (red) obtained from the NBO analysis. (B) Key stabilizing orbital interactions:  $N \cdots C=O$   $n \rightarrow \pi^*$  interaction with azide **1** and  $N \cdots H-N$  hydrogen bond with diazo compound **2**.

**Figure 2.1.5.** Second-order rate constants for the 1,3-dipolar cycloaddition of DIBO or ABC with dipoles **5–7** in  $CH_2Cl_2$ . Values are the mean from triplicate experiments.

**Figure 2.1.6.** Effect of hydrogen bonding on the 1,3-dipolar cycloaddition of ABC with *N*-benzyldiazoacetamide (**6**). (A)  $^1H$  NMR shifts of the C3-H (red) proton in the product of the cycloaddition of ABC with dipole **6** or its *N*-methyl derivative in  $CH_2Cl_2$ . (B) Second-order rate constants for the reaction of ABC with dipoles **5** and **6** in  $CH_2Cl_2$  (as in Figure 2.1.5), MeOH, and PBS containing DMSO (2% v/v). Values are the mean from triplicate experiments.

**Figure 2.1.7.** Kinetic traces for the reactions of ABC with (A) azide **5**, (B) diazo compound **6**, (C) diazo compound **7**, (D) azide **11** ( $k = 1.0 \text{ M}^{-1}\text{s}^{-1}$ ), and (E) diazo compound **12** ( $k = 0.75 \text{ M}^{-1}\text{s}^{-1}$ ); and the reactions of DIBO with (F) azide **5**, (G) diazo compound **6**, and (H) diazo compound **7**. All reactions were carried out in  $\text{CH}_2\text{Cl}_2$  at  $26 \text{ }^\circ\text{C}$  and were monitored by HPLC. Values are the mean  $\pm$  SD for triplicate experiments.

**Figure 2.1.8.** Kinetic traces for the reactions of ABC with (A) azide **5**, (B) diazo compound **6**, (C) azide **11**, and (D) diazo compound **12**. All reactions were carried out in MeOH at  $26 \text{ }^\circ\text{C}$  and were monitored by HPLC. Values are the mean  $\pm$  SD for triplicate experiments.

**Figure 2.1.9.** Kinetic traces for the reactions of ABC with (A) azide **5**, (B) diazo compound **6**, (C) azide **11**, and (D) diazo compound **12**. All reactions were carried out in PBS containing DMSO (2% v/v) at  $26 \text{ }^\circ\text{C}$  and were monitored by HPLC. Values are the mean  $\pm$  SD for triplicate experiments.

**Figure 2.1.S1.** Optimized transition state geometries for the *syn* reaction of *N*-methylazidoacetamide **1** with 2-ABC at (A) the M06-2X/6-311++G(d,p) employing the IEFPCM solvation model for water, and (B) the B97D/6-311+G(d,p) employing the CPCM solvation model for water.

**Figure 2.1.S2.** Optimized transition state geometries for the reaction of *N*-methylazidoacetamide **1** and *N*-methyldiazoacetamide **2** with ABC at the M06-2X/6-311++G(d,p) employing the IEFPCM solvation model for water (A), and the B97D/6-311+G(d,p) employing the CPCM solvation model for water (B).

**Figure 2.1.S3.** Isodesmic equations used to calculate strain energies of dibenzocyclooctyne (DIBO), dibenzoazacyclooctyne (DIBAC), 2-azabenzobenzocyclooctyne (2-ABC), and 6-azabenzobenzocyclooctyne (6-ABC) calculated at the M06-2X/6-311++G(d,p) employing the IEFPCM solvation model (water). A correction of 2.2 kcal/mol was used to account for the nonzero strain energy of cyclohexane.



**Figure 2.1.S4.** Combining increased strain with electronic activation. (A) Optimized geometries and NBO charge on each alkyne carbon of dibenzocyclooctyne (DIBO), dibenzoazacyclooctyne (DIBAC), 2-azabenzobenzocyclooctyne (2-ABC), and 6-azabenzobenzocyclooctyne (6-ABC) calculated at the B97D/6-311+G(d,p) employing the CPCM solvation model (water). (B,C) Natural bonding orbitals depicting  $\pi_{CC} \rightarrow \sigma^*_{CN}$  interactions with the the *syn*-periplanar C–N bond in 2-ABC (B) and *anti*-periplanar C–N bond in 6-ABC (C).

**Figure 2.1.S5.** Computational analysis of cycloadditions with *N*-methylazidoacetamide **1** and *N*-methyldiazoacetamide **2**. (A,B) Optimized transition state geometries and free energies of activation (kcal/mol) calculated at the B97D/6-311+G(d,p) level employing the CPCM solvation model (water). (C) Distortion/Interaction (Strain–Activation) analysis.

**Figure 2.1.S6.** Comparison of hydrogen bonding interactions in 2-ABC cycloadditions with *N*-methylazidoacetamide **1** (left) and *N*-methyldiazoacetamide **2** (right). The N $\cdots$ N distance (red) is the basis for steric repulsion. Second-order perturbations obtained from the NBO analysis provide a measure of relative hydrogen bond strengths. Optimized transition state geometries are from Figure S5.

**Figure 2.1.S7.** Effect of hydrogen bonding on the 1,3-dipolar cycloaddition of ABC with *N*-benzylazidoacetamide (**5**) and its *N*-methylated derivative.  $^1\text{H}$  NMR shifts of the C3-H (red) proton in the product of the cycloaddition of ABC with dipole **5** or its *N*-methyl derivative in  $\text{CH}_2\text{Cl}_2$ . A single regioisomer is observed with dipole **5** whereas two regioisomers are observed for the *N*-methylated derivative.

**Figure 2.1.S8.** Stability of DIBAC and ABC in the presence of 1 mM reduced glutathione and 0.2 mM oxidized glutathione in PBS containing DMSO (2% v/v) at 37 °C. (A) Concentration of remaining DIBAC and ABC as determined by HPLC. (B) Natural logarithm of the concentration of DIBAC and ABC over time in order to determine second order rate constants of degradation. With respect to reduced glutathione, the second-order rate constants were  $0.05 \text{ M}^{-1}\text{s}^{-1}$  and

$0.10 \text{ M}^{-1}\text{s}^{-1}$  for DIBAC and ABC, respectively. Values are the mean  $\pm$  SD for triplicate experiments. (Error bars are smaller than the data points.)

## List of Tables

**Table 1.1.1.** Pyrrolidine ring puckers preferred at the Xaa and Yaa position of natural and fluoro substituted proline.

**Table 1.2.1.** Relative Xaa···Yaa interaction energies (kcal/mol) of 4-substituted proline residues in a cross-section of a collagen triple helix.

**Table 2.1.1.** Effect of nitrogen placement in dibenzocyclooctynes. Activation parameters (kcal/mol) were calculated at the M06-2X/6-311++G(d,p) employing the IEFPCM solvation model (water). Preferred regioisomers are indicated with energies in bold typeface.

**Table 2.1.S1.** Energies and free energies of activation (kcal/mol) for cycloadditions of *N*-methyl diazoacetamide and *N*-methyl azidoacetamide with constitutional isomers of dibenzoazacyclooctyne (DIBAC). Geometries were optimized at both M06-2X/6-311++G(d,p) employing the IEFPCM solvation model and B97D/6-311+G(d,p) employing the CPCM solvation model for either CH<sub>2</sub>Cl<sub>2</sub> or water.<sup>a</sup> Energies for the preferred regioisomer are in bold typeface.

**Table 2.1.S2.** Distortion/Interaction (Activation–Strain) analysis of energies (kcal/mol) for cycloadditions of *N*-methyl azidoacetamide **1** with constitutional isomers of dibenzoazacyclooctyne (DIBAC). Geometries optimized at both M06-2X/6-311++G(d,p) employing the IEFPCM solvation model for either CH<sub>2</sub>Cl<sub>2</sub> or water, and B97D/6-311+G(d,p) employing the CPCM solvation model for either CH<sub>2</sub>Cl<sub>2</sub> or water. Energies for the preferred regioisomer are in bold typeface.

**Table 2.1.S3.** Distortion/Interaction (Activation–Strain) analysis of energies (kcal/mol) for cycloadditions of *N*-methyl diazoacetamide **2** with constitutional isomers of dibenzoazacyclooctyne (DIBAC). Geometries optimized at both M06-2X/6-311++G(d,p) employing the IEFPCM solvation model for either CH<sub>2</sub>Cl<sub>2</sub> or water, and B97D/6-311+G(d,p) employing the CPCM solvation model for either CH<sub>2</sub>Cl<sub>2</sub> or water. Energies for the preferred regioisomer are in bold typeface.

**Table 2.1.S4.** Distortion/Interaction (Activation–Strain) analysis of energies (kcal/mol) for cycloadditions of *N*-methyl diazoacetamide **2** with constitutional isomers of dibenzoazacyclooctyne (DIBAC). Geometries optimized at both M06-2X/6-311++G(d,p) employing the IEFPCM solvation model for either CH<sub>2</sub>Cl<sub>2</sub> or water, and B97D/6-311+G(d,p) employing the CPCM solvation model for either CH<sub>2</sub>Cl<sub>2</sub> or water. Energies for the preferred regioisomer are in bold typeface.

**Table of Scheme**

**Scheme 1.** Synthesis of ABC and Putative Mechanism for the Alkylidene Carbene Ring-Expansion of the Intermediate.

### List of Abbreviations

ACN	acetonitrile
CD	circular dichroism
CHCA	$\alpha$ -cyano-4-hydroxycinnamic acid
CMP	collagen mimetic peptide
DIC	<i>N,N'</i> -diisopropylcarbodiimide
DCM	dichloromethane
DMF	dimethylformamide
Fmoc	fluorenylmethyloxycarbonyl
HOBt	hydroxybenzotriazole
MALDI–TOF MS	matrix-assisted laser desorption/ionization time-of-flight mass spectrometry
TEA	triethylamine
<i>t</i> Bu	<i>tert</i> -butyl
TFA	trifluoroacetic acid
TIS	triisopropylsilane
ABC	2-azabenzocyclooctyne
CPCM	conductor-like polarizable continuum model
DIBAC	dibenzoazacyclooctyne
DIBO	dibenzocyclooctyne
DIFO	difluorocyclooctyne
diF-SNO-OCT	difluoro-sulfur, nitrogen, and oxygen-containing heterocyclic cyclooctyne
DMSO	dimethyl sulfoxide
EDC	1-ethyl-3-(3-dimethylaminopropyl)carbodiimide
HPLC	high-performance liquid chromatography
IEFPCM	integral equation formalism of the polarizable continuum model

LiHMDS	lithium bis(trimethylsilyl)amide
NBO	natural bonding orbital
<i>n</i> -ABC	<i>n</i> -azabenzobenzocyclooctyne ( $n = 2-6$ )
OCT	cyclooctyne
PBS	phosphate-buffered saline
PNBO	pre-orthogonal natural bonding orbital
SPAAC	strain-promoted azide-alkyne cycloaddition
TFA	trifluoroacetic acid
THF	tetrahydrofuran
TS	transition state
UFF	universal force field

## **Part I**

### **Chapter 1**

#### **Introduction: Collagen Mimetic Peptides as a Selective Binder for Damaged Collagen**



### 1.1.1 Abstract

Collagen is the most abundant protein in animals, making up to 30% of the whole-body protein content. In humans, collagen is the main structural protein of the connective tissues and the most prevalent component of the extra-cellular matrix. Type I fibrillar collagen is ubiquitous in bones, skin, and tendons, providing elasticity, stability and support. The term “collagen disease” was first introduced by Klemperer and coworkers in the 1950s. This type of disease can cause fibrinoid degeneration or changes in the collagen fibers that denature the collagen triple helix. Collagen mimetic peptides (CMPs), variants that are monomeric in solution but have high ability to anneal with damaged collagen, is a growing tool in the biomedical field for the detection and treatment of collagen-related diseases. This chapter provides a review of recent developments in the field of damaged collagen targeting for studying collagen-related diseases and injuries.

### 1.1.2 Introduction

Collagen is the most abundant protein in animals, making up to 30% of the whole-body protein content. In humans it is the main structural protein of the connective tissues, comprising 75% of the human skin, and is the most prevalent component of the extra-cellular matrix.<sup>1</sup> Collagen consist of three parallel polypeptide strands in a right-handed, polyproline type II helical conformation (Figure 1.1.1).<sup>2</sup> Structurally, collagen is mainly constituted of three amino acids: glycine, proline, and hydroxyproline. Each  $\alpha$  chain in the collagen triple helix is composed of thousands of amino acids in which every third residue is glycine (Gly) and results in the Xaa-Yaa-Gly repeat unit.<sup>7</sup> Although the amino acids in positions Xaa and Yaa can vary depending on the type of collagen (I, II, III, and IV), (2*S*,4*R*)-4-hydroxyproline (Hyp) and (2*S*)-proline (Pro) are the most common, making Pro-Hyp-Gly the most common triple repeat in collagen strands (10.5%).<sup>3</sup>

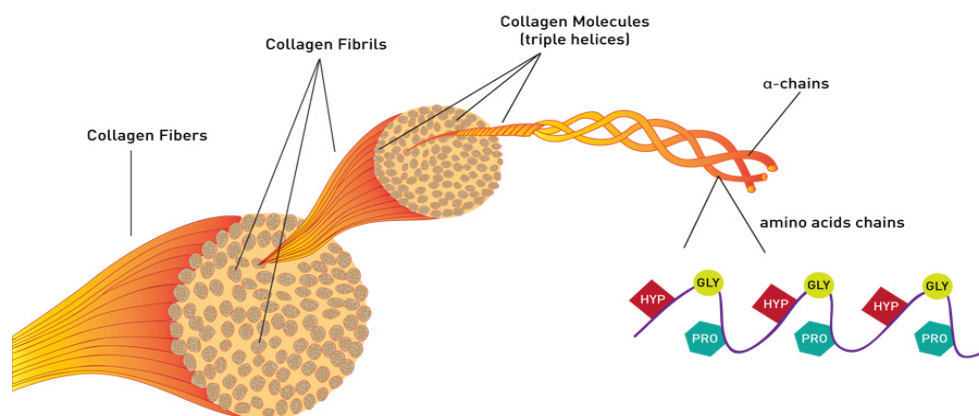


**Figure 1.1.1.** Collagen depiction from fibrils to individual amino acids within each  $\alpha$  chains.

The unique alpha helical structure of collagen allows, through chemical modifications, alteration to the stability of collagen strands. This has allowed a range of CMPs, from hyperstable constructs to CMPs that lack the necessary stability to form collagen triple helices. Even though these chemically modified CMPs are not capable of forming homotrimeric triple helices, natural collagen lacks such modification, allowing for binding. Utilizing this invading strand strategy, research in the field has shown that damaged collagen can be targeted for detection and/or treatment of such atypical collagen (Figure 1.1.2). The ubiquity of collagen and the prevalence of injuries and diseases that disrupt endogenous collagen suggest widespread utility for this approach but still the biological applicability is poorly understood.

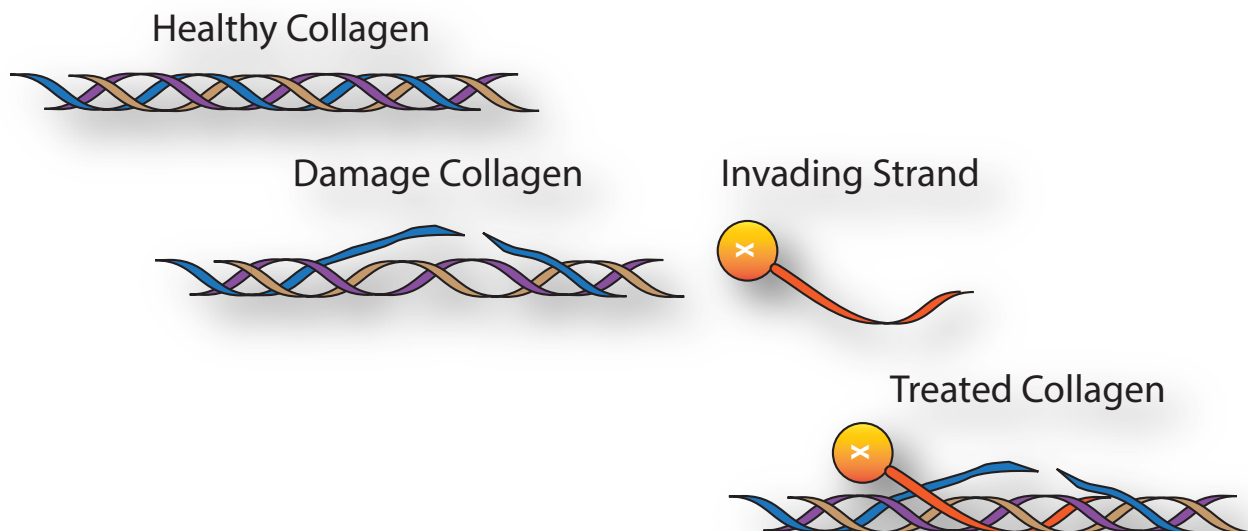


**Figure 1.1.2.** Collagen Mimetic Peptides that have been chemically modified to prevent the formation of homotrimeric collagen binding selectively to damaged collagen.

### 1.1.3 Collagen Stability

Collagen is a family of extracellular matrix proteins with broad diversity in both structure and function. Among the 28 different types of collagen, type I fibrillar collagen is highly prevalent in bones, skin and tendons, providing elasticity, stability and support.<sup>4</sup> Its distinctive structure comes from three parallel polypeptide chains packed together in a polyproline-II-like helix that come together in a right-handed triple helix.<sup>2</sup> These triple helical structures are composed of three amino acid repeats Xaa-Yaa-Gly, where Xaa and Yaa can be any amino acid.

The formation of stable collagen structure is possible through various stereoelectronic effects. Although amino acids at the Xaa and Yaa positions can vary, the tight packing of PPII helices mandates that every third residue be Gly.<sup>5</sup> Furthermore, collagen staggers with a one-residue offset of the polypeptide chains, allowing the ideal arrangement for stabilizing interactions, such as N-H $\cdots$ O=C hydrogen bonds, the *gauche* effect, and n $\rightarrow$  $\pi^*$  interactions (Figure 1.1.3).<sup>6-9</sup> Even though

Pro analogs are not required at the Xaa and Yaa position, the abundance of such amino acids predisposes the  $\phi$  and  $\psi$  angles of the amino acid for a triple-helix formation.<sup>1</sup>

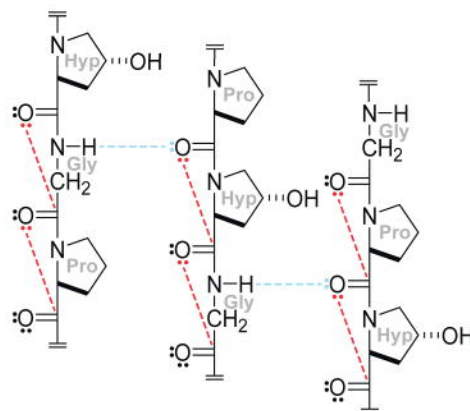
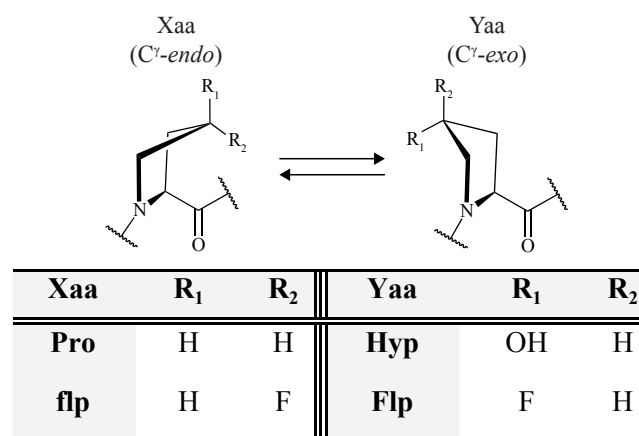


**Figure 1.1.3.** Structure of triple-helical collagen. Hydrogen bonds, blue dashed lines;  $n \rightarrow \pi^*$  interactions, red dashed lines. Image adapted from Chattopadhyay et al. 2014.

Abundant research has been conducted in the past few decades in deciphering the role of different amino acid residues and proline analogs that form hyperstable collagen. In nature, the post-translational modification by prolyl hydroxylase of Pro to Hyp at the Yaa position of collagen is the single most prevalent modification in humans. Using CMPs (ProProGly)<sub>10</sub> and (ProHypGly)<sub>10</sub>, Prockop and co-workers showed that this subtle change in Nature's most-common repeat (ProHypGly) greatly enhances the thermostability ( $T_m$ )—temperature at the midpoint of the thermal transition between a triple helix and its component strands—of the triple-helix.<sup>10</sup> Berman and coworkers attribute this stability to the water-mediated hydrogen bonding in Hyp, but when exchanged with (2S,4R)-4-fluoroproline (Flp), which cannot form strong hydrogen bonds, the stabilizing effect increases.<sup>11</sup> Stabilization is rather attributed to the gauche effect and the preferred conformation of the pyrrolidine-ring pucker at the Xaa and Yaa position. A  $C^\gamma$ -endo and  $C^\gamma$ -exo pyrrolidine-ring pucker is preferred at the Xaa and Yaa position, respectively, in stable triple-helical structures (Table 1.1.1).<sup>12</sup> Substituents at the 4-position of a proline residue can enforce the

preferred pyrrolidine-ring pucker via a gauche<sup>13</sup> or steric<sup>14</sup> effect, lowering the entropic cost for forming a triple helix and increasing its conformational stability.<sup>1</sup> For example, the stereospecific installation of a more electronegative atom, the fluoro group, generates a gauche effect that leads to a *C<sup>γ</sup>-endo* pucker in (2*S*,4*S*)-4-fluoroproline (flp) and strengthens the *C<sup>γ</sup>-exo* pucker in Flp to a greater extent than does the 4*R*-hydroxy group of Hyp.<sup>8, 15, 16</sup>

**Table 1.1.1.** Pyrrolidine ring puckers preferred at the Xaa and Yaa positions of natural and fluoro substituted proline.



A hyperstable CMP can also be achieved by the substitution of natural amino acids with their aza-amino acid counterparts. Even though hydrogen bonds in collagen are already maximized, by incorporating an aza-glycine (replace the  $\alpha$ -C of Gly with a N-atom) within the collagen backbone, the Chenoweth lab was able to increase the number of interfacial cross-strand hydrogen bonds, leading to hyperstability in the triple-helical form.<sup>17, 18</sup> For example, a single addition of an aza-glycine moiety to a CMPs such as (ProHypGly)<sub>7</sub> increases the thermal stability of its triple helix by around 10 °C.<sup>19</sup> This study reiterates the fundamental importance of hydrogen bonding and its stabilizing potential in collagen systems. Although the combination of both the

fluoro group and aza-glycine has yet to be explored, it presents a new unique way to modulate the stability of collagen mimetic peptides.

#### 1.1.4 CMPs as Invading Strands

Strand invasion plays a key role in molecular biology. Natural collagen contains loops or interruptions in its triple helix, making these domains accessible to certain CMPs and collagen proteins.<sup>20-22</sup> When considering an optimal CMP invading strand, multiple routes have been taken to engineer such peptides. These approaches can be separated in two groups, thermal denaturation of collagen strands prior to application and chemical modifications to the collagen backbone that destabilize the homotrimeric triple helix formation and allows for binding to natural damaged collagen.

Even though (ProHypGly)<sub>n</sub> forms monomeric triple helices of collagen, Yu and coworkers have shown that when they thermally dissociate CMPs to single strands before application, such peptides are capable of binding to denatured collagen.<sup>23, 24</sup> Although successful, competition between homotrimerization and heterotrimerization after the thermal denaturation can lessen the effectiveness of the probe, affecting the overall binding.

Chemical modification of CMPs can be exploited to destabilize triple helix formation through stereoelectronic effects and compatibility of each residue in the Xaa-Yaa-Gly repeat. This phenomenon can be seen in Nature in cases such as osteogenesis imperfecta (OI), a hereditary disorder that causes mutation of Gly to a bulkier residue (Ala, Arg, Asp, Cys, Glu, Ser, and Val) destabilizing the collagen matrix and affecting the connective tissues in the body.<sup>25, 26</sup> Analogous to Nature, the chemical modifications of Gly to develop CMPs have a significant toll on stability due to its internal position within the helix, preventing binding even in the presence of natural damaged collagen.<sup>6</sup>

Similarly, deficiency of prolyl 4-hydroxylase (P4H), which catalyzes the hydroxylation of proline in the Yaa position, has been correlated to a number of pathophysiological diseases such

as fibrotic diseases<sup>27</sup> and breast cancer<sup>28</sup>. In this particular case, proline's tertiary amide has a significant population of both the trans and the cis isomers, whereas all peptide bonds in collagen are trans, causing destabilization of the strand.<sup>29</sup> As mentioned before, hydroxylation of the Yaa position forces the C<sup>γ</sup>-*exo* pyrrolidine-ring pucker, stabilizing the overall triple helical stability. Using stereoelectronic effects, the field has worked on developing the optimal CMP invading strand utilizing proline analogs.

An optimal invading strand CMP is a highly soluble monomer under physiological conditions, but forms strong triple helices with denatured natural collagen strands. To search for such (XaaYaaGly)<sub>7</sub> variants, it is required to define two sets of proline analogs that are compatible with the steric and electronic requirements at the Xaa and Yaa positions.<sup>1</sup> Two known examples of monomeric CMPs—(ProProGly)<sub>7</sub>, (flpFlpGly)<sub>7</sub>—have shown to be successful in binding both in vitro and ex vivo denatured collagen.<sup>30</sup> In the case of (ProProGly)<sub>7</sub>, the lack of preorganization of the pyrrolidine rings results in a lower  $K_{trans/cis}$  at the Yaa position, destabilizing the triple helical formation. For (flpFlpGly)<sub>7</sub>, despite appropriate preorganization of main chain torsion angles, the fluorine atoms of flp and Flp residues in alternating strands are proximal, and the C–F dipoles interact unfavorably, preventing the formation of collagen triple helices. Still, mixtures of (flpFlpGly)<sub>7</sub> and (ProProGly)<sub>7</sub> produce stable triple helices because of the preorganization of (flpFlpGly)<sub>7</sub> and the minimal steric clashes between flp/Flp and neighboring Pro residues. This strategy has led CMPs to emerge as viable invading strands technology for targeting of collagen degradation and remodeling.<sup>31</sup>

Even though selective recognition by collagen-binding domains such as fibronectin, integrins, and laminin allows for the detection and treatment of collagen-related diseases, these collagen binders mostly focus on intact collagen binding and show no selectivity between damaged and nondamaged collagen triple helices.<sup>32-35</sup> To circumvent this nonselective binding, delivery of therapeutics typically involves systemic administration of therapeutics or localized delivery of

therapeutics to the target site. On the other hand, CMPs can selectively identify denatured collagen by preventing homotrimerization and hybridizing with the host tissue through the creation of a triple helix (Figure 1.1.2). Their capacity to target unfolded collagen is of prime interest for the detection and treatment of pathological conditions that cause collagen degradation, such as cancer, atherosclerosis, arthritis, and fibrosis.

Currently, the field has focused on detection of damaged collagen using CMPs as imaging agent carriers; nevertheless, effective treatment procedures are yet to be explored. It has been shown that the addition of small molecules and peptides to either end of the polypeptide chain does not affect the heterotrimeric stability of the collagen triple helix. Combining CMPs' targeted delivery with bioorthogonal uncaging reactions or "click to release" chemistry can significantly enhance control over chemical and biological manipulations in collagen-related diseases, enabling instantaneous, self-immolative, and traceless release of the drug of interest at the target site (Figure 1.1.4).<sup>36, 37</sup> Understanding how collagen manifests in normal tissues and in a pathological state is crucial for understanding damaged collagen and its potential as a therapeutic target.

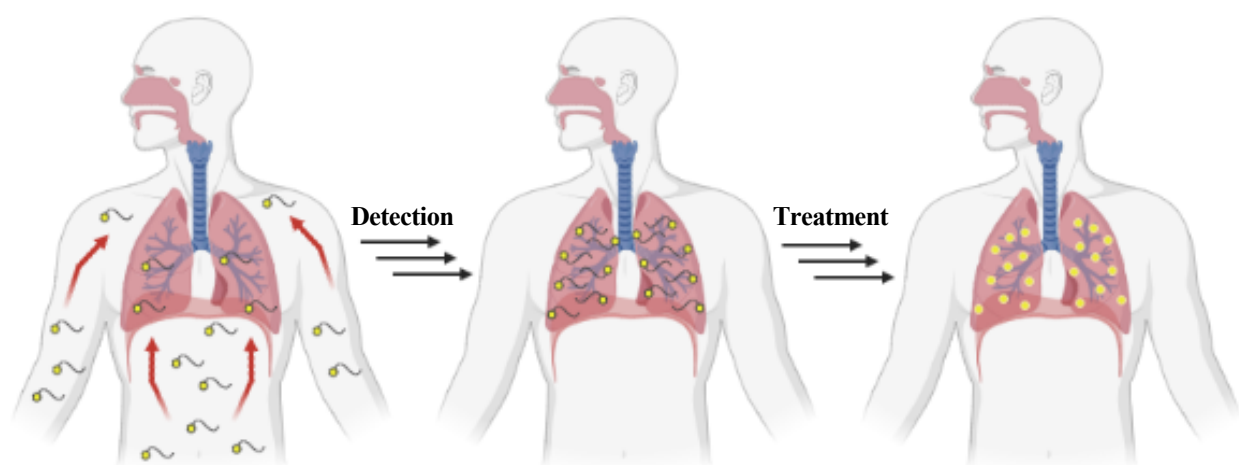


**Figure 1.1.4.** Cartoon depiction of CMPs selectively annealing the heavily collagen damage site. Upon delivery, "click to release" chemistry can allow drug release specifically at the targeted site.



### 1.1.5 Damaged Collagen

Collagen's ubiquitous presence throughout the extracellular matrix and connective tissues plays a key role in maintaining structural integrity of the human body. As first introduced by Klemperer and coworkers in the 1950s, the term "collagen disease" was based on the morphological observation of fibrinoid degeneration or changes in the collagen fibers.<sup>38</sup> Since then, abnormality in the structure, synthesis, or degradation of collagen has been correlated with diseases such as fibrosis, cancer, arthritis and osteoporosis.<sup>39-43</sup> Better understanding the constitutional and biological pathology of collagen diseases is crucial to aid the design and construction of probes that can detect and treat such diseases.

Collagen visualization in the past decades has soared thanks to the early developments of multiphoton microscopy (MPM) to probe live cells and tissues.<sup>44-46</sup> This technology largely solved long-standing problems of confocal microscopy including photobleaching and penetration-depth limitations. By the late 1990s, other nonlinear optical methods such as second harmonic generation (SHG) emerged in the biological realm, increasing imaging depths due to longer excitation wavelengths and applicability to a wide range of tissues, even those like collagen that do not autofluoresce.<sup>47, 48</sup> These developments have put SHG microscopy at the forefront of fibrillar collagen imaging.

SHG occurs when two incident photons interact with a non-centrosymmetric sample and combine to form a single emitted photon of exactly half the wavelength or twice the energy, offering measurements with high spatial resolution, optical three-dimensional (3-D) sectioning, minimal invasiveness, deep penetration, and the absence of interference from background light.<sup>49</sup> The non-centrosymmetric triple helix of three polypeptide chains in the collagen molecule is ideal for SHG visualization and permits up to 0.2–0.3  $\mu\text{m}$  resolution with little to no tissue damage. Most importantly from the viewpoint of damaged collagen assessment, thermal denaturation of collagen fibrils changes the structure to a centrosymmetric random coil, decreasing or even

eliminating the fluorescence. These provide a mean to study collagen diseases through the changes in SHG signal as an indicator of collagen damage.<sup>50</sup>

In cancer, tissue microenvironments play an important role in maintaining normal cell behavior. Cancer cells reversely reshape collagen to form a reinforcing cell-collagen loop, which gradually fosters cancer progression.<sup>43</sup> Despite the many advances in the diagnosis of carcinomas, the development of a real-time, non-invasive imaging method that can assess cancer progression is still a challenge. In breast cancer, SHG studies have revealed that tumor cells often localize near dense collagen areas that then promote tumor growth and expansion of the collagen matrix, leading to matrix reorganization.<sup>51</sup> This response is assisted by proteolytic cleavage to release collagen fibers, creating a heavily damaged collagen milieu. Similarly, basal cell carcinoma reflects higher collagenolytic activity surrounding the tumor areas as seen through SHG and in agreement with histopathological images.<sup>52</sup>

Analogous to cancer, fibrosis is associated with dense collagen fibrils through excessive deposition of extracellular matrix (ECM) proteins, such as collagen. Even though biopsies continue to be the current standard for assessing and staging fibrosis, these techniques often lack the sensitivity and specificity needed to examine the extracellular matrix (ECM) changes and their role, along with appreciable sampling error, high inter-observer variability, and risk of complications.<sup>53</sup> Utilizing SHG to determine macro/supramolecular and fibril changes in the fibrotic collagen has confirmed that there is a significant increase in disorder (damaged collagen) between normal and fibrotic tissues.<sup>54, 55</sup> Nevertheless, a fundamental limitation continues to be a lack of knowledge of the underlying collagen damage in diseases, as this could lead to better diagnostics, prognostics, and measures of treatment efficacy.

Injuries have also greatly benefited from SHG microscopy by providing a better understanding of the effect of non-fatal thermal injuries on collagen fibers. Non-fatal thermal injuries are a leading cause of morbidity worldwide, with roughly 40,000 hospitalizations a year

required in the United States.<sup>56</sup> While considered largely preventable, burns can leave patients with debilitating injuries and scarring.<sup>57</sup> A major challenge lies in the variable healing time for burns that are less than full thickness, along with the disparity between clinical identification of burn depth, histopathologic determination of cellular and extracellular matrix (ECM) damage and the regenerative potential of the tissue. Tanaka *et al.* performed SHG imaging on *in vivo* samples to observe changes in dermal collagen fibers in living rat burn models. Through this study it was confirmed that the influence of thermal denaturation of collagen molecules could be visualized in the form of signal vanishing patterns in the SHG image. Furthermore, SHG was able to determine differences depending on the degree of burn, allowing for injury assessment based on SHG depth profile.<sup>58</sup>

As mentioned above, SHG has allowed greater visualization of collagen fibrils leading to a better understanding of the underlying alterations in injuries and diseases. However, SHG has several issues that limit its clinical application, including being expensive, bulky, utilizing non-eye-safe class IV lasers and not currently having US Food and Drug Administration (FDA) approval.<sup>59</sup> Combining such a technique with probes that anneal selectively to damaged collagen will allow for a better understanding of the relationship between this damage and the diseases. Through these studies, the field therapeutic development could be directed toward targeting damaged collagen detection and treatment.

## Part I

### Chapter 2

#### **Optimization of Interstrand Interactions Enables Burn Detection with a Collagen-Mimetic Peptide**

This chapter has been published under the same title.

Jesús M. Dones, I. Caglar Tanrikulu, Jenu V. Chacko, Alexandra B. Schroeder, Trish T. Hoang,  
Angela L. F. Gibson, Kevin W. Eliceiri, and Ronald T. Raines  
*Organic & Biomolecular Chemistry* **2019**, *17* (46), 9906–9912

#### Contribution

Jesús M. Dones performed all the synthesis, characterization and experimental designs for the CMPs as well as drafted the original manuscript and figures. I. Caglar Tanrikulu performed the computational studies and edited the manuscript and figures. Trish T. Hoang performed the toxicity assays in the manuscript. Jenu V. Chacko and Alexandra B. Schroeder performed the imaging of the collagen fibers. Ronald T. Raines planned experiments, analyzed data, and edited the manuscript and figures.

### 1.2.1 Abstract

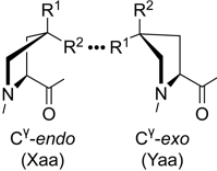
Collagen is an abundant component of the extracellular matrix and connective tissues. Some collagen-mimetic peptides (CMPs) that do not form homotrimers can anneal to damaged tissue. Here, through a computational screen, we identify (flpHypGly)<sub>7</sub> as an optimal monomeric CMP for heterotrimer formation. We find that (flpHypGly)<sub>7</sub> forms stable triple helices with (ProProGly)<sub>7</sub> but not with itself. The nonnatural amino acid HflpOH, which is (2*S*,4*S*)-4-fluoroproline, is not toxic to human fibroblasts or keratinocytes. Conjugation of (flpHypGly)<sub>7</sub> to a fluorescent dye enables the facile detection of burned collagenous tissue with high specificity. The ubiquity of collagen and the prevalence of injuries and diseases that disrupt endogenous collagen suggests widespread utility for this approach.

### 1.2.2 Introduction

Collagen—the basic building block of the extracellular matrix (ECM)—is the most abundant protein in vertebrates. Comprising a third of the total protein and three quarters of the dry weight of skin in humans, collagen is an essential component of all connective tissues.<sup>1</sup> Collagen also plays a crucial role in maintaining the biological and structural integrity of the ECM. Its continual remodeling impacts and controls cell differentiation and proliferation,<sup>60</sup> and atypical organization of the collagen matrix is a biomarker for various diseases, including fibrosis, connective tissue disorders, and cancer.<sup>40, 61-64</sup>

Natural collagen is comprised of three left-handed, polyproline II-type (PPII) helices aligned in a parallel manner and coiled with each other to form a right-handed triple helix.<sup>1, 65</sup> Each of the peptide strands is constituted by a continuous repeat of Xaa-Yaa-Gly units. Even though the Xaa and Yaa positions can accommodate any amino acid, (2*S*)-proline (Pro; 28% abundance) and (2*S*,4*R*)-4-hydroxyproline (Hyp; 38% abundance) are the most prevalent, respectively. As a result, ProHypGly is the most common triplet in collagen (10.5%).<sup>3</sup> These natural preferences at the Xaa and Yaa positions promote the conformational stability of the collagen triple helix.<sup>1</sup>

**Table 1.2.1.** Relative Xaa···Yaa interaction energies (kcal/mol) of 4-substituted proline residues in a cross-section of a collagen triple helix<sup>a</sup>

		Yaa (R <sup>1</sup> ,R <sup>2</sup> )						T <sub>m</sub> (°C) <sup>b</sup>	
		Flp (F,H)	Mop (OMe,H)	Hyp (OH,H)	Mep (H,CH <sub>3</sub> )	Clp (Cl,H)	Pro (H,H)	(XaaProGly) <sub>7</sub>	(XaaProGly) <sub>10</sub>
Xaa (R <sup>1</sup> ,R <sup>2</sup> )									
flp (H,F)	2.8	3.4	3.0	1.1	5.6	1.3	33	58	
mep (CH <sub>3</sub> ,H)	-0.4	-0.3	-0.1	-0.6	2.4	-0.4	13	ND	
Pro (H,H)	-0.1	-0.6	0.3	-0.2	1.2	0.0	NH	31–41	
T <sub>m</sub> (°C) <sup>b</sup>									
(ProYaaGly) <sub>7</sub>	45	ND	36	29	23	NH			
(ProYaaGly) <sub>10</sub>	91	70	61–69	ND	52	31–41			

<sup>a</sup>Values of *IE* were calculated with molecular mechanics. Values <2.8 kcal/mol are depicted in gray typeface.<sup>§§</sup> <sup>b</sup>Values of *T<sub>m</sub>* for the denaturation of the indicated triple helix were determined previously by circular dichroism spectroscopy.<sup>1</sup> ND, not determined; NH, no helix.

Collagen stability is governed by stereoelectronic effects that preorganize its prevalent pyrrolidine rings.<sup>1</sup> A *C<sup>γ</sup>-endo* and *C<sup>γ</sup>-exo* pyrrolidine-ring pucker is preferred at the Xaa and Yaa position, respectively, in stable triple-helical structures. Substituents at the 4-position of a proline residue can enforce the preferred pyrrolidine-ring pucker via a *gauche*<sup>13</sup> or *steric*<sup>14</sup> effect, lowering the entropic cost for forming a triple helix and increasing its conformational stability (Table 1.2.1).<sup>1</sup> For example, the stereospecific installation of a fluoro group generates a *gauche* effect that leads to a *C<sup>γ</sup>-endo* pucker in (2*S*,4*S*)-4-fluoroproline (flp) and supports the *C<sup>γ</sup>-exo* pucker in (2*S*,4*R*)-4-fluoroproline (Flp) to a greater extent than does the 4*R*-hydroxy group of Hyp.<sup>8, 15, 16</sup> The impact of such substitutions are apparent in the thermostability of collagen-mimetic peptides (CMPs). The value of *T<sub>m</sub>*, which is the temperature at the midpoint of the thermal transition between a triple helix and its component strands, tracks the strength of the inductive effect induced by the substitutions.<sup>66</sup> For example, replacing Hyp with Flp at the Yaa position in (ProYaaGly)<sub>7</sub> leads to Δ*T<sub>m</sub>* = 9 °C (Table 1.2.1).

Not all Xaa and Yaa pairings are compatible. The register of the strands in a triple helix is staggered such that each cross-section contains an Xaa, Yaa, and Gly residue.<sup>1</sup> Even though

(flpProGly)<sub>7</sub> and (ProFlpGly)<sub>7</sub> form highly stable triple helices (Table 1),<sup>67</sup> (flpFlpGly)<sub>7</sub> is a monomer in solution due to unfavorable steric interactions between neighboring flp and Flp residues (Figure 1).<sup>30</sup> Still, mixtures of (flpFlpGly)<sub>7</sub> and (ProProGly)<sub>7</sub> produce stable triple helices because of the preorganization of (flpFlpGly)<sub>7</sub> and the minimal steric clashes between flp/Flp and neighboring Pro residues.<sup>30</sup>

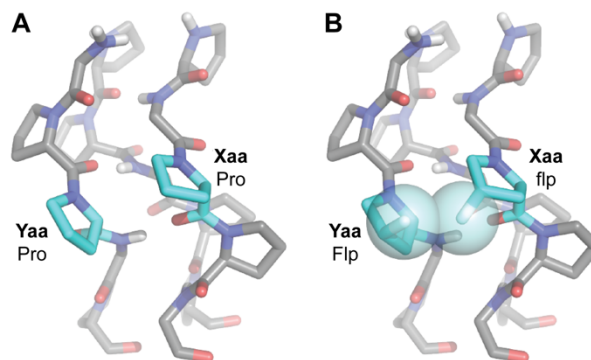


**Figure 1.2.1.** Molecular models of neighboring Xaa and Yaa positions on strands of a collagen triple helix. (A) When Xaa and Yaa are Pro, there is not a steric clash between the neighboring side chains (cyan). (B) When flp and Flp are placed similarly, clashing fluoro groups (cyan spheres) deter strand-association.<sup>30</sup>

Because (flpFlpGly)<sub>7</sub> and (ProProGly)<sub>7</sub> form only heterotrimeric triple helices,<sup>§</sup> they can anneal readily to exposed strands on denatured collagen (Figure 1.2.1). Such annealing could allow for the development of diagnostic or therapeutic agents conjugated to a monomeric CMP.<sup>68-71</sup> Previously, we have used CMP-conjugates to deliver fluorescent dyes,<sup>72</sup> a sunscreen,<sup>73</sup> and growth factors<sup>74</sup> to damaged collagen. Although (flpFlpGly)<sub>7</sub> seemed to outperform (ProProGly)<sub>7</sub> as an annealing strand,<sup>72</sup> its exceptional propensity was hindered by its poor solubility, which can complicate formulation and dosing, and diminish bioavailability.<sup>75</sup> The highly soluble (ProHypGly)<sub>7</sub> peptide can be successful in this context, but its homotrimerization necessitates a denaturation step prior to application,<sup>23, 24</sup> complicating its use. Another approach invokes

protecting groups to deter triple-helix formation,<sup>76, 77</sup> but their removal introduces operational complexity.

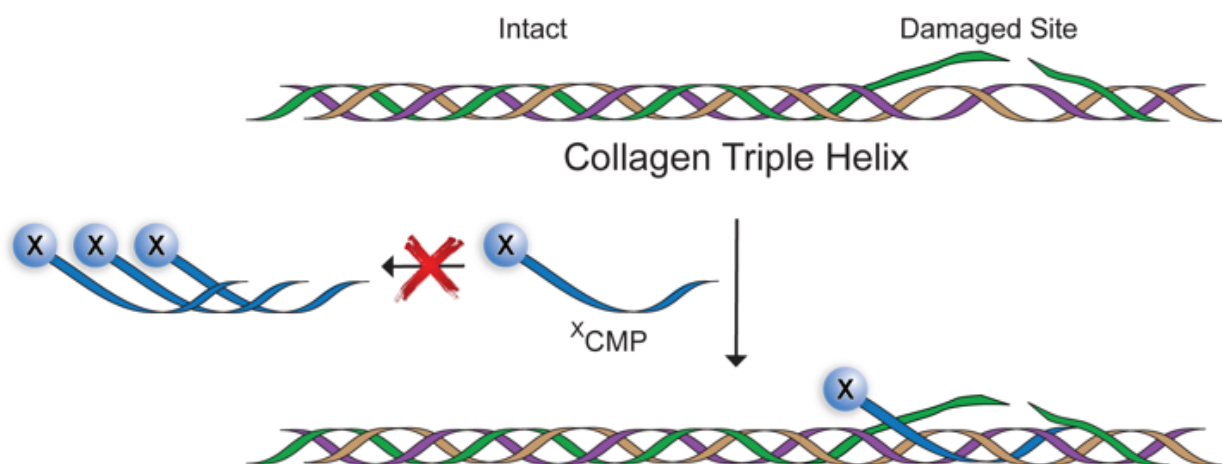


**Figure 1.2.2.** Representation of a collagen-mimetic peptide with a pendant moiety ( $^X\text{CMP}$ ) annealing selectively to a damaged site within the collagen triple helix but not forming a homotrimeric triple helix.

Here, we conduct a computational survey of proline analogs to identify  $(\text{XaaYaaGly})_7$  variants that are monomeric in solution, but have high ability to anneal with damaged collagen. We confirm the association characteristics of our design *in vitro* and demonstrate its specificity for damaged collagen by identifying a burned region on a rat-tail tendon *ex vivo*.

### 1.2.3 Results and Discussion

#### $(\text{flpHypGly})_7$ is an optimal CMP

An optimal CMP is a highly soluble monomer under physiological conditions, but forms strong triple helices with natural collagen strands. To search for such  $(\text{XaaYaaGly})_7$  variants, we defined two sets of proline analogs that are compatible with the steric and electronic requirements at the Xaa and Yaa positions (Table 1.2.1).<sup>1</sup> The resulting 18 combinatorial Xaa $\cdots$ Yaa pairs represent interactions between Xaa and Yaa residues on the neighboring strands of an  $(\text{XaaYaaGly})_7$  homotrimer. To determine the extent of steric repulsion in each homotrimer, we



applied molecular mechanics calculations to models derived from a high-resolution structure of a (ProProGly)<sub>10</sub> triple helix (PDB entry 1kf6).<sup>78</sup> Briefly, Xaa and Yaa residues were positioned on neighboring positions on the triple helix. Following energy minimization, the interaction between the Xaa···Yaa pair was calculated as the energy difference between the homotrimeric helix and the free strands.<sup>79, 80</sup> Three known examples of monomeric CMPs—(ProProGly)<sub>7</sub>, (flpFlpGly)<sub>7</sub>, and (clpClpGly)<sub>7</sub>—served as experimental benchmarks for data analysis.<sup>30, 81</sup>

Interaction energies (*IE*) revealed that four combinations—Xaa flp···Flp, flp···Mop, flp···Hyp, and flp···Clp—engender unfavorable interactions (Table 1.2.1).<sup>§§</sup> Among these four, a flp···Flp pair of Xaa···Yaa residues (*IE* = 2.8 kcal/mol) merits special consideration. flp in the Xaa position and Flp in the Yaa position are individually the most stabilizing 4-substituted proline analogs. Yet, (flpFlpGly)<sub>7</sub> does not form a stable triple helix, suggesting that Xaa···Yaa clashes of *IE* ≥ 2.8 kcal/mol are likely to produce monomeric peptides. Peptides that satisfied this criterion include (flpMopGly)<sub>7</sub>, (flpHypGly)<sub>7</sub>, and (flpClpGly)<sub>7</sub> (*IE* = 3.4, 3.0, and 5.6 kcal/mol, respectively). The higher solubility bestowed by Hyp (hydroxy group) compared to Mop (methoxy group) or Clp (chloro group) led to explore (flpHypGly)<sub>7</sub> experimentally.<sup>§§§</sup> Notably, a stereospecific H→F substitution is the only difference between a flp-Hyp-Gly unit and the isologous Pro-Hyp-Gly unit of natural collagen. Moreover, deleterious O)(F steric clashes engendered by (flpHypGly)<sub>7</sub> will not preclude annealing to strands of human collagen, which lack flp entirely and have Hyp in only 38% of its Xaa-Yaa-Gly units.<sup>3</sup> Finally, the HflpOH monomer is readily accessible from natural HypOH by an S<sub>N</sub>2 reaction.<sup>82</sup> We note that CMPs containing flp-Hyp-Gly units have been examined previously,<sup>83, 84</sup> though in contexts distinct from those described herein. For example, (flpHypGly)<sub>9</sub> was found to form a stable triple helix at ambient temperature, complicating its use in biological contexts.<sup>37</sup> Hence, we examined a shorter peptide: (flpHypGly)<sub>7</sub>.

**(flpHypGly)<sub>7</sub> is structured only as a heterotrimer**

The (flpHypGly)<sub>7</sub> peptide and its variants were synthesized by microwave-assisted solid-phase peptide synthesis and purified by reversed-phase HPLC. Samples prepared in 50 mM HOAc were heated to 65 °C, cooled to 4 °C, and equilibrated at 4 °C for  $\geq 24$  h prior to analysis. The structure of peptides and their mixtures was assessed with circular dichroism (CD) spectroscopy, following the characteristic CD signature for the collagen triple helix and PPII helix at  $\sim 225$  nm.

CD spectra for (flpHypGly)<sub>7</sub> and (ProProGly)<sub>7</sub> reveal shallow peaks near 225 nm (Figure 1.2.3 A). These samples exhibit no cooperative denaturation with increasing temperature, indicating the absence of triple helices in solution (Figure 1.2.3 B). This behavior is typical for PPII structures that do not associate into triple helices.<sup>36-85</sup> In marked contrast, a 1:2 (flpHypGly)<sub>7</sub>/(ProProGly)<sub>7</sub> solution exhibits a strong collagen signature in its CD spectrum (3A), as well as cooperative denaturation with  $T_m = 28$  °C (Figure 1.2.3 B and 1.2.4 A). A 2:1 (flpHypGly)<sub>7</sub>/(ProProGly)<sub>7</sub> solution exhibits similar thermostability (Figure 1.2.5 A, 1.2.5 B, and 1.2.4B). The results of these mixing experiments indicate that (flpHypGly)<sub>7</sub> can form a stable triple helix with (ProProGly)<sub>7</sub> strands, but not with itself.

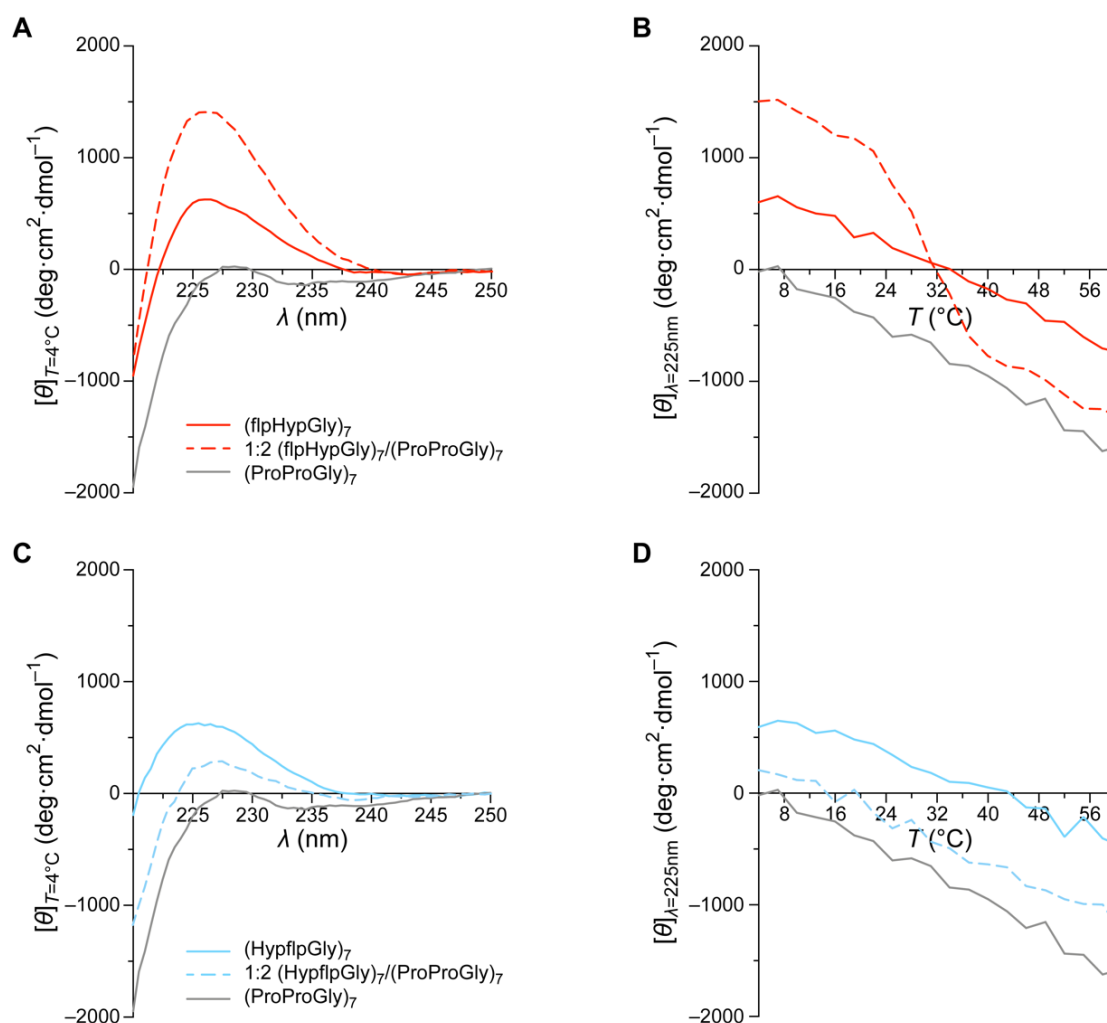


**Figure 1.2.3.** Analyses of CMPs (0.8 mM) in 50 mM acetic acid by circular dichroism spectroscopy. (A) Spectra of  $(\text{flpHypGly})_7$ ,  $(\text{ProProGly})_7$ , and a 1:2 mixture at 4 °C. (B) Graph showing the effect of temperature on the molar ellipticity at 225 nm of  $(\text{flpHypGly})_7$ ,  $(\text{ProProGly})_7$ , and a 1:2 mixture. The mixture had  $T_m = 28\text{ }^{\circ}\text{C}$ . (C) Spectra of  $(\text{HypflpGly})_7$ ,  $(\text{ProProGly})_7$ , and a 1:2 mixture at 4 °C. and its mixture at 4 °C. (D) Graph showing the effect of temperature on the molar ellipticity at 225 nm of  $(\text{HypflpGly})_7$ ,  $(\text{ProProGly})_7$ , and a 1:2 mixture.

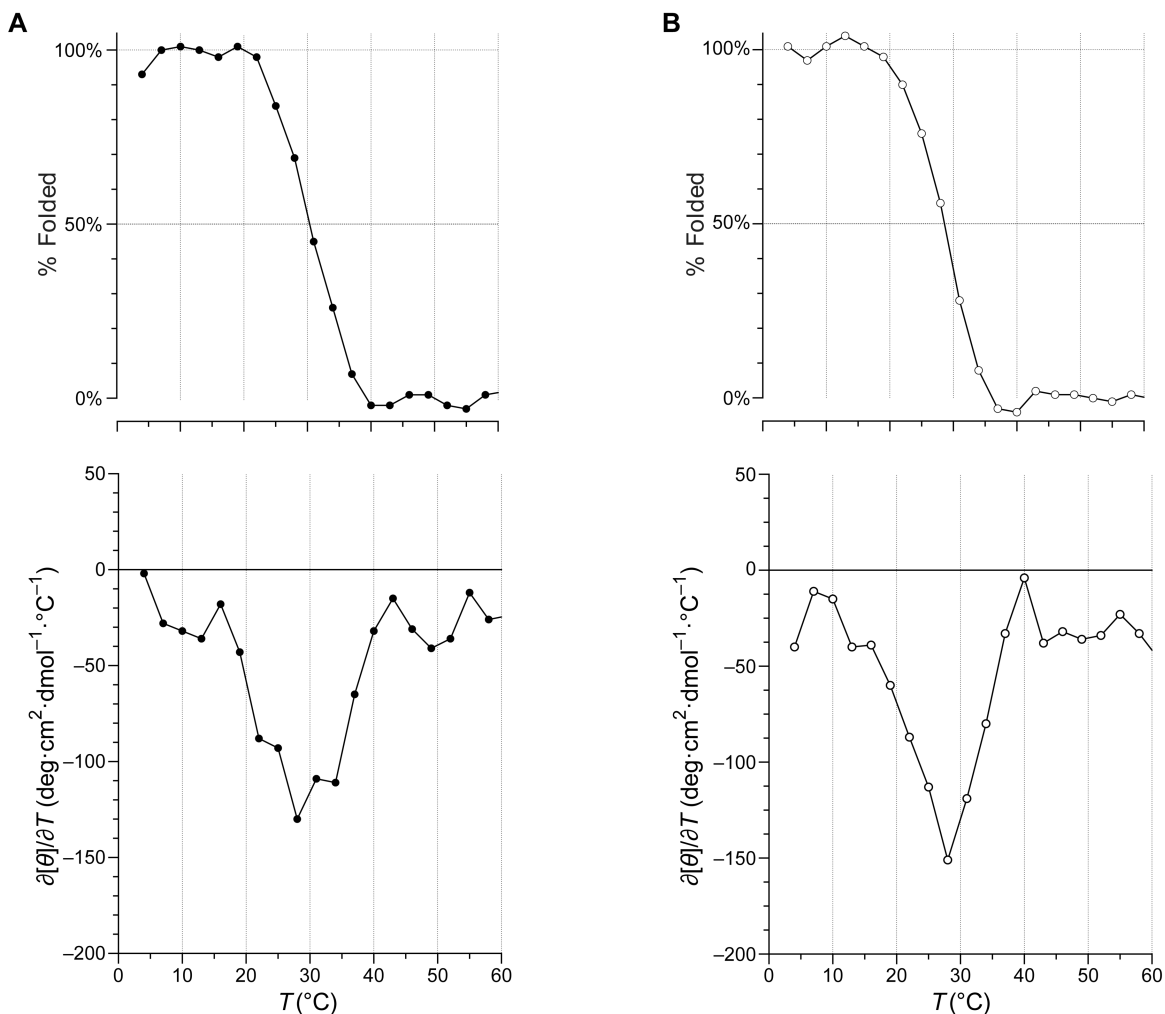


**Figure 1.2.4.** Transformed circular dichroism data for the thermal denaturation of CMP mixtures based on two-state model for triple-helix unfolding. (A) Transformed data of 1:2 (flpHypGly)<sub>7</sub>/(ProProGly)<sub>7</sub> (Figure 1.2.3 B);  $T_m = 28$  °C (B) Transformed data of 2:1 (flpHypGly)<sub>7</sub>/(ProProGly)<sub>7</sub> (Figure 1.2.5 B);  $T_m = 28$  °C.

### (HypflpGly)<sub>7</sub> does not form a triple helix

Next, we sought to use a (flpHypGly)<sub>7</sub>-dye conjugate in a physiological context, but we needed a negative control. A free (that is, unconjugated) dye could serve as a negative control for such experiments. The disparity between the physicochemical attributes of a CMP-dye conjugate and the dye alone could, however, compromise data-interpretation.

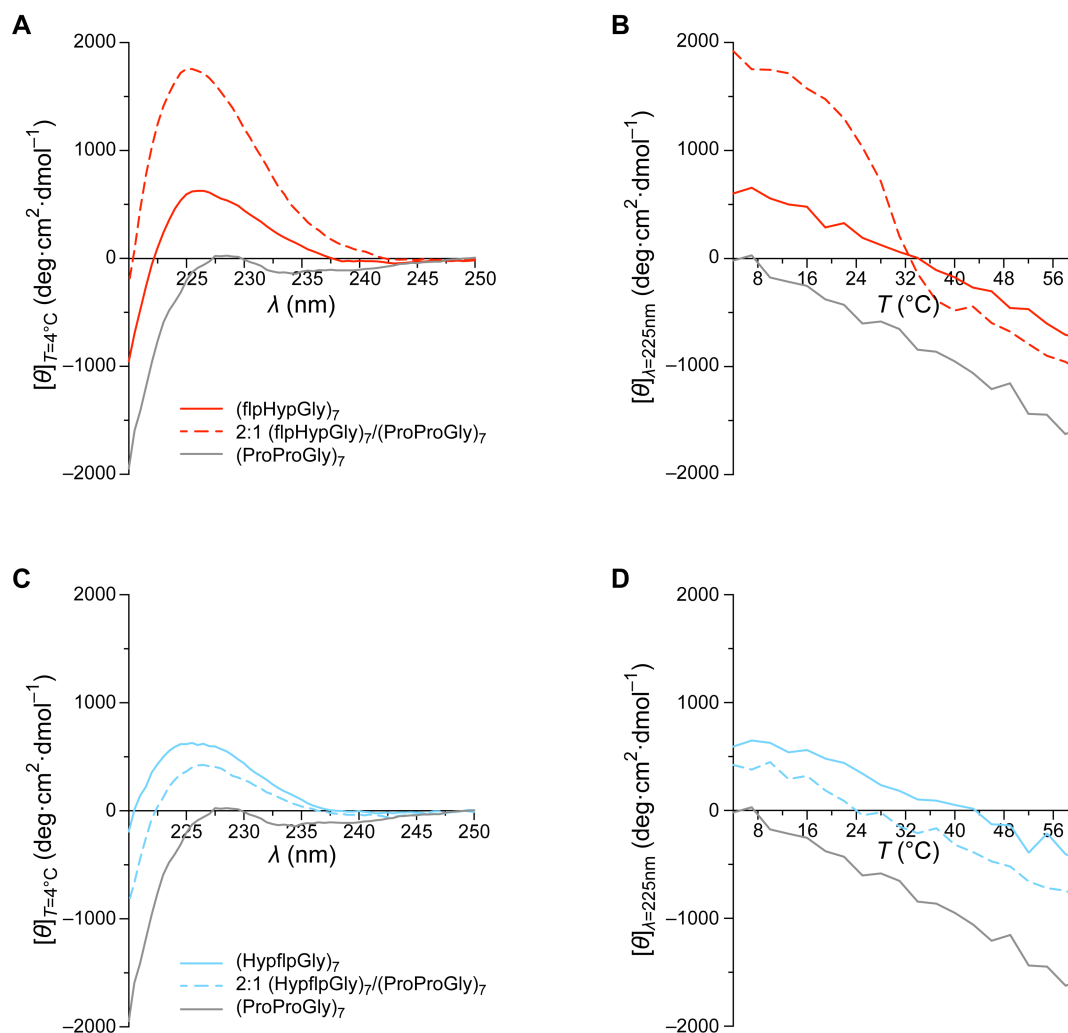


**Figure 1.2.5.** Analyses of CMPs with circular dichroism spectroscopy. Each solution contained 0.8 mM CMP (or a mixture) in 50 mM acetic acid. Data for (flpHypGly)<sub>7</sub>, (HypflpGly)<sub>7</sub>, and (ProProGly)<sub>7</sub>, but not the 2:1 mixtures, are identical to those in Figure 3. (A) Spectra of (flpHypGly)<sub>7</sub>, (ProProGly)<sub>7</sub>, and a 2:1 mixture at 4 °C. (B) Graph showing the effect of temperature on the molar ellipticity at 225 nm of (flpHypGly)<sub>7</sub>, (ProProGly)<sub>7</sub>, and a 2:1 mixture. The mixture had  $T_m = 28^\circ\text{C}$ . (C) Spectra of (HypflpGly)<sub>7</sub>, (ProProGly)<sub>7</sub>, and a 2:1 mixture at 4 °C. (D) Graph showing the effect of temperature on the molar ellipticity at 225 nm of (HypflpGly)<sub>7</sub>, (ProProGly)<sub>7</sub>, and a 2:1 mixture.

To mimic the attributes of the (flpHypGly)<sub>7</sub> peptide, we synthesized (HypflpGly)<sub>7</sub>, which is a compositional isomer (CI). Swapping the flp and Hyp residues generates a sequence that violates the conformational restrictions of the Xaa and Yaa positions (Table 1.1.1), and should preclude triple-helix formation.<sup>8, 86</sup> Indeed, the CD spectrum of (HypflpGly)<sub>7</sub> mimics closely that of (flpHypGly)<sub>7</sub> (Figure 1.2.3 C), and does not exhibit the cooperative transition of triple-helix denaturation (Figure 1.2.3 D). Further, the CD spectrum of a 1:2 or 2:1 (HypflpGly)<sub>7</sub>/(ProProGly)<sub>7</sub> mixture is a linear combination of the individual (ProProGly)<sub>7</sub> and (HypflpGly)<sub>7</sub> spectra and exhibits no evidence of a triple helix (Figure 1.2.3 C and 1.2.5 C). These spectra, together with the absence of a cooperative transition (Figure 1.2.3 D and 1.2.5 D), provide strong evidence that (HypflpGly)<sub>7</sub> does not interact with (ProProGly)<sub>7</sub>. Because (HypflpGly)<sub>7</sub> has the same composition as does (flpHypGly)<sub>7</sub> but lacks its annealing properties, (HypflpGly)<sub>7</sub> serves as an ideal negative control for our physiological experiments.

### **HflpOH is not cytotoxic**

The proteolysis of (flpHypGly)<sub>7</sub> would generate three amino acids: HflpOH, HHypOH, and HGlyOH. Two of these amino acids, HHypOH and HGlyOH, are prevalent in human collagen; HflpOH, though, is nonnatural. As 1/3 of FDA-approved drugs contain fluorine,<sup>87</sup> we expected HflpOH to be well-tolerated in humans. Nevertheless, HflpOH itself is not a component of any approved drug. Accordingly, we tested the tolerance of two relevant cell types for this amino acid: human fibroblasts and primary human epidermal keratinocytes. Fibroblasts are the most common cells in human connective tissue, and maintain its health and integrity. Keratinocytes constitute 90% of the cells in the epidermis, which is the barrier against environmental damage. We found that HflpOH is not detectably toxic to either fibroblasts or keratinocytes at concentrations up to 1 mM (Figure 1.2.6).

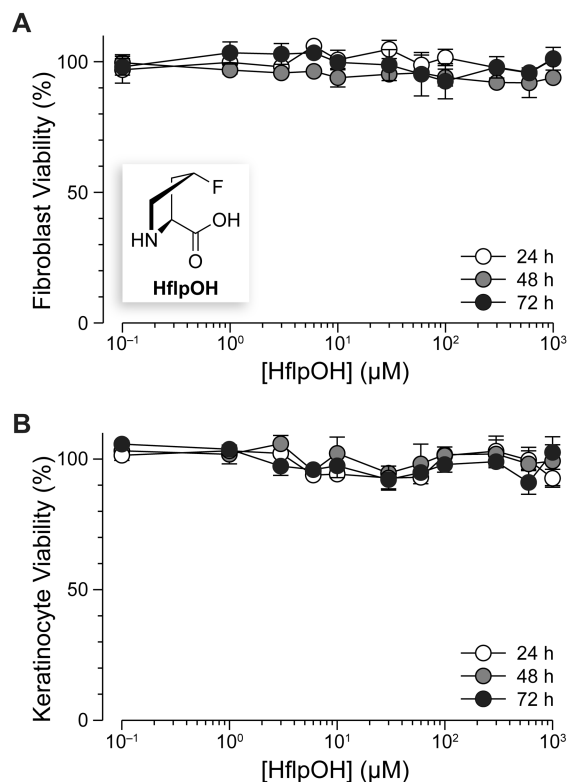


**Figure 1.2.6.** Graph showing the effect of HflpOH on the viability of human fibroblasts (A) and primary human epidermal keratinocytes (B). Data were obtained with a tetrazolium dye-based assay for metabolic activity.<sup>88</sup> Values are the mean  $\pm$  SEM ( $n = 3$ , biological replicates).

### (flpHypGly)<sub>7</sub> anneals to damaged collagen *ex vivo*

To evaluate the binding of a (flpHypGly)<sub>7</sub>-dye conjugate to fibrillar collagen, we used the rat-tail tendon as a testbed, as it is comprised primarily of fibrillar collagen.<sup>89</sup> Type I collagen from rat-tail tendons has been studied extensively, and is accessible by well-developed procedures.<sup>90</sup> For the treatment of rat-tail tendon, we prepared variants of (flpHypGly)<sub>7</sub> and (HypflpGly)<sub>7</sub> that are conjugated via their N-terminal amino group to a cyanine 5 (Cy5) dye, obtaining Cy<sup>5</sup>CMP and Cy<sup>5</sup>CI, respectively (Figure 1.2.8 A). We choose Cy5 because of the far-red wavelength of its fluorescence excitation ( $\lambda_{\text{max}} = 652 \text{ nm}$ ) and emission ( $\lambda_{\text{em}} = 672 \text{ nm}$ ), which allows for detection in tissue, as well as its high brightness ( $\epsilon \times \Phi = 0.18$ ).<sup>91</sup> To test whether (flpHypGly)<sub>7</sub> can distinguish damaged collagen from healthy collagen, we used a 350-°C soldering iron to burn a

rat-tail tendon through glass (Figure 1.2.8 B). We then treated the tendon with  $\text{Cy}^5\text{CMP}$  and  $\text{Cy}^5\text{CI}$ , incubated for 1 h at 37 °C, and washed extensively with PBS.

Second harmonic generation (SHG) microscopy is a nonlinear optical method that is used extensively to identify and visualize fibrillar collagens in tissues.<sup>92-94</sup> Using a multiphoton laser-scanning microscope, data can be acquired from both SHG and Cy5 channels, revealing the distinction between damaged and healthy collagen (SHG) and its detection with our probe (Cy5). The fibrils exposed to 350 °C show little or no signal through the SHG channel, confirming the absence of intact collagen structure in the burn area (Figure 1.2.7). Upon treatment with  $\text{Cy}^5\text{CMP}$ , the regions that fail to show a strong SHG signal exhibit a strong Cy5 fluorescence (Figure 1.2.8 C), indicating the association  $\text{Cy}^5\text{CMP}$  with damaged collagen. Importantly, the same intensity is not observed in intact regions. In contrast, the distinction between damaged and healthy collagen is not apparent with the negative control,  $\text{Cy}^5\text{CI}$  (Figure 1.2.8 D).

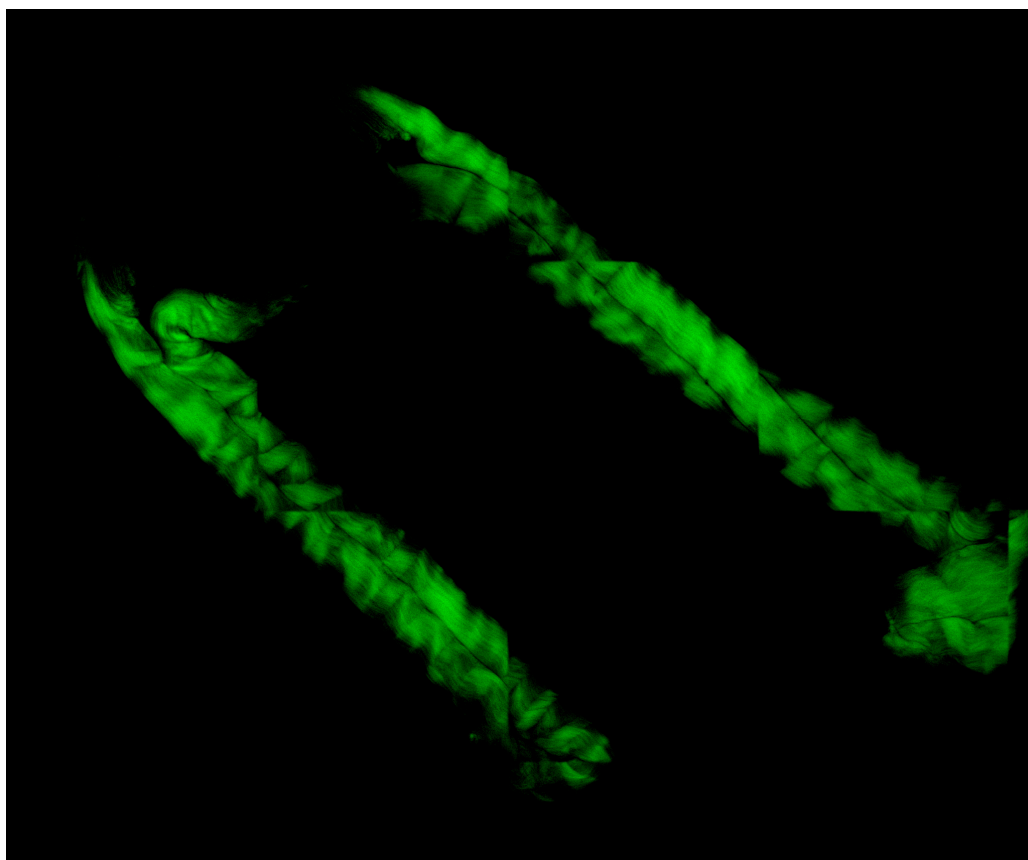


**Figure 1.2.7.** Second Harmonic Generation (SHG) channel of collagen fibrils. Scale bar, 500  $\mu\text{m}$ .



Quantification of Cy5 fluorescence reveals that the localization of  $\text{Cy}^5\text{CMP}$  on burned collagen is greater by 25-fold (*i.e.*, 148/6) than its fluorescence on intact collagen (Figure 1.2.8 E). Similarly, the labeling of these regions by  $\text{Cy}^5\text{CMP}$  is greater by 5.3-fold (*i.e.*, 148/28) than that by the  $\text{Cy}^5\text{CI}$  peptide. These results confirm annealing by  $(\text{flpHypGly})_7$  to regions of collagen damage. Finally, we note that  $\text{Cy}^5\text{CMP}$  is highly soluble in water, showing no evidence of precipitation despite its pendant hydrophobic dye.

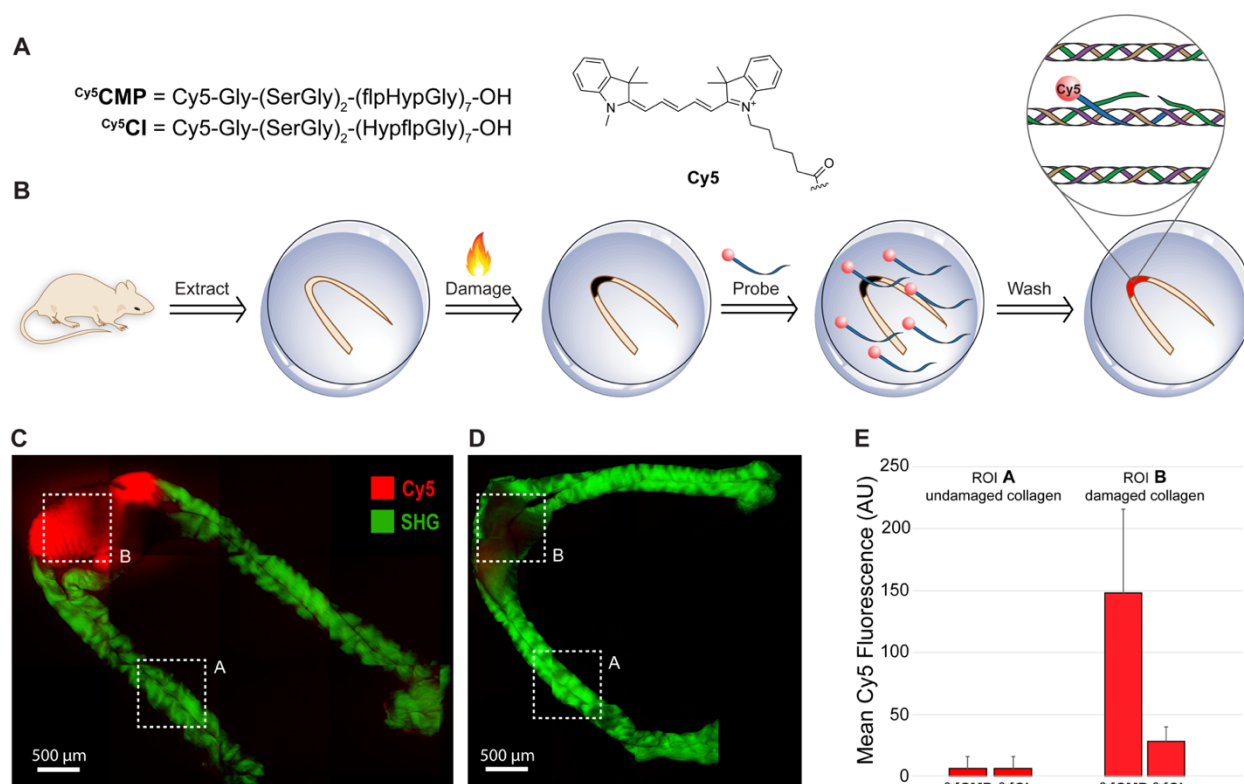


**Figure 1.2.8.** Multiphoton microscopy images of the annealing of fluorescently labeled CMP and its compositional isomer to collagen fibers from rat tails. (A) Amino acid sequences of the  $\text{Cy}^5\text{CMP}$  and  $\text{Cy}^5\text{CI}$  peptides. (B) Method for probing for damaged collagen in a rat-tail tendon. (C) Superimposed images of a damaged rat-tail tendon using second harmonic generation (SHG) in the green channel and the fluorescence from  $\text{Cy}^5\text{CMP}$  in the red channel. (D) Superimposed images of the SHG channel of a damaged rat-tail tendon and the fluorescence from the compositional isomer,  $\text{Cy}^5\text{CI}$ . (E) Bar graph of the mean fluorescence intensity in the indicated regions of interest (ROIs) as determined with ImageJ software.<sup>95</sup>

### 1.2.4 Conclusions

An optimized CMP can act as a vehicle for the detection of mammalian collagen that has suffered burn damage. Burn injuries affect more than 7 million individuals worldwide and result in significant morbidity and mortality.<sup>96</sup> Current methods to diagnose burns face challenges, such as the disparity between the clinical identification of burn depth and the histopathologic determination of cellular and ECM damage.<sup>97</sup> Further, only 70% of visual assessments of full-thickness burn injuries are accurate.<sup>98</sup> Our approach could enable the reliable detection of thermally damaged collagen in a clinical setting. The ubiquity of collagen as well as the disruptive effects of fibrosis, connective-tissue disorders, and cancer on collagen in the ECM suggest its utility in other regimens as well.

### 1.2.5 Acknowledgements

This work was supported by grant R56 AR044276 (NIH), the Laboratory for Optical and Computational Instrumentation, and the Morgridge Institute for Research. We thank Dr. Ellen Arena for useful input on the manuscript and image analysis.

### 1.2.6 Notes and references

§ Neither (flpFlpGly)<sub>7</sub> nor (ProProGly)<sub>7</sub> forms a stable homotrimeric triple helix, though for different reasons. (flpFlpGly)<sub>7</sub> strands are highly preorganized for triple-helix formation, but experience strong interstrand F)(F clashes in a triple helix.<sup>30</sup> (ProProGly)<sub>7</sub> strands do not engender steric clashes upon association, but are not especially well-organized for triple-helix formation.<sup>99</sup>

§§ We also tested clp (R<sup>1</sup>=H, R<sup>2</sup>=Cl) as a candidate at the Xaa position. Its use, however, produces extremely unfavorable interactions, even when its neighbor is Pro (*IE* = 13.8 kcal/mol). This incompatibility is consistent with the low thermostability of triple helices with clpProGly units,<sup>81</sup> and disqualifies the use of clp at the Xaa position of an annealing strand.

§§§ Log $P$  values are HHypOH, -2.64; HMopOH, -2.02; HProOH, -1.72; HFlpOH, -1.71; and HClpOH, -1.40; as calculated with software from Molinspiration (Slovenský Grob, Slovak Republic).

## 1.2.7 Experimental

### Computational Evaluation of Interstrand Xaa···Yaa Side-Chain Interactions

Calculations were performed on Intel Xeon 2.33-GHz processors at the Materials and Process Simulation Center at the California Institute of Technology (Pasadena, CA). Computational models built based on the crystal structure of the (PPG)<sub>10</sub> trimer (PDB entry 1kf6)<sup>78</sup> were supplemented with hydrogen atoms using REDUCE (version 3.03),<sup>100</sup> and the complete model was minimized fully. Minimizations were carried out to a 0.2 (kcal/mol)/Å RMS-force convergence criterion using conjugate gradient minimization on MPSIM.<sup>101</sup> Interatomic forces were described by the DREIDING force-field<sup>79</sup> using CHARMM22 charges<sup>80</sup> and without solvation. Charges on non-canonical amino acids were assigned based on using Mulliken charges obtained through density functional theory calculations at B3LYP/6-311G\*\* level of theory implemented using JAGUAR (version 7.0) from Schrödinger (New York, NY).

Xaa–Yaa interaction energies ( $IE$ ) were calculated on a (ProProGly)<sub>3</sub> background. Pro or Pro analogs were installed at the Xaa and Yaa position of neighboring sites on separate strands. Substituents on C $\gamma$  of each Pro or Pro analog were minimized both in a triple helix (*i.e.*, with a neighbor) and in the absence of other strands (*i.e.*, without a neighbor), and their energies were calculated. The energy of an Xaa···Yaa interaction is defined as the energy of the triple helix hosting the Xaa···Yaa pair relative to the sum of the energies for individual strands making up the triple helix.

### Reagents

Commercial chemicals were of reagent grade or better, and were used without further purification. Natural amino , flpOH, and HOBt were from Chem-Impex International (Wood Dale,

IL). FmocIleOH and FmocHyp(*t*Bu)OH were from OmegaChem (Saint-Romuald, Canada). FmocGly-loaded Wang resin was from MilliporeSigma (Burlington, MA). Cyanine5 NHS ester was from Lumiprobe (Hunt Valley, MD). DIC and 4-methylpiperidine were from Oakwood Chemical (Tampa, FL). Anhydrous DMSO, TIS, TFA, and PBS (product P3813) were from Sigma–Aldrich (St. Louis, MO). All other reagents were from Fisher Scientific (Hampton, NH).

### **Conditions**

All procedures were performed at ambient temperature (~23 °C) and pressure (1.0 atm) unless indicated otherwise.

### **Peptide Synthesis–General**

Peptides were synthesized with a Liberty Blue™ Automated Microwave Peptide Synthesizer from CEM (Matthews, NC). All peptides were synthesized following CEM standard methods for both microwave and coupling cycles. Standard solutions of monohydrated HOBt (1 M in DMF), DIC (0.5 M in DMF), 4-methylpiperidine (20% v/v in DMF), and Fmoc-protected amino acids (0.2 M in DMF) were prepared for each synthesis.

*Standard Microwave-Assisted Deprotection.* The microwave was set to 155 W at 75 °C for 15 s, followed by 30 W at 90 °C for 50 s.

*Standard Microwave-Assisted Coupling.* The microwave was set to 170 W at 75 °C for 15 s, followed by 30 W at 90 °C for 225 s.

*Standard Coupling Cycle.* FmocGly-loaded Wang resin (1 equiv) was added to the CEM reaction vessel, and the resin was allowed to swell for 5 min in DMF. The Fmoc group was removed using the standard deprotection solution and the microwave-assisted deprotection methods described above. The resin was then washed (4×), and Fmoc-AA-OH (5 equiv) was added, followed by DIC (20 equiv) and HOBt monohydrate (40 equiv). Standard microwave-assisted coupling was performed with additional Fmoc-protected amino acids, and the resin was

washed (2×) and drained. When double-coupling was required, the cycle was repeated without the deprotection step.

*Cleavage and Precipitation.* After the final deprotection step, the resin was removed from the reaction vessel into a cleavage filter, washed with DCM (4×), and air-dried. Crude peptides were then cleaved from the resin using a cleavage cocktail composed of H<sub>2</sub>O/TIS/TFA 2.5:2.5:95 for 2 h. Peptide mixtures were then filtered and precipitated in ice-cold diethyl ether (10×). The peptides were collected by centrifugation, the supernatants were decanted, and the solid peptide was dissolved in 5 mL of H<sub>2</sub>O/ACN 70:30. The solutions were frozen and lyophilized using a FreeZone benchtop instrument from Labconco (Kansas City, MO). The crude peptide mixture was then subjected to purification.

*Purification.* The crude peptide products were purified by preparative reverse-phase HPLC using a VP 250/21 Nucleosil 100-5 C18 column from Macherey–Nagel (Bethlehem, PA) and a 1260 Infinity II instrument from Agilent Technologies (Santa Clara, CA). Crude products were dissolved in the minimum amount of ACN and eluted with a linear gradient of 5–80% ACN/H<sub>2</sub>O containing TFA (0.1% v/v). After reviewing the initial chromatogram, the method was updated, if necessary. Chromatography fractions were analyzed by MALDI–TOF MS using a microflex LRF instrument and a CHCA matrix from Bruker (Billerica, MA). Fractions containing purified peptide were pooled and lyophilized, and analyzed by reverse-phase HPLC using an EC 250/4.6 Nucleosil 100-5 C18 column from Macherey–Nagel and a 1260 Infinity II instrument from Agilent Technologies.

*CD Spectroscopy.* Peptides were dried under vacuum for ≥48 h before being weighed and dissolved to 0.8 mM in 50 mM acetic acid (pH 3.0). The resulting solutions were heated to 65 °C and cooled to 4 °C at a rate of 1 °C every 5 min. The solution was then incubated at ≤4 °C for ≥24 h before its CD spectrum was acquired with a Model J-1500 spectrometer from JASCO (Easton, MD) at the MIT Biophysics Instrumentation Facility. Spectra were measured with a band-

pass of 1 nm. The signal was averaged for 3 s during the wavelength scan. At each temperature, solutions were allowed to equilibrate for a minimum of 8 min before data acquisition. Values of  $T_m$  were determined by fitting the molar ellipticity at 225 nm to a two-state model.

### Peptide Synthesis–Specific

*(ProProGly)<sub>7</sub>*. *(ProProGly)<sub>7</sub>* was synthesized by a non-interrupted continuous method. After deprotection of FmocGly-loaded Wang resin, Fmoc-protected amino acids were coupled through a single standard coupling cycle until completion. Following deprotection, the peptide was cleaved from the resin and precipitated to afford a crude peptide product. The crude product was purified with preparative reverse-phase HPLC, and chromatography fractions were analyzed by MALDI–TOF MS in positive-ion mode. Fractions containing pure material were pooled and lyophilized.

*(flpHypGly)<sub>7</sub>*, *(HypflpGly)<sub>7</sub>*, *Gly-(SerGly)<sub>2</sub>-(flpHypGly)<sub>7</sub>*, and *Gly-(SerGly)<sub>2</sub>-(HypflpGly)<sub>7</sub>*. CMPs were synthesized by a non-interrupted continuous method. After deprotection of FmocGly-loaded Wang resin, Fmoc-protected amino acids were coupled by either a single or a double standard coupling cycle until completion. The low nucleophilicity of flp and Hyp required a double standard coupling cycle. Following deprotection, the peptide was cleaved from the resin and precipitated to afford a crude peptide product. The crude product was purified with preparative reverse-phase HPLC, and chromatography fractions were analyzed by MALDI–TOF MS in positive-ion mode. Fractions containing pure material were pooled and lyophilized.

*Cy5–Gly-(SerGly)<sub>2</sub>-(flpHypGly)<sub>7</sub>* and *Cy5–Gly-(SerGly)<sub>2</sub>-(HypflpGly)<sub>7</sub>* Conjugates. The peptide was dissolved in DMSO containing TEA (4 equiv), and the resulting solution was allowed to stir for 15 min. Cy5-NHS ester (2 equiv) was added to the mixture, and the resulting solution was allowed to react overnight in the dark. The reaction mixture was then diluted with water (5 equiv), frozen, and lyophilized. The peptide conjugate was purified with preparative reverse-

phase HPLC, and chromatography fractions were analyzed by MALDI–TOF MS in positive-ion mode. Fractions containing pure material were pooled, lyophilized, and stored in the dark.

### **Cytotoxicity Assays**

Human fibroblasts (strain HTB-102) were from ATCC (Manassas, VA). Primary human epidermal keratinocytes were a generous gift from Dr. Jean Christopher Chamcheu and Professor Hasan Mukhtar (University of Wisconsin–Madison). Cells were treated for 24, 48, or 72 h with HflpOH (0.1  $\mu$ M→1 mM). Cell viability was measured in triplicate with a tetrazolium dye-based assay for metabolic activity<sup>88</sup> (CellTiter 96<sup>®</sup> AQueous One Solution Cell Proliferation Assay) from Promega (Madison, WI).

### **Rat-Tail Tendon Extraction and Imaging**

Rat tails were obtained from the Animal Surgery Laboratory of the Research Animal Resource Center at the University of Wisconsin–Madison. The tails were excised postmortem and stored at  $-80$  °C. To extract a tendon, a tail was rolled between the hand and a hard surface (table top) to loosen the tendons within the tail. Two transverse cuts were made spaced at the desired tendon length using a bone-cleaving knife to separate the tail. At this stage, the skin could be removed for visualizing the packed tendons inside and avoiding the skin cut debris. The tendon was exposed from the distal end using a pair of tweezers. Three identical tendons were used for burning and imaging. The tendons were wounded by burns using a hot soldering iron set at 350 °C. A glass microscope slide was placed atop the tendon to prevent charring from direct metal contact. After creating the burn wound, 100  $\mu$ L of PBS or PBS containing CMP (100  $\mu$ M) or CI (100  $\mu$ M) was applied to the burn site. The tendons were incubated in the dark for 1 h and then washed three times with PBS and retained in PBS to prevent dehydration.

Tendons were imaged using an upright multiphoton laser scanning microscope (Ultima IV multiphoton Microscope System, Bruker Nano Surface Division, Middleton, WI) equipped with a tunable ultrafast pulsed laser (Insight DeepSee, Spectra-Physics, Santa Clara, CA). The best

multiphoton excitation efficiency of the Cy5 dye using Insight laser was determined to be at 820 nm by measuring a multiphoton excitation spectrum in the excitation range from 800 to 1200 nm. The Cy5 emission was collected using a 690/50 nm emission bandpass filter (AT690/50m, Chroma Technology Corporation, VT). Second harmonic Generation (SHG) imaging of collagen was collected using a 445/40 nm bandpass filter (FF01-445/40-25, Semrock, Rochester, NY) using illumination at 890 nm. Sequentially, both channels (CY5, SHG) imaged the entire tendon using a 10× objective (Nikon, 0.75 N.A.) tiling the image area using an automated mechanical xy stage on the multiphoton microscope. The images were stitched, and average intensities within the damaged and undamaged regions of interest were determined with ImageJ software (NIH).<sup>95</sup> Experiments were performed in duplicate.

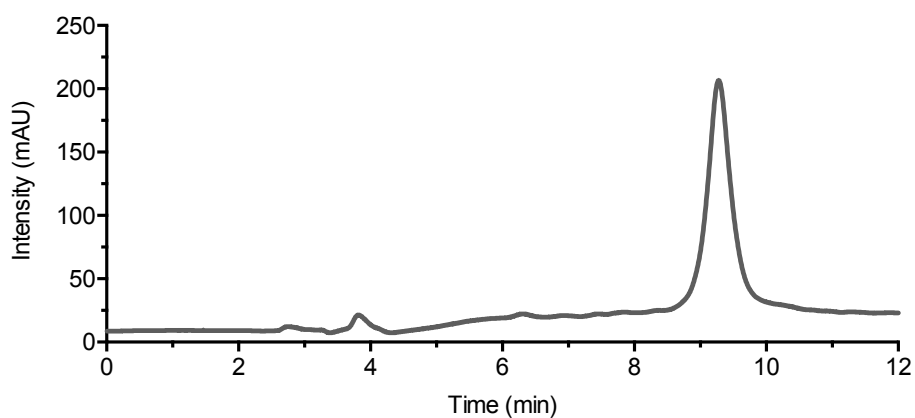


### 1.2.8 Analytical HPLC Traces

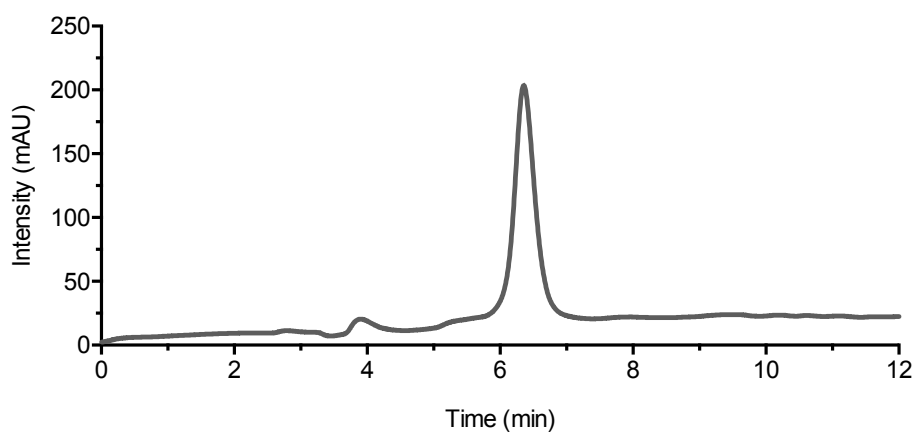
Gradient: 5–70% acetonitrile/H<sub>2</sub>O containing TFA (0.1% v/v) over 12 min

Note that traces for mixtures are the summation of those from component peptides.

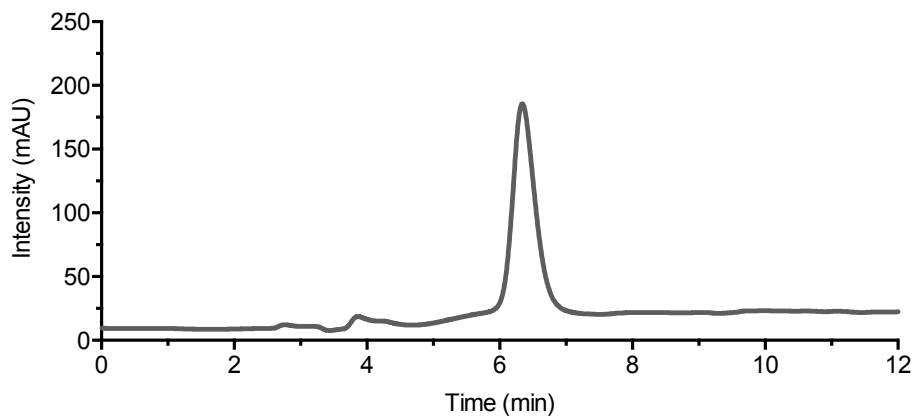
#### (ProProGly)<sub>7</sub>



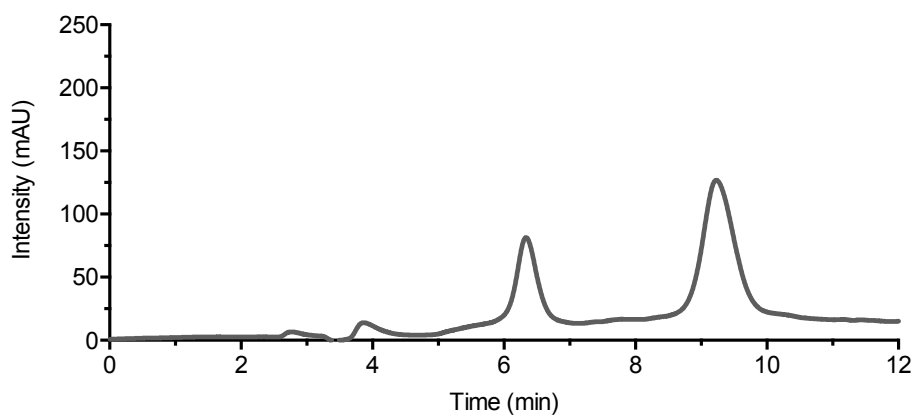
#### (flpHypGly)<sub>7</sub>



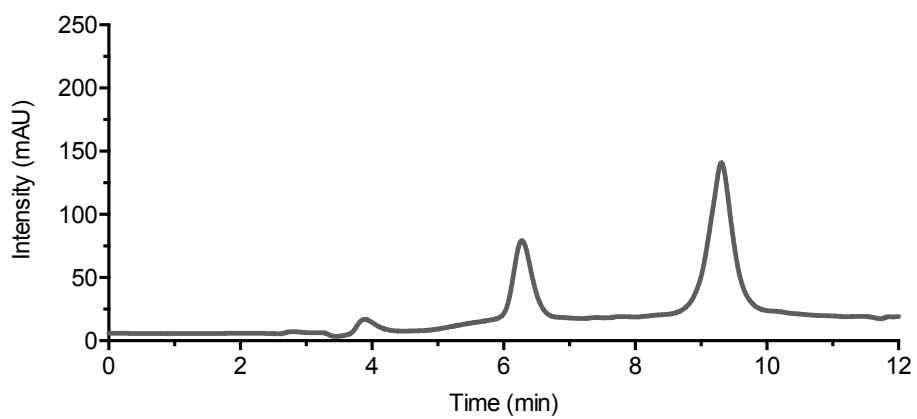
#### (HypflpGly)<sub>7</sub>

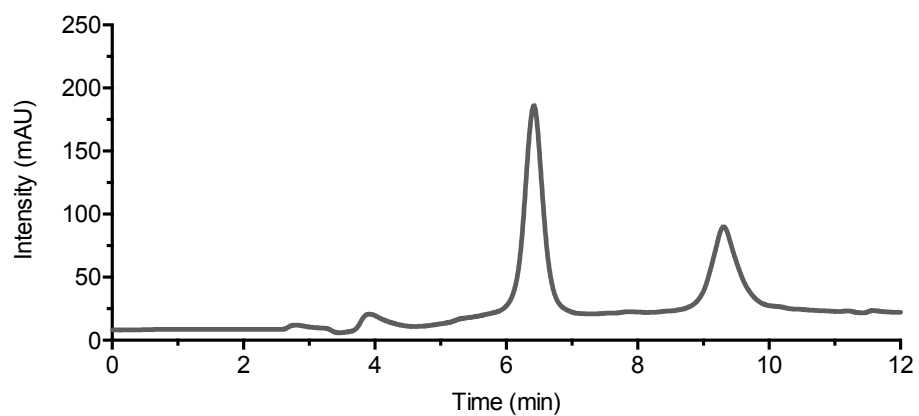
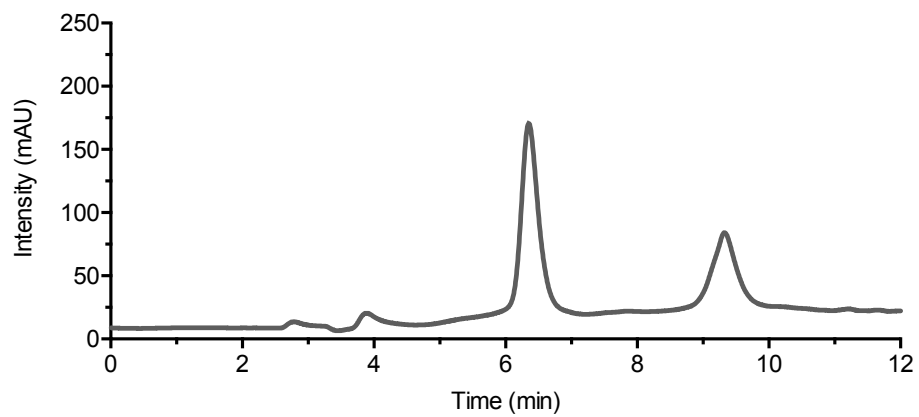


**1:2 (flpHypGly)<sub>7</sub>/(ProProGly)<sub>7</sub>**



**1:2 (HypflpGly)<sub>7</sub>/(ProProGly)<sub>7</sub>**

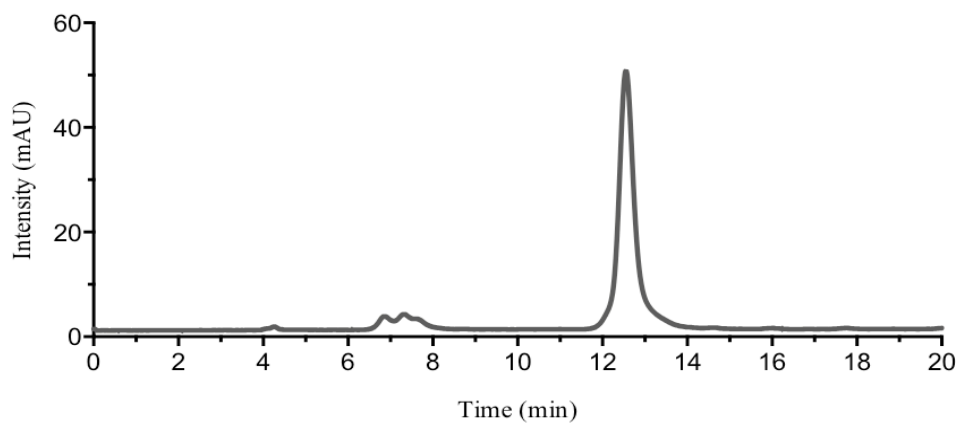


**2:1 (flpHypGly)<sub>7</sub>/(ProProGly)<sub>7</sub>****2:1 (HypflpGly)<sub>7</sub>/(ProProGly)<sub>7</sub>**

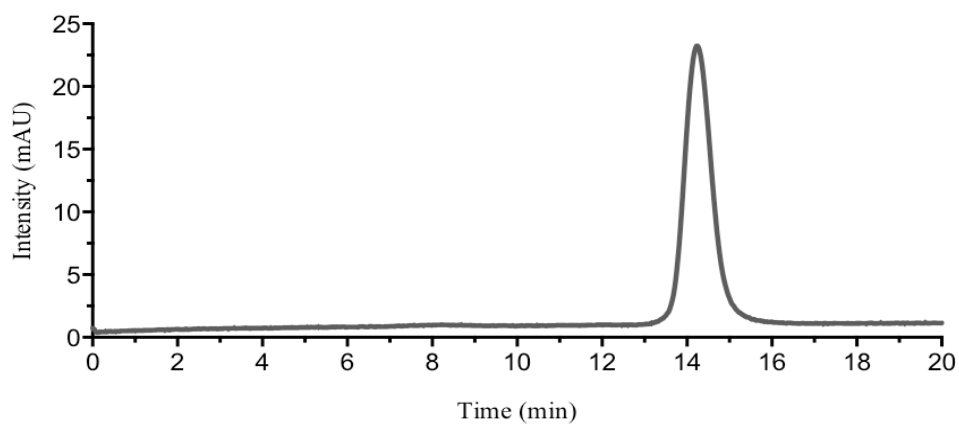
## Fluorescently Labeled CMPs

Gradient: 35–42% acetonitrile/H<sub>2</sub>O containing TFA (0.1% v/v) over 20 min

### Cy<sup>5</sup>CMP



### Cy<sup>5</sup>CI

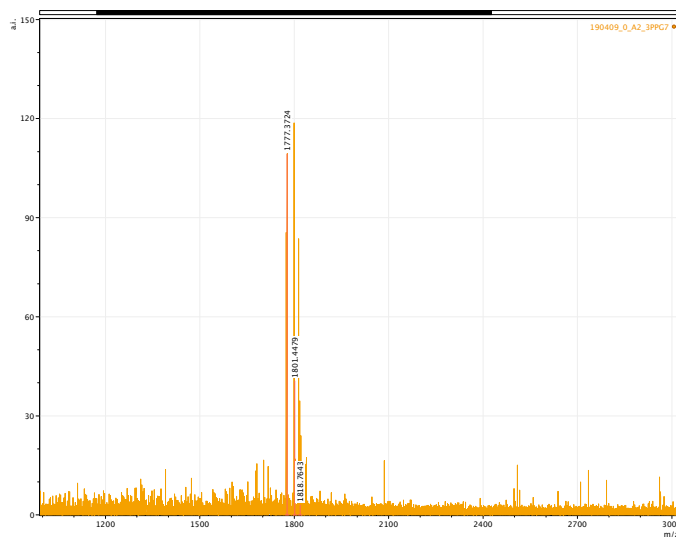


## 1.2.9 MALDI-TOF Mass Spectra

### (ProProGly)<sub>7</sub>

[M + H]<sup>+</sup> (DA) calculated, 1777.02; found, 1777.87

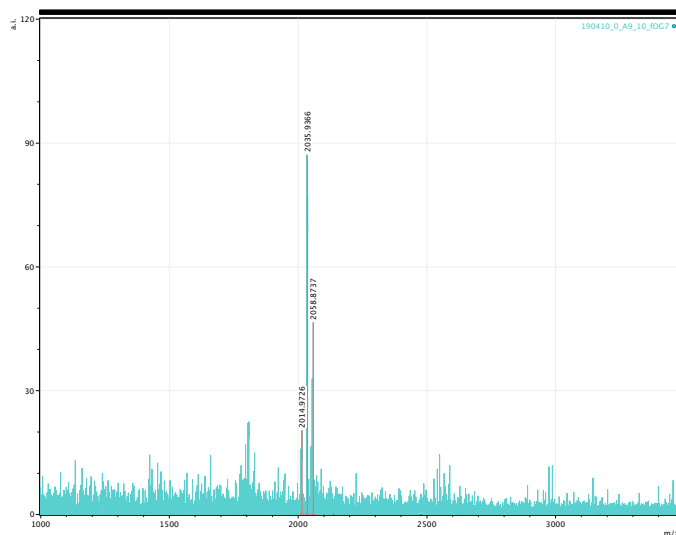
[M + Na]<sup>+</sup> (DA) calculated, 1800.01; found: 1801.47



### (flpHypGly)<sub>7</sub>

[M + H]<sup>+</sup> (DA) calculated, 2014.94; found, 2014.97

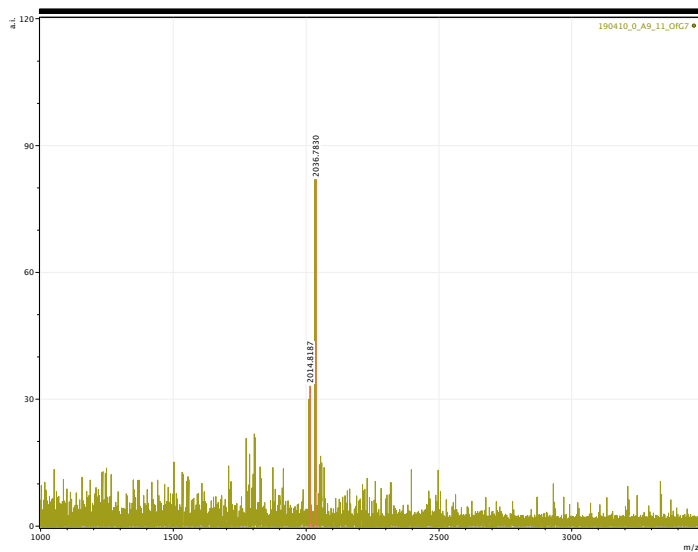
[M + Na]<sup>+</sup> (DA) calculated, 2036.92; found, 2035.94



### (HypflpGly)<sub>7</sub>

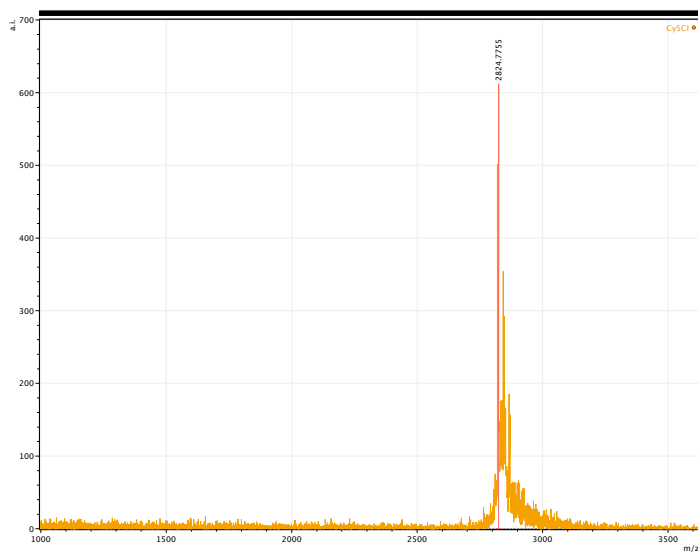
$[M + H]^+$  (DA) calculated, 2014.94; found, 2014.82

$[M + Na]^+$  (DA) calculated, 2036.92; found, 2036.78



**Cy5CI**

$[M + H]^+$  (DA) calculated, 2825.92; found, 2824.78



## Part I

### Chapter 3

#### A Cyclic Peptide Mimetic of Damaged Collagen

This chapter has been published under the same title.

Aubrey J. Ellison, I. Caglar Tanrikulu, Jesús M. Dones, and Ronald T. Raines

*Biomacromolecules* **2020**, *21* (4), 1539–1547

#### Contribution

Ronald T. Raines proposed creation of a collagen duplex. Aubrey J. Ellison synthesized and characterized collagen duplexes. I. Caglar Tanrikulu performed analytical centrifugation and analyzed the resulting data. Jesús M Dones synthesized and characterized (flp-Hyp-Gly)<sub>7</sub> and edited the manuscript and figures. Aubrey J. Ellison performed all other experiments and drafted the original manuscript and figures. Aubrey J. Ellison, I. Caglar Tanrikulu, and Ronald T. Raines planned experiments and analyzed data. Aubrey J. Ellison and Ronald T. Raines edited the manuscript and figures.

### 1.3.1 Abstract

Collagen is the most abundant protein in humans and the major component of human skin. Collagen mimetic peptides (CMPs) can anneal to damaged collagen *in vitro* and *in vivo*. A duplex of CMPs was envisioned as a macromolecular mimic for damaged collagen. The duplex was synthesized on a solid support from the amino groups of a lysine residue and by using olefin metathesis to link the N termini. The resulting cyclic peptide, which is a monomer in solution, binds to CMPs to form a triple helix. Among these, CMPs that are engineered to avoid the formation of homotrimers but preorganized to adopt the conformation of a collagen strand exhibit enhanced association. Thus, this cyclic peptide enables the assessment of CMPs for utility in annealing to damaged collagen. Such CMPs have potential use in the diagnosis and treatment of fibrotic diseases and wounds.

### 1.3.2 Introduction

The collagen triple helix is the most abundant structure adopted by a biopolymer within the human body. There, collagen comprises  $\frac{1}{3}$  of the total protein, accounts for  $\frac{3}{4}$  of the dry weight of skin, and is the most prevalent component of the extracellular matrix.<sup>1</sup>

Collagen is damaged in fibrotic and other diseases and in wounds. Collagen mimetic peptides (CMPs) can anneal to damaged collagen.<sup>68, 70, 71, 102</sup> Such annealing could allow for the delivery of diagnostic or therapeutic agents that are conjugated to the CMP. Indeed, we have used such CMP conjugates to anneal fluorescent dyes,<sup>103-105</sup> a growth factor,<sup>106</sup> and even a sunscreen<sup>73</sup> to natural collagen. Damaged collagen in a human body is, however, a complex target that confounds physicochemical analyses, complicating the assessment of therapeutic potential for new CMP designs.

We sought to develop a molecular mimic of damaged collagen. We envisioned doing so with a collagen “duplex”, that is, two cross-linked CMPs. Several double-stranded duplexes have been synthesized and used to form collagen triple helices.<sup>107-112</sup> In most of these precedents, one



or both ends of the peptides are free, allowing for the assembly of many possible complexes. To make a duplex more amenable to rigorous analyses and more biomimetic, we sought to tether two parallel strands at *both* termini (Figure 1.3.1). This design not only minimizes the conformational entropy of the duplex, but also mimics natural collagen fibers that have a disrupted triple helix, as might be found in damaged collagen. Here, we describe the creation of a “host” and report on its interaction with “guest” strands, that is, CMPs.

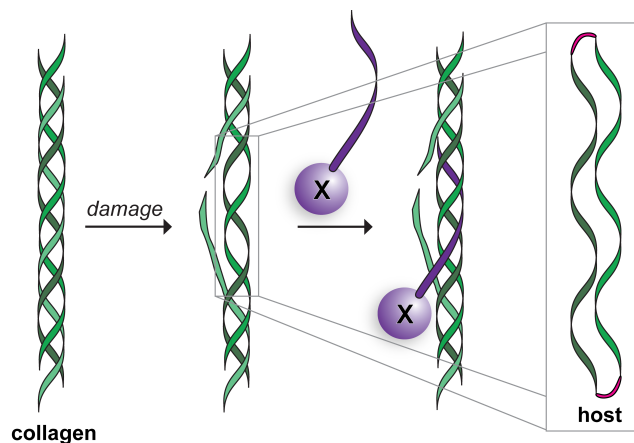


**Figure 1.3.1.** Scheme showing the molecular mimicry of damaged collagen by a cyclic “host” of two parallel collagen strands. A collagen mimetic peptide with a conjugated pendant “X” (purple) is shown annealing to the damaged collagen.

### 1.3.3 Results

#### Design and Synthesis of a Host

We sought to design a host in which two parallel CMPs are tethered together at both ends. Because lysine has two amino groups that could serve to initiate synthesis, we began with lysine immobilized via its carboxyl group. The collagen triple helix forms with a one-residue stagger between its strands, which the distance between the  $\alpha$  and  $\epsilon$  amino groups of lysine helps to recreate. We reasoned that the linkers on both ends must be flexible to allow for proper folding. Accordingly, we condensed Fmoc-6-aminohexanoic acid spacer to both of the amino groups of

lysine. Then, we used standard solid-phase peptide synthesis methods to add a (Pro-Pro-Gly)<sub>10</sub> sequence to each amino group.

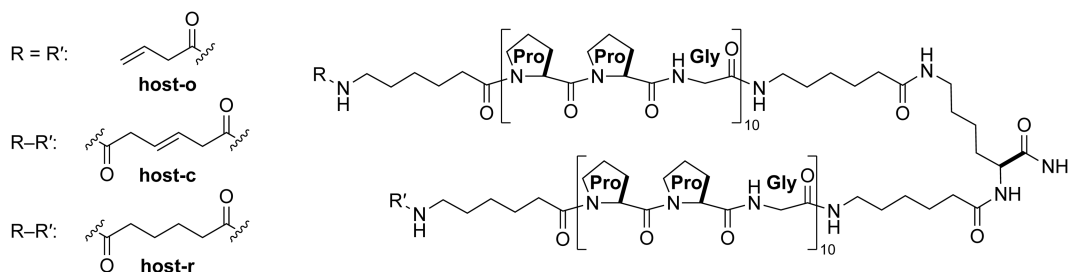


**Figure 1.3.2.** Chemical structures of the open host (host-o), closed host (host-c), and closed, reduced host (host-r). The macrocyclic rings of host-c and host-r contain 221 atoms.

We considered flexibility as well in the design of the N-terminal linker, which would close the macrocycle. 6-Aminohexanoic acid spacers were attached at the N-termini of the two (Pro-Pro-Gly)<sub>10</sub> peptides while still on the solid support. Initial attempts to close the macrocycle enlisted small molecules. Glutaric acid resulted in a mixture of products containing one or two amides but no detectable macrocycle. Similarly, adding a cysteine to each end and treating with dibromobimane<sup>113, 114</sup> provided a mixture of products containing one or two thioethers but no macrocycle. A cyclic duplex that has been optimized to anneal to endogenous single strands of collagen has been closed by forming a disulfide bond,<sup>115, 116</sup> but that methodology was unsuccessful in our hands. Finally, we sought to deploy peptide “stapling”<sup>117, 118</sup> by condensing 3-butenic acid to the N termini (generating the open host) and using olefin metathesis on-resin with Grubbs G2 catalyst to form a macrocycle (the closed host). Mass spectrometry revealed a decrease of 28 amu, consistent with the loss of ethylene and successful tethering of the two ends (Figure 1.3.3). We reduced the nascent alkene to endow greater flexibility (the reduced host). The open, closed, and reduced hosts (host-o, host-c, and host-r, respectively) are depicted in Figure 1.3.2.

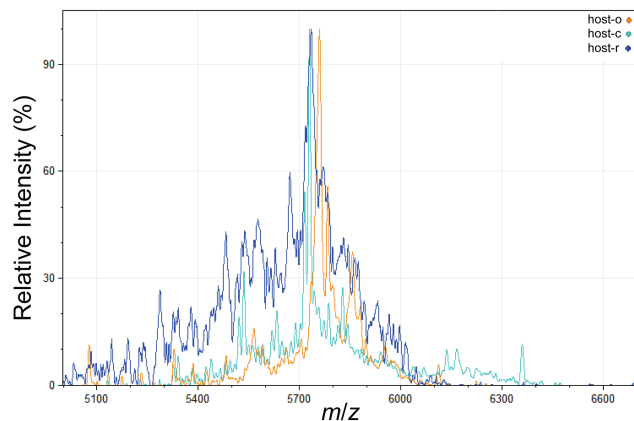


**Figure 1.3.3.** MALDI–TOF mass spectra of host-o (5757.07), host-c (5728.55), and host-r (5731.67).

### Analysis of Host Self-Association with Ultracentrifugation

To assess the aggregation state of host-o and host-r in solution, we subjected their solutions to analytical ultracentrifugation (AUC). Although sedimentation-equilibrium data fitted to a single-species model presents host-o as a dimer and host-r as a monomer in solution, introduction of a multimer in the models improves fits significantly by better representing the contributions from high-molecular weight (MW) species. Monomer–pentamer and monomer–trimer models best explain the high-MW species observed in host-o and host-r gradients, respectively (Figure 1.3.4). Monomer-multimer models for host-o and host-r data collected at 34,000 rpm exemplifies the abundance of each species across the gradients. The presence of high-MW species in the host-o sample results in an appreciable deviation from linearity (Figure 1.3.5 A), while the host-r gradient remains linear with only minor deviation from sedimentation expected of a monomer (Figure 1.3.5 B). Thus, AUC indicates multimerization of host-o, whereas host-r remains essentially in a monomeric state.

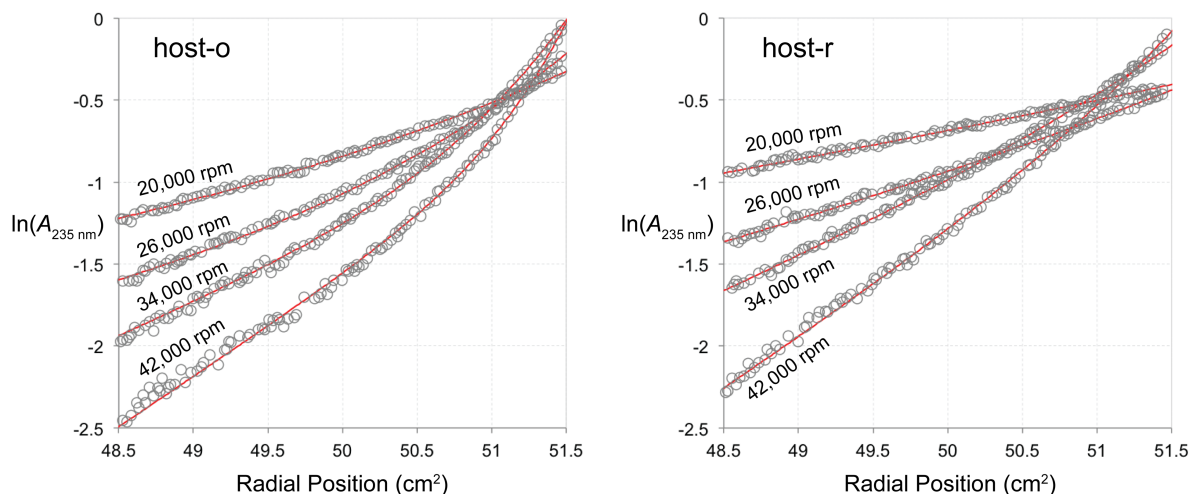


**Figure 1.3.4.** Sedimentation equilibrium analysis. Equilibrium gradients (gray circles) for host-o and host-r are shown at four different speeds (20, 26, 34, and 42 k rpm) with models that provide optimal fits (red lines). The host-o data are modeled best as a mixture of monomers and pentamers, whereas the host-r data are modeled best as a mixture of monomers and trimers. The gradients for host-r are mostly linear, due to a near-uniform composition dominated by monomers. In contrast, non-linear behavior seen in host-o gradients indicate appreciable levels of high-molecular weight species present in solution. These trends are apparent at all speeds.

### Analysis of Host·CMP Complex Formation with Fluorescence Spectroscopy

To reveal whether a triple helix forms between the hosts and a CMP, we employed fluorescence spectroscopy. Host-o and host-r were conjugated to biotin, and then complexed to fluorescent beads that were coated with streptavidin. A fluorescein probe was tethered to a CMP, (Pro-Pro-Gly)<sub>7</sub>. Upon mixing, coinciding fluorescence would indicate association and, presumably, triple-helix formation (Figure 1.3.6 A). Application of the positive control biotin–fluorescein, (Ser-Gly)<sub>3</sub>

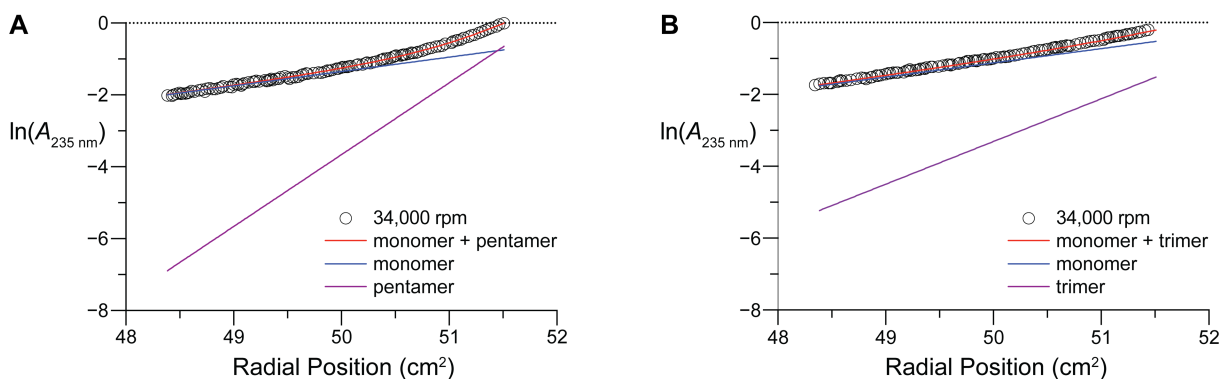


**Figure 1.3.5.** Graphs of analytical ultracentrifugation data obtained at 34,000 rpm for host-o and host-r. (A) Data for host-o fitted to a monomer + pentamer mode. (B) Data for host-r fitted to a monomer + trimer mode.

conjugated to both biotin and fluorescein, reveals a green halo upon the red fluorescence of beads under confocal microscopy where the focal plane bisects the bead (Figure 1.3.6 B). No fluorescent quenching was observed upon bead-labeling. The same pattern was apparent for host-o and host-r coated beads when mixed with the fluorescein–CMP conjugate. In contrast, treatment with fluorescein–CMP alone did not lead to green fluorescence (data not shown). Host-coated beads mixed with fluorescein–D–CMP, the enantiomeric peptide incapable of forming a triple helix with either host, showed a substantial reduction in bead-labeling (Figure 1.3.7). This reduction is indicative of the specific binding of fluorescein–CMP to hosts on the bead surface.

The qualitative results obtained with microscopy were quantified by examining beads with flow cytometry, where 10,000 events were evaluated for each sample in a single run. Again, beads coated with both host-o and host-r showed substantial labeling upon incubation with the fluorescein–CMP conjugate (Figure 1.3.8). The fluorescence with host-r was greater than that with host-o, which is not closed on its N terminus. Moreover, the triple helix formed by host-r with a CMP has greater kinetic stability than does that with host-o, where agitation for 9 h diminished fluorescence.

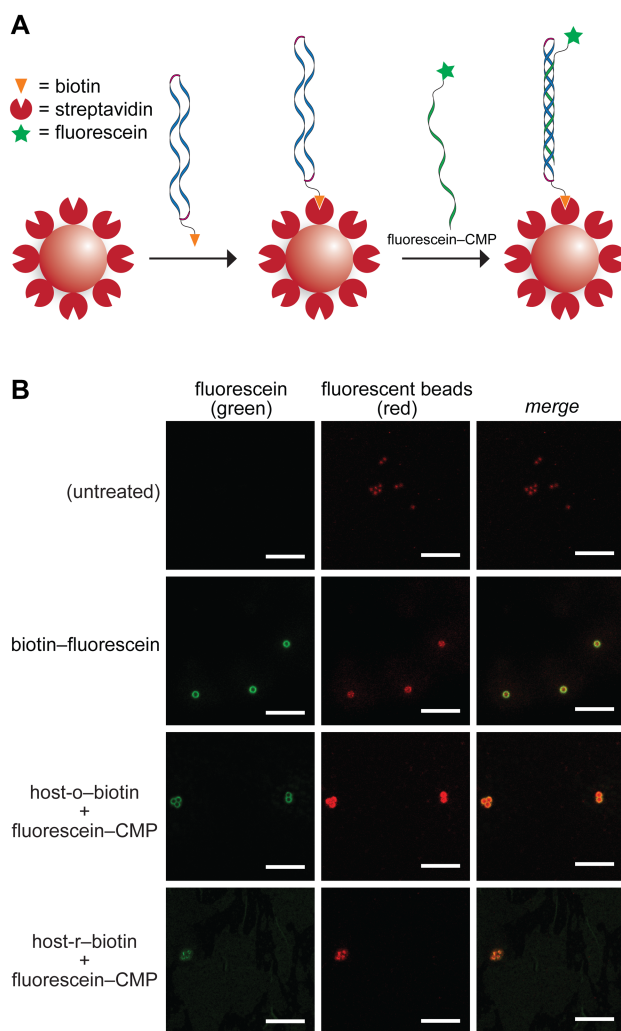


**Figure 1.3.6.** Binding of immobilized host-o and host-r to a fluorescent CMP. (A) Scheme showing the experimental design. (B) Representative confocal microscopy images. Streptavidin-coated fluorescent beads (red) were treated with biotin-conjugated host-o or host-r and then incubated with fluorescein-CMP (green), which is Ac-Lys(fluorescein)-(Ser-Gly)<sub>3</sub>-(Pro-Pro-Gly)<sub>7</sub>. Also shown are images from a negative control of untreated beads and a positive control of beads treated with a biotin-fluorescein conjugate (green), which is biotin-(Gly-Ser)<sub>3</sub>-Lys(fluorescein)-NH<sub>2</sub>. Scale bar: 10 μm.

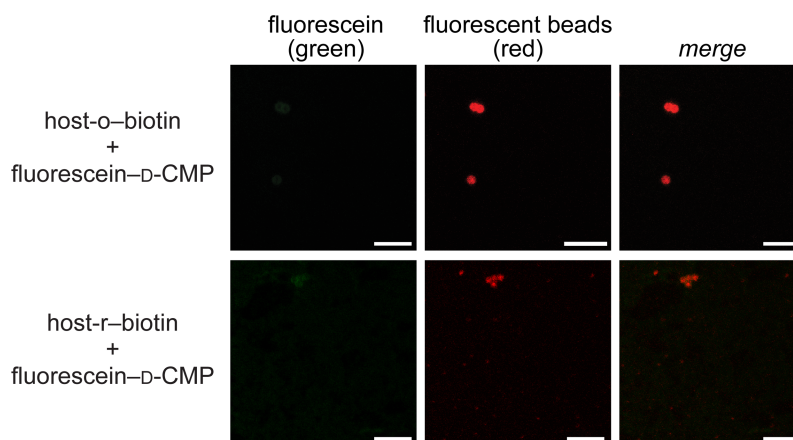


**Figure 1.3.7.** Binding of immobilized host-o and host-r to a fluorescent d-CMP, which is (D-Pro-D-Pro-Gly)<sub>7</sub>. Representative confocal microscopy images are shown. Streptavidin-coated fluorescent beads (red) were treated with host-o or host-r and then incubated with D-CMP-fluorescein (green), as in Figure 1.3.6. Scale bar: 10  $\mu$ m.

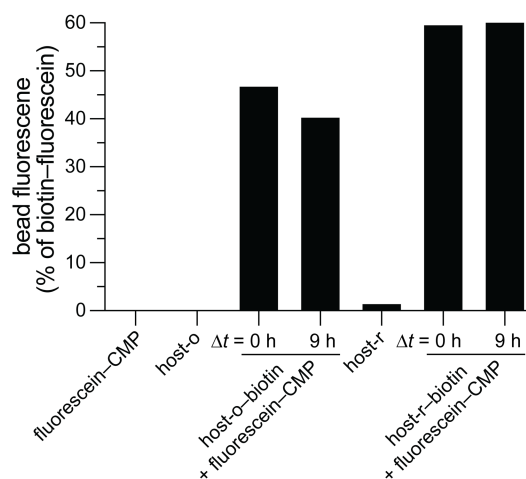


**Figure 1.3.8.** Quantification of binding of immobilized host-o and host-r to a CMP. Streptavidin-coated fluorescent beads were treated with host-o-biotin or host-r-biotin, and then with fluorescein-CMP, which is Ac-Lys(fluorescein)-(Ser-Gly)<sub>3</sub>-(Pro-Pro-Gly)<sub>7</sub>. Beads were also treated with biotin-fluorescein conjugate (which is biotin-(Gly-Ser)<sub>3</sub>-Lys(fluorescein)-NH<sub>2</sub>), host-o alone, or host-r alone. Values represent the percent of the sample population with fluorescein-labeling relative to that from treatment with biotin-fluorescein.

### **Analysis of Host·CMP Complex Formation with Circular Dichroism Spectroscopy.**

The collagen triple helix generates a distinct circular dichroism (CD) spectrum with maximum ellipticity near 226 nm.<sup>119</sup> In our host·guest system, however, that diagnostic method is complicated by two factors. First, the hosts themselves have CD spectra like that of a triple helix (Figure 1.3.9 A). Second, guest strands alone can form a homotrimeric helix as well as a host·guest complex, and those two triple helices are likely to have indistinguishable CD spectra. Nonetheless, interactions with a monomeric host (*e.g.*, host-r) could reveal trends, especially if analyses are restricted to strands that do not form homotrimers. Accordingly, changes in CD signal upon mixing such strands with a host could be attributed to the formation of a host·guest triple helix. The CMPs (flp-Hyp-Gly)<sub>7</sub>,<sup>84, 103</sup> (flp-Flp-Gly)<sub>7</sub>,<sup>120</sup> (Pro-Pro-Gly)<sub>7</sub>,<sup>120</sup> and (Pro-Ile-Gly)<sub>7</sub><sup>121, 122</sup> cannot form stable homotrimeric triple helices, exhibit low CD signal, and are ideal for testing the utility of host-r as a mimic for damaged collagen (Figure 1.3.9 B). In contrast, a collagen signature is apparent in their mixtures with host-r (Figure 1.3.9 C). To determine the extent of interaction between host-r and each guest, we used data on individual species to calculate CD spectra where the components of the mixture do not interact. The calculated spectra explain the CD signal observed for mixtures of host-r with (Pro-Pro-Gly)<sub>7</sub> and (Pro-Ile-Gly)<sub>7</sub> (Figure 1.3.9 C). In contrast, (flp-Hyp-Gly)<sub>7</sub> and (flp-Flp-Gly)<sub>7</sub> interact cooperatively with host-r, producing significantly higher triple-helix signal than each species can independently contribute. In comparison, host-o·guest complexes do not yield similar levels of cooperativity (Figure 1.3.10).

The results from temperature-denaturation experiments are consistent with the spectral analysis above, and also highlight the impact of macrocycle formation on host structure. Although similar folded states can be imagined for all hosts, macrocycle formation and flexibility limit their



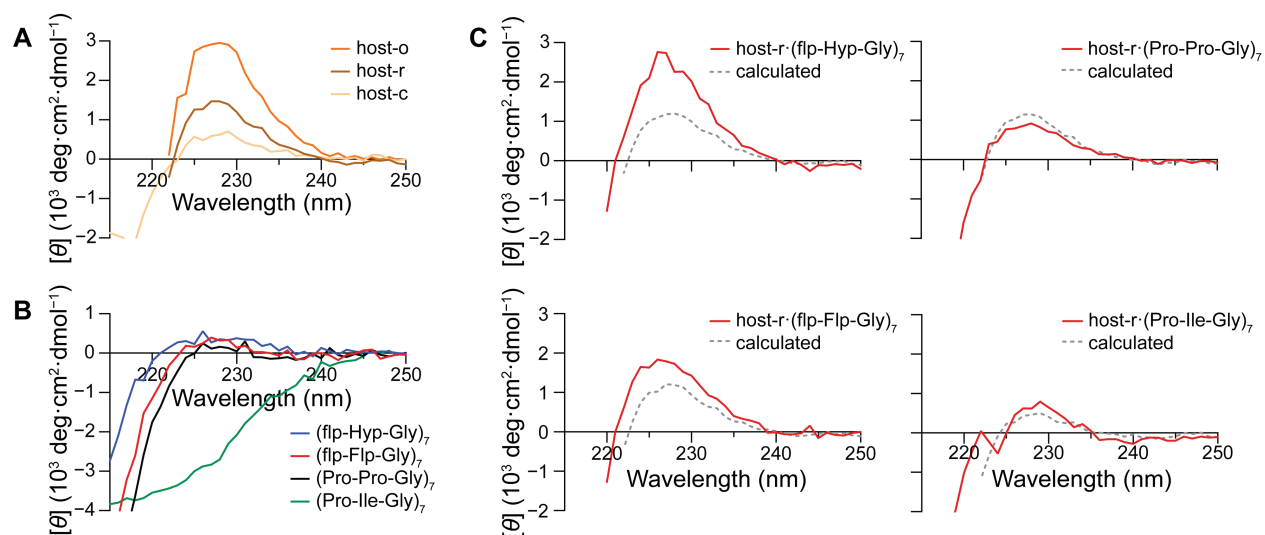


**Figure 1.3.9.** Circular dichroism spectra of hosts (A), guest CMPs (B) and host·CMP complexes (C). Calculated spectra for noninteracting mixtures of host-r and CMPs are shown (dashed gray lines) together with acquired spectra for host-r·CMP complexes (red lines). Spectra were obtained in 50 mM HOAc at 4 °C.

conformations upon denaturation. This is clearly reflected in their denaturation profiles (Figure 11 A). Whereas a distinct transition is apparent for host-o ( $T_m = 45.6 \text{ °C}$ ), an extremely shallow transition is apparent for the highly constrained host-c and increases after reduction to host-r. This trend is consistent with that observed in CD spectra (Figure 1.3.9 A). Furthermore, the thermal transitions for host-r·guest complexes become increasingly recognizable when a more cooperative guest is selected (Figure 1.3.11 B), consistent with our analysis of host·guest cooperativity (Figure 1.3.6 C).

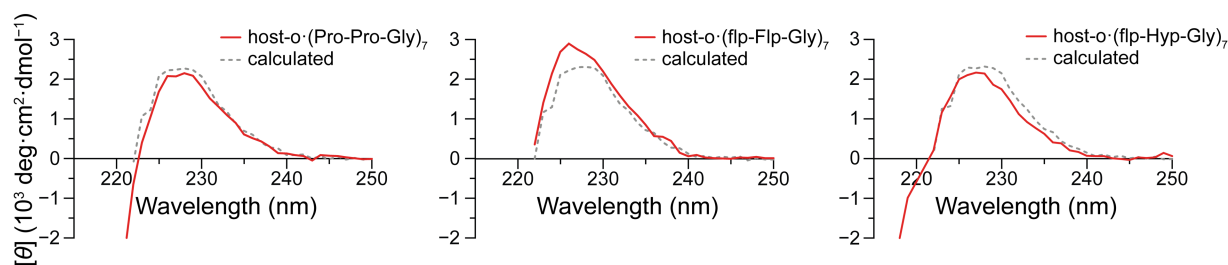


**Figure 1.3.10.** Circular dichroism spectra of host-o·CMP complexes. Calculated spectra for non-interacting mixtures of host-o and CMPs are shown (dashed gray lines) together with acquired spectra for host-o·CMP complexes (red lines). Spectra were obtained in 50 mM HOAc at 4 °C.

The peptides (flp-Hyp-Gly)<sub>7</sub>, (flp-Flp-Gly)<sub>7</sub>, and (Pro-Pro-Gly)<sub>7</sub> were used previously as invasive strands to deliver cargo to damaged collagen.<sup>73, 103, 104, 106</sup> (Pro-Hyp-Gly)<sub>7</sub> has also been employed for this purpose.<sup>23, 123</sup> Unlike the other peptides, however, (Pro-Hyp-Gly)<sub>7</sub> readily forms homotrimers at room temperature, complicating its therapeutic use. As anticipated, application of (Pro-Hyp-Gly)<sub>7</sub> to host-r does not enhance triple-helical content (Figure 1.3.12).

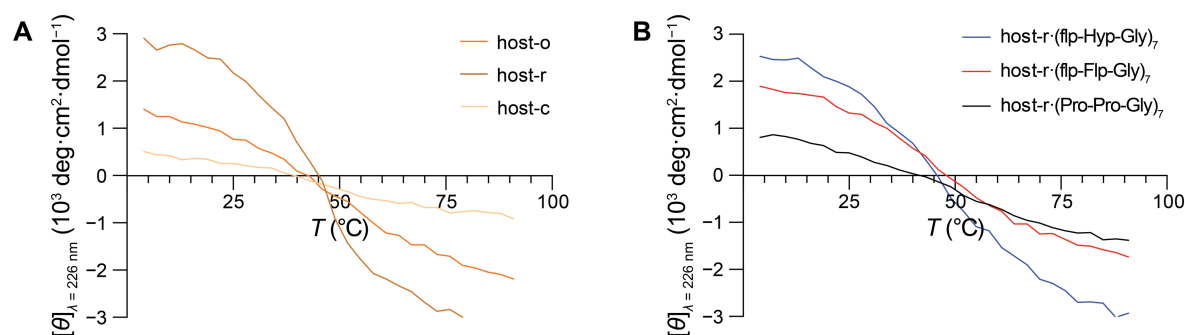


**Figure 1.3.11.** Circular dichroism temperature-denaturation experiments for all three hosts alone (A) and host-r·CMP complexes (B).

### 1.3.4 Discussion

A collagen duplex could be an effective mimic of damaged collagen (Figure 1.3.1). To optimize a duplex for this purpose, we synthesized two parallel strands of (Pro-Pro-Gly)<sub>10</sub> from the amino groups of an immobilized lysine residue. The N-terminal closing of this acyclic duplex,

host-o, was achieved by olefin metathesis using the Grubbs G2 catalyst. Reduction of the ensuing alkene afforded a cyclic duplex, host-r (Figure 1.3.2). This simple modification appears to be critical, as it results in a dramatic increase in CD signal (Figure 1.3.9 A).

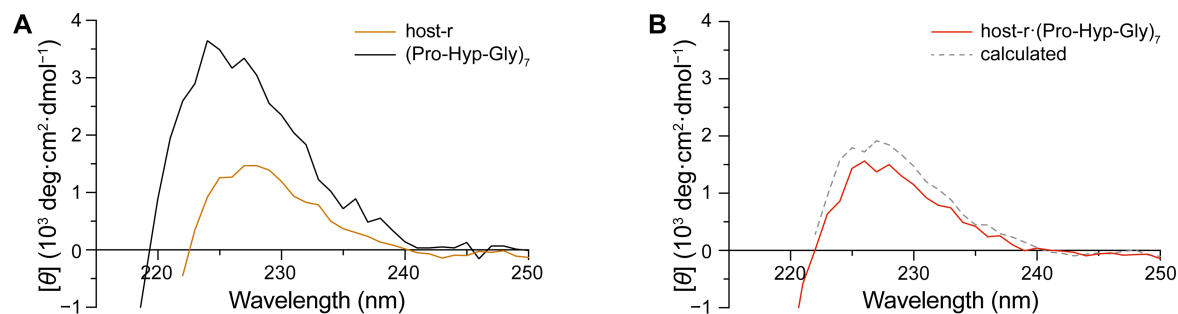


**Figure 1.3.12.** Circular dichroism spectra of host-r and (Pro-Hyp-Gly)<sub>7</sub> alone (A), and their complex (B). A spectrum calculated assuming a mixture of non-interacting species is shown as a comparison (dashed gray line). Spectra were obtained in 50 mM HOAc at 4 °C.

host-o, was achieved by olefin metathesis using the Grubbs G2 catalyst. Reduction of the ensuing alkene afforded a cyclic duplex, host-r (Figure 1.3.2). This simple modification appears to be critical, as it results in a dramatic increase in CD signal (Figure 1.3.9 A).

Analytical ultracentrifugation revealed that host-r exists primarily as a monomer in solution (Figure 1.3.5 B). Yet, it exhibits triple-helical character by CD spectroscopy, despite its topological inability to form a triple helix. This finding is consistent with our recent discovery that two singly cross-linked CMPs adopt a collagen-like structure even in the absence of a third strand.<sup>124</sup>

Although host-r exhibits a lower triple-helix signal than does host-o (Figure 1.3.9 A), the benefits of macrocycle formation outweigh any accompanying structural penalty. Closing the macrocycle reduces multimerization (Figure 1.3.5), improves the cooperativity of host-guest association (*cf.*: Figures 1.3.6 C and 1.3.10), and enables better retention of a CMP on a host-coated bead surface (Figure 1.3.8). The kinetically stable interaction of such beads with (Pro-Pro-Gly)<sub>7</sub> is especially interesting, as this CMP displays little cooperativity with host-r. CD spectra

calculated for noninteracting species are likely overestimations due to higher concentrations used to obtain data for individual species. Perhaps more importantly, the bead-retention experiment is unique in being a measurement done on a solid support, which can enhance ligand association as compared to solution-state measurements.<sup>125, 126</sup> Interestingly, (Pro-Pro-Gly)<sub>7</sub> has been used as an invasive strand to deliver cargo to wound beds, which similarly display damaged collagen on a 3-D surface.<sup>73, 104, 106</sup>

Different CMPs were examined as “guests”—third strands. Of those, (flp-Hyp-Gly)<sub>7</sub> and (flp-Flp-Gly)<sub>7</sub> are superior at promoting the formation of a triple helix with host-r (Figure 1.3.9 C). Their ability to form a stable triple helix can be attributed to the preorganization endowed by their flp residues (which adopt a requisite *C<sup>γ</sup>-endo* ring pucker and  $\phi \sim -75^\circ$  dihedral angle) and Hyp and Flp residues (which adopt a requisite *C<sup>γ</sup>-exo* ring pucker and smaller  $\phi \sim -60^\circ$  dihedral angle).<sup>1</sup> Interestingly, the interaction of host-r with (flp-Hyp-Gly)<sub>7</sub> produces a greater rise in CD signal than that with (flp-Flp-Gly)<sub>7</sub>, even though Flp-to-Hyp substitutions at the Yaa position of a (Pro-Yaa-Gly)<sub>7</sub> peptide lowers thermostability.<sup>127, 128</sup> This finding is consistent with our recent discovery that (flp-Hyp-Gly)<sub>7</sub> is an optimal strand for annealing to damaged collagen *in vitro* and *ex vivo*.<sup>103</sup> Hence, we conclude that host-r provides a reliable mimic of damaged collagen.

Although all CMPs tested are deficient in homotrimer formation, they are so due to different factors. The peptides, (flp-Hyp-Gly)<sub>7</sub> and (flp-Flp-Gly)<sub>7</sub>, feature residues with high triple-helical propensity, but cannot form triple helices due to severe steric hindrance between Xaa = flp and Yaa = Flp or Hyp residues on neighboring strands.<sup>30, 103</sup> In contrast to their spectra alone, (Pro-Pro-Gly)<sub>7</sub> and (Pro-Ile-Gly)<sub>7</sub> lack the preorganization of their counterparts, and their triple helices are not stable above 4 °C despite being unhindered by sterics. Thus, (Pro-Pro-Gly)<sub>7</sub> and (Pro-Ile-Gly)<sub>7</sub> are not well-positioned for cooperative interactions with host-r, which is corroborated by our findings (Figure 1.3.9 C). Interestingly, we also observe similar uncooperative behavior in mixtures of host-r and (Pro-Hyp-Gly)<sub>7</sub>, a peptide that forms stable homotrimers up to 36 °C (Figure

1.3.11).<sup>129</sup> Together, our results point to engineered guest peptides, and especially to (flp-Hyp-Gly)<sub>7</sub>, as the optimal CMPs for targeting collagen damage.

### 1.3.5 Conclusion

Host-r is a macrocycle that contains two collagen-mimetic peptides and forms a collagen triple helix with a third collagen-mimetic peptide. Its development provides opportunities for new types of analyses. Historically, the rigorous analysis of triple-helix formation has been complicated by the process being termolecular. For example, hysteresis often confounds analyses of the unfolding–refolding transition with three strands.<sup>130-133</sup> As the basis of a bimolecular rather than a termolecular system, host-r could provide clarity as well as new insight.

In addition, we note that human type-I collagen, which is the most abundant protein in the extracellular matrix and connective tissue,<sup>1</sup> is composed of two  $\alpha 1$ [I] strands and one  $\alpha 2$ [I] strand. In collagen fibrils, a Gly-Phe-Hyp-Gly-Glu-Arg sequence clusters integrins on the surface of endothelial cells and promotes wound healing.<sup>32, 134-136</sup> Disruption of the triple helix in this region could be especially deleterious to wound repair. Host-r variants composed of two copies of the GAOGPSGARGERG**FOGER**GVQGPAGPR sequence of human  $\alpha 1$ [I] strands (where “O” refers to Hyp) could lead to the discovery of CMPs that enable new therapeutic interventions.<sup>115</sup>

### 1.3.6 Acknowledgment

We are grateful to Dr. Darrell R. McCaslin and Dr. Martha M. Vestling for facility support and contributive discussions, and to Prof. Clark R. Landis for use of his glovebox. A.J.E. was supported by Chemistry–Biology Interface (CBI) Training Grant T32 GM008505 (NIH). This work was supported by Grant R56 AR044276 (NIH).

### 1.3.7 Experimental

#### Experimental methods

##### General

Boc-flp-OH and Fmoc-flp-OH were from OmegaChem (Lévis, Québec). (Here, “flp” refers to (2*S*,4*S*)-4-fluoroproline.) Boc-Flp-OH, Fmoc-Hyp-OH, and other amino acid derivatives, resins, Fmoc-OSu, and HOBt were from Chem-Impex International (Wood Dale, IL). (Here, “Flp” refers to (2*S*,4*R*)-4-fluoroproline and “Hyp” refers to (2*S*,4*R*)-4-hydroxyproline.) DIC and 4-methyl-piperidine were from Oakwood Chemical (Estill, SC). Streptavidin-coated fluorescent blue particles were product SVFP-106805 from Spherotech (Lake Forest, IL). 6-Aminohexanoic acid and all other reagents were from Sigma–Aldrich (St. Louis, MO) and were used without further purification.

DMF was dried with a Glass Contour system from Pure Process Technology (Nashua, NH). In addition, DMF was passed through an associated isocyanate “scrubbing” column to remove any amines. Water was purified with an Arium Pro system from Sartorius (Göttingen, Germany).

The phrase “concentrated under reduced pressure” refers to the removal of solvents and other volatile materials with a rotary evaporator at water-aspirator pressure (<20 Torr) while maintaining a water bath below 40 °C. Residual solvent was removed from samples with a high vacuum (<0.1 Torr).

All procedures were performed in air at ambient temperature (~22 °C) and pressure (1.0 atm) unless indicated otherwise.

##### Instrumentation

Solid-phase peptide synthesis was performed with a Liberty Blue Peptide Synthesizer from CEM (Matthews, NC). Synthetic peptides were purified by HPLC with a Prominence instrument from Shimadzu (Kyoto, Japan) equipped with a VarioPrep 250/21 C18 column from Macherey–Nagel (Düren, Germany). Molecular mass was determined by matrix-assisted laser

desorption/ionization–time-of-flight (MALDI–TOF) mass spectrometry on an  $\alpha$ -cyano-4-hydroxycinnamic acid or sinapic acid matrix with a microflex LRF™ instrument from Bruker (Billerica, MA). Purity analyses were performed with an Acquity UPLC® H-Class system from Waters that was equipped with an Acquity photodiode array detector, Acquity quaternary solvent manager, Acquity sample manager with a flow-through needle, Acquity UPLC® BEH C18 column (2.1 × 50 mm, 1.7- $\mu$ m particle size) and Empower 3 software.  $^1\text{H}$  and  $^{13}\text{C}$  NMR spectra were acquired with an Avance III 400 spectrometer from Bruker. Sedimentation equilibrium experiments were performed with an XL-A analytical ultracentrifuge and An-60 Ti rotor from Beckman Coulter (Brea, CA) at the Biophysics Instrumentation Facility of the University of Wisconsin–Madison (UW BIF). Beads were imaged using a Eclipse Ti inverted confocal microscope from Nikon (Melville, NY) at the Biochemistry Optical Core of the University of Wisconsin–Madison. Flow cytometry was performed with an Accuri Flow Cytometer with C-Sampler from BD (San Jose, CA) at the UW BIF. CD data were acquired with a 420 CD spectrophotometer from Aviv Biomedical (Lakewood, NJ) at the UW BIF.

### Small-Molecule Synthesis

*Fmoc-6-aminohexanoic acid.* 6-Aminohexanoic acid (1.00 g, 7.62 mmol) was dissolved in a saturated aqueous solution of  $\text{NaHCO}_3$  (50 mL). In a separate flask, Fmoc-OSu (2.82 g, 8.38 mmol) was dissolved in dioxane (50 mL). The two solutions were combined, and the reaction mixture became cloudy and was stirred for 16 h. The mixture was then concentrated under reduced pressure. The residue was dissolved in EtOAc and washed with aqueous 1.0 M HCl and brine. The organic layer was dried over  $\text{Na}_2\text{SO}_4(\text{s})$ , decanted, and concentrated under reduced pressure. Crude product was purified by chromatography on silica-gel, eluting with EtOAc (40% v/v) and acetic acid (1% v/v) in hexanes to yield Fmoc-6-aminohexanoic acid (2.56 g, 95%) as a white solid. HRMS–ESI ( $m/z$ ):  $[\text{M} + \text{H}]^+$  calcd, 354.17; found, 354.17.  $^1\text{H}$  NMR (400 MHz, MeOD,  $\delta$ ): 7.78 (d,  $J = 7.5$  Hz, 2H), 7.63 (d,  $J = 7.5$  Hz, 2H), 7.37 (t,  $J = 7.4$  Hz, 2H), 7.33–7.26 (m, 2H), 4.33 (d,

$J = 6.8$  Hz, 2H), 4.18 (t,  $J = 6.9$  Hz, 1H), 3.08 (t,  $J = 7.0$  Hz, 2H), 2.27 (t,  $J = 7.4$  Hz, 2H), 1.60 (p,  $J = 7.5$  Hz, 2H), 1.49 (p,  $J = 7.1$  Hz, 2H), 1.33 (p,  $J = 10.1, 6.0$  Hz, 2H).  $^{13}\text{C}$  NMR (101 MHz, MeOD,  $\delta$ ): 157.49, 143.95, 141.20, 127.34, 126.71, 124.75, 119.50, 66.11, 47.13, 40.17, 33.71, 29.18, 25.97, 24.45.

*Boc-Flp-OBn*. Boc-Flp-OH (2.5 g, 10.7 mmol) was dissolved in DMF. Solid  $\text{Cs}_2\text{CO}_3$  (1.5 g, 10.7 mmol) was added, and the reaction mixture was stirred for 10 min. Benzyl bromide (1.27 mL, 10.7 mmol) was added dropwise, and the mixture was stirred for 16 h. The mixture was then concentrated under reduced pressure. Crude product was purified by chromatography on silica gel, eluting with EtOAc (10% v/v) in hexanes to yield product (2.26 g, 65%). HRMS–ESI ( $m/z$ ):  $[\text{M} + \text{H}]^+$  calcd, 324.15; found, 324.16.  $^1\text{H}$  NMR (400 MHz,  $\text{CDCl}_3$ ,  $\delta$ ): 7.35 (d,  $J = 4.5$  Hz, 5H), 5.32–5.19 (m, 1H), 5.19–5.14 (m, 1H), 5.14–5.04 (m, 1H), 4.58–4.38 (m, 1H), 3.99–3.75 (m, 1H), 3.61 (ddt,  $J = 36.1, 13.0, 3.9$  Hz, 1H), 2.70–2.47 (m, 1H), 2.20–1.97 (m, 1H), 1.53–1.31 (m, 9H), which are consistent with literature values for this known compound.<sup>30</sup>

*Boc-flp-Flp-OBn*. Boc-Flp-OBn (2.26 g, 6.99 mmol) was dissolved in 4 N HCl (8.0 mL), and the reaction mixture was stirred for 30 min. The reaction mixture was then concentrated under reduced pressure. The residue was dissolved in DMF. DIEA (4.87 mL, 27.96 mmol) was added dropwise. Solid PyBrOP (3.91 g, 8.39 mmol) and Boc-flp-OH (1.79 g, 7.69 mmol) were added, and the reaction mixture was stirred for 16 h. The residue was concentrated under reduced pressure, taken up in EtOAc, and washed successively with 1.0 M HCl (2 $\times$ ), saturated aqueous  $\text{NaHCO}_3$  (2 $\times$ ), and brine (2 $\times$ ). The organic layer was dried over  $\text{Na}_2\text{SO}_4(\text{s})$ , filtered, and concentrated under reduced pressure to yield crude product (3.96 g), which was carried forward without further purification. HRMS–ESI ( $m/z$ ):  $[\text{M} + \text{H}]^+$  calcd, 439.20; found, 439.20.  $^1\text{H}$  NMR (400 MHz,  $\text{CDCl}_3$ ,  $\delta$ ): 7.35 (d,  $J = 4.0$  Hz, 6H), 5.32–5.10 (m, 4H), 4.55 (dt,  $J = 20.6, 8.4$  Hz, 1H), 4.06–3.77 (m, 4H), 3.66 (ddt,  $J = 36.6, 13.0, 3.5$  Hz, 1H), 2.62 (ddd,  $J = 28.3, 16.6, 8.0, 1.8$  Hz, 1H), 2.22–1.99 (m, 2H), 1.85 (ddt,  $J = 71.3, 13.3, 6.7$  Hz, 1H), 0.94 (d,  $J = 6.7$  Hz, 3H), 0.85 (dd,  $J = 6.7, 2.3$



Hz, 4H).  $^{13}\text{C}$  NMR (101 MHz,  $\text{CDCl}_3$ ,  $\delta$ ): 172.16, 172.04, 155.00, 154.56, 135.47, 135.28, 128.65, 128.58, 128.52, 128.42, 128.33, 128.16, 92.65, 91.86, 90.86, 90.08, 77.25, 71.88, 71.83, 67.09, 67.02, 60.40, 57.72, 57.48, 53.58, 53.35, 53.15, 52.93, 37.77, 37.54, 36.71, 36.48, 28.36, 28.17, 27.98, 27.86, 19.03, 18.96, 18.92, 14.22.

*Fmoc-Gly-flp-Flp-OBn*. Crude Boc-flp-Flp-OBn (3.96 g) was dissolved in 4 N HCl (8.0 mL), and the reaction mixture was stirred for 30 min. The mixture was then concentrated under reduced pressure. The residue was dissolved in DCM. DIEA (3.65 mL, 20.97 mmol) was added dropwise to the resulting solution. Solid Fmoc-Gly-OPfp (3.24 g, 6.99 mmol) was added, and the reaction mixture was stirred for 16 h. The residue was concentrated under reduced pressure, taken up in EtOAc, and washed successively with 1.0 M HCl (2 $\times$ ), saturated aqueous  $\text{NaHCO}_3$  (2 $\times$ ), and brine (2 $\times$ ). The organic layer was dried over  $\text{Na}_2\text{SO}_4(\text{s})$ , filtered, and concentrated under reduced pressure. Crude product was purified by chromatography on silica gel, eluting with dichloromethane followed by a methanol flush to yield product (3.70 g, 83%). HRMS–ESI ( $m/z$ ):  $[\text{M} + \text{NH}_4]^+$  calcd, 635.23; found, 635.27.  $^1\text{H}$  NMR (400 MHz,  $\text{CDCl}_3$ ,  $\delta$ ): 7.75 (d,  $J = 7.5$  Hz, 2H), 7.59 (dd,  $J = 7.5, 3.2$  Hz, 2H), 7.43–7.26 (m, 9H), 5.86–5.48 (m, 1H), 5.44–5.02 (m, 4H), 4.85–4.67 (m, 2H), 4.45–4.02 (m, 4H), 4.03–3.60 (m, 3H), 2.62 (ddd,  $J = 20.3, 14.1, 8.1$  Hz, 1H), 2.56–2.22 (m, 2H), 2.08 (dddd,  $J = 40.9, 18.3, 9.1, 4.8$  Hz, 1H), 1.82 (s, 2H).  $^{13}\text{C}$  NMR (101 MHz,  $\text{CDCl}_3$ ,  $\delta$ ): 171.14, 168.75, 167.23, 156.27, 143.88, 141.26, 135.40, 128.58, 128.39, 128.29, 127.69, 127.10, 125.21, 119.95, 91.95, 77.25, 67.21, 57.96, 57.13, 47.08, 43.41, 35.31, 34.48, 34.26.

*Fmoc-Gly-flp-Flp-OH*. (3.70 g, 5.98 mmol) was dissolved in methanol (25 mL). The head space was purged with  $\text{N}_2(\text{g})$ . Pd/C (10% w/w, 0.64 g) was added, and the flask was capped with a septum.  $\text{H}_2(\text{g})$  was added via a balloon. The reaction was monitored by thin-layer chromatography and observed to be complete at 6 h. The reaction mixture was filtered through diatomaceous earth and concentrated under reduced pressure. Crude product was purified by

chromatography on silica gel, eluting with 1% v/v acetic acid and 20% v/v methanol in EtOAc to yield product (2.95 g, 93%). HRMS–ESI ( $m/z$ ):  $[M - H]^-$  calcd, 526.52; found, 526.18.  $^1\text{H}$  NMR (400 MHz, MeOD,  $\delta$ ): 7.81 (d,  $J = 7.6$  Hz, 2H), 7.74–7.64 (m, 2H), 7.48–7.28 (m, 4H), 5.49–5.03 (m, 3H), 4.72–4.20 (m, 4H), 4.20–3.43 (m, 5H), 2.85–2.27 (m, 3H), 2.26–2.06 (m, 1H).  $^{13}\text{C}$  NMR (101 MHz,  $\text{CDCl}_3$ ,  $\delta$ ): 177.16, 173.49, 172.00, 160.94, 147.71, 145.13, 132.21, 131.59, 131.14, 130.97, 130.78, 128.99, 123.79, 96.63, 96.29, 94.84, 94.48, 71.07, 68.30, 61.94, 61.35, 50.96, 46.99, 39.48, 39.26, 38.24, 38.03.

### Peptide Synthesis

Peptides were prepared by automated solid-phase peptide synthesis. Fmoc-deprotection was achieved by treatment with 4-methyl-piperidine (20% v/v) in DMF. Tripeptides, amino acids, and small-molecule carboxylic acids (5 equiv) were activated by using DIC and HOBt. Peptides were cleaved from the resin with 96.5:2.5:1.0 TFA/ $\text{H}_2\text{O}$ /TIPSH (5 mL), precipitated from diethyl ether at  $-80$  °C, and isolated by centrifugation. Peptides were purified by preparative HPLC using a gradient of 10–50% B (single strands) or 40–65% B (hosts) over 50 min (A:  $\text{H}_2\text{O}$  containing 0.1% v/v TFA; B: acetonitrile containing 0.1% v/v TFA). The purity of each peptide was assessed to be >95% by UPLC.

*Host-o*. The open host was synthesized by first doing a 0.05-mmol coupling of Fmoc-Lys(Fmoc)-OH to TGT S RAM resin (0.22 mmol/g). Next, Fmoc-6-aminohexanoic acid was single-coupled at a 0.10-mmol scale. Additional amino acid and small-molecule carboxylic acid additions were done at a 0.10-mmol scale and double-coupled. MALDI ( $m/z$ ):  $[M + H]^+$  calcd, 5757.05; found, 5757.07. A 0.05-mmol scale synthesis afforded 7.6 mg (2.7%) of host-o after purification.

*Host-c*. The closed host was synthesized by olefin metathesis on the N-terminal 4-butenic acids of the open next on resin, following a procedure similar to that for the stapling of peptide side chains.<sup>117</sup> Peptide bound to resin was added to a Schlenk flask. The resin was then dried for

at least 3 h on a high-vacuum manifold. Then, the flask was purged rigorously with N<sub>2</sub>(g). While under N<sub>2</sub>(g), the resin was pre-swelled in 2.5 mL of dry CH<sub>2</sub>Cl<sub>2</sub> for at least 15 min prior to the addition 0.5 mL of a 2.5 mM solution of the Grubbs G2 catalyst (C<sub>46</sub>H<sub>65</sub>Cl<sub>2</sub>N<sub>2</sub>PRu)<sup>137</sup> in dry CH<sub>2</sub>Cl<sub>2</sub> using standard Schlenk techniques. The reaction flask was equipped quickly with an oven-dried reflux condenser, purged with N<sub>2</sub>(g), and heated in an oil bath at 40 °C for 36 h under N<sub>2</sub>(g). After 36 h, another 0.5-mL aliquot of the Grubbs G2 catalyst solution was added, and the flask was heated at 40 °C for another 36 h under N<sub>2</sub>(g). Dry solvent was added over the course of the reaction to maintain at least 3 mL of CH<sub>2</sub>Cl<sub>2</sub>. The reaction mixture was then allowed to cool to room temperature and filtered. The resin was washed with DCM to remove any remaining catalyst. MALDI (*m/z*): [M + H]<sup>+</sup> calcd, 5729.02; found, 5728.55. A 0.05-mmol scale synthesis afforded 7.0 mg (2.4%) of host-c after purification.

*Host-r*. Following olefin metathesis, the resin was filtered to remove catalyst and a small sample was taken to confirm the generation of host-c by MALDI mass spectrometry. The resin was returned to a Schlenk flask and suspended in DCE. Again following a literature precedent,<sup>138</sup> Umicore M2 (46.5 mg, 0.05 mmol) and Et<sub>3</sub>SiH (0.80 mL, 9.4 mmol) were added to the flask. The vessel was capped with a septum, and the reaction mixture was heated to 60 °C for 72 h. The resin was washed with DCM to remove any remaining catalyst. MALDI (*m/z*): [M + H]<sup>+</sup> calcd, 5731.03; found, 5731.67. A 0.05-mmol scale synthesis afforded 9.8 mg (3.4%) of host-r after purification.

*Host-o-biotin and host-r-biotin*. Biotin was conjugated to the N<sup>ε</sup>-amino group of a lysine residue installed near the C-terminus of host-o and host-r. Specifically, Fmoc-Lys(Boc)-OH was coupled to TGT S RAM resin (0.22 mmol/g) followed by a (Gly-Ser)<sub>3</sub> sequence synthesized by the addition of Fmoc-protected amino acids. The remainder of the host-o and host-r syntheses followed as described above.

After cleavage from the resin, crude host-o (5.3 mg, 0.84 μmol) was dissolved in 500 μL of DMSO. A solution of biotin-NHS ester (4.0 mg, 11.7 μmol) and DIEA (0.1 mL, 0.57 mmol) in

500  $\mu\text{L}$  of DMSO was added, and the mixture was allowed to react for 12 h. The host-o-biotin conjugate was purified by HPLC. MALDI ( $m/z$ ):  $[\text{M} + \text{H}]^+$  calcd, 6543.38; found, 6541.63. A 0.05-mmol scale synthesis afforded 0.4 mg (0.52%) of host-o-biotin after purification.

After cleavage from the resin, crude host-r (4.3 mg, 0.68 mmol) was dissolved in 500  $\mu\text{L}$  of DMSO. A solution of biotin-NHS ester (6.7 g, 19.6  $\mu\text{mol}$ ) and DIEA (0.1 mL, 0.57 mmol) in 500  $\mu\text{L}$  of DMSO was added, and the mixture was allowed to react for 12 h. The host-r-biotin conjugate was purified by HPLC. MALDI ( $m/z$ ):  $[\text{M} + \text{H}]^+$  calcd, 6517.37; found, 6519.48. A 0.05-mmol scale synthesis afforded 0.2 mg (0.14%) of host-r-biotin after purification.

*(flp-Hyp-Gly)<sub>7</sub>*. *(flp-Hyp-Gly)<sub>7</sub>* was synthesized by the addition (double-coupling) of Fmoc-protected amino acids to preloaded Fmoc-Gly-Wang resin (0.65 mmol/g). MALDI ( $m/z$ ):  $[\text{M} + \text{H}]^+$  calcd, 2015.80; found, 2015.10. A 0.05-mmol scale synthesis afforded 6.4 mg (6.4%) of *(flp-Hyp-Gly)<sub>7</sub>* after purification.

*(flp-Flp-Gly)<sub>7</sub>*. *(flp-Flp-Gly)<sub>7</sub>* was synthesized by using Fmoc-Gly-flp-Flp-OH tripeptide and Fmoc-flp-OH and Fmoc-Flp-OH monomers. Six segment condensations of tripeptide were followed by the addition of each monomer, with each addition being double-coupled on preloaded Fmoc-Gly-Wang resin (0.65 mmol/g). The peptide was then cleaved from the resin and purified by HPLC. MALDI ( $m/z$ ):  $[\text{M} + \text{H}]^+$  calcd, 2028.77; found, 2028.75. A 0.05-mmol scale synthesis afforded 8.3 mg (8.1%) of *(flp-Flp-Gly)<sub>7</sub>* after purification.

*(Pro-Pro-Gly)<sub>7</sub>*. *(Pro-Pro-Gly)<sub>7</sub>* was synthesized by the addition of Fmoc-protected amino acids to preloaded Fmoc-Gly-Wang resin (0.65 mmol/g). MALDI ( $m/z$ ):  $[\text{M} + \text{H}]^+$  calcd, 1777.02; found, 1776.87. A 0.05-mmol scale synthesis afforded 18.0 mg (20.2%) of *(Pro-Pro-Gly)<sub>7</sub>* after purification.

*(Pro-Ile-Gly)<sub>7</sub>*. *(Pro-Ile-Gly)<sub>7</sub>* was synthesized by the addition of Fmoc-protected amino acids to preloaded Fmoc-Gly-Wang resin (0.65 mmol/g). MALDI ( $m/z$ ):  $[\text{M} + \text{H}]^+$  calcd, 1890.31;

found, 1890.30. A 0.05-mmol scale synthesis afforded 9.6 mg (10.2%) of (Pro-Ile-Gly)<sub>7</sub> after purification.

*Fluorescein-CMP.* Ac-Lys-(Ser-Gly)<sub>3</sub>-(Pro-Pro-Gly)<sub>7</sub> was synthesized by the addition of Fmoc-protected amino acids to preloaded Fmoc-Gly-Wang resin (0.65 mmol/g) and then cleaved from the resin. 5(6)-Carboxyfluorescein (112.4 mg, 0.30 mmol), HATU (104.8 mg, 0.28 mmol), and DIEA (100  $\mu$ L, 0.57 mmol) were incubated for 15 min in 500  $\mu$ L of DMSO. This solution was added to a solution of crude Ac-Lys-(Ser-Gly)<sub>3</sub>-(Pro-Pro-Gly)<sub>7</sub> (74.2 mg) in 500  $\mu$ L of DMSO, and the mixture was allowed to react for 12 h. MALDI ( $m/z$ ): [M + Na]<sup>+</sup> calcd, 2759.20; found, 2760.47. A 0.05-mmol scale synthesis afforded 3.5 mg (2.5%) of Ac-Lys(fluorescein)-(Ser-Gly)<sub>3</sub>-(Pro-Pro-Gly)<sub>7</sub> after purification.

*Fluorescein-D-CMP.* Ac-Lys-(Ser-Gly)<sub>3</sub>-(D-Pro-D-Pro-Gly)<sub>7</sub> was synthesized by amino acid addition on preloaded Fmoc-Gly-Wang resin (0.65 mmol/g). Fmoc-deprotection was achieved by treatment with 4-methyl-piperidine (20% v/v) in DMF. The amino acid monomer (5 equiv) was converted to an active ester by using DIC and HOBt. The peptide was then cleaved from the resin. A solution of 5(6)-carboxyfluorescein (9.7 mg, 25.7  $\mu$ mol), HATU (9.1 mg, 23.9  $\mu$ mol), and DIEA (100  $\mu$ L, 0.57 mmol) in 500  $\mu$ L DMSO was allowed to react for 15 min. A solution of crude Ac-Lys-(Ser-Gly)<sub>3</sub>-(D-Pro-D-Pro-Gly)<sub>7</sub> (36.0 mg) dissolved in 500  $\mu$ L of DMSO was added to the solution and allowed to react for 12 h. The peptide was then purified by HPLC. MALDI ( $m/z$ ): [M + Na]<sup>+</sup> calcd, 2759.20; found, 2760.47. A 0.05-mmol synthesis afforded 2.5 mg (1.8%) of Ac-Lys(fluorescein)-(Ser-Gly)<sub>3</sub>-(D-Pro-D-Pro-Gly)<sub>7</sub> after purification.

*Biotin-fluorescein.* Fmoc-Lys(Boc)-OH was coupled first to TGT S RAM resin (0.22 mmol/g) followed by a (Gly-Ser)<sub>3</sub> sequence that was synthesized by the addition of Fmoc-protected amino acids. The resulting decapeptide was treated on-resin with biotin-NHS ester (5 equiv). The peptide was then cleaved from the resin and deprotected. A solution of 5(6)-

carboxyfluorescein (9.5 mg, 25.2  $\mu\text{mol}$ ), HATU (8.7 mg, 22.8  $\mu\text{mol}$ ), and DIEA (100  $\mu\text{L}$ , 0.57 mmol) in 500  $\mu\text{L}$  DMSO were incubated for 15 min. This solution was added to a solution of crude biotin-(Gly-Ser)<sub>3</sub>-Lys-NH<sub>2</sub> (12.3 mg) in 500  $\mu\text{L}$  of DMSO, and the mixture was allowed to react for 12 h. The biotin-fluorescein conjugate was then purified by HPLC. MALDI ( $m/z$ ):  $[\text{M} + \text{H}]^+$  calcd, 1162.41; found, 1162.52. A 0.05-mmol synthesis afforded 1.5 mg (2.5%) of biotin-(Gly-Ser)<sub>3</sub>-Lys(fluorescein)-NH<sub>2</sub> after purification.

### **Analytical Ultracentrifugation**

A host (100  $\mu\text{L}$  of a 45  $\mu\text{M}$  solution) and matching buffer (110  $\mu\text{L}$ ) were placed in a cell with an Epon 12 mm double-sector charcoal-filled centerpiece from Beckman Coulter. Experiments were run at 4 °C for more than seven days at speeds of 20,000, 26,000, 34,000, and 42,000 rpm, and gradients recorded at 235 nm were monitored until superimposable 4 h apart. Equilibrium gradients at 4 °C were modeled as single and multiple noninteracting species through nonlinear least-squares fits to the gradient data, using a buffer density of 1.00037 g/mL and partial specific volumes of 0.7471 and 0.7460 mL/g calculated based on amino acid and functional group content for host-o and host-r, respectively.<sup>139</sup> Nonsedimenting baseline-attenuance was applied during data analysis, which was performed with programs written by D. R. McCaslin (UW BIF) for IGOR PRO software from WaveMetrics (Lake Oswego, OR).

### **Confocal Microscopy and Flow Cytometry**

A 200- $\mu\text{L}$  suspension of streptavidin-coated fluorescent blue particles was added to 200  $\mu\text{L}$  of a 58- $\mu\text{M}$  solution of biotinylated host-o or host-r in H<sub>2</sub>O, and the mixture was agitated for 9 h. Beads were pelleted by centrifugation at 12,000 rpm on a benchtop centrifuge for 2 min. The supernatant was removed, and the beads were resuspended in 200  $\mu\text{L}$  of H<sub>2</sub>O and stored at 4 °C.

A 10- $\mu\text{L}$  aliquot of suspended beads was treated with Ac-Lys(fluorescein)-(Ser-Gly)<sub>3</sub>-(Pro-Pro-Gly)<sub>7</sub> such that the final concentration of added peptide was 60  $\mu\text{M}$ . Mixtures were

allowed to anneal by heating the samples to 65 °C and cooling slowly to 4 °C at a rate of  $-12$  °C per hour. At 4 °C, beads were pelleted, the supernatant was removed, and the beads were resuspended in water. This process was repeated three times to wash the beads. Finally, beads were resuspended in 300  $\mu$ L of water. For confocal images, beads (3  $\mu$ L) were spotted on a microscope slide and allowed to dry. For flow cytometry, resuspended beads were imaged with 488-nm and 640-nm lasers by using 530/30-nm and 675/25-nm filters, respectively.

### **Circular Dichroism Spectroscopy**

Solutions of peptide were prepared in 50 mM HOAc. Many experiments in this study involve mixtures of hosts and guest peptides, and preparation of equimolar mixtures of the components is of vital importance. To ensure equimolar mixtures, relative concentrations were determined by integrating the absorbance of peptides at 218 nm during UPLC, and concentrations of each peptide were calculated based on the absorbance of 180  $\mu$ M (Pro-Pro-Gly)<sub>10</sub> and the assumption that the extinction coefficient of all Xaa-Yaa-Gly repeats were identical at 218 nm. Analyte solutions were prepared such that the concentration of individual collagen strands was 180  $\mu$ M. For example, solutions contained 60  $\mu$ M of a double-stranded host and 60  $\mu$ M of a (Xaa-Yaa-Gly)<sub>7</sub> peptide. To facilitate formation of the most stable complex, analyte solutions were heated to 65 °C, then cooled to 4 °C at a rate of  $-12$  °C per hour. Samples were left at 4 °C for at least 48 h before data acquisition.

CD spectra of peptides at 180  $\mu$ M strand concentration were recorded at 4 °C with a 1-nm band-pass filter and an averaging time of 3 s in a 0.1-cm path-length quartz cuvette. For thermal denaturation experiments, the CD signal was monitored at 226 nm as the sample was heated at a rate of 12 °C/h in 3-°C steps. The value of  $T_m$ , which is the temperature at the midpoint of the thermal transition, was calculated by fitting the data to a Boltzmann sigmoidal curve with the program Prism from GraphPad (La Jolla, CA).

CD spectra of equimolar noninteracting host and guest mixtures,  $[\theta]_{\text{host+guest}}$ , were calculated based on the spectra of individual components by using the following equation:

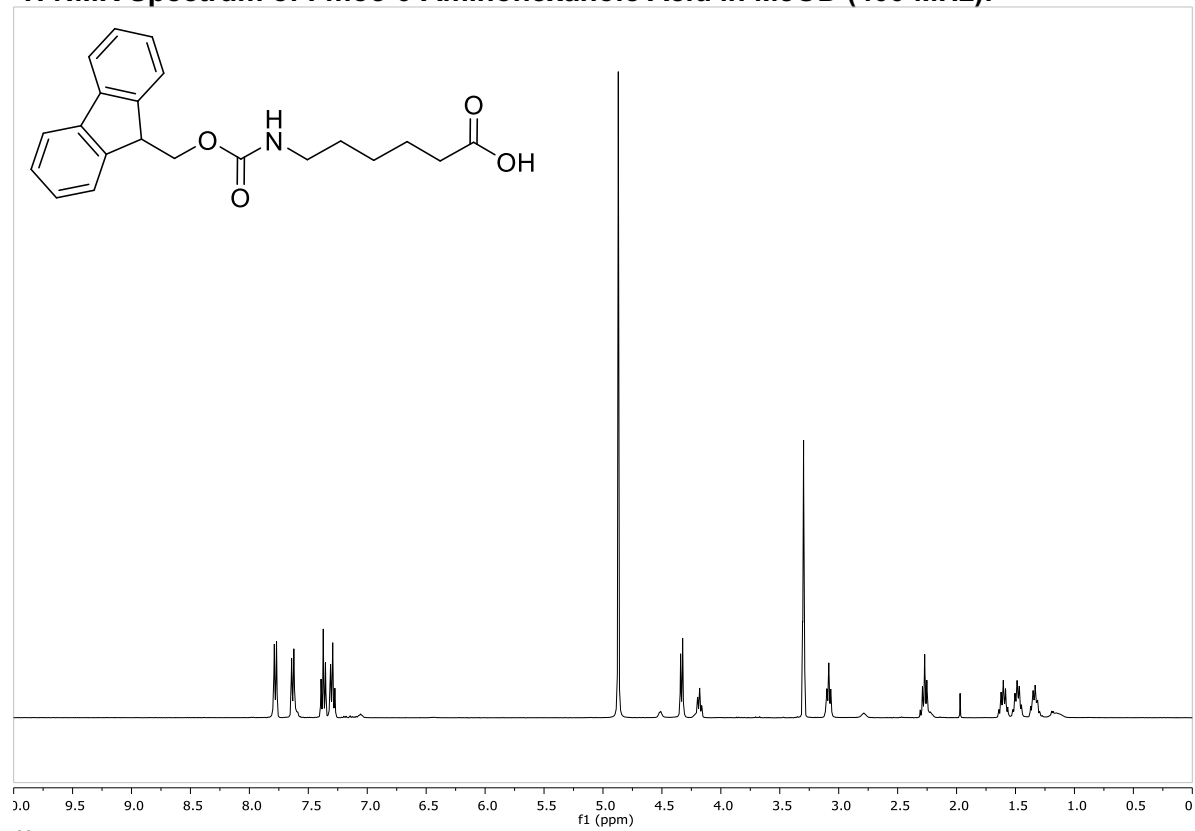
$$[\theta]_{\text{host+guest}} = \frac{([\theta]_{\text{host}} \times n_{\text{res,host}}) + ([\theta]_{\text{guest}} \times n_{\text{res,guest}})}{n_{\text{res,host}} + n_{\text{res,guest}}} \quad (1)$$

where  $[\theta]_{\text{host}}$  and  $[\theta]_{\text{guest}}$  are the respective mean residue ellipticities for a host with  $n_{\text{res,host}}$  residues and a guest with  $n_{\text{res,guest}}$  residues.

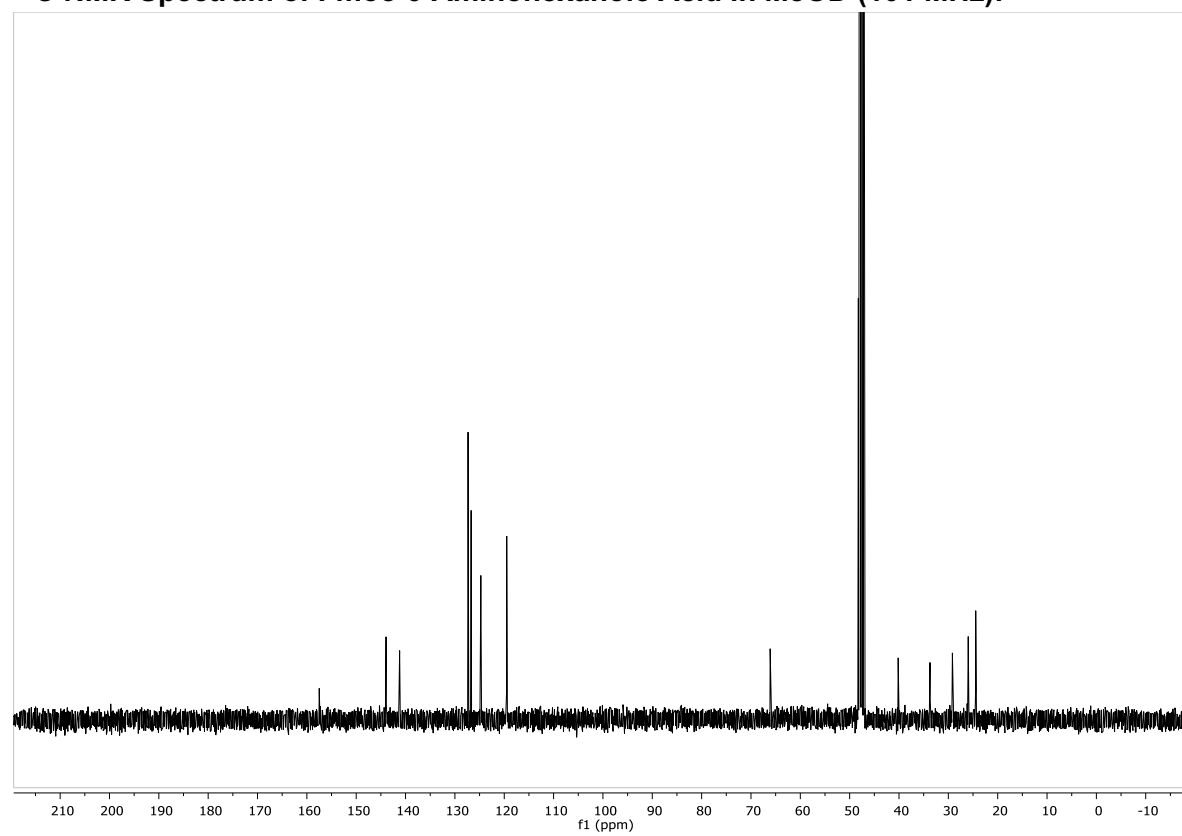


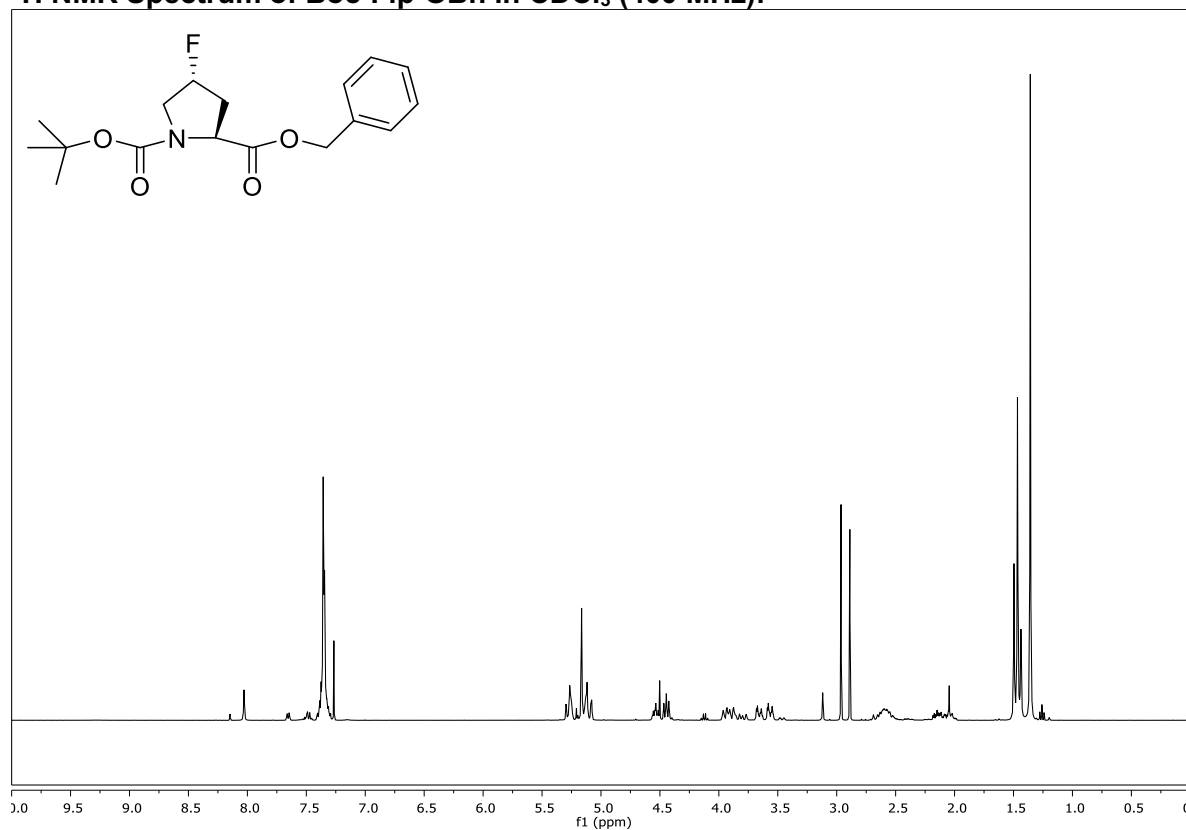
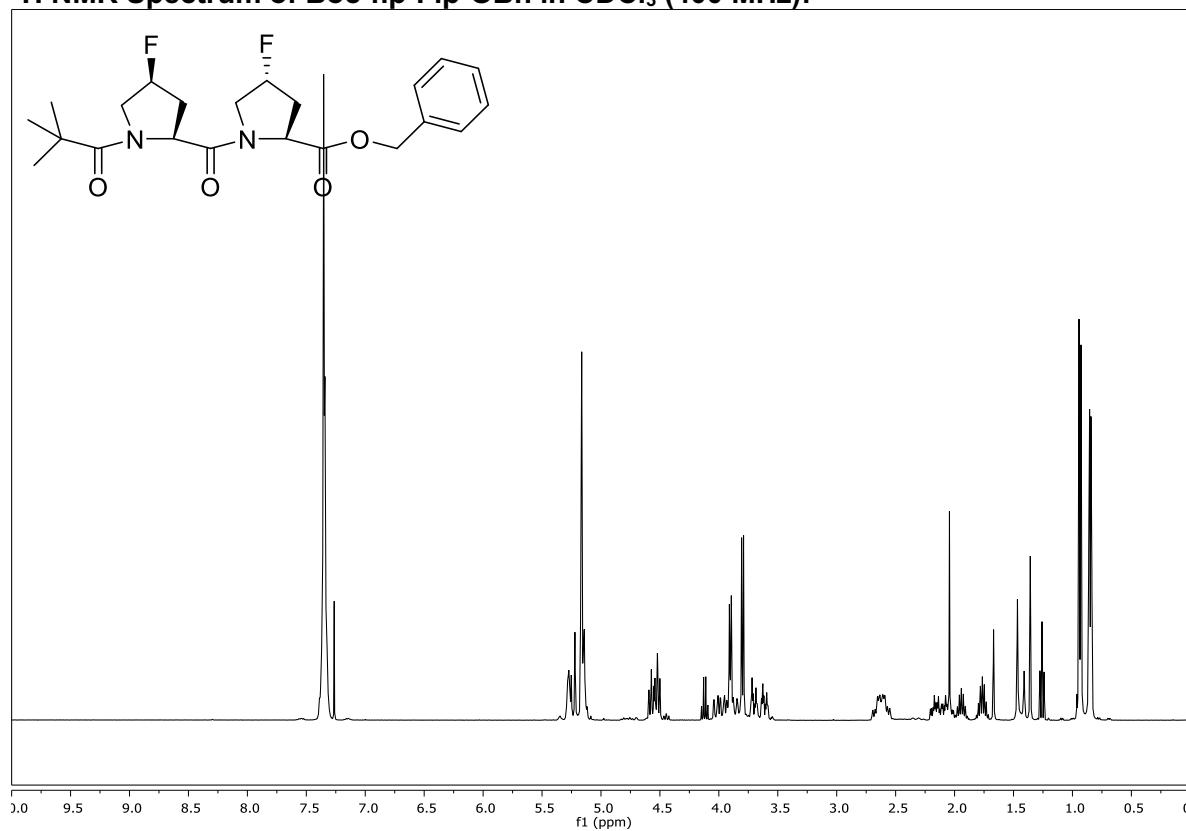
### 1.3.8 NMR Spectra

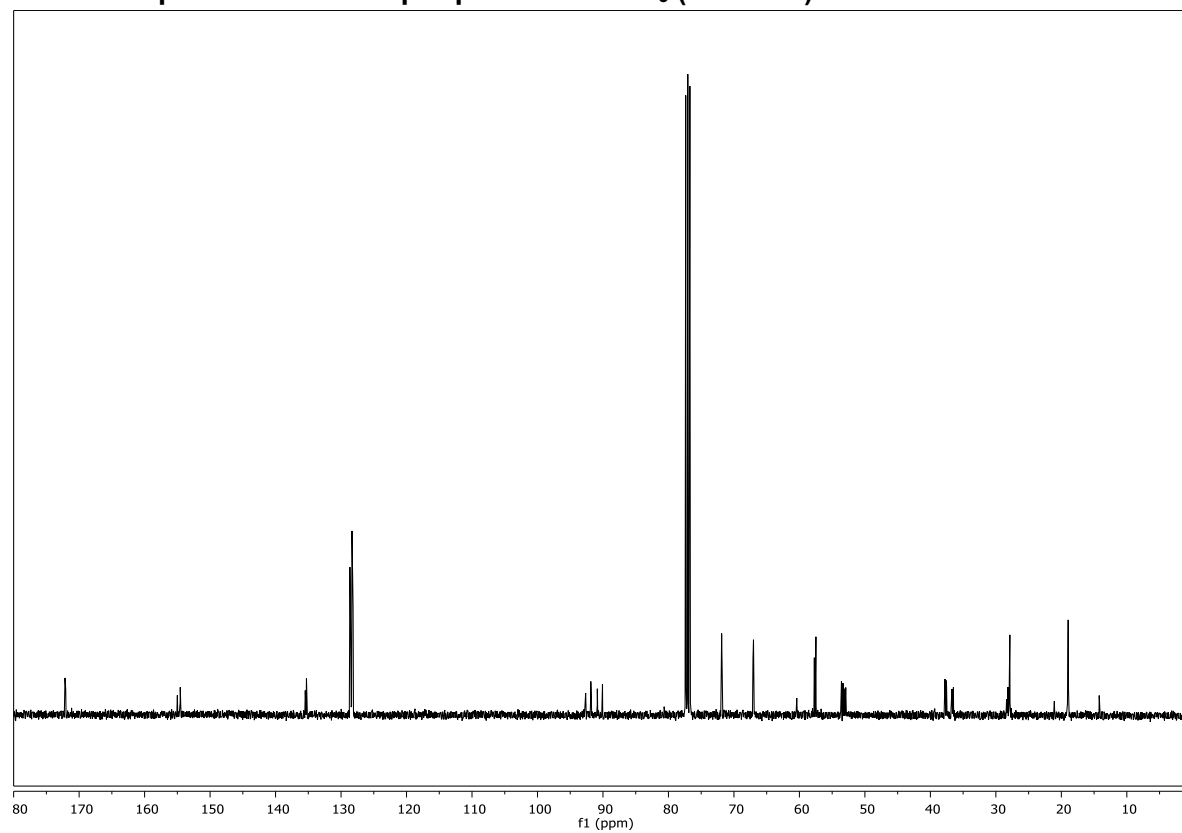
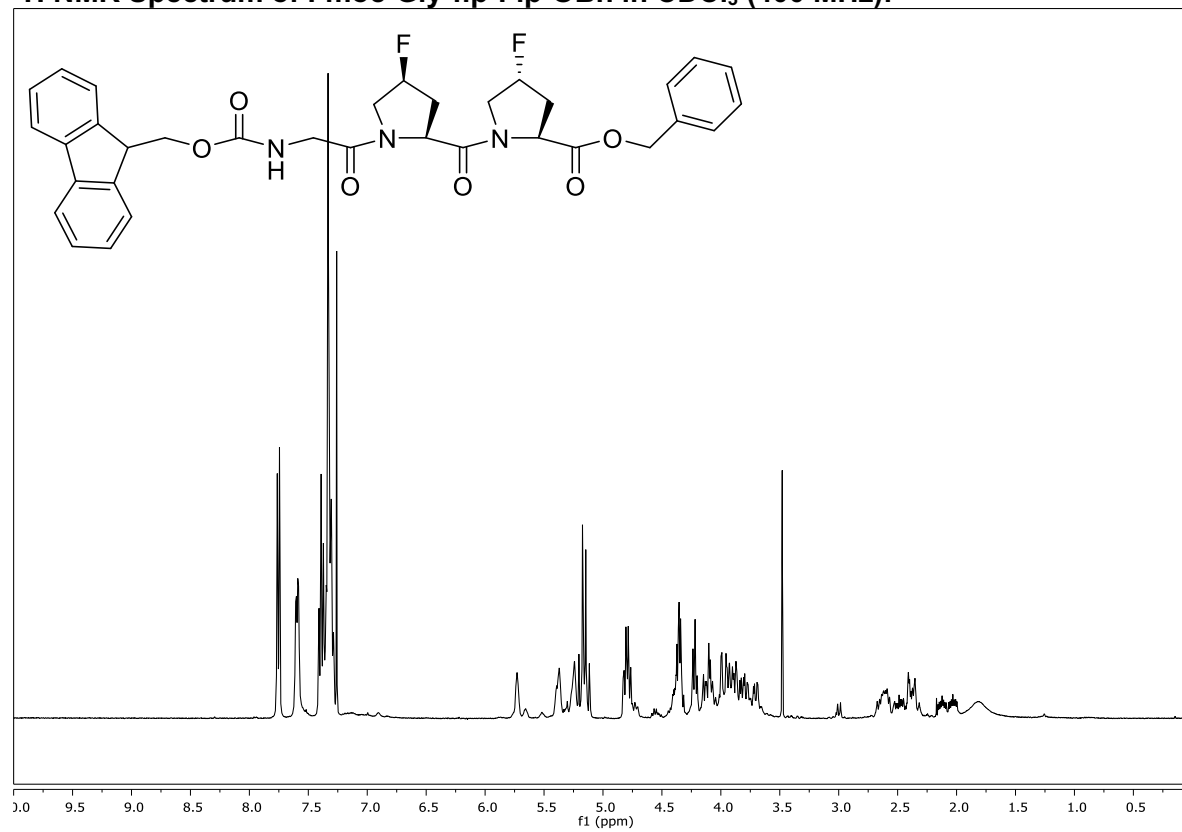
#### <sup>1</sup>H NMR Spectrum of Fmoc-6-Aminohexanoic Acid in MeOD (400 MHz):

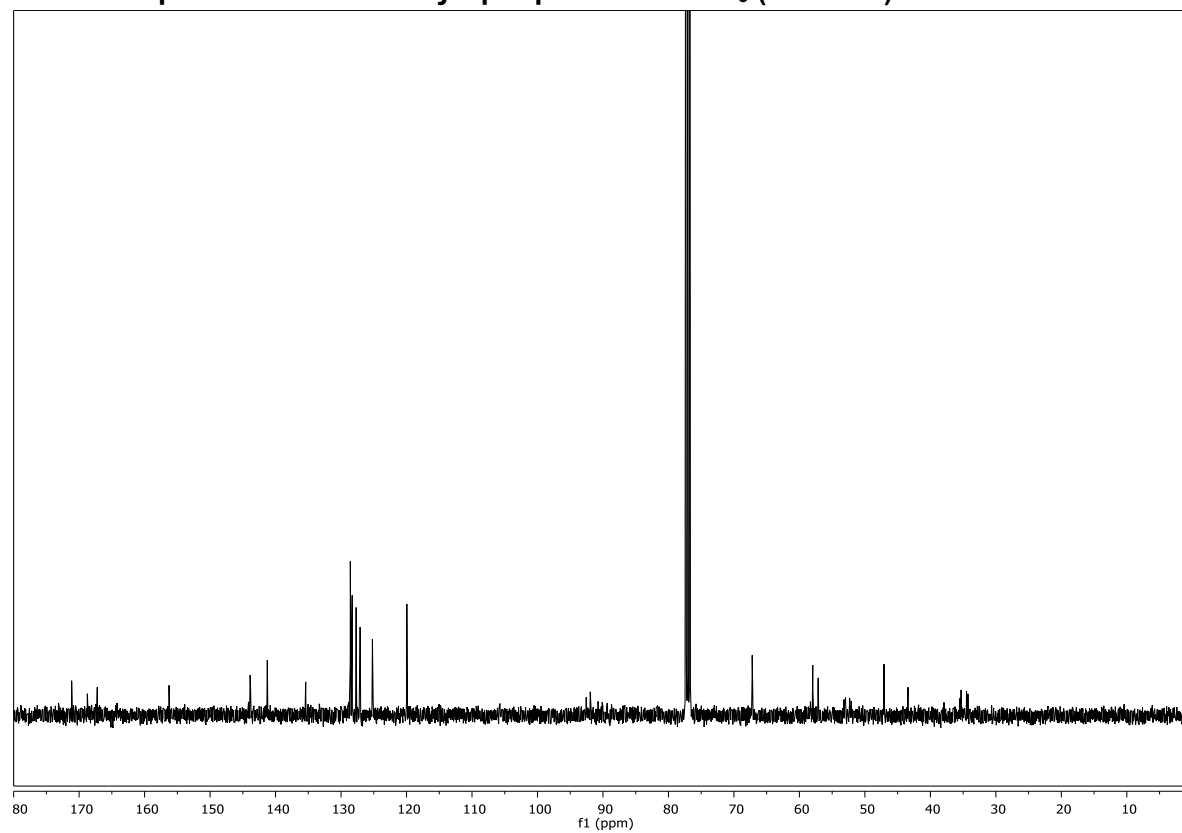
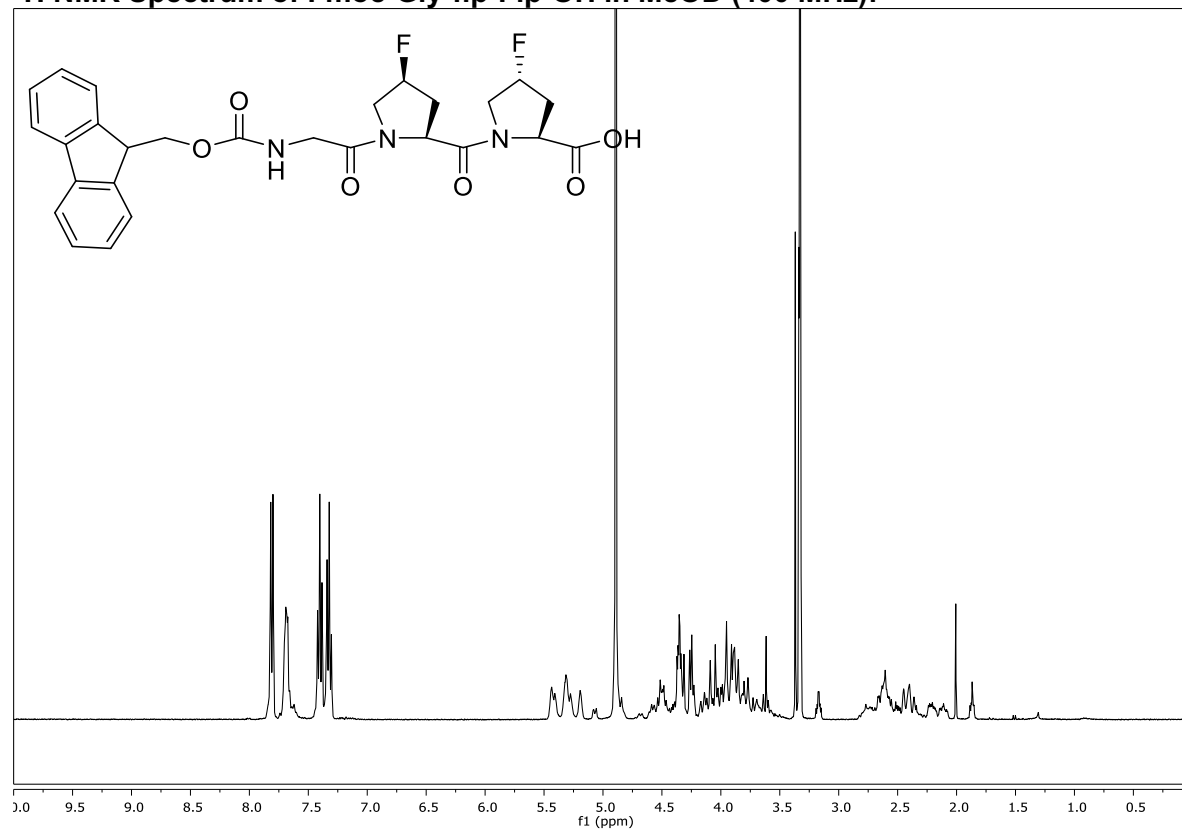


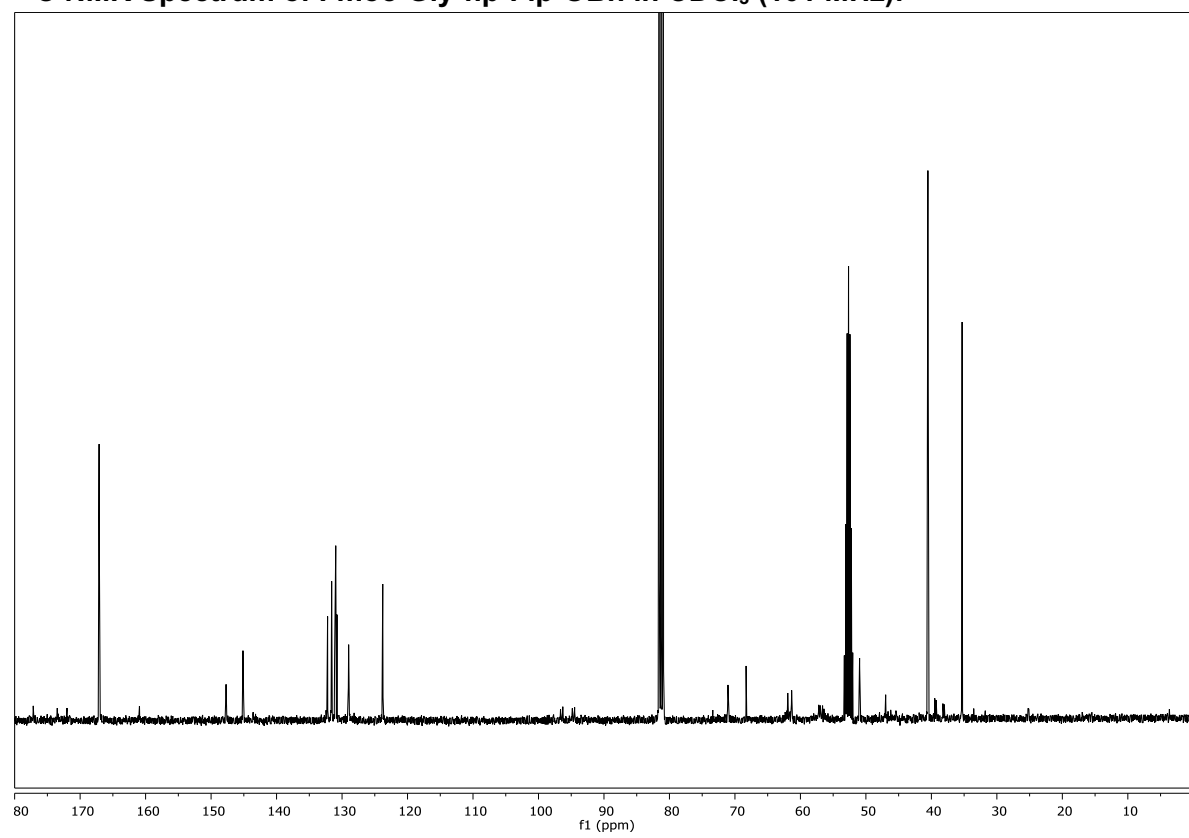
#### <sup>13</sup>C NMR Spectrum of Fmoc-6-Aminohexanoic Acid in MeOD (101 MHz):



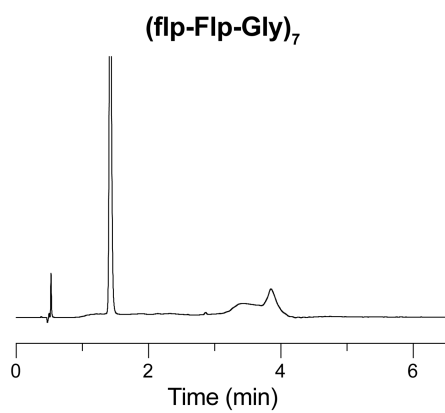
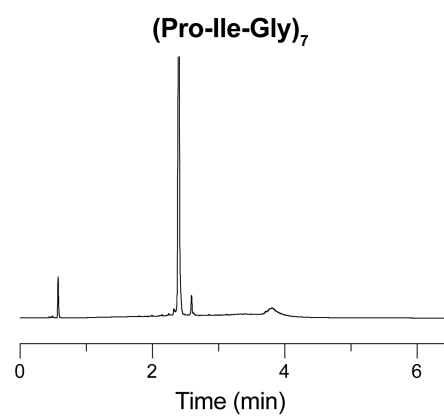
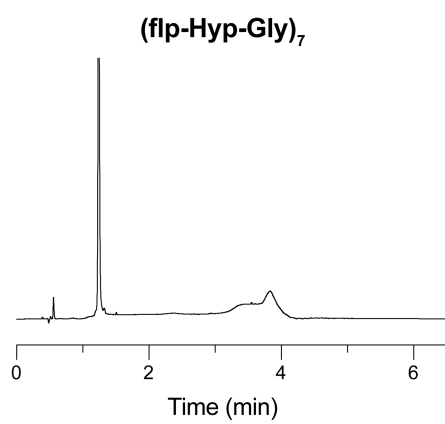
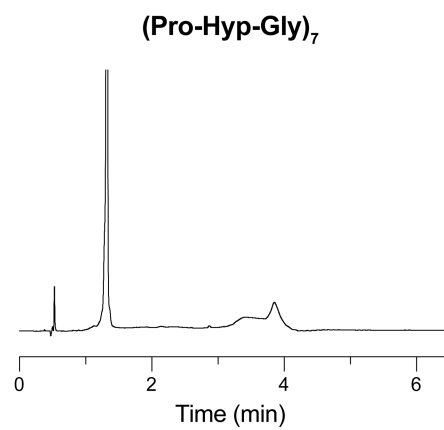
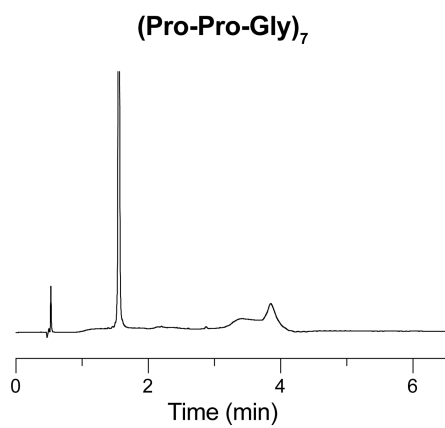
**<sup>1</sup>H NMR Spectrum of Boc-Flp-OBn in CDCl<sub>3</sub> (400 MHz):****<sup>1</sup>H NMR Spectrum of Boc-flp-Flp-OBn in CDCl<sub>3</sub> (400 MHz):**

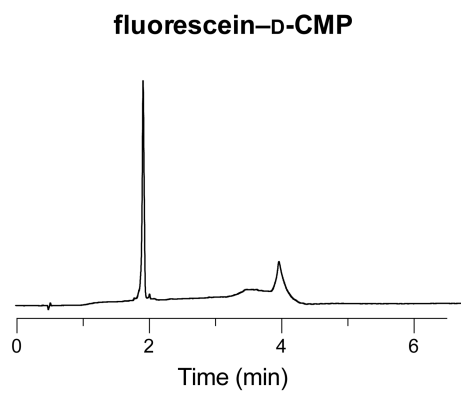
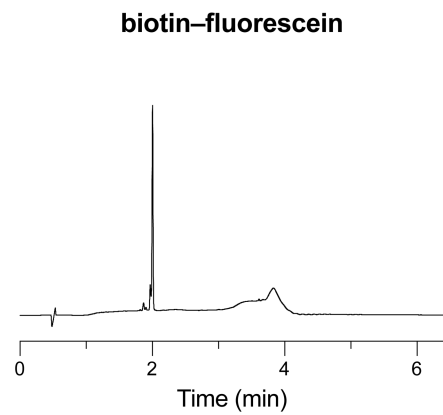
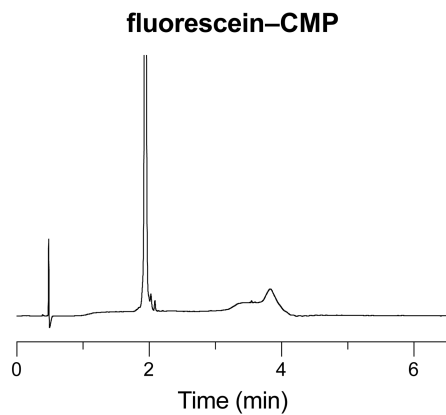
**$^{13}\text{C}$  NMR Spectrum of Boc-flp-Flp-OBn in  $\text{CDCl}_3$  (101 MHz):** **$^1\text{H}$  NMR Spectrum of Fmoc-Gly-flp-Flp-OBn in  $\text{CDCl}_3$  (400 MHz):**

**$^{13}\text{C}$  NMR Spectrum of Fmoc-Gly-flp-Flp-OBn in  $\text{CDCl}_3$  (101 MHz):** **$^1\text{H}$  NMR Spectrum of Fmoc-Gly-flp-Flp-OH in MeOD (400 MHz):**

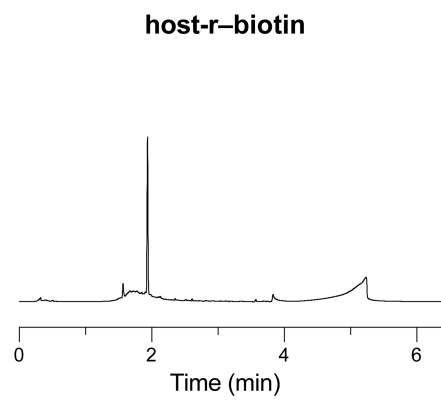
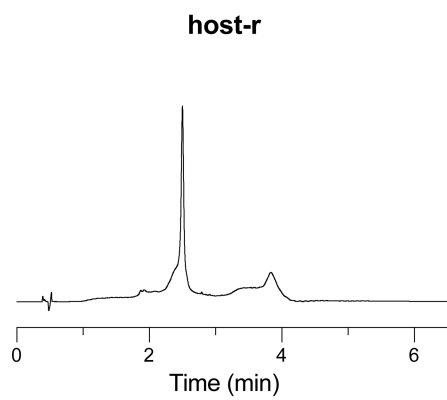
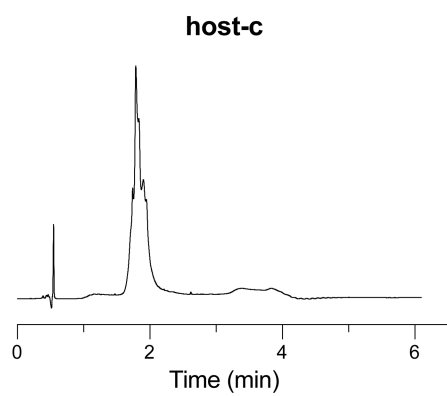
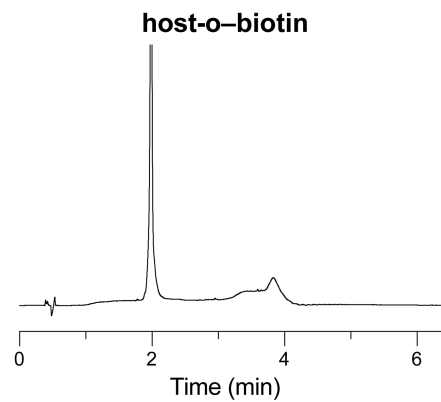
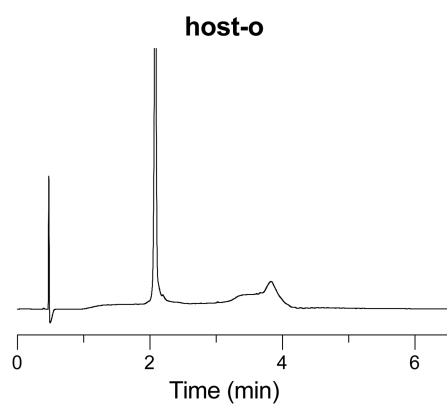
**$^{13}\text{C}$  NMR Spectrum of Fmoc-Gly-flp-Flp-OBn in  $\text{CDCl}_3$  (101 MHz):**

### 1.3.9 UPLC Traces of CMPs



**UPLC Traces of fluorescein-CMP, biotin-fluorescein, and fluorescein-D-CMP**

## UPLC Traces of Hosts





## **Part I**

### **Chapter 4**

#### **Optical Imaging of Collagen Fiber Damage to Assess Thermally Injured Human Skin**

This chapter has been published under the same title.

Alexandra B. Schroeder, Aos Karim, Edgar Ocotl, Jesús M. Dones, Jenu V. Chacko, Aiping Liu,

Ronald T. Raines, Angela L.F. Gibson, and Kevin W. Eliceiri

*Wound Repair and Regeneration* **2020**, 28 (6), 848–855

#### Contribution

Jesús M Dones synthesized and characterized all peptides, planned experiments, and edited the manuscript and figures. Ronald T. Raines planned experiments and edited the manuscript and figures. Alexandra B. Schroeder, Aos Karim, Edgar Ocotl, Aiping Liu, Angela L.F. Gibson, and Kevin W. Eliceiri performed all the imaging and drafted the original manuscript.

### 1.4.1 Abstract

Surgery is the definitive treatment for burn patients who sustain full thickness burn injuries. Visual assessment of burn depth is made by the clinician early after injury but is accurate only up to 70% of the time among experienced surgeons. Collagen undergoes denaturation as a result of thermal injury; however, the association of collagen denaturation and cellular death in response to thermal injury is unknown. While gene expression assays and histologic staining allow for *ex vivo* identification of collagen changes, these methods do not provide spatial or integrity information *in vivo*. Thermal effects on collagen and the role of collagen in wound repair have been understudied in human burn models due to a lack of methods to visualize both intact and denatured collagen. Hence, there is a critical need for a clinically applicable method to discriminate between damaged and intact collagen fibers in tissues. We present two complementary candidate methods for visualization of collagen structure in three dimensions. Second harmonic generation imaging offers a label-free, high-resolution method to identify intact collagen. Simultaneously, a fluorophore-tagged collagen-mimetic peptide can detect damaged collagen. Together, these methods enable the characterization of collagen damage in human skin biopsies from burn patients, as well as *ex vivo* thermally injured human skin samples. These combined methods could enhance the understanding of the role of collagen in human wound healing after thermal injury and potentially assist in clinical decision-making.

### 1.4.2 Introduction

Non-fatal thermal injuries are a leading cause of morbidity worldwide, with roughly 40,000 hospitalizations a year required in the United States.<sup>56</sup> While considered largely preventable, burns can leave patients with debilitating injuries and scarring.<sup>57</sup> A major challenge lies in the variable healing time for burns that are less than full thickness, along with the disparity between clinical identification of burn depth, histopathologic determination of cellular and extracellular matrix (ECM) damage and the regenerative potential of the tissue.<sup>140</sup> More severe, full thickness burns

that damage the subcutaneous layer require excision and autologous skin grafts while dermal burns may heal spontaneously if thermal damage is confined to the more superficial dermis.<sup>57, 141</sup> Surgical removal of necrotic tissue is necessary to remove the inflammatory burden, allowing viable cells to regenerate. Conversely, over-excision of burns can result in scarring and morbidity in the form of donor site wounds, as well as increase the cost of care incurred by the patient.<sup>57</sup> In an attempt to understand the potential for wound healing, tissue excised from the initial surgical intervention may be analyzed through gene expression assays and histological staining. Gene expression can identify the types of collagen expressed but this method does not provide spatial information regarding collagen structure. Histologic stains like Picrosirius red<sup>142</sup> and Masson's trichrome<sup>143</sup> can identify collagen structures and organization but only on a thin, single slice of tissue *ex vivo*. These methods are not applicable for identifying damaged collagen on a patient in a clinical setting. Additionally, the exact depth of burn injury that will heal without surgery and the association between cellular and collagen damage is unknown. Thus, there is a critical need for developing robust minimally-invasive techniques that are clinically translatable to quantify the extent of thermal damage to collagen in the ECM in three dimensions.

Collagen is the most abundant protein in the body, comprising 75% of the dry weight of the skin.<sup>1</sup> Collagen provides the structural scaffold of the ECM upon which cellular epithelialization takes place. It also serves a significant role within the dermal layer of the skin for cell adhesion and migration.<sup>144, 145</sup> Our group has shown that this migration potential can be hijacked during metastasis in breast and ovarian cancer, such that collagen structure and alignment can be a prognostic indicator of cancer progression,<sup>40, 59</sup> implicating collagen as a significant cell behavior mediator. During wound repair, deposition of collagen occurs alongside regeneration of the ECM thereby playing an important role in determining morphological skin properties.<sup>145</sup> Thermal injuries result in collagen denaturation and structural changes.<sup>58</sup> Despite efforts to visualize architectural changes of collagen in the ECM in wound models, the clinical impact of

collagen assessment for determining burn severity or depth after burn injury is still relatively unexplored.<sup>146</sup> Characterization of the wound healing response from thermal injury in a zebrafish model indicates a dramatic loss of collagen fibers associated with delayed healing when compared to a transection wound.<sup>14</sup> With better visualization of collagen damage *in vivo* and an understanding of the relationship between this damage and cellular viability, therapeutic development could be directed toward collagen repair. The current inability to assess the role of collagen in thermal injury is due largely to the lack of available methods to visualize damaged collagen *in vivo* and a lack of human models of thermal injury.

Clinically, understanding the changes to collagen architecture at varying depths of burn injury is important, as collagen plays a major role in the mechanical integrity of the skin and the resultant functional outcomes and scarring. Tanaka *et al.* performed second harmonic generation (SHG) imaging on *in vivo* samples to observe changes in dermal collagen fibers in living rat burn models.<sup>58</sup> SHG occurs when two incident photons interact with the non-centrosymmetric triple-helical structure of collagen and combine to form a single emitted photon of exactly half the wavelength or twice the energy, offering a label-free, quantitative measure of intact collagen with high spatial resolution.<sup>40, 58, 59</sup> However, SHG has several issues that limit its clinical application including being expensive, bulky, utilizes non eye-safe class IV lasers and does not currently have US Food and Drug Administration (FDA) approval<sup>59</sup>. Therefore, exploring other imaging techniques to specifically identify denatured collagen may prove useful during burn excision.

Currently, approximately 80% of burn surgeons in the United States determine burn depth by visualization alone, an assessment method that is accurate in only 64–76% of cases.<sup>57, 147</sup> Furthermore, indeterminate burn depths—the burn depth at which decisions about surgical intervention necessity is least clear—are even less accurately identified.<sup>148, 149</sup> The next most common method to determine healing potential of a thermal injury is Laser Doppler imaging (LDI),<sup>150, 151</sup> which has a 95–100% positive predictive value for prognosing healing within three

weeks, increasing over time as does visual interpretation.<sup>152</sup> Use of LDI is limited by day-to-day and intra-operator differences resulting from training variability.<sup>152</sup> Furthermore, LDI is not useful intraoperatively during excision when the wound is excised under tourniquet as the blood flow is artificially decreased. Optical Coherence Tomography (OCT) offers high-resolution, multi-sectional imaging but the long acquisition times limit the applicability.<sup>153</sup> Fluorescence guidance based techniques can be used to assess wounds, but the availability of specifically targeted probes and instrumentation is limited. The clinically approved fluorescence agent Indocyanine green (ICG), is used for determining vascular flow during reconstructive surgery. However, it can be challenging to interpret when applied for burn cases.<sup>154</sup> The use of perfusion as a readout for viability is particularly challenging where tourniquets or vasoconstriction injections are used, as is common intraoperatively. Furthermore, ICG does not provide any information regarding collagen structural damage to the ECM.<sup>140, 155</sup> Visualization of ICG requires injection and is more invasive than potentially non-intravenous alternatives that may identify thermal collagen damage more explicitly, such as a fluorescently tagged collagen-mimetic peptide.

Collagen-mimetic peptides (CMPs) are laboratory-synthesized chains of amino acid residues that replicate the triple-helical structure of collagen fibers.<sup>1</sup> These collagen-binding molecules have been used for several purposes, including identifying atherosclerotic plaques through their affinity for those plaques, which are rich in collagen.<sup>156</sup> We synthesized a CMP that contains three types of residue: (2*S*,4*S*)-4-fluoroproline (flp), (2*S*,4*R*)-4-hydroxyproline (Hyp), and glycine. This CMP, (flpHypGly)<sub>7</sub>,<sup>157</sup> anneals to damaged collagen but not to itself.<sup>158</sup> By appending a cyanine 5 (Cy5) dye, we imaged damaged collagen in burned rat tendon by excitation ( $\lambda_{\text{ex}} = 652 \text{ nm}$ ) using either multiphoton or single-photon fluorescence microscopy, and capturing emission ( $\lambda_{\text{em}} = 672 \text{ nm}$ ).<sup>158</sup> We validated the binding of the Cy5-CMP conjugate specifically to damaged collagen through SHG imaging, which generates a signal only for intact collagen.<sup>158</sup>

Here, we probe collagen damage following thermal injury in human skin by leveraging signals obtained from the fluorescence of Cy5-CMP adhered to denatured collagen, combined with SHG imaging of intact collagen. We show that Cy5-CMP binds specifically to regions of denatured collagen in human *in vivo* clinical burn biopsies and provides contrast from normal tissue. The images add insight alongside histologic staining with lactate dehydrogenase (LDH) for cellular viability in an *ex vivo* thermally injured skin model. Finally, we demonstrate the potential for Cy5-CMP to be visualized in the clinic through the use of single-photon fluorescence imaging.

### 1.4.3 Results

#### **Collagen mimetic peptides are specific to sites of collagen denaturation in excised human burn tissue**

Tissues obtained from patients who sustained thermal injuries, diagnosed at the time of excision (6–13 days after burn injury) as deep partial thickness,<sup>140</sup> were imaged after treatment with Cy5-CMP (n=6). Cy5-CI washes from the denatured collagen and the fluorescence intensity of Cy5-CMP was 25 times greater at the burn site compared to neighboring regions of normal tissue. Multiphoton images taken of the deep dermal surfaces of human burn tissue reveal that Cy5-CMP binds specifically to regions of denatured collagen as validated by the inverse relationship of these images to those obtained using SHG imaging, which detects only intact collagen (Figure 1.4.1 A–C). Burn depth is heterogeneous within a given wound; therefore, during surgical excision of burn wounds it is expected that the deep surface of an excision will have a mixture of intact and denatured collagen present. Figure 1.4.1 B illustrates this phenomenon where the SHG imaging identifies the intact collagen, while the Cy5-CMP image correlates with the low-signal regions in the SHG image (Figure 1.4.1 A and B, yellow circles), representing regions of denatured collagen that remained after surgical excision. In this case, CMP was able to clearly identify and confirm that regions of collagen damage were residually present. These data show the

potential for Cy5-CMP to be used to identify regions of damaged collagen resulting from thermal injury in human patients.

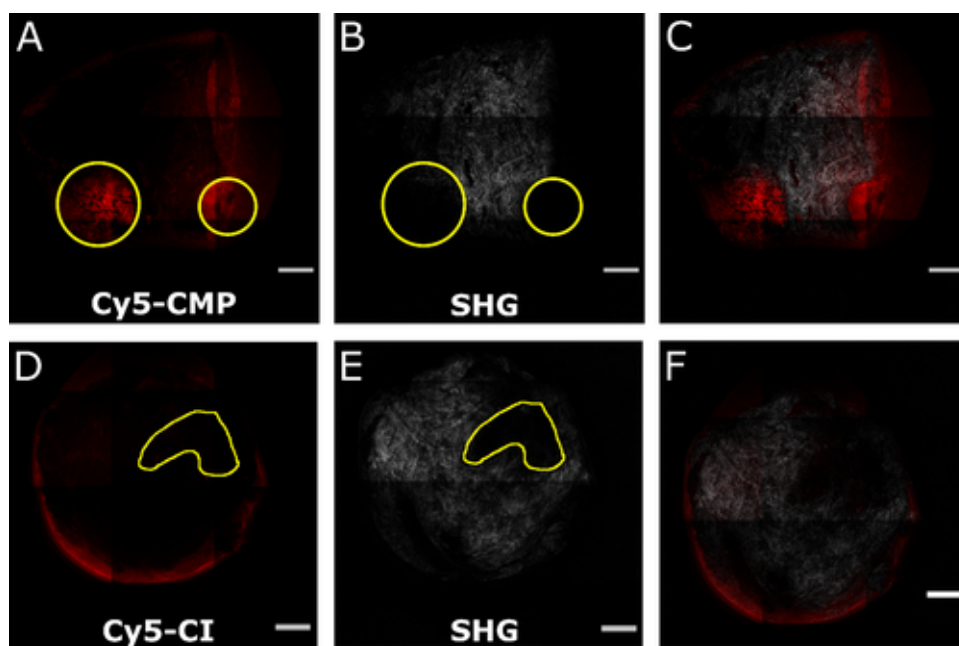


**Figure 1.4.1.** The specificity of Cy5-CMP to denatured collagen in patient burn tissue. Stacked  $z$ -projections of multiphoton micrographs of (A) Cy5 fluorescence image with regions of interest (ROIs) (yellow circles) showing Cy5-CMP labeling on the deep surface (en face view) of 6 mm biopsies of tangentially excised deep partial-thickness burn tissue, and (B) absence of SHG signal in the same ROIs (yellow circles). (C) Composite image of Cy5 fluorescence and SHG. The region of brighter Cy5 fluorescence near the right side of the image corresponds to a portion of the cut edge of the biopsy where we see some fluorescence signal from the superficial side of the biopsy penetrating through the  $z$  stacked images. (D) Burn tissue sample labeled with Cy5-CI (negative control) imaged with Cy5 parameters and (E) SHG parameters. Yellow ROIs and (F) the composite image of tissue labeled with Cy5-CI indicating that the dark regions in panel E are not fluorescent in panel D. The Cy5 fluorescence on the circumference of the biopsy corresponds to non-specific binding around the superficial cut edge of the biopsy. Scale bars = 1 mm.

### Cy5-CMP and SHG on *ex vivo* thermally injured human tissue

Using an *ex vivo* human burn injury model, we qualitatively evaluated Cy5-CMP penetration on thicker sections in experimentally generated burns by generating a histogram of pixel intensities from Cy5 fluorescence throughout the sample as measured in FIJI<sup>159</sup>, as well as determined the relationship between collagen denaturation and cell viability with LDH-staining (Figure 1.4.2). Deep partial thickness thermal injuries were generated in *ex vivo* human skin. Burned tissue was cultured for 48 hours prior to Cy5-CMP application and imaging to simulate the clinically relevant period of time in which initial depth determination for operative planning occurs. The non-burned control (Figure 1.4.2 A) shows very little Cy5 signal, with no specific binding to the intact dermal collagen, as determined by the correlation with the SHG signal (Figure 1.4.2 B). LDH-staining shows cell viability, that is blue color, throughout the depth of the tissue (Figure 1.4.2D). The 3s burns show higher Cy5-CMP uptake where SHG signal is low and, conversely, low Cy5-CMP binding where SHG is brighter (Figure 1.4.2 E–G). This region of intact collagen appears to localize near the region with viable cells identified with LDH-staining (Figure 1.4.2 H). This suggests that, following thermal injury, the location of viable cells correlates with the areas of intact collagen.

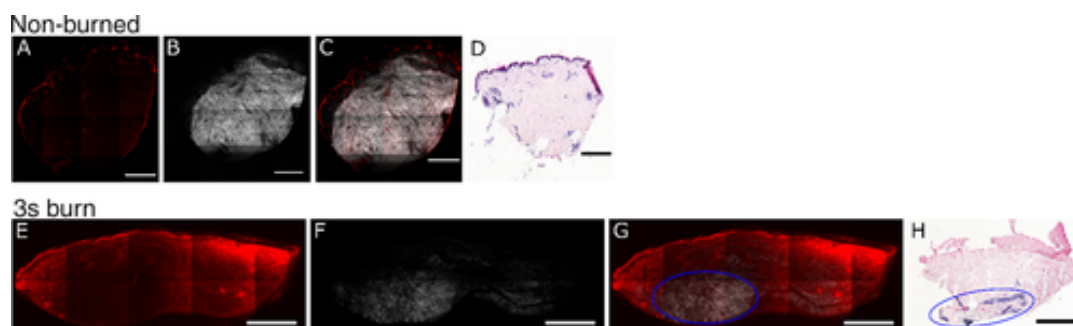


**Figure 1.4.2.** Cy5 excitation of Cy5-CMP reveals collagen damage with depth on cross-sectional views. Shown are the side profiles of a 6 mm biopsy of (A-D) normal non-burned skin and (E-H) skin burned for 3 seconds at 150°C with a custom burn device. (A) Multiphoton excitation of Cy5-CMP shows little fluorescence, while (B) SHG image reveals intact collagen throughout the



normal biopsy. In contrast, (E) Cy5-CMP extensively labels the burned sample while the (F) SHG signal is minimal. SHG signal exhibits an inversion of signal intensity to the Cy5 channel, highlighted by the composite images of (C) Cy5-CMP + SHG for normal skin and (G) 3 seconds burned skin. LDH images show that viable cells (blue) are present throughout the (D) non-burned skin and in the (H) deep portion in the 3 seconds burned skin, correlating with intact collagen. Scale bar = 1 mm.

### **Wide field fluorescence excitation of Cy5-CMP can distinguish between normal skin and thermally injured skin**

To demonstrate that visualization of Cy5-CMP would not be limited to multiphoton excitation, which would greatly curtail any clinical application given the cumbersome methods needed for image acquisition, we imaged the superficial surface of a control non-burned and *ex vivo* thermally injured human skin sample with Cy5-CMP using wide field fluorescence excitation (Figure 1.4.3). Using a mercury-arc light source, we found intensely bright Cy5 fluorescence on the superficial face of an *ex vivo* thermal injury post Cy5-CMP application when compared to the non-burned control (Figure 1.4.3 A and B). Alongside the wide field images, we captured images on the same microscope platform with multiphoton microscopy for the same sample conditions of non-burned control and thermally injured skin (Figure 1.4.3 C and D). Wide field fluorescence excitation provides sufficient contrast to substantially excite Cy5-CMP and discriminate burned from non-burned human skin.

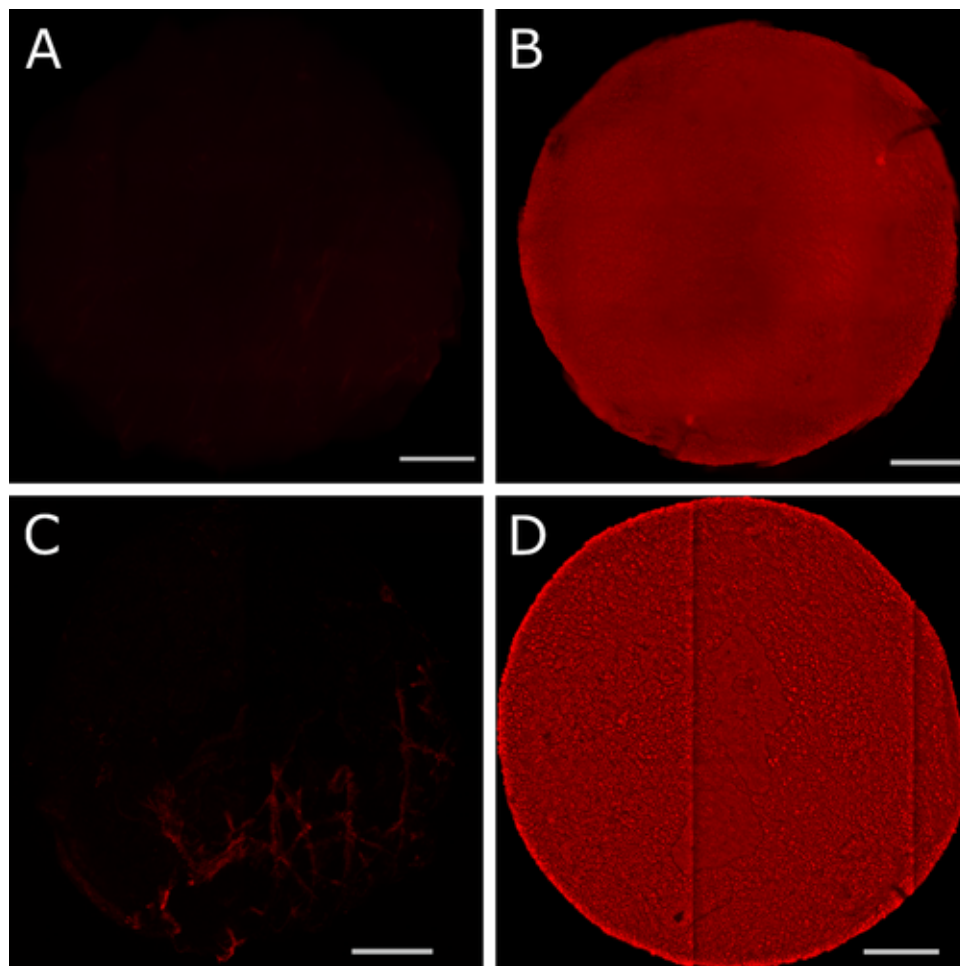


**Figure 1.4.3.** Assessment of Cy5-CMP labeling using widefield fluorescence microscopy. Fluorescence of an ex vivo 6 mm biopsy from (A) normal non-burned skin and (B) burned skin relative to the same samples imaged with multiphoton microscopy in (C) non-burned and (D) burned skin. Scale bar = 1 mm.

### **Collagen mimetic peptides bind with greater fluorescence intensity than CI on burn patient tissue**

To better simulate a clinical application we also tried Cy5-CMP binding with human burn patient tissue to visualize between bright Cy5-CMP fluorescence on a burn site vs non-burned normal skin on the same patient. We tested Cy5-CMP vs Cy5-CI, which is a compositional isomer,<sup>158</sup> to validate the specificity of Cy5-CMP for binding to damaged collagen. Briefly,

multiple 6 mm biopsies were taken from the excised burn tissue of a patient ( $n = 2$ ) 11 days post-burn and from normal skin ( $n = 2$ ) to be used for grafting. Cy5-CMP was applied onto the superficial side of one of each of the burned and non-burned biopsies, while Cy5-CI was applied to the other set of burned and non-burned biopsies. Biopsies were incubated 1 hour before washing  $3\times$  with  $1\times$  PBS to remove unbound dye. Multiphoton imaging was first performed on the two burned samples to excite Cy5, followed by the two normal samples. White light photographs with a digital camera were then taken of the biopsies showing the retention on burned skin and washing from normal uninjured skin.

We found that when applied onto biopsied burned human skin, Cy5-CMP is retained and shows higher fluorescence intensity than does Cy5-CI ( $n = 6$ ). Figure 1.4.4 includes biopsies from normal uninjured skin and burned skin from the same patient. These data demonstrate that the washing of both Cy5-CMP and Cy5-CI from non-burned skin is nearly complete (Figure 1.4.4 A and B), while the Cy5-CMP binds to the clinical thermal wound (Figure 1.4.4 C), but the Cy5-CI control does not (Figure 1.4.4 D). The gross visual comparison of the blue dye associated with Cy5-CMP and Cy5-CI in ambient room lighting confirms that all tissues took up the dye; however, the Cy5-CMP in the burned tissue has the highest signal intensity (Figure 1.4.4 G).

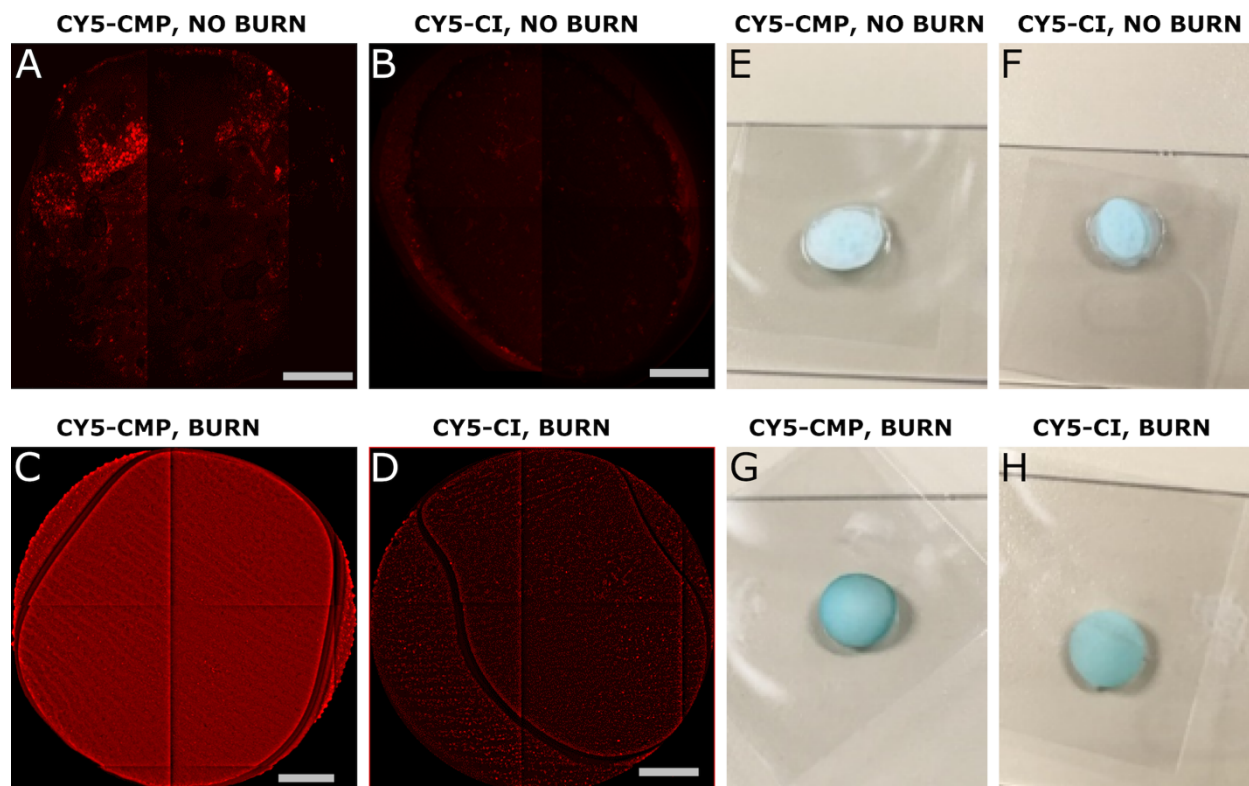


**Figure 1.4.4.** Cy5 multiphoton excitation fluorescence images of 6 mm biopsy punches from (A,B) normal non-burned skin and (C,D) burned skin excised from a patient treated with (A,C) Cy5-CMP or (B,D) Cy5-CI. Cy5-CMP shows enhanced binding with greater contrast on the superficial surface of these clinical biopsies. (E) Cy5-CMP and (F) Cy5-CI on non-burned skin compared to (G) Cy5-CMP and (H) Cy5-CI on burned skin, displaying what a wound treated with Cy5-CMP would look like vs normal skin after washing. Cy5-CMP and Cy5-CI appear blue to the naked eye under white light. Note: in images (C) and (D) a liquid droplet from the dye application is visible as an artifact surrounding the punch. Scale bars = 1 mm.

#### 1.4.4 Discussion

Collagen plays a significant role in maintaining the structural integrity of human skin as it provides a scaffold for cells to migrate and regenerate in the wound healing process.<sup>1, 144, 145</sup> Currently, there are few clinically viable imaging techniques to probe collagen, and fewer still that permit real-time visualization of regions of denatured collagen. SHG offers the ability to image

intact collagen without exogenous contrast at a high spatial resolution. Tanaka *et al.* assessed whether a change in SHG signal could be associated with burn degree, where the vanishing of the signal corresponds to denatured collagen, and proposed a quantitative parameter for burn-assessment based on the depth profile of the mean SHG intensity across the entire image.<sup>58</sup> Pierce *et al.* used polarization-sensitive optical coherence tomography (OCT) to show that partial thickness burns had a loss of collagen birefringence due to denaturation.<sup>160</sup> These previous studies suggest that collagen denaturation can be quantified with SHG and OCT and correlated to burn severity. Still, both techniques can only image intact collagen rather than identifying regions of damage. Our results show that in clinical burn tissue, the Cy5-CMP specifically labels damaged collagen. SHG provides an opportunity to validate the Cy5 signal from Cy5-CMP on the same multiphoton microscope platform.

We aimed to test whether a thermal injury can be assessed using Cy5-CMP and whether the binding of Cy5-CMP correlated with injury depth using an *ex vivo* skin model of burn injury. Future studies would be directed to understand the mechanism of how the temperature of the wound affects collagen damage and how this damage correlates further with cellular viability in physiological models. It is likely that, at certain temperatures, cells are more sensitive to damage than collagen is to denaturation, but the basis for this observation requires future investigation. *Ex vivo* skin also lacks the vascular flow of blood and lymphatics present in the clinical *in vivo* patient samples. This perfusion undoubtedly plays a crucial role in wound repair and may affect collagen response to injury. Further, it would be beneficial to explore other dye delivery solvents, such as DMSO, that might improve the ability for the superficial application of Cy5-CMP to penetrate the skin surface.

Widefield fluorescence imaging offers the capability to visualize subcellular structures and dynamic biological processes with high spatial resolution in the clinic.<sup>161</sup> While multiphoton excitation successfully allowed us to visualize Cy5-CMP-labeled damaged collagen, in

conjunction with the intact collagen structures provided by SHG, neither modality is currently clinically available. Therefore, we showed that the far-red fluorescence of Cy5-CMP can be captured using the more readily available widefield fluorescence with a mercury arc lamp and appropriate filters with a CMOS camera system. Such a widefield imaging instrumentation setup is potentially suitable for fluorescence-guided surgery. Cy5-CMP may provide a clinically viable labeling methodology for assessing the extent of collagen damage following thermal injury.

#### **1.4.5 Conclusion**

Cy5-CMP anneals to the damaged collagen of thermally injured skin while washing away from skin with intact collagen. This peptide could be beneficial in conjunction with current histologic methods to assist in visualizing locations of collagen denaturation as a result of thermal injury. This integrative approach would allow the correlation of collagen and cellular damage, which could help to illuminate the molecular mechanism of injury progression and wound repair following thermal injury. Moreover, Cy5-CMP could serve as the basis for the intraoperative labeling of thermally damaged tissue to be removed during burn excision.

#### **1.4.6 Acknowledgments**

We thank Dr. Jayne Squirrel for useful comments on the manuscript and Josiah Wolf for assistance with the burn device. We acknowledge funding from the Laboratory for Optical and Computational Instrumentation (LOCI), the Morgridge Institute for Research (KWE), the UW Department of Surgery (AG), and the National Institute of Arthritis and Musculoskeletal and Skin Diseases (RTR).

#### **1.4.7 Methods**

##### **Cy5-Collagen mimetic peptide synthesis, preparation and validation**

A Cy5-CMP conjugate, Cy5-(flpHypGly)<sub>7</sub>, was prepared as described in Dones *et al.*<sup>158</sup> Briefly, the peptide was synthesized by microwave-assisted solid-phase peptide synthesis, purified

by reverse-phase HPLC, and conjugated at its N terminus to Cy5. The specific binding of Cy5-CMP to damaged collagen was validated by using a Cy5-CI conjugate, Cy5-(HypflpGly)<sub>7</sub> (a compositional isomer), as a negative control. Cy5-CI contains the same three amino acid residues as does Cy5-CMP but arranged in an order that does not allow for specific annealing to damaged natural collagen.<sup>158</sup> Washing of residual unbound Cy5-CMP or Cy5-CI from human skin samples was performed with 1× PBS (Sigma, St. Louis, MO) (see Supplemental Data, Figure 1.4.4).

### **Clinical *in vivo* patient selection and tissue preparation**

Clinical tissue samples were obtained through the University of Wisconsin Hospital as described previously.<sup>140</sup> This study was approved by the University of Wisconsin Human Subjects Committee Institutional Review Board in compliance with the 1975 Declaration of Helsinki. Briefly, samples were obtained from patients with indeterminate depth burn injury at the time of surgery, 6–13 days after burn injury following a period of observation to assess healing trajectory. Intraoperatively, burn wound depth was determined by the burn surgeon using visual assessment prior to and during excision.<sup>140</sup> Normal skin tissue used as a control was obtained from non-burn related elective reconstructive surgery. Control non-burned and burned tissue samples were stored for up to 1 hour in normal saline (Baxter) prior to further processing. A 6-mm biopsy punch was taken from the skin samples and 100 μL of 100 μM Cy5-CMP or 100 μL of 100 μM Cy5-CI was applied directly onto the superficial side of the biopsy and incubated in a petri dish covered with aluminum foil at room temperature for 1 hour. The samples (n=6 burn pairs) were washed three times in rapid succession with 1× PBS (Sigma) prior to imaging and kept covered in 1× PBS. Images were collected from both superficial and deep surfaces of the biopsies immediately following rinsing.

### **Tissue sample preparation**

Normal skin tissue for use in the *ex vivo* model was obtained from patients receiving elective surgery at the University of Wisconsin Hospital (Madison, WI). Discarded de-identified tissue was transported in normal saline after surgical excision.

### **Thermal injury, tissue culture and CMP labeling**

A novel burn device was created in collaboration with the Morgridge Institute for Research FabLab group (Madison, WI) (unpublished results). Briefly, the device generated a burn on the *ex vivo* skin with an 8 mm circular face applied with uniform pressure of 0.12 kg/cm<sup>2</sup> at 150°C for 3 seconds to simulate a partial thickness burn. After thermal injury, the tissues (including non-burn control skin) were biopsied using a 6 mm punch and cultured in Dulbecco's Modified Eagle's Medium (Gibco) supplemented with 10% bovine calf serum (Hyclone), 0.625 µg/ml amphotericin B (Gemini Bio Products), and 100 µg/ml of Pen/Strep (Gibco by Life Technologies) at 37°C for 48 hours prior to Cy5-CMP application and imaging. After 48 hours, the necrotic epidermis on the 3s samples was mechanically debrided with a forceps to expose the dermis. All biopsies received 100 µL of 100 µM Cy5-CMP, were incubated 1 hour and washed 3 times with 1× PBS, as described above. After Cy5-CMP application, incubation and washing, the 6 mm *ex vivo* thermally injured and debrided biopsies were bisected. One-half of the biopsy was used for multiphoton imaging of Cy5 and SHG, the other half was cryopreserved and sectioned for lactate dehydrogenase (LDH) staining.

### **Lactate dehydrogenase staining on histological sections**

Lactate dehydrogenase (LDH) staining was performed on cryosections of *ex vivo* tissue sections to assess cell viability. Staining was performed as described in Gibson *et al.*<sup>27</sup> Briefly, sections were air-dried for a minimum of 3 hours (range 3–18 hours) then washed twice with PBS for 5 minutes each time. Sections were incubated with freshly prepared LDH solution containing 5% Polypep (Sigma); 2 mM Gly-Gly (Sigma); 0.75% NaCl (Fisher, Hampton, NH); 60 mM lactic



acid (Dot Scientific, Burton, MI); 1.75 mg/ml  $\beta$ -nicotinamide adenine (Sigma, St. Louis, MO); and 3 mg/ml Nitroblue Tetrazolium (Sigma) pH 8.0, for 3.5 hours at 37°C. Slides were washed twice for 2 minutes each with 50°C tap water, followed by two washes with PBS for 2 minutes each. Tissues were counterstained with aqueous eosin (Newcomer Supply, Middleton, WI) for 4 minutes. Slides were washed with PBS for 1 second, dehydrated with acetone for 30 seconds followed by acetone:xylene (1:1) for 1 minute, and finally with xylene alone for 1 minute. Slides were then cover slipped with Cytoseal 60 (Thermo Fisher Scientific).

### **Multiphoton excitation of Cy5 and second harmonic generation**

All imaging was performed on the Bruker Ultima IV multiphoton microscope system described in Dones *et al.*, 2019.<sup>158</sup> A Ti:Sapphire pulsed laser (Spectra-Physics Insight DeepSee) was tuned to 820 nm to excite the Cy5 fluorophore of Cy5-CMP, using a 690 (50) nm emission bandpass filter (Chroma Technology Corporation, VT) to isolate the fluorescence emission. SHG of intact collagen was performed on all tissues on the same microscope by tuning the laser wavelength to 890 nm and using a 445 (50) nm bandpass filter (Semrock Filters, Rochester, NY). Samples were imaged using a 10 $\times$  CFI Super Fluor objective lens (Nikon, NA = 0.50). Images generated were acquired as z-stacks from superficial to deep at 40 micron intervals spanning 800–1200 microns in depth. Slices were summed and stitched to capture the full field of view using FIJI.<sup>28</sup> A high pass Gaussian filter was used to correct for gradients in the images in Figures 1.4.3 and 1.4.4, which were taken with a 4 $\times$  Super Fluor objective (Nikon, NA = 0.20).

### **Wide field fluorescence with CMOS camera**

Wide field fluorescence imaging was performed on Cy5-CMP applied to a 6-mm *ex vivo* human skin biopsy that was burned as described above. A PhotoFluor II mercury halogen lamp (Chroma) excited the Cy5-CMP fluorescence through a Cy5.5 dichroic cube (Chroma) consisting of a 685 nm long pass beam splitter, a 650 (50) nm bandpass excitation filter and a 720 nm (50) nm bandpass emission filter. The resulting signal was captured with a complementary metal-oxide

semiconductor (CMOS) camera (Digital Sight DS-U3, Nikon) using a 4× Super Fluor objective (Nikon, NA = 0.20) on the same Bruker Ultima microscope as the multiphoton imaging was performed. A non-burned biopsy labeled with Cy5-CMP was used as a control. Images generated were stitched to capture the full field of view using FIJI.<sup>159</sup>

## **Part I**

### **Chapter 5**

#### **Hox Genes Maintain Critical Roles in the Adult Skeleton**

This chapter has been published under the same title.

Jane Y. Song, Kyriel M. Pineault, Jesús M. Dones, Ronald T. Raines, and Deneen M. Wellik

*Proceedings of the National Academy of Sciences USA* **2020**, *117* (13), 7296–7304

#### Contributions

Jesús M. Dones synthesized and characterized all peptides, edited the manuscript and figures. Ronald T. Raines edited the manuscript and figures. Jane Y. Song, Kyriel M. Pineault, and Deneen M. Wellik planned and did all other experiments as well as drafted the original manuscript and figures.

### 1.5.1 Abstract

*Hox* genes are indispensable for the proper patterning of the skeletal morphology of the axial and appendicular skeleton during embryonic development. Recently, it has been demonstrated that *Hox* expression continues from embryonic stages through postnatal and adult stages exclusively in a skeletal stem cell population. However, whether *Hox* genes continue to function after development has not been rigorously investigated. We generated a *Hoxd11* conditional allele and induced genetic deletion at adult stages to show that *Hox11* genes play critical roles in skeletal homeostasis of the forelimb zeugopod (radius and ulna). Conditional loss of *Hox11* function at adult stages leads to replacement of normal lamellar bone with an abnormal woven bone-like matrix of highly disorganized collagen fibers. Examining the lineage from the *Hox*-expressing mutant cells demonstrates no loss of stem cell population. Differentiation in the osteoblast lineage initiates with *Runx2* expression, which is observed similarly in mutants and controls. With loss of *Hox11* function, however, osteoblasts fail to mature, with no progression to osteopontin or osteocalcin expression. Osteocyte-like cells become embedded within the abnormal bony matrix, but they completely lack dendrites, as well as the characteristic lacuno-canalicular network, and do not express *SOST*. Together, our studies show that *Hox11* genes continuously function in the adult skeleton in a region-specific manner by regulating differentiation of *Hox*-expressing skeletal stem cells into the osteolineage.

### 1.5.2 Introduction

*Hox* genes are important transcription factors responsible for establishing vertebral axial morphology along the anteroposterior (AP) axis during embryogenesis.<sup>162</sup> Additionally, the *Hox9-Hox13* paralogs are indispensable for development of the proximodistal (PD) axis of the limb.<sup>163-</sup><sup>166</sup> The *Hox11* paralogous group, *Hoxa11*, *Hoxc11* and *Hoxd11*, regulate the patterning of the sacral region of the vertebral column and the zeugopod skeleton of the forelimb and hindlimb (radius/ulna, tibia/fibula).<sup>165, 166</sup> *Hox* paralogous genes functionally compensate for one another in

skeletal patterning, and all paralogs expressed in a region need to be removed for defects to fully manifest. In the forelimb, only the *Hoxa11* and *Hoxd11* paralogs are expressed; thus, the removal of these two genes leads to a severe malformation of the zeugopod skeletal elements.<sup>165, 166</sup>

A *Hoxa11*eGFP knock-in reporter allele shows that *Hox* expression initiates broadly at embryonic day (E) ~9.5 within the developing limb bud mesenchyme but very quickly becomes restricted to the zeugopod region.<sup>167, 168</sup> While previous work has focused largely on the embryonic role of *Hox* genes, we observed that expression is continuous in the skeleton and extends beyond development into postnatal and adult stages.<sup>168-172</sup> Importantly, *Hox* expression remains regionally restricted and maintains the expression pattern that has been established during development.<sup>170, 173, 174</sup> Conditional adult loss-of-function has not been examined, but *Hox11* compound mutants (animals in which three of the four paralogs are mutated) appear nearly normal at birth but begin to exhibit significant skeletal growth phenotypes at postnatal stages and are not able to enact proper fracture repair at adult stages, consistent with potential continuing functions.<sup>169-171</sup> The interpretation of this phenotype is complicated by the fact that three of the four alleles are absent throughout embryonic development, making it impossible to separate embryonic defects that manifest later in life from continued function at adult stages.

We previously demonstrated that *Hox11* expression in the skeleton is exclusively restricted to a population of regional, progenitor-enriched mesenchymal stem/stromal cells (MSCs).<sup>170, 172</sup> Using a *Hoxa11-CreER<sup>T2</sup>* lineage-tracing system, we recently established that the *Hox11* lineage contributes to the development, growth, and homeostasis of the zeugopod skeleton by giving rise to all of the mesenchymal lineages in the bone—osteoblasts, osteocytes, chondrocytes, and bone marrow adipocytes. Notably, this *Hox11*-expressing cell population is also maintained as self-renewing adult stem cells throughout life, demonstrating that *Hox*-expressing cells are bona fide skeletal stem cells (SSCs), continuously supplying the progenitors for bone maintenance and repair throughout the life of the animal.<sup>172</sup>

While these previous studies have provided rigorous information on *Hox* lineage, they have not addressed whether *Hox* function is required at later stages. This study sought to examine whether *Hox* genes continue to function in the adult skeleton within the skeletal stem cell population. In order to interrogate this potential, we generated a conditional *Hoxd11* allele that, when combined with a *Hoxa11* null allele, allows us to completely delete *Hox11* function at any stage. We find that deleting *Hox11* function at adult stages results in a progressive and dramatic remodeling of the forelimb zeugopod skeleton. Using our *Hoxa11CreER<sup>T2</sup>* allele to simultaneously delete *Hox11* function and lineage-label *Hox11* mutant cells, we establish that the phenotype spatiotemporally correlates with the initiation of *Hoxd11* deletion. Adult conditional mutants accumulate a woven bone-like matrix with disorganized collagen that progressively replaces normal lamellar bone. Further, we find that the *Hox11* conditional mutant animals generate preosteoblasts, but osteoblasts and osteocytes do not mature. We establish that *Hox* genes do not function solely as embryonic patterning factors in the skeleton but continue to play an important role throughout life in the skeleton.

### 1.5.3 Results

#### **Regional Adult *Hoxa11*-Expressing Skeletal Stem Cells Continuously Contribute to the Adult Zeugopod Skeleton**

During development, *Hox11* expression is restricted to the zeugopod region where it is observed in the perichondrium region surrounding the developing cartilage anlage.<sup>168</sup> *Hox11* expression continues in cells present in the perichondrium/periosteum as the skeleton develops, also becoming visible on the endosteal bone surface and trabecular bone surface, as well as in bone marrow stromal cells as the bone marrow space is created during late embryogenesis.<sup>170, 172</sup> This expression pattern is then maintained throughout life<sup>170</sup> (Figure 1.5.1 A, Inset). Our previous work demonstrated that embryonic and postnatal *Hox11*-expressing cells are regionally restricted skeletal stem cells and that this lineage provides progenitors for all skeletal mesenchymal lineages,

as well as exhibits continuous self-renewal as stem cells throughout life.<sup>172</sup> As expected, this lineage and behavior are recapitulated when lineage labeling is initiated at adult stages. By initiating lineage labeling at adult stages in *Hoxa11-CreER<sup>T2</sup>;ROSA-LSL-tdTomato* animals, we show downstream lineage cells become osteoblasts on the trabecular as well as endosteal bone surfaces, and sclerostinexpressing osteocytes embedded within the cortical bone (Figure 1.5.1 B and C and Figure 1.5.2 A and B).

### **Cas9/CRISPR Generation and Functional Validation of a Conditional *Hoxd11* Allele**

To induce loss of *Hox11* function at adult stages after the normal development and growth of the zeugopod skeleton, we generated a *Hoxd11* conditional allele. As all *Hox* genes contain two exons with the DNA-binding homeodomain present in exon 2, we flanked exon 2 with loxP sites using CRISPR/Cas9- mediated gene editing.<sup>175</sup> *Cre*-mediated removal of exon 2 is expected to lead to loss of function of *Hoxd11* (Figure 1.5.3 A). In brief, two guide RNAs were targeted to regions of low conservation 5' and 3' of *Hoxd11* exon 2, and single-stranded oligo donors were designed containing a loxP sequence and 60 base pairs (bp) of flanking homology sequence on each side for targeted insertion of LoxP sites flanking *Hoxd11* exon 2. The loxP sites were targeted sequentially

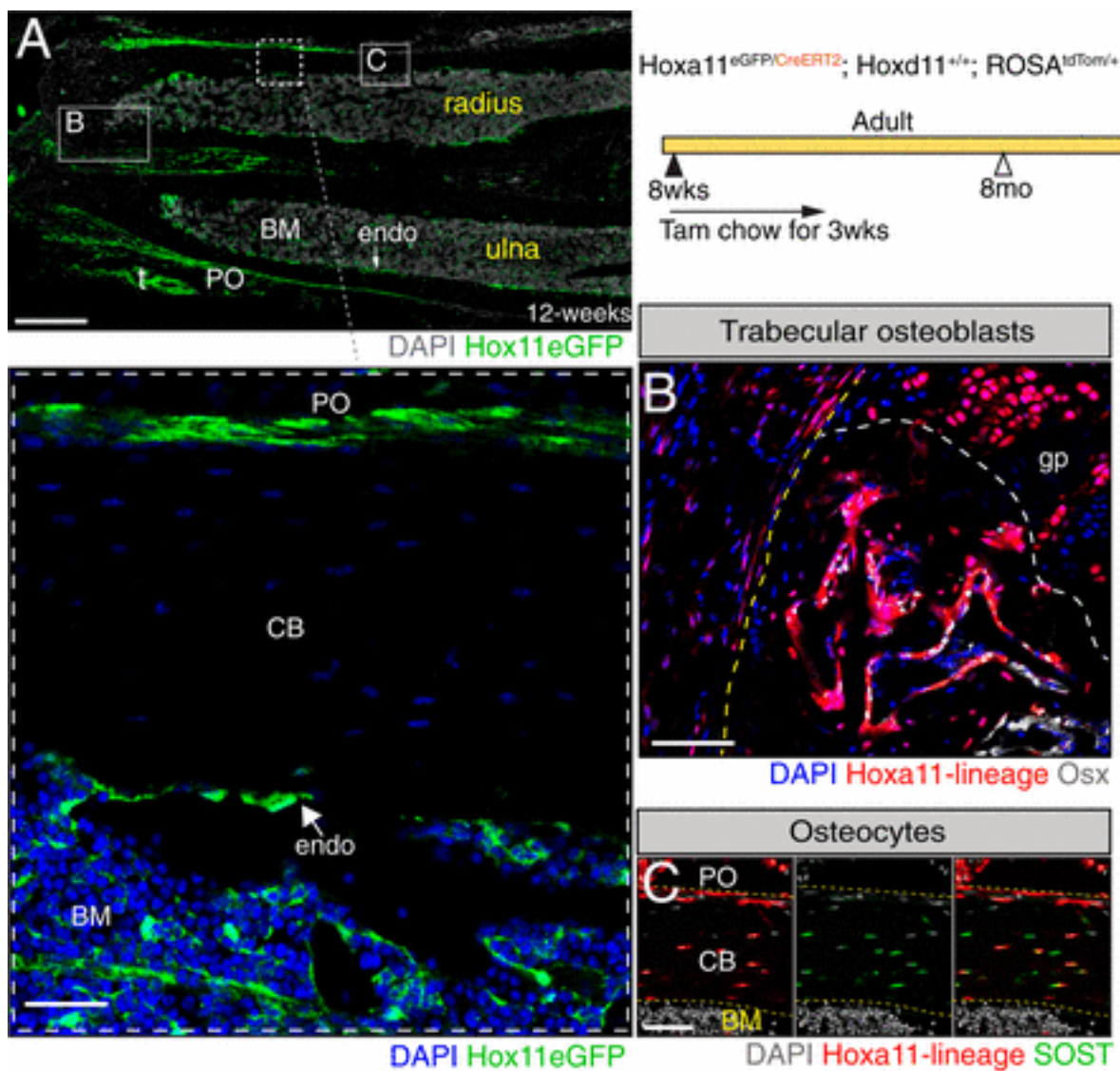


**Figure 1.5.1.** Adult Hox11-expressing skeletal stem cells continuously give rise to osteoblasts and osteocytes. (A) Hoxa11-eGFP real-time reporter allele demonstrates continuous expression of Hoxa11 (green) at 12 wk of age. The panel was created by stitching 17 individual 10× images. t, tendon. DAPI, gray. (Scale bar: 200  $\mu$ m.) Shown is a higher magnification image of the boxed area in A showing localization of Hoxa11 expression (green) in the periosteum, endosteum, and bone marrow compartment. BM, bone marrow; CB, cortical bone; endo, endosteum; PO, periosteum. DAPI, blue. (Scale bar: 75  $\mu$ m.) Animals of the indicated genotype were fed on tamoxifen (Tam) chow at 8 to 10 wk of age for a duration of 3 wk to induce deletion and collected at 8 mo of age. Boxes marked “B” and “C” in A represent the approximate locations of magnified images shown



in *B* and *C*. (*B*) *Hoxa11*-lineage marked cells (red) are found in the trabecular bone coexpressing osterix (*Osx*) (white). The yellow dashed line outlines the cortical bone, and the white dashed line demarcates the growth plate border. gp, growth plate. DAPI, blue. (Scale bar: 75  $\mu\text{m}$ .) (*C*) *Hoxa11*-lineage marked cells (red) are also found as osteocytes embedded within the cortical bone coexpressing *SOST* (green). *Hoxa11*-lineage marked cells and DAPI (gray) in the far-left, *SOST* (green) and DAPI (gray) in the middle, and the merged image is shown in the far-right. (Scale bar: 60  $\mu\text{m}$ .) All images: BM, bone marrow; CB, cortical bone; endo, endosteum; PO, periosteum.

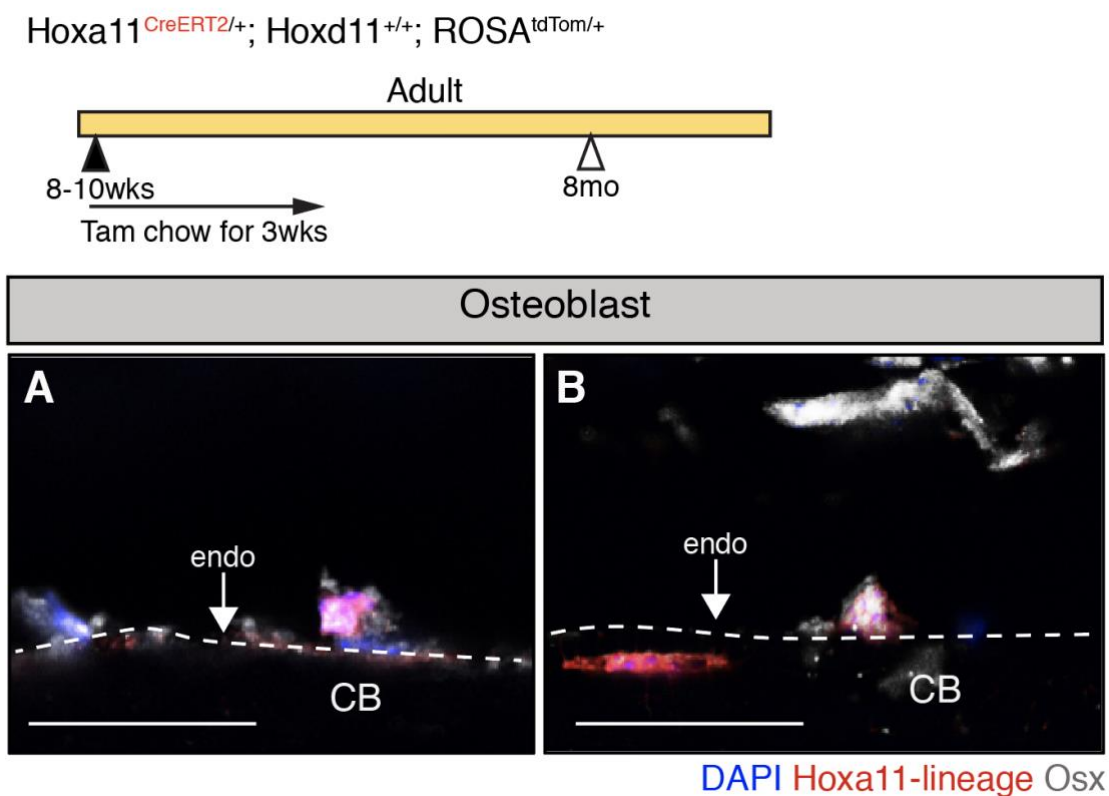


**Figure 1.5.2.** Adult *Hox11*-expressing skeletal stem cells continuously contribute to endosteal osteoblasts. Animals harboring the *Hoxa11-CreERT2* allele (genotype indicated) were fed on tamoxifen chow for 3 weeks starting at 8- 10 weeks of age and collected at 8-months of age. (*A*, *B*) High magnification images of *Hoxa11*-lineage marked osteoblasts (red) co-expressing *Osx*

(white) on the endosteal surface. White dashed line demarcates the endosteal surface. DAPI: blue. All images are from the ulna, endo = endosteum, CB = cortical bone. Scale bar, 25 $\mu$ m.

to the locus to generate a *Hoxd11* conditional allele through two rounds of zygote microinjection. Targeted insertion of each loxP site was confirmed by PCR and subsequent sequencing (Figure 1.5.4 A and B).

The *Hoxd11* conditional allele was first assessed for deletion of the region flanked by the loxP sites. Females with the genotype *Hoxa11*<sup>eGFP/+</sup>;*Hoxd11*<sup>loxP/loxP</sup> were mated to males with the genotype *ROSA**CreERT*<sup>2/+</sup>;*Hoxa11*<sup>+/-</sup>;*Hoxd11*<sup>loxP/loxP</sup> to generate embryos with the genotype *ROSA*<sup>CreERT2/+</sup>;*Hoxa11*<sup>eGFP/-</sup>;*Hoxd11*<sup>loxP/loxP</sup>. PCR analyses on embryonic tissue were performed, and the *Hox11* conditional mutant embryos produced a robust recombined band and an absence of a detectable control band, indicating efficient deletion (Figure 1.5.3 B).

To functionally validate this allele, we deleted *Hoxd11* at embryonic stages in the background of *Hoxa11*-null mutants. It is important to note that the *Hoxa11*-eGFP is a knock-in allele that renders it nonfunctional. Therefore, animals that carry the genotype *Hoxa11*<sup>eGFP/-</sup> are functionally null for *Hoxa11*, but their forelimbs are indistinguishable from that of wild-type (WT) littermates from embryonic through adult stages, serving as a good control for the conditional mutants (compare Figure 1.5.3 C and D).<sup>166</sup> We induced deletion by feeding pregnant dams tamoxifen chow for 1 wk beginning at E9.5. This stage is approximately when *Hox11* expression begins within the limb bud and therefore should recapitulate the *Hox11*-null phenotype. Embryos were collected at E17.5, and skeletal preparations demonstrate that *Hox11* conditional mutants phenocopy *Hoxa11*<sup>-/-</sup>; *Hoxd11*<sup>-/-</sup> mutants, confirming that the *Hoxd11* conditional allele results in deletion of *Hoxd11* function (compare Figure 1.5.3 E and F).

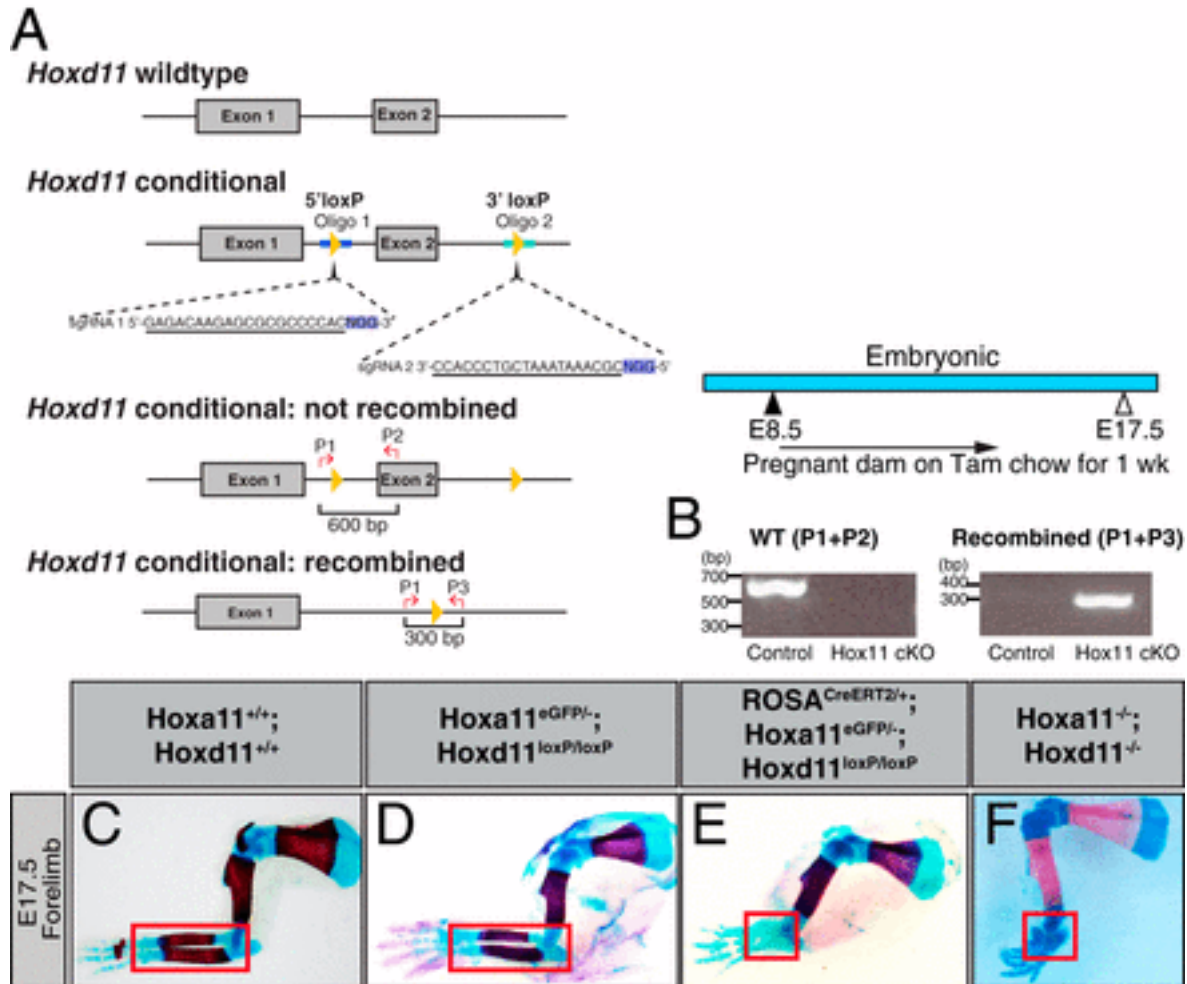


**Figure 1.5.3.** Conditional deletion of *Hox11* function recapitulates the germline null mutation. (A) Schematic illustrating the *Hoxd11* locus. Yellow arrowheads illustrate the inserted loxP sites. Two guide RNAs with the indicated sequences (underlined) along with their corresponding PAM (highlighted blue) were used to flank exon 2 of *Hoxd11* in order to insert loxP sites. Homology sequences used in the donor sequences are highlighted with thick dark blue line (5' loxP) and thick light blue line (3' loxP). Red arrows marked with P1, P2, and P3 mark the location of the PCR primers used to confirm recombination. Corresponding PCR product sizes are indicated as well. The PCR elongation time was adjusted so that a 300-bp PCR product would appear only if recombination had occurred between the loxP sites. Pregnant dams were fed on tamoxifen chow for 1 wk to induce recombination, and the resulting embryos were collected at E17.5. (B) PCR analysis using the PCR primers produces a robust 600-bp control band only present in the controls

and a 300-bp recombined band only present in the conditional mutants. cKO denotes Hox11 conditional mutants. Skeletal preparations of limbs from (C) WT, (D) littermate control for Hox11 conditional mutant, (E) Hox11<sup>ROSA<sup>CreERT2</sup></sup> conditional mutant, and (F) Hox11 germline-null mutant. The red box highlights the zeugopod skeleton.

### **Adult Deletion of Hox11 Function Results in a Progressive Replacement of Lamellar Bone with Abnormal Bony Matrix**

To assess the role of *Hox11* during adult skeletal homeostasis, animals with the genotype *ROSA<sup>CreERT2/+</sup>;Hoxa11<sup>eGFP/-</sup>;Hoxd11<sup>loxP/loxP</sup>* (referred to as *Hox11<sup>ROSA<sup>CreERT2</sup></sup>* conditional mutants) and corresponding controls (including animals of identical genotype minus the *ROSA26-CreERT<sup>2</sup>* with tamoxifen administration, and animals with the *ROSA26-CreERT<sup>2</sup>* in the absence of tamoxifen administration) were examined. Of note, there was minimal recombination in the absence of tamoxifen administration in animals with the *ROSA26-CreERT<sup>2</sup>* allele; these animals did not produce a phenotype or show any evidence of recombination at the *Hoxd11* locus as assessed by PCR (Figure 1.5.4 C and D).

Both control and conditional mutant adult animals were fed tamoxifen chow for 3 wk beginning at 8 to 10 wk of age and evaluated at 2, 4, or 10 mo after the initiation of deletion. Tail samples were processed for PCR analysis and confirmed high levels of recombination, even out to the 1-y time point (Figure 1.5.5 A).

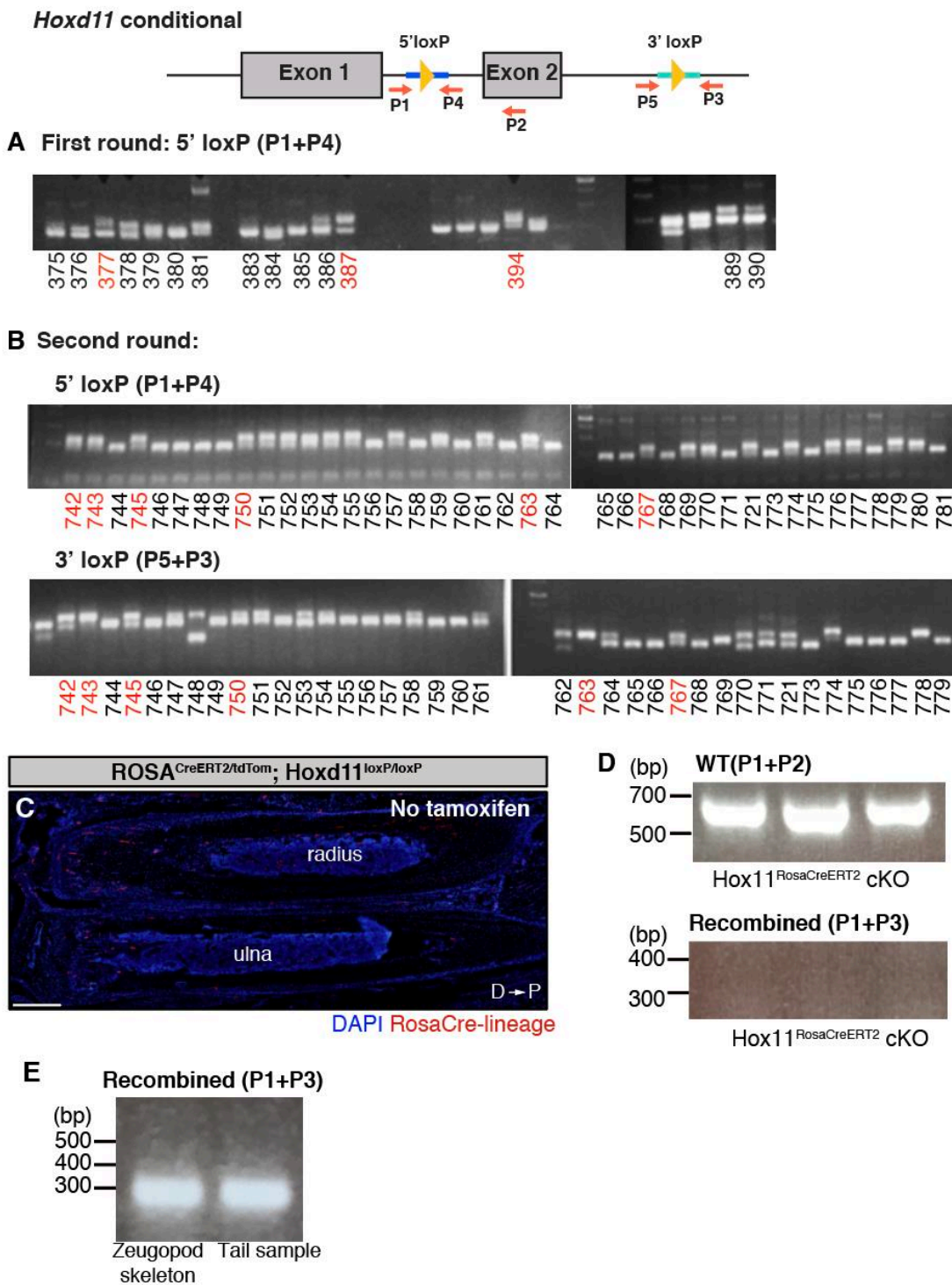


**Figure 1.5.4.** CRISPR/Cas9 generation of the *Hoxd11* conditional allele. LoxP sites were sequentially targeted both 5' and 3' of *Hoxd11* exon2. Homology sequence used in the donor sequences are highlighted with thick dark blue line (5' loxP) and thick light blue line (3 loxP). Orange arrows mark the approximate location of the PCR primers used to confirm correct

targeting. (A) PCR genotyping of founder (F0) animals for insertion of the 5' loxP site. Animals #377, 387, and 394 were sequence verified and male F1 animals were used as stud males for second round of targeting. (B) PCR genotyping of F0 animals for insertion at the 5' loxP (top panel) and 3' loxP (bottom panel). Animals # 742, 743, 745, 750, 763 and 767 were heterozygous for 5' loxP and sequence verified to harbor correctly targeted 3' loxP. Animals #742 and 745 were found to be chimeric. Animal #763 contained the loxP sites in *trans*. Animals # 743, 750 and 767 contained the loxP sites in *cis* and #743 was selected to be the final founder. (C) 8-week old adult with the genotype  $ROSA^{CreERT2/LSL-tdTomato}; Hoxd11^{loxP/loxP}$  without tamoxifen administration shows minimal recombination visualized by ROSA-lineage marked cells (red). DAPI: blue. Scale bar: 200 $\mu$ m. (D) PCR analysis shows that the minimal recombination seen in the zeugopod bones do not result in detectable recombined bands (bottom panel) and robust control band (top panel). Three samples are biological replicates of the same genotype. (E) Equally strong detection of the recombined PCR band between zeugopod skeleton and tail sample taken from  $Hox11_{ROSACreERT2}$  conditional mutants collected at 6 months of age.

Notably, recombination was measured at the same degree in tail samples as in the zeugopod skeleton (Figure 1.5.4 E). A small number of the  $Hox11^{ROSACreERT2}$  conditional mutants displayed a residual WT band, indicating incomplete recombination; however, qRT-PCR analyses revealed robust loss of *Hoxd11* in all cases (Figure 1.5.5 B). Despite robust loss of function, it is critical to note that the *Hox11*-expressing skeletal stem cells are maintained in the conditional mutant bones out to the 1-y-old time points, as supported by continued *Hoxa11eGFP* expression (Figure 1.5.6 A and B).

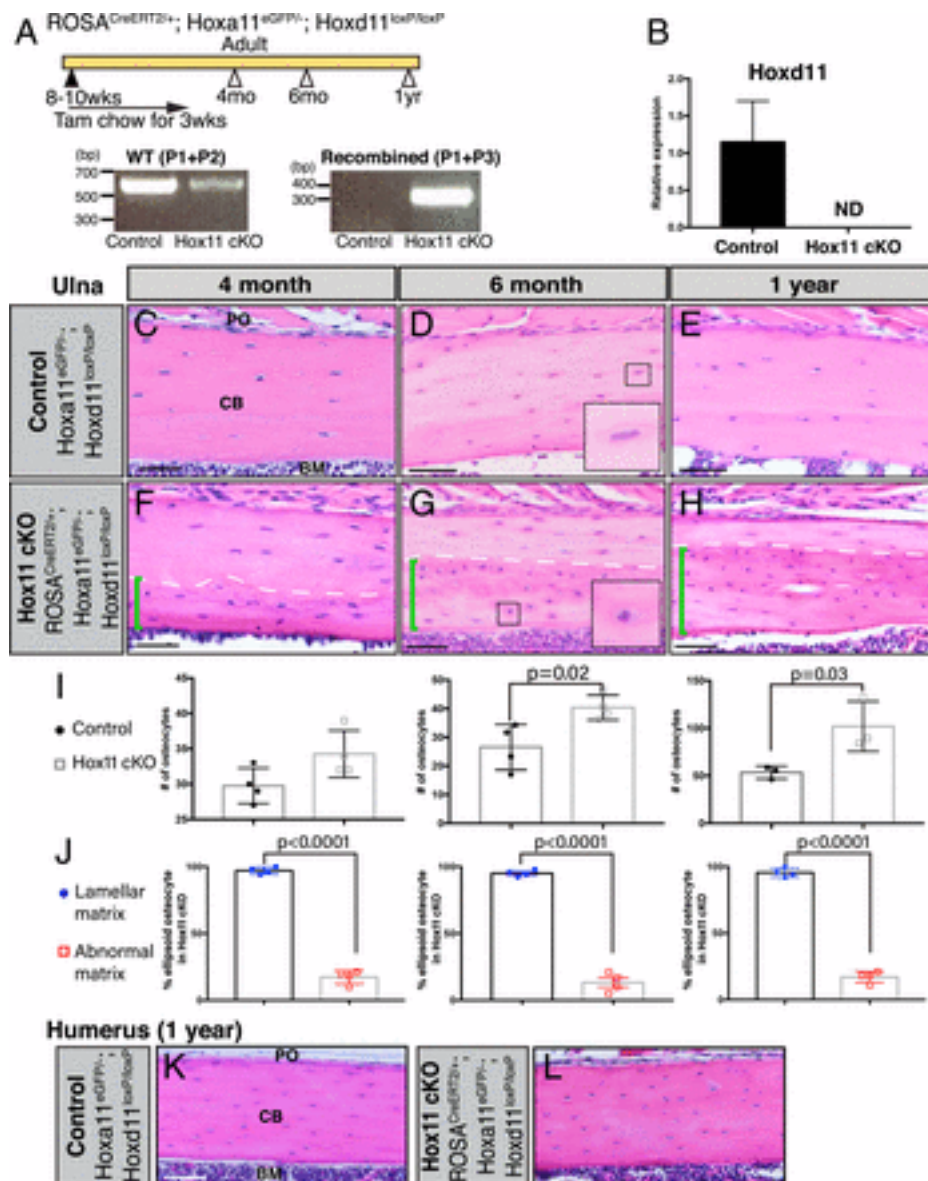


**Figure 1.5.5.** Deletion of *Hox11* function at adult stages results in the regional disruption in cortical bone homeostasis. *Hox11* conditional mutants with the *ROSA-CreER<sup>T2</sup>* (genotype indicated) allele along with control animals were fed on tamoxifen chow beginning at 8 to 10 wk of age for a total of 3 wk to delete *Hox11* function. Animals were evaluated at 4 mo of age, 6 mo of age, and 1 y of age. (A) Tail samples from all animals collected were analyzed via PCR to assess recombination. A robust 300-bp band in the conditional mutants demonstrates strong recombination. (B) qRT-PCR of *Hoxa11*eGFP-expressing zeugopod skeletal cells from the conditional mutants show robust deletion of *Hoxd11* in the conditional mutants. Data are presented

relative to mouse GAPDH using the  $\Delta\Delta\text{Ct}$  method. ND, none detected. Error is represented as mean  $\pm$  SEM. (C–H) H&E stains of paraffin bone sections (ulna) of control and  $\text{Hox11}^{\text{ROSACreERT2}}$  conditional mutant animals. The dashed line demarcates the border between lamellar (above) and abnormal (below) bone. Green brackets demarcate the abnormal matrix. Boxed areas in D and G represent high-magnification images of an individual matrix-embedded cell highlighting the morphological differences between control and *Hox11* conditional mutant osteocyte-like cells. (I) Quantification of cells embedded within the abnormal matrix at 4 mo, 6 mo, and 1 y of age shows a significant increase in cell number in  $\text{Hox11}^{\text{ROSACreERT2}}$  conditional mutant bone. Error is represented as mean  $\pm$  SEM. Statistics by Student's *t* test. (J) Percentage of osteocytes or osteocyte-like cells in *Hox11* conditional mutant bones that exhibit an ellipsoid shape within lamellar (above dotted line in F–H) and abnormal (below dotted line, green bracket in F–H) bony matrix. Error is represented as mean  $\pm$  SEM. Statistics by Student's *t* test. (K and L) H&E stains of bones from the humerus of control (K) and *Hox11* conditional mutant (L) show no differences in morphology at 1 y of age. All images: BM, bone marrow; CB, cortical bone; PO, periosteum. (Scale bar in all images: 100  $\mu\text{m}$ .)

Microcomputed tomography (microCT) measurements did not reveal significant distinctions between the control and  $\text{Hox11}^{\text{ROSACreERT2}}$  conditional mutants at any of the time points examined (Figure 1.5.7 A and B). However, histological inspection revealed progressive changes in the appearance of the cortical bone in  $\text{Hox11}^{\text{ROSACreERT2}}$  conditional mutants compared to controls.



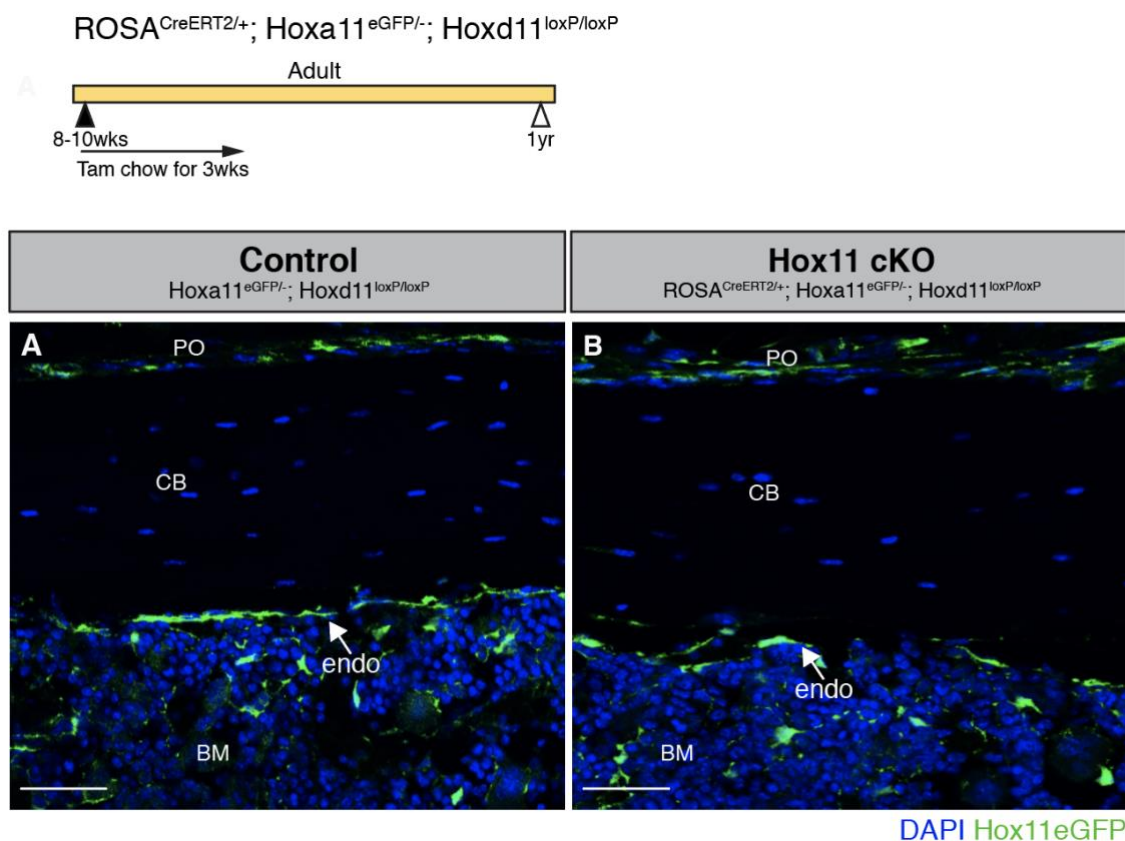


**Figure 1.5.6.** Hox11-expressing skeletal stem cells are maintained in the Hox11 conditional mutants.  $Hox11^{ROSA^{CreERT2}}$  conditional mutants were fed on tamoxifen chow for 3 weeks starting at 8-10 weeks of age and collected at 1-year of age. (A, B) Hox11eGFP-expressing skeletal stem cells (green) are present in the expected locations at 1-year of age in both the control (A) and Hox11 conditional mutants (B). All images are from the ulna, PO = periosteum, CB = cortical bone, endo = endosteum, BM = bone marrow. DAPI: blue. Scale bar, 75 $\mu$ m.

Conditional mutant bones become notably hypercellular, and quantification revealed significantly higher cell numbers in the abnormal bony matrix (Figure 1.5.5 C–I). Presumed osteocytes embedded within the hypercellular matrix displayed a round morphology compared to the ellipsoid morphology in controls (compare Figure 1.5.5 D and G, Inset). Presumed osteocytes embedded within the hypercellular matrix displayed a round morphology compared to the ellipsoid morphology in controls (compare Figure 1.5.5 D and G, Inset). Comparing the percentage of

osteocytes exhibiting an ellipsoid morphology in the lamellar bone (Figure 1.5.5 F–H, above the dashed line) to those in the abnormal bony matrix (Figure 1.5.5 F–H, below the dashed line, green bracket) in the *Hox11*<sup>ROSACreERT2</sup> conditional mutants revealed a significant decrease in the presence of ellipsoid osteocytes in the abnormal bone matrix (Figure 1.5.5 F–H and J). This phenotype resembles the histology of woven bone, which has a higher density of osteocytes within its matrix along with the round shape of the lacunae.<sup>176</sup> It is important to note that these abnormalities remain regionally restricted as the humerus of *Hox11*<sup>ROSACreERT2</sup> conditional mutants was not affected even as late as the 1-y time point (Figure 1.5.5 K and L).

### **Abnormal Bony Matrix in Adult Hox11 Conditional Mutants Displays Disorganized Collagen**

The shape of osteocyte lacunae is strongly influenced by the orientation of the collagen fibers within the bone. Normal adult bone is comprised of lamellar bone, with collagen fibers arranged in organized parallel sheets or layers, and this contributes to the ellipsoid shape of the lacunae.<sup>176, 177</sup> Woven bone, in contrast, is characterized by a haphazard organization of collagen fibers and contains osteocyte lacunae with a spherical shape, similar to what is observed in the abnormal matrix of the *Hox11* conditional mutants. The collagen network within cortical bone can be visualized by picosirius red stain. Picosirius red increases the birefringence of the collagen fibers, and subsequent observation under polarized light reveals the organization of the collagen network.<sup>178, 179</sup> The picosirius red staining in control bone demonstrates a well-organized, parallel structure of collagen fibers characteristic of normal, mature lamellar bone while the *Hox11*<sup>ROSACreERT2</sup> conditional mutant bones displayed a striking disorganization of the-

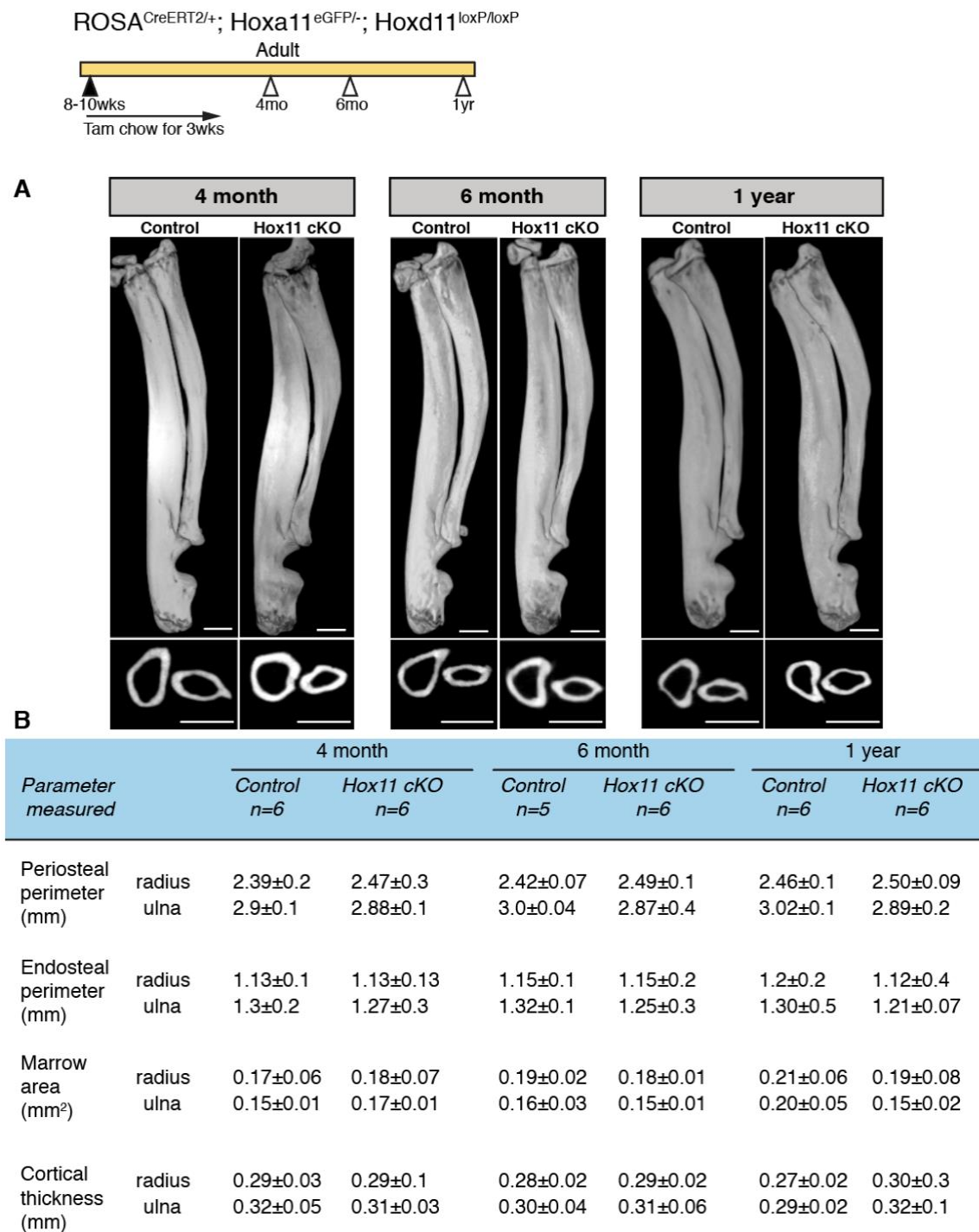


**Figure 1.5.7.** Long-term deletion of *Hox11* function at adult stages do not lead to noticeable gross morphological differences. *Hox11* conditional mutants with the *ROSA-CreER<sup>T2</sup>* (genotype indicated) allele along with control animals were fed on tamoxifen chow for 3 weeks beginning at 8-10 weeks of age to delete *Hox11* function and evaluated at 4-months, 6-months, and 1 year of age. (A) Top panel: 3D rendering from microCT scans of the zeugopod skeleton (radius/ulna) from

control and *Hox11*<sup>ROSACreERT2</sup> conditional mutants. Bottom panel: Cross section of the zeugopod skeleton through the distal end at 10% of the entire length of the ulna. (B) Table outlining the morphological measurements generated from microCT scans. Statistics by Student's t test; \* $p < 0.05$ .

collagen matrix that correlates with the hypercellular region (Figure 1.5.8 A–F). Notably, both the region of disorganized collagen matrix and the hypercellular region increase with increasing time after deletion (Figure 1.5.5 and 1.5.9 A–L).

In efforts to further examine collagen organization, a (flpHypGly)<sup>7</sup> collagen mimetic peptide (CMP) conjugated to a cyanine 5 (Cy5) dye was used to stain sections of control and *Hox11*<sup>ROSACreERT2</sup> conditional mutant bone. The <sup>Cy5</sup>CMP mimics the proline-hydroxyproline-glycine amino acid triplet motif that is prevalent in collagen (constituting ~10.5% of the protein sequence) and selectively anneals to disrupted sites in collagen.<sup>158</sup> Control bone sections were virtually devoid of any staining, as expected for a highly organized collagen matrix, but conditional mutant bones displayed strong binding throughout the regions of abnormal matrix (Figure 1.5.8 G–J). Use of a compositional isomer (<sup>Cy5</sup>CI) control demonstrated no binding to either control or mutant bone sections (Figure 1.5.9 M and N).<sup>158</sup>

As osteoclasts have a strong influence on bone integrity, we examined osteoclast number and localization in the controls and conditional mutants. Tartrate-resistant acid phosphatase (TRAP) is a metallophosphoesterase that participates in osteoclast-mediated bone resorption and is used to

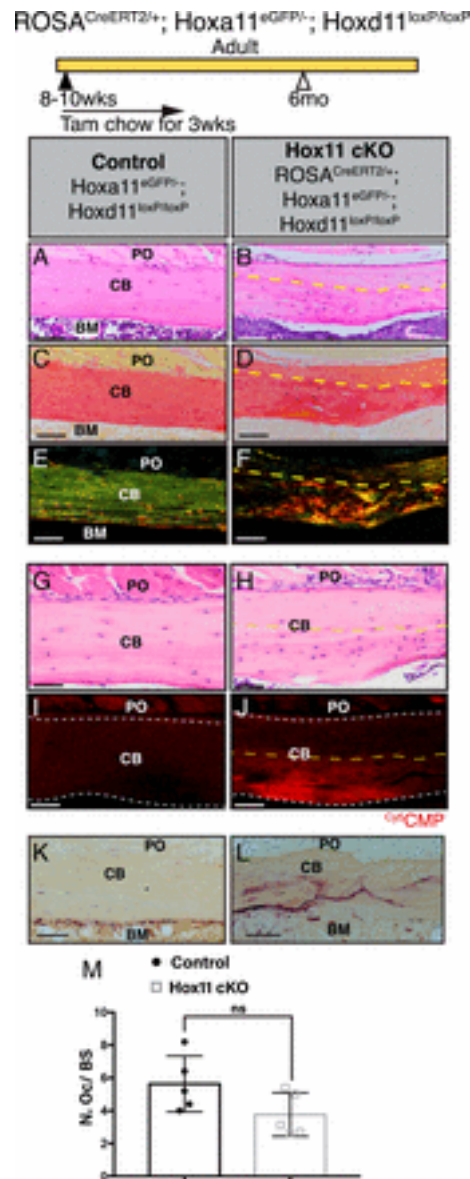


**Figure 1.5.8.** Woven bone-like region in the Hox11 conditional mutant bones has a disorganized collagen matrix. Hox11 conditional mutants with the  $ROSA-CreER^{T2}$  (genotype indicated) allele along with control animals were fed on tamoxifen chow for 3 wk beginning at 8 to 10 wk of age to induce deletion, and animals were examined at 6 mo of age. (A and B) H&E stains of paraffin-processed bone sections of control and Hox11<sup>ROSA CreERT2</sup> conditional mutant animals. (C and D) Brightfield images of picrosirius red stain of consecutive bone sections from A and B. (E and F) Polarized light images of picrosirius red stain of bone sections from C and D. (G and H) H&E stains of paraffin-processed bone sections of control and Hox11<sup>ROSA CreERT2</sup> conditional mutant

animals. (*I* and *J*) Consecutive bone sections from *G* and *H* stained with <sup>Cy5</sup>CMP (red). White dashed line marks border of cortical bone. (*K* and *L*) Control (*K*) and *Hox11*<sup>ROSACreERT2</sup> conditional mutant (*L*) bone sections stained with TRAP. Note the distinct distribution of TRAP stain in conditional mutant. (*M*) Quantification of osteoclast number (N. Oc) on bone surface (BS) using the Bioquant Osteo software. Statistics by Student's *t* test. Error is represented as mean ± SEM. All images are from the ulna. BM, bone marrow; CB, cortical bone; PO, periosteum. The yellow dashed line demarcates border between lamellar (above) and abnormal (below) bone. ns, not significant. (Scale bar in all images: 100 μm.)

visualize osteoclasts.<sup>180</sup> In control bones, TRAP staining is concentrated along the endosteal bone surface. In the *Hox11*<sup>ROSACreERT2</sup> conditional mutant bones, TRAP staining is also observed on the endosteal bone surface; however, there are trails of TRAP stain present within the abnormal cortex of the conditional mutant bones (Figure 1.5.8 K and L). A higher magnification of the osteoclasts on the control bone surface demonstrates that the osteoclasts and TRAP stain localize at the surface of the bone as expected while conditional mutant bone additionally shows TRAP enzyme within the abnormal bone matrix (Figure 1.5.10 A and B). However, there were no cells associated with the TRAP stain, leading to the conclusion that the abnormal matrix is allowing diffusion of the enzyme into the matrix (Figure 1.5.10 C and D). As TRAP expression by osteoclasts has been shown to influence normal endochondral bone formation and bone remodeling<sup>181, 182</sup>, it is possible that the diffusion of the TRAP enzyme into the bone matrix exacerbates the abnormal matrix phenotype observed in the *Hox11* conditional mutants. While TRAP staining is expanded in the conditional mutant bones, quantification of the bone surface osteoclasts show no significant

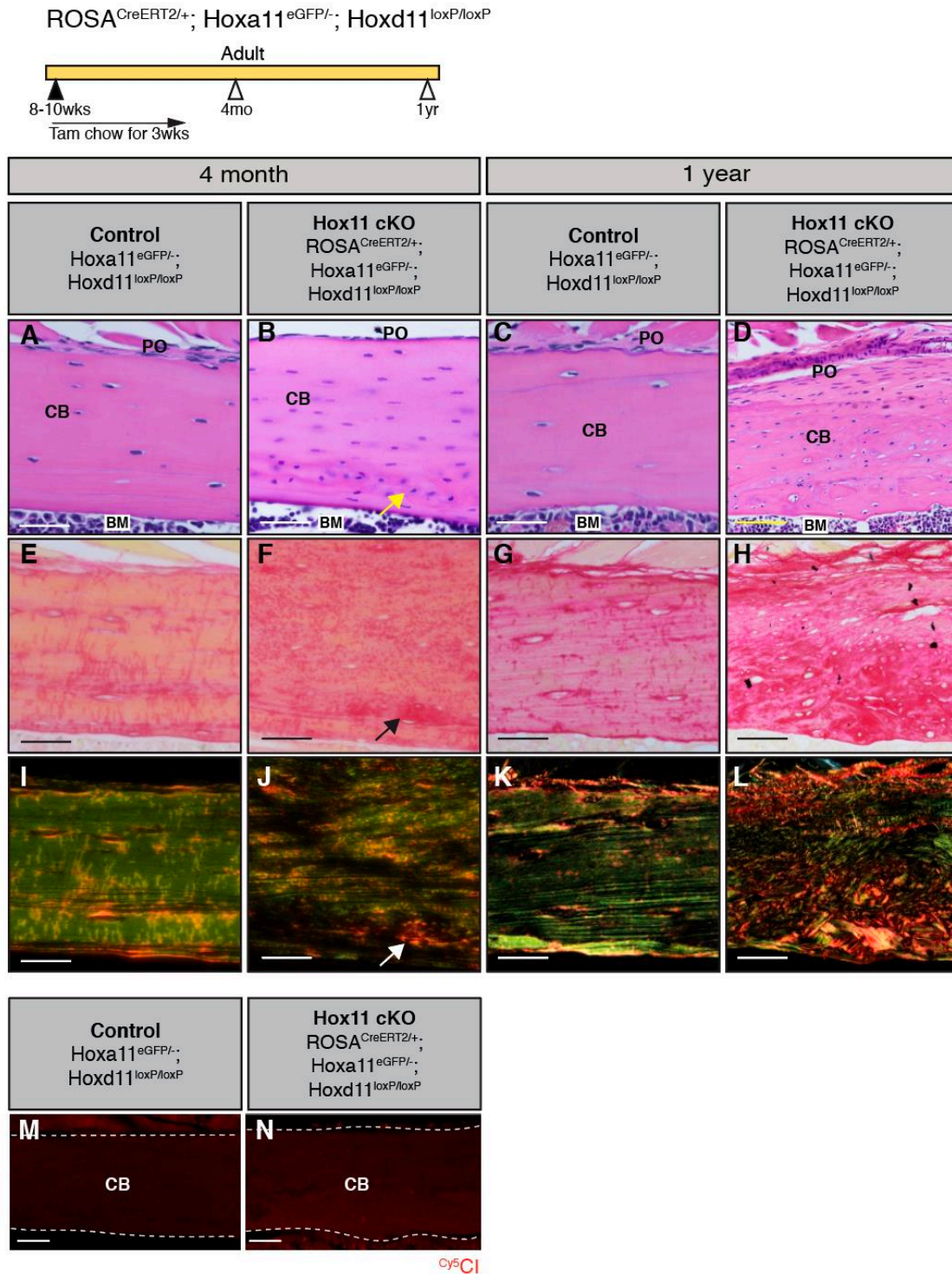


**Figure 1.5.9. Adult conditional deletion of Hox11 function lead abnormal matrix at all times points examined.** Hox11 conditional mutants with the *ROSA-CreER<sup>T2</sup>* (genotype indicated) allele along with control animals were fed on tamoxifen chow at 8-10 weeks of age for 3 weeks to delete *Hox11* function and evaluated at 4-months of age, 6-months of age, and 1 year of age. (A-D) H&E

stains of control (A, C) and  $Hox11^{ROSACreERT2}$  conditional mutant (B, D) at 4- months and 1-year of age. (E-H) Brightfield images of picosirius red stain of consecutive bone sections from A-D. (I-L) Polarized light images of picosirius red stain of bone sections from E-H. Yellow (B), black (F) white (J) arrows highlight the abnormal matrix in the 4-month old conditional mutant bone. (M, N) Bone sections from control (M) and  $Hox11^{ROSACreERT2}$  conditional mutant (N, 4- months following deletion) were stained with  $Cy^5CI$ . Both bone sections do not show staining. White dashed line marks border of cortical bone. All images are from the ulna, PO = periosteum, CB = cortical bone, BM = bone marrow. Scale bar in all images: 100 $\mu$ m.

difference in the number of osteoclasts in the control and conditional mutants (Figure 1.5.8 M). The disorganized collagen matrix, in conjunction with the diffusion of TRAP staining in the cortical matrices, indicates the presence of a defective matrix in the  $Hox11^{ROSACreERT2}$  conditional mutant bone.

### **Abnormal Bony Matrix Arises from Hox11-Lineage Cells**

We next used the  $Hoxa11-CreERT^2$  allele to simultaneously delete the function of  $Hox11$  and lineage-trace the  $Hox$ -expressing cells by including a ROSA26-LSL-tdTomato allele. Females with the genotype  $Hoxa11^{eGFP/+};Hoxd11^{loxP/loxP}$  were mated to males with the genotype  $Hoxa11^{CreERT2/+};Hoxd11^{loxP/loxP}; ROSA^{LSL-tdTom/LSL-tdTom}$  to generate embryos with the genotype  $Hoxa11^{CreERT2/eGFP};Hoxd11^{loxP/loxP};ROSA^{LSL-tdTom/+}$  (referred to as  $Hox11^{Hoxa11CreERT2}$  conditional mutants). The genotype of the control animals for the  $Hox11^{Hoxa11CreERT2}$  conditional mutants was  $Hoxa11^{CreERT2/eGFP};ROSA^{LSLtdTom/+}$  where both the  $Hoxa11-CreERT^2$  and  $Hoxa11-eGFP$  are knock-in alleles rendering the  $Hoxa11$  alleles nonfunctional. Conditional mutant animals, along with their



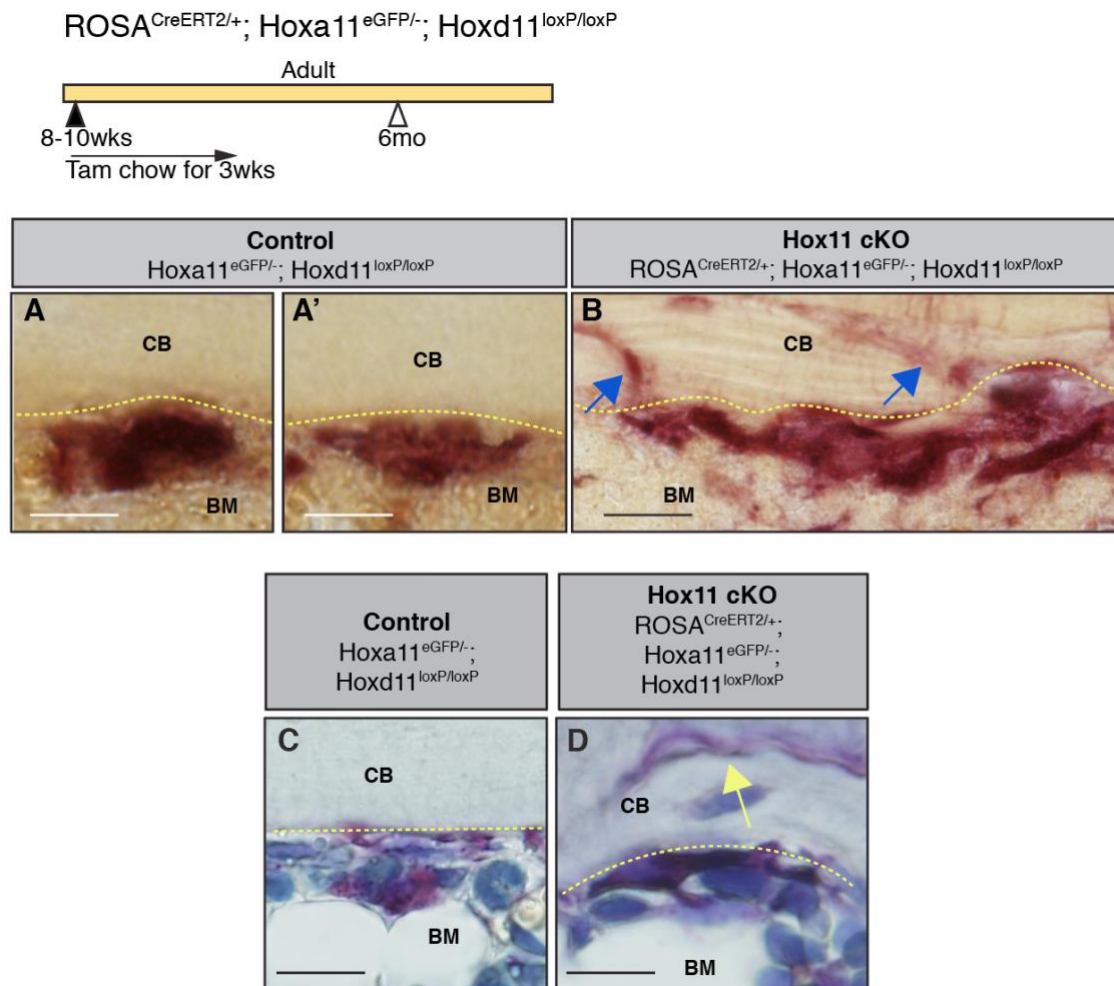


**Figure 1.5.10. Distribution of TRAP staining, but not number of osteoclasts is distinct in Hox11 conditional mutant bones.** Hox11 conditional mutants with the *ROSA-CreER<sup>T2</sup>* (genotype indicated) allele along with control animals were fed on tamoxifen chow at 8-10 weeks of age for 3 weeks to induce deletion of *Hox11* function and collected at 6-months of age. (A-B) Higher magnification of osteoclasts to show apparent TRAP stain leakage into cortical bone matrix. Yellow dashed line demarcates the endosteal bone surface. TRAP enzyme leaked into the bone matrix in mutants (blue arrow). Scale bar: 25 $\mu$ m (C, D) TRAP stain with hematoxylin for visualization of nuclei. No cells were associated with TRAP stain in cortical bone (yellow arrow).

corresponding controls, were given tamoxifen chow for 3 wk, and the contribution of the *Hox11* lineage-labeled cells to bone was examined 2 mo following the initiation of deletion. The extent

of lineage contribution observed between the control and *Hox11<sup>Hoxa11CreERT2</sup>* conditional mutant bones is similar, with no obvious differences in the cortical thickness of lineage-marked cells embedded in the bone matrix (Figure 1.5.11 A and B). Control bones display a well-organized bone structure, with lineage-labeled osteocytes embedded in the lamellar bone (Figure 1.5.11 A). In contrast, the region with *Hox11*-lineage mutant cells precisely correlates with the abnormal matrix region clearly distinguishable in brightfield images (Figure 1.5.11 B, black bracket). These results strongly support that the abnormal matrix formed in the conditional mutant bones arises from the descendants of the cells that have lost *Hox11* function.

### **Hox11 Conditional Mutant Osteoblasts Exhibit Deficient Differentiation**

During normal osteoblast differentiation, *Runx2* marks cells that have committed to the osteoblast lineage (preosteoblasts). Maturation of osteoblasts leads to the expression of osteopontin (*Opn*) at relatively early stages of osteoblastic differentiation, and osteocalcin (*Ocn*) is expressed in fully mature osteoblasts coincident with their assuming the characteristic cuboidal shape.<sup>183</sup> To determine whether *Hox* mutant cells initiate osteoblast differentiation, *Runx2* expression was examined. *Runx2* expression was observed in both control and mutant bones on the cell surface of the endosteal bone, supporting the initiation of osteoblast differentiation in both controls and mutants (Figure 1.5.11 C and D). However, *Hox11<sup>Hoxa11CreERT2</sup>* conditional mutant bones were almost completely devoid of both *Opn* and *Ocn* staining whereas the expression of both markers lined the endosteal surface of the control bones (Figure 1.5.11 E–H). These data provide strong evidence that differentiation toward the osteoblast lineages is able to initiate in *Hox11* mutant skeletal stem cells, but terminal differentiation of osteoblasts is disrupted.

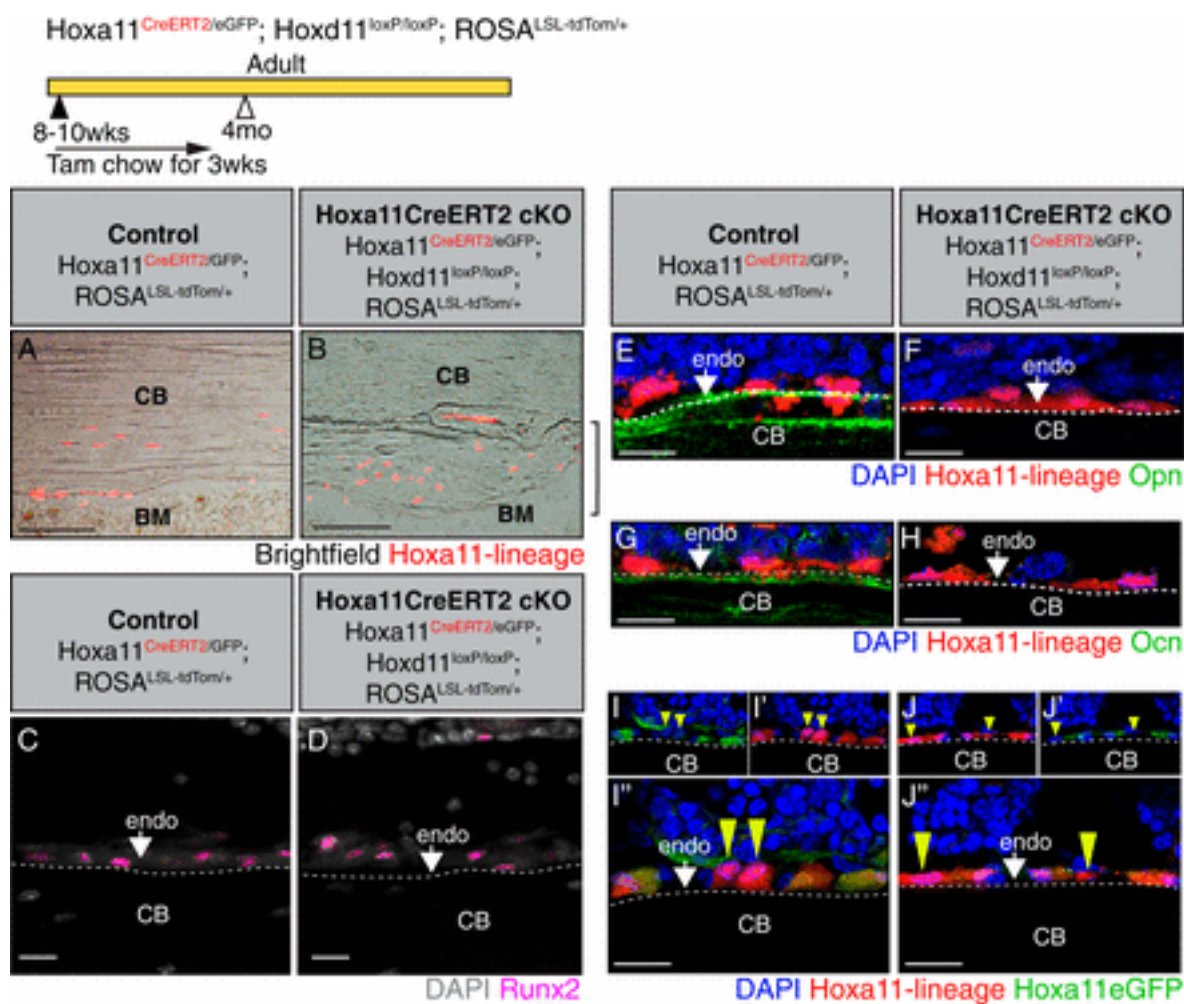


**Figure 1.5.11.** Osteoblast differentiation is perturbed in Hox11 conditional mutant bone. Hox11 conditional mutants with the *Hoxa11-CreERT<sup>2</sup>* allele (genotype indicated) along with control animals were fed on tamoxifen chow for 3 wk starting at 8 to 10 wk of age and collected at 4 mo of age. (A) Brightfield image of a bone section from a control animal overlaid with Hox11-lineage marked cells (red) shows contribution to osteocytes. (B) Brightfield image of bone section from a Hox11<sup>Hoxa11CreERT<sup>2</sup></sup> conditional mutant overlaid with Hox11-lineage-positive cells (red) shows contribution to abnormal bone matrix. (C and D) Control (C) and Hox11<sup>Hoxa11CreERT<sup>2</sup></sup> conditional mutant (D) bone stained with RUNX2 (magenta). DAPI, gray. White arrows in C and D mark the endosteal bone surfaces. (E and F) Control (E) and Hox11<sup>Hoxa11CreERT<sup>2</sup></sup> conditional mutant (F) bone stained with osteopontin (Opn, green). (G and H) Control (G) and Hox11<sup>Hoxa11CreERT<sup>2</sup></sup> conditional mutant (H) bone sections stained with osteocalcin (Ocn, green). (I–J'') Hoxa11eGFP (green) and

DAPI (blue) in *I* and *J*, Hoxa11-lineage marked cells (red) and DAPI (blue) in *I'* and *J'*, and merged images in *I''* and *J''*. Control (*I–I''*) and Hox11<sup>Hoxa11CreERT2</sup> conditional mutant (*J–J''*) bone sections show Hoxa11-lineage marked (red), non-Hoxa11eGFP endosteal surface osteoblasts (yellow arrowhead). Notice stark difference in morphology. All images are from the ulna. DAPI, blue (unless noted otherwise); Hox11-lineage marked cells, red. CB, cortical bone; endo, endosteum. The white dashed line demarcates the endosteal surface. (Scale bars in all images: 50  $\mu\text{m}$ .)

Morphologically, mature osteoblasts are recognizable as large cuboidal cells, with a round nucleus located in the cell away from the bone surface.<sup>184</sup> As we have previously established that *Hox11* is not expressed in osteoblasts, but only the stem/progenitor cells, we identified probable bone surface osteoblasts as *Hoxa11eGFP*-negative, *Hoxa11* lineage-positive (red) cells. In control bones, we observed mature osteoblasts that present the classical, cuboidal morphology and nuclear localization (Figure 1.5.11 I–I'', yellow arrowheads). Noticeably, bone surface cells that retained *Hoxa11eGFP* expression displayed a rounder morphology but were not cuboidal in shape, nor was the localization of the nucleus polarized away from the bone surface. In notable contrast to controls, all bone surface cells in conditional mutant bones appeared flatter compared to those in controls with no nuclear migration away from bone surface, consistent with loss of fully differentiated osteoblasts (Figure 1.5.11 J–J'', yellow arrowheads).

### **Osteocyte Differentiation and Morphology Is Disrupted with Loss of Hox11 Function**

Osteocytes are terminally differentiated osteoblasts that become embedded within the bone matrix and are the primary mechanosensory cells of the bone, with important roles in bone homeostasis.<sup>185, 186</sup> Long dendritic processes are characteristic of osteocytes; these structures connect neighboring osteocytes to each other, as well as to bone surface, including to the cell surface osteoblasts and osteoclasts.<sup>187, 188</sup> To examine whether osteocytes were also affected by the

loss of *Hox11* function, we used a silver nitrate stain to visualize osteocyte morphology. After deletion, the *Hoxa11<sup>CreERT2</sup>* conditional mutant matrix-embedded cells form no dendrites and display a complete absence of the normal lacuno-canalicular network within abnormal bone matrix regions.

Mature osteocytes produce and secrete the protein sclerostin, encoded by the *SOST* gene. Using our *Hoxa11-CreERT2* allele with deletion enacted at 8 wk and animals evaluated 2 mo later, *Hox11*-lineage marked cells are found embedded in both the control and *Hox11<sup>Hoxa11CreERT2</sup>* conditional mutant bones (Figure 1.5.12 E and F). While virtually all of the lineage-marked osteocytes in the control bone express SOST, most *Hox11<sup>Hoxa11CreERT2</sup>* conditional mutant lineage-marked, bone-embedded cells failed to express SOST (Figure 1.5.12 E–M), demonstrating a requirement for *Hox* function in proper osteocyte differentiation.

#### 5.4 Discussion

Woven bone is made primarily during the rapid bone growth of embryogenesis or following bone injury (e.g., fracture).<sup>189, 190</sup> In both cases, the initial woven bone matrix is remodeled and replaced by lamellar bone through a process that is not fully understood. The haphazard organization of collagen in the woven bone matrix causes the bone to be mechanically weak<sup>191</sup>; therefore, the replacement of the woven bone matrix by lamellar bone is imperative for proper bone function and homeostasis. The accumulation of woven bone with no signs of lamellar remodeling in our *Hox11* conditional mutants demonstrates that maintaining the integrity of the skeletal matrix requires *Hox* function. All of the evidence presented in this study supports defective differentiation of osteolineage cells with the loss of *Hox11* function. Osteoblasts originate from

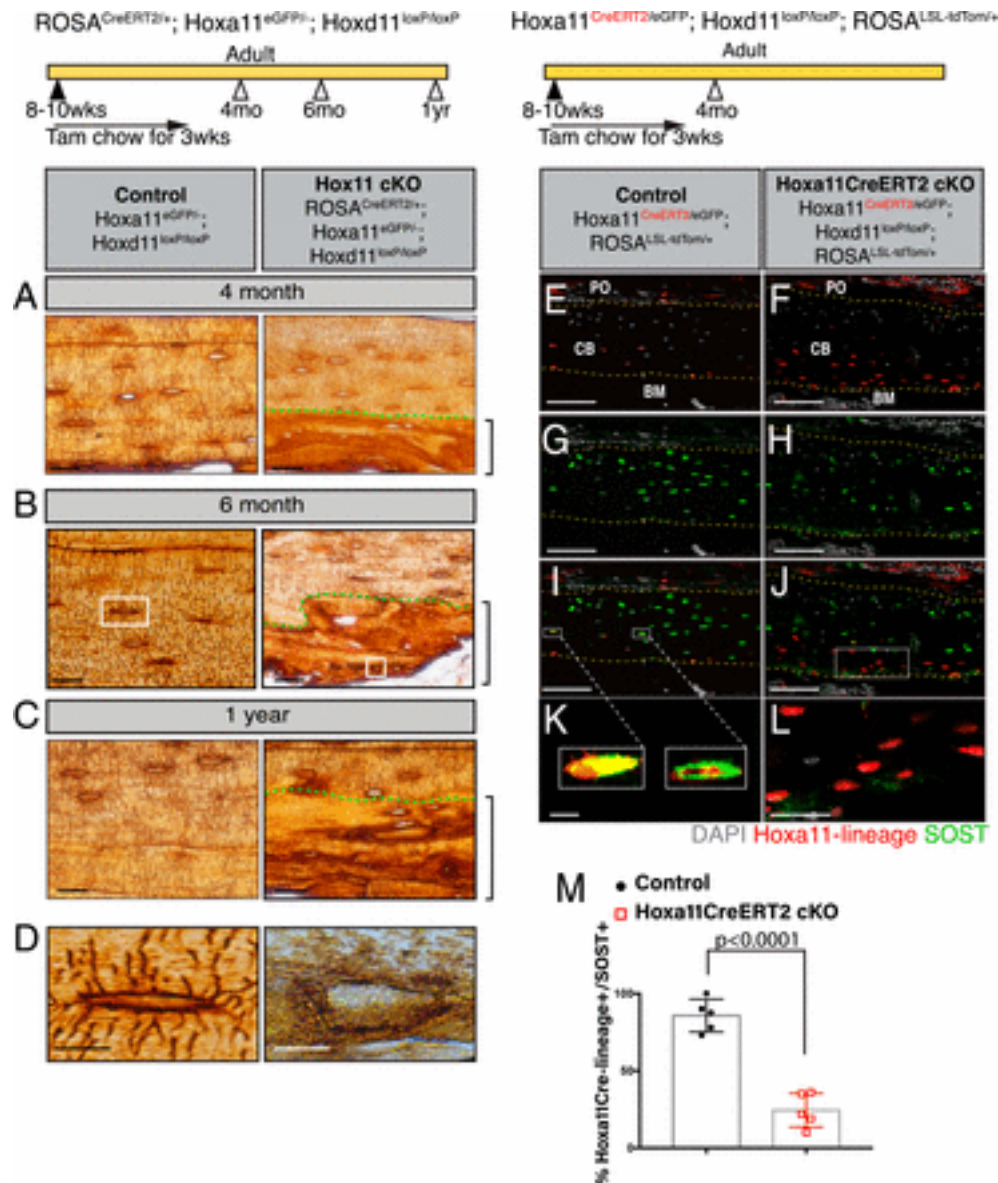


**Figure 1.5.12.** Hox11 conditional mutant osteocytes fail to form dendrites or express SOST. Hox11 conditional mutants with the *ROSA-CreERT<sup>2</sup>* (genotype indicated) allele along with control animals were fed on tamoxifen chow beginning at 8 to 10 wk of age for 3 wk to delete *Hox11* function, and animals were evaluated at 4 mo of age, 6 mo of age, and 1 y of age for C–E. (A–C) Control (Left) and Hox11<sup>ROSA-CreERT<sup>2</sup></sup> conditional mutants (Right) were treated with silver nitrate. Green dashed lines demarcate the lamellar (above) and abnormal (below) bone. Brackets outline abnormal bone matrix. (D) High magnification of osteocytes from the white-boxed area in B. Hox11 conditional mutants with the *Hoxa11-CreERT<sup>2</sup>* allele (genotype indicated)

along with control animals were fed on tamoxifen chow for 3 wk starting at 8 to 10 wk of age and collected at 4 mo of age for *E–M*. (*E* and *F*) Control (*E*) and  $Hox11^{Hoxa11CreERT2}$  conditional mutant (*F*) bone sections showing *Hox11*-lineage marked cells (red) that contributed to osteocytes. (*G* and *H*) Control (*G*) and  $Hox11^{Hoxa11CreERT2}$  conditional mutant (*H*) bone sections stained with SOST (green). (*I* and *J*) Merged images of *E* and *G* in *I* or *F* and *H* in *J* showing overlap or the lack thereof of *Hox11*-lineage marked cells (red) and SOST (green). The yellow dashed line in *E–J* outline the cortical bone. (*K* and *L*) Close-up of osteocytes in white-boxed region in *I* and *J*. (*M*) Quantification of *Hox11*-lineage marked cells (red) that also express SOST (green). Error is represented as mean  $\pm$  SEM. Statistics by Student's *t* test. All images are from the ulna. DAPI, gray. BM, bone marrow; CB, cortical bone; PO, periosteum. (Scale bar: 25  $\mu$ m [*A–C*], 10  $\mu$ m [*D*], 100  $\mu$ m [*E–J*], 10  $\mu$ m [*K* and *L*].)

skeletal stem cells, and previous work from our laboratory, as well as results presented here, unequivocally demonstrates that *Hox11*-expressing skeletal stem cells give rise to osteoblasts in the skeleton. As *Hox11* expression is restricted to the stem cell population and is not observed in differentiated skeletal cells, we conclude that *Hox* proteins function in the skeletal stem cells at early stages of differentiation.

The results from our conditional *Hox11* loss-of-function model correlate with earlier investigations into embryonic null mutants. When *Hoxa11/Hoxd11*-null mutants were examined at E14.5, the stage at which overt osteoblasts are beginning to differentiate in the zeugopod skeletal anlage, *Runx2* expression was observed in the perichondrial region.<sup>192</sup> However, subsequent zeugopod skeletal development in the *Hoxa11/Hoxd11*-null mutants is grossly stunted, consistent with aberrant osteoblast differentiation. Intriguingly, these results are consistent with a similar function for *Hox* in the skeleton throughout life; however, this idea requires further investigation.

The abnormal collagen matrix secreted by the adult conditional mutant osteoblasts may have a compounding role in the skeletal phenotype. Mice that harbor a mutation in *Coll1a1* that produces type 1 collagen molecules resistant to cleavage by collagenase manifest a haphazard endosteal bone growth reminiscent of the *Hox11* conditional mutant bones.<sup>193</sup> The binding of <sup>Cy5</sup>CMP to collagen strands in our *Hox11* conditional mutant bone supports the presence of abnormal collagen in the matrix. The similarity in bone phenotypes suggests that the abnormal collagen matrix is a critical manifestation of the *Hox* conditional loss-of-function phenotype. It is possible that collagen helices produced by *Hox* mutant osteoblasts are not processed properly for the normal organization to lamellar bone, or there may be an absence of enzymes or other molecules necessary for proper remodeling of the collagen matrix. This abnormal collagen matrix may create a more permissive environment for osteoblast incorporation, leading to the apparent increase in the number of osteocyte-like cells.

Our results test a hypothesis recently put forward by Leucht and coworkers that *Hox* expression in periosteal stem/progenitor cells determines the cell fate of those stem/progenitor cells in adult animals.<sup>194</sup> In this report, the authors associated *Hox* expressing periosteal stem/progenitor cells with more primitive, stem cell-like gene ontology terms that exhibited more accessible chromatin at transcriptional start sites. This is consistent with recent work from our laboratory demonstrating that *Hox* expression is associated with skeletal stem cells and lineage label into downstream skeletal lineages.<sup>170, 172</sup> Further, results presented here provide direct, genetic support for their hypothesis that *Hox* genes confer differentiation cues to these stem cells throughout life. Leucht and coworkers also hypothesize that *Hox* function may be required for maintenance of the stem cell population.<sup>194</sup> However, we have previously shown that *Hox11*-expressing skeletal stem cells are maintained in *Hox11* compound mutants at relatively comparable numbers compared to controls.<sup>170</sup> In this study, we precisely test complete loss of function and find that *Hox11*eGFP-positive skeletal stem cells are still present 10 mo after deletion of *Hox*



function. Furthermore, the progressive nature of the phenotype observed in our *Hox11* conditional mutants supports maintenance of the *Hox11* expressing skeletal stem population for continued (abnormal) contribution to the osteolineage. Cumulatively, these data provide compelling evidence that proper differentiation of skeletal stem cells requires *Hox* function but that maintenance of the skeletal stem cell pool is independent of regional *Hox* function. Despite the demonstration that regional *Hox* expression is maintained throughout the skeleton, it is important to note our results cannot rule out more broadly redundant roles for *Hox* genes that are not addressed by paralogous deletion.

### 1.5.5 Conclusion

Herein, we show that *Hox* gene function in the skeleton is not restricted to development and that *Hox* genes play a crucial, functional role in adult bone homeostasis. Adult *Hox11* loss of function leads to a replacement of the lamellar cortical bone with an abnormal woven bone-like matrix. We have demonstrated strong evidence that this woven bone matrix is directly produced by the *Hox11* conditional mutant cells and that the woven bone matrix is associated with the defective differentiation and maturation of osteoblasts resulting from the loss of function of *Hox11* in skeletal stem cells.

Whether other *Hox* paralogous genes function to maintain the adult skeleton remains an intriguing question for future studies. Previous studies from our laboratory showing the preservation of region-specific *Hox* expression specifically within progenitor-enriched stem cell populations at adult stages support this likelihood.<sup>170</sup> While embryonic loss of function has clearly established that *Hox* genes impart region-specific function that differentially controls skeletal patterning and morphology, results from this study raise the question of whether differential *Hox* gene function continues to be conveyed in a region-specific manner or whether all *Hox* function is similar once the skeleton has been established.

### 1.5.6 Acknowledgments

We thank Chris Stephan for technical assistance in microCT scanning of the bone specimens. We also thank Drs. Ernestina Schipani, Karl Jepsen, and Kenneth Kozloff for their input and advice on experiments. We acknowledge the help and service provided by the Orthopedic Research Laboratory (ORL) staff. We acknowledge the help and service of the Transgenic Animal Model Core of the University of Michigan's Biomedical Research Core Facilities. Research reported in this publication was mainly supported by National Institute of Arthritis and Musculoskeletal and Skin Diseases of the National Institutes of Health (NIH) Award R01 AR061402 (to D.M.W.). Support was also provided by Michigan Integrative Musculoskeletal Health Core Center Award P30 AR069620, by training awards granted by the National Institute of Dental and Craniofacial Research of the NIH under Award T32 DE007057 (to K.M.P. and J.Y.S.), by the National Institute of Child Health and Human Development of the NIH under Award T32 HD007505 (to K.M.P.), a Warner-Lambert Fellowship from the University of Michigan Cellular and Molecular Biology training program (to J.Y.S.), and National Institute of Arthritis and Musculoskeletal and Skin Diseases of the NIH Award R56 AR044276 (to R.T.R.). D.M.W. and R.T.R. would like to dedicate this manuscript to Dr. Hector F. DeLuca (former PhD mentor and former chair of Biochemistry at University of Wisconsin-Madison, respectively) on the occasion of his 90th birthday.

### 1.5.7 Materials and Methods

#### Mice

All mice were maintained in a C57BL/6 background. Both male and female mice were used for all experiments. The mouse models *Hoxa11-eGFP*<sup>167</sup> and *Hoxa11-CreERT2*<sup>169</sup> have been previously described. The ROSA26-CAG-loxP-stop-loxP-tdTomato (JAX stock no. 007909) and ROSA26-CreERT2 (JAX stock no. 008463) were purchased from The Jackson Laboratory. The *Hoxd11*-floxed animals were obtained by breeding founder *Hoxd11*-floxed animals to WT

C57BL/6 animals for five generations, followed by breeding *Hoxd11*-loxP heterozygotes to each other to produce *Hoxd11*-floxed animals. These animals were periodically bred to WT C57BL/6 animals to avoid genetic drift. The Col2.3-GFP mice<sup>195</sup> (kindly provided by Noriaki Ono, University of Michigan, Ann Arbor, Michigan) were then bred with our *Hoxa11* and *Hoxd11* mice to generate animals of appropriate genotype. All animal experiments described in this article were reviewed and approved by the University of Michigan's Committee on Use and Care of Animals, protocol PRO00008674 (to D.M.W.).

### Generation of *Hoxd11* Conditional Allele

The *Hoxd11* conditional allele was generated in two injection rounds, targeting each loxP site sequentially. Two guide sequences were targeted to regions of low conservation within the *Hoxd11* intron (5', upstream) and downstream of the 3' untranslated region (UTR) (3', downstream) flanking exon 2 of the *Hoxd11* locus and were cloned into the pT7-Guide Vector (Blue Heron Biotech, LLC). The guide sequence, approximate locations and corresponding protospacer adjacent motif (PAM) sequences are indicated in Figure 1.5.3A. Donor oligos contained 60 bp of flanking homology sequence, the loxP sequence (bold letters), and a unique restriction site (EcoRI [5' loxP] or NheI [3' loxP], capital letters) for optional use in confirming accurate targeting. Single-stranded DNA oligos were purchased from Integrated DNA Technologies. The 5' loxP donor oligo sequence (from 5' to 3') is as follows:

gttgatgagtggaacacgagagcctcctgccttcagggagagggtaagtgatctgcc GAATTC

ataactcgtataatgtatgctatacgaagtat gcactggacttaacccaacctctggctg

gcgctcagctcggagttgagcagatgctcctg. The 3' loxP donor oligo sequence (from 5' to 3') is as follows:

tctgattagacttacatctctagcatttgaaagcaatttgccaccctgctaaataa GCTAGC

ataactcgtataatgtatgctatacgaagtat acgctggcactttataaaatagaa caagtaaaatagttatattgtttcgtaaac.

The guide RNAs were in vitro transcribed from the pT7-Guide Vector using the MEGAscript T7 kit (AM1354; Life Technologies), and products were subsequently purified using the

MEGAclear kit (AM1908; Life Technologies). Using the pT7-Cas9-Nuclease vector (gift from Moises Mallo, Instituto Gulbenkian de Ciencia, Oeiras, Portugal), the Cas9 messenger RNA (mRNA) was in vitro transcribed using the mMESSAGE mMACHINE T7 ULTRA kit (AMB13455; Life Technologies) and purified using the MEGAclear kit (AM1908; Life Technologies).

Zygote injections were performed as previously described with minor modifications (14). C57BL/6 and SJL mixed background female mice were superovulated and mated with C57BL/6 and SJL mixed background male mice, and one-cell stage embryos were collected for microinjection. CRISPR reagents were microinjected at the following concentrations: Cas9 mRNA (100 ng/ $\mu$ L), single guide RNA (sgRNA) (50 ng/ $\mu$ L), and DNA oligo (50 ng/ $\mu$ L). Injected zygotes were transferred into pseudopregnant females, and resulting progeny were initially screened for potential recombination events via PCR.

The intronic loxP site was targeted first. PCR primers 5'-ATGAGTGGGAACACGAGAGC-3' and 5'-AGGCTGGCACTGAGATAGGA-3' were used to screen for loxP insertion. PCR products were cloned for sequencing using the TOPO TA cloning kit (450071; Thermo Fisher). Male mice validated to contain correctly targeted loxP sequence from the first round of injection were used as stud males for targeting of the 3' region of *Hoxd11* exon 2. PCR primers 5'-AAAGCAATTTGCCACCCTGC-3' and 5'-ACAGGTAAACCAATGCCCAGA-3' were used to screen for loxP insertion at the 3' region of the *Hoxd11* exon 2. Targeting was verified by PCR and sequencing as above. Animals (male or female) confirmed to contain two correctly targeted loxP sites were mated to WT Bl6 animals, and genotyping analyses of the resulting progeny using the PCR primers indicated above were used to screen for germline transmission and the presence of both loxP sites in cis along the chromosome.

### **Tamoxifen Treatment**

Mice were fed on tamoxifen chow (TD. 130860; Envigo) at 8 to 10 wk of age for a duration of 3 wk. Based on approximate daily food intake of 4 g per mouse<sup>196</sup> and body weight of 20 to 25 g, mice consumed a concentration of 40 mg/kg tamoxifen per day. The chow was replaced weekly. Both control and conditional mutants were fed on tamoxifen chow.

### **Bone Tissue Preparations**

Mice were killed, and both forelimb zeugopod skeletons were collected by dissecting off the soft tissue, taking care not to disturb the periosteum. All bones were then fixed shaking in 4% paraformaldehyde (PFA) for 2 d at 4 °C and then scanned for microCT if required. Specimens for frozen sections were decalcified in 14% ethylenediaminetetraacetic acid (EDTA) for 7 d and equilibrated in 30% sucrose overnight prior to embedding in OCT media. Cryosections were collected at 10 to 12  $\mu\text{m}$  using the Kawamoto tape method.<sup>197</sup> Specimens for paraffin sections were decalcified in 14% EDTA for 7 d and dehydrated in 70% ethanol prior to overnight paraffin processing. Paraffin sections were collected at 5  $\mu\text{m}$ .

### **Histology, Immunohistochemistry, and Histomorphometry**

For all experiments presented, four to eight animals from each genotype were examined. Sample size was determined based on previous literature and our previous experiments. Feasible generation of experimental animals was considered. As *Hox11* expression within the zeugopod skeleton is higher in the ulna compared to the radius, all detailed analyses were carried out in the ulna. Histological stains were performed using standard methods.<sup>198</sup> Paraffin sections were deparaffinized and rehydrated by incubating in xylene, followed by a series of washes in decreasing ethanol content (100%, 95%, 70%, ddH<sub>2</sub>O). Hematoxylin/eosin (H&E) stains were processed as previously reported.<sup>198</sup> Tartrate-resistant acidic phosphatase (TRAP) staining (387A-1KT; SigmaAldrich) and picosirius red stain (ab150681; Abcam) were performed according to the manufacturer's protocol. For the visualization of the osteocyte lacunocanalicular network, the

bone sections were processed as previously reported with minor modifications.<sup>199</sup> All histological images were acquired on an Eclipse E800 microscope (Nikon).

For immunostaining, cryosections were blocked with 5% donkey serum and incubated with primary antibodies overnight at 4 °C against osterix (ab22552, 1: 300; Abcam), osteopontin (AF808, 1:200; R&D Systems), and osteocalcin (DS-PB-01521, 1:200, antibody no longer commercially available; RayBiotech). Secondary antibodies were incubated at room temperature for 1 h: donkey-anti-rabbit–Alexa Fluor 647 (A31573, 1:500; Thermo Fisher) and donkey-anti-goat–Alexa Fluor 488 (A11055, 1:500; Thermo Fisher). SOST was visualized using a modified signal amplification protocol. Sections were incubated in SOST (AF1589, 1:100; R&D Systems) overnight at 4 °C followed by donkey-anti-goat–biotin secondary (705-067-003, 1:400; Jackson ImmunoResearch). The biotinylated secondary was detected using the Vectastain Elite ABC kit (PK-6100; Vector Laboratories), and the signal was amplified by Alexa Fluor 488 Tyramide reagent (B40853; Thermo Fisher). Endogenous *Hoxa11eGFP* fluorescence was quenched after the decalcification process and was visualized using chicken-anti-GFP (ab13970, 1:1,000; Abcam) and donkey-anti-chicken–Alexa Fluor 488 (A11039, 1:500; Invitrogen). All fluorescent images were acquired on a Leica Upright SP5x two-photon confocal microscope. Confocal z-stacks were captured through entire sections at a thickness of 1 to 2 μm, and images were stacked using Photoshop. Large images were stitched (when necessary) using Photoshop.

Fluorophore-labeled CMP and CI were synthesized as described previously (20). Briefly, Cy5CMP has the sequence: Cy5-Gly-(SerGly)<sub>2</sub>-(flpHypGly)<sub>7</sub>-OH, where flp refers to (2S,4S)-4-fluoroproline and Hyp refers to (2S,4R)-4-hydroxyproline. Cy5CI has the sequence: Cy5-Gly-(SerGly)<sub>2</sub>-(HypFlpGly)<sub>7</sub>-OH. Paraffin bone sections were stained in the dark for 1 h at room temperature and then washed with 1× phosphate-buffered saline (PBS) followed by imaging.

### **MicroCT and Quantification of Images**

MicroCT analyses were performed using a lab microCT (Skyscan 1176; Bruker, Billerica, MA, USA) at 9  $\mu\text{m}$  isotropic resolution utilizing a  $0.3^\circ$  rotation step, 0.5 mm aluminum filter, and 2 frame averaging. Data from the microCT scans were processed and analyzed using MicroView (v2.1.2 Advanced Bone Application; GE Healthcare Preclinical Imaging).

Quantification of osteocytes and tdTomato<sup>+</sup>/SOST<sup>+</sup> cells were obtained by taking three 40X images at the distal, medial, and proximal region along the ulna and the cells were manually quantified using ImageJ. An average among the three regions was calculated for each animal. Quantification of the ellipsoid osteocytes were performed by manually quantifying ellipsoid osteocytes and all osteocytes within the normal and abnormal bony matrix in a 40X image of the ulna to calculate the percentage of ellipsoid-shaped osteocytes. Quantification of osteoclasts was performed using the Bioquant Osteo software V17.2.6 (Bioquant Image Analysis Corp., Nashville, TN) according to standard procedures<sup>1</sup>.

### **Skeletal Preparations**

E17.5 embryos were skinned and eviscerated, fixed in 100% ethanol overnight then in acetone overnight. Specimens were stained with Alcian blue in a solution containing 15mg Alcian blue (Alcian blue 8GX, Sigma, A5268), 80ml of 95% ethanol and 20ml of glacial acetic acid up to two days. The skeletons were rinsed in 100% ethanol overnight and cleared in 2% KOH for 3 hrs. The specimens were transferred into alizarin red staining solution with 50mg/L alizarin red (Alizarin Red S, Sigma, A5533) in 2% KOH for 3-5 hrs. The tissue was then cleared in 1% KOH with 20% glycerol and transferred through an increasing glycerol series (20%, 50%, 80%), finally into 100% for long-term storage.

### **qRT-PCR for *Hoxd11* Expression**

To analyze deletion of *Hoxd11* following recombination, control and *Hox11* conditional mutant were collected after 1-month following the initiation of deletion. The soft tissue from both

forelimb zeugopod skeletons were removed and the bone marrow was flushed from both the radius and ulna into 1ml of digestion buffer (2mg/ml of collagenase type IV (Thermo Scientific, 17104-019) and 3mg/ml of dispase II (Thermo Scientific, 17105-041) in 1X PBS) using a 30G needle. The bones were subsequently minced with a razor in a petri dish under a tissue culture hood and the resulting pulp was transferred into digestion buffer with the flushed bone marrow. Three digestion steps were carried out at 37°C with periodic agitation to obtain a single cell suspension. After each period of digestion, cells in suspension were collected into cell culture media containing DMEM with 4.5 g/L D-glucose (Gibco), 1X Glutamax (Gibco), 1mM sodium pyruvate (Gibco), 15% fetal bovine serum (FBS), 100 mg/mL streptomycin, and 100 U/mL penicillin. Red blood cells were lysed on ice at a final concentration of 0.5X. The cells were then strained through a 100µM cell strainer and plated. The cells were expanded, passaged twice, then subsequently sorted by a MA900 (Sony) cell sorter to obtain *Hoxd11*eGFP-expressing cells. RNA was extracted using the Qiagen RNeasy micro kit (Qiagen, 74004) and cDNA was synthesized using Superscript™ (Thermo Fisher, 11904018). *Hoxd11* expression was measured relative to GAPDH. qPCR was performed with the following primer set using Roche PowerUp™ SYBR™ Green Mastermix: *Hoxd11R* AGTGAGGTTGAGCATCCGAG, *Hoxd11F* ACA CCAAGTACCAGATCCGC. ΔCt values were calculated relative to GAPDH.



## **Part II**

### **Chapter 1**

#### **Acceleration of 1,3-Dipolar Cycloadditions by Integration of Strain and Electronic-Tuning**

Jesús M. Dones, Nile S. Abularrage, Namrata Khanal, Brian Gold, and Ronald T. Raines

Submitted for Publication

#### Contributions

Namrata Khanal and Brian Gold performed all the computational studies. Jesús M. Dones, Nile S. Abularrage, and Brian Gold planned experiments and drafted the original manuscript and figures. Jesús M. Dones and Nile S. Abularrage performed all the experiments and data analysis. Ronald T. Raines planned experiments and edited the manuscript and figures.

### 2.1.1 Abstract:

The 1,3-dipolar cycloaddition between azides and alkynes is enabling new means to probe and control biological processes. A major challenge is to achieve high reaction rates with stable reagents. The optimization of alkynyl reagents has relied on two strategies: increasing strain and tuning electronics. We report on the integration of these strategies. A computational analysis suggested that a CH→N aryl substitution in dibenzocyclooctyne (DIBO) could be beneficial. In transition states, the nitrogen of 2-azabenzobenzocyclooctyne (ABC) engages in an n→π\* interaction with the C=O of α-azidoacetamides and forms a hydrogen bond with the N–H of α-diazoacetamides. These interactions act cooperatively with electronic activation of the strained π-bond to increase reactivity. We found that 2-azabenzobenzocyclooctyne (ABC) reacts more quickly with α-azidoacetamides and α-diazoacetamides than does its constitutional isomer, dibenzoazocyclooctyne (DIBAC). ABC and DIBAC have comparable chemical stability in a biomimetic solution. Both ABC and DIBO are accessible in three steps by the alkylidene carbene-mediated ring expansion of commercial cycloheptanones. Our findings enhance the accessibility and utility of 1,3-dipolar cycloadditions and encourage further innovation.

### 2.1.2 Introduction

The discovery of “spring-loaded”<sup>200</sup> but chemoselective reactions has transformed chemical biology, polymer chemistry, materials chemistry, and allied fields. In this realm, a particular 1,3-dipolar cycloaddition<sup>201</sup>—the strain-promoted azide–alkyne cycloaddition (SPAAC)<sup>202-204</sup>—has been at the forefront. Its preeminence is attributable to the attractive features of the azido group<sup>205-207</sup> along with the formation of an aromatic product,<sup>208, 209</sup> enabling high chemoselectivity.<sup>210, 211</sup>

Efforts to both understand<sup>212-221</sup> and optimize<sup>222-227</sup> SPAAC reactivity have focused on two general strategies: (1) increasing strain (*i.e.*, pre-distortion), and (2) tuning electronics (Figure 2.1.1A).<sup>228-230</sup> After the discovery of the reactivity of cycloalkynes in SPAAC in chemical

contexts,<sup>202-204</sup> the utility of OCT was demonstrated in a biological context.<sup>206</sup> Installing fluoro groups at the propargylic position via a 10-step synthetic route generated DIFO<sup>222</sup> and further increased reaction rates while compromising reagent stability.<sup>231</sup> Theoretical investigations attributed the higher reactivity to LUMO-lowering,<sup>213, 215</sup> though specific orbital interactions that elicit a low-energy transition state (TS) have become apparent.<sup>218, 219</sup> The exocyclic fluoro groups are *gauche* relative to the forming C–N bonds. In contrast, optimal orbital overlap (*i.e.*, anti-periplanar) is achievable with endocyclic heteroatoms. Studies in model systems<sup>232, 233</sup> and the subsequent substitution of heteroatoms into cyclooctynes such as diF-SNO-OCT and cyclononynes demonstrated the efficacy of this design principle.<sup>218, 219, 223, 225, 227</sup>

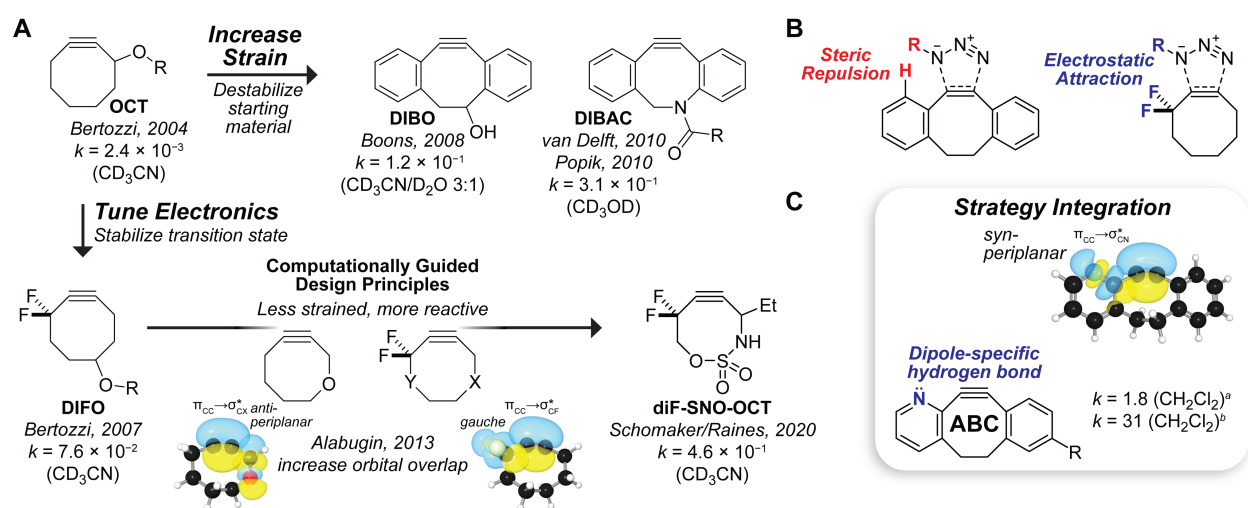


**Figure 2.1.1.** Optimization strategies employed to accelerate the strain-promoted cycloaddition reactivity of cyclooctynes. (A) Heteroatom-incorporation tunes alkyne electronics; benzannulation increases strain. (B) Cyclooctyne substitutions can engender steric repulsion or electrostatic attraction. (C) Strategic heteroatom placement in azabenzocyclooctyne (ABC) combines electronic-tuning with increasing strain while replacing steric repulsion with a potentially dipole-specific hydrogen bond. Second-order rate constants ( $\text{M}^{-1}\text{s}^{-1}$ ) are for the reaction with benzyl azide,<sup>230</sup> *N*-benzylazidoacetamide,<sup>a</sup> or *N*-benzyl diazoacetamide<sup>b</sup> (this work).

In parallel efforts, rate acceleration was pursued by increasing strain. In particular, benzannulation to give DIBO<sup>234</sup> and DIBAC<sup>235, 236</sup> led to reaction rates comparable to those attained with electronic tuning and without compromise to reagent stability (Figure 2.1.1 A). Computations revealed, however, steric repulsion between the incoming dipole and the “flagpole” C–H group (Figure 2.1.1 B).<sup>217</sup>

Limited success has been achieved in integrating electronic tuning with strain. The installation of remote heteroatoms has led to only incremental increases in reactivity<sup>237</sup> and compromised reagent stability.<sup>226, 238, 38</sup> Hence, reagents that harness both strategies are absent from the landscape.

We sought a hybrid cyclooctyne reagent for SPAAC. To begin, we performed computational analyses to guide reagent development. We discovered that a single C–H→N substitution at the “flagpole” position effects electronic activation in a dibenzocyclooctyne (Figure 2.1.1 C). Notably, the aryl  $\sigma^*_{\text{C-N}}$  of 2-azabenzobenzocyclooctyne (2-ABC) lies syn-periplanar relative to forming bonds, effectively stabilizing the transition state. Additional stabilization can be attained by dipole-specific hydrogen bonds between substituents on the dipole and the azabenzobenzocyclooctyne lone pair. This new class of cyclooctyne provides a rate for cycloadditions that surpasses those of commercially available cyclooctyne reagents with negligible impact on stability in the presence of biological nucleophiles.

### 2.1.3 Design of an Optimal Dipolarophile

Our goal was to identify a modification of the dibenzocyclooctyne scaffold to accelerate its 1,3-dipolar cycloaddition with azides and diazo compounds. We focused our computations on nitrogen substitution, as the valency of nitrogen enables an isologous C–H→N substitution within a benzo group. In accordance with recent studies,<sup>221, 239</sup> we used Gaussian 16 to employ both the M06-2X level of theory<sup>240, 241</sup> with the 6-311++G(d,p) basis set (including the IEFPCM solvation) and the B97D level of theory<sup>242</sup> with the 6-311+G(d,p) basis set (including the CPCM solvation

model). First, we modeled the 1,3-dipolar cycloaddition reactions of both *N*-methylazidoacetamide (**1**) and *N*-methyldiazoacetamide (**2**) with DIBO and DIBAC, as well as a series of constitutional isomers of DIBAC: azabenzobenzocyclooctynes (ABCs; Tables 2.1.1, 2.1.S1, and 2.1.S2).

We found that installing a nitrogen in DIBO can lower the predicted energy barriers for cycloaddition with dipoles **1** and **2** (Table 2.1.1). Negligible differences in activation energies ( $\Delta E^\ddagger$ ) and free energies of activation ( $\Delta G^\ddagger$ ) were observed for 3-, 4-, and 5-ABC in their reactions with dipoles **1** and **2**. In contrast, 2-ABC and 6-ABC were predicted to be more reactive than the other constitutional isomers. Notably, 2-ABC and 6-ABC contain a propargylic C–N bond that enables a direct interaction between the alkyne  $\pi$ -bond and the C–N antibonding orbital ( $\sigma^*_{\text{C-N}}$ ).<sup>219</sup> Interestingly, the preferred regioisomeric transition states generally favored the *anti* approach of substituents on **1** or **2** relative to the azabenzobenzocyclooctyne group in all reactions except that with 2-ABC.

**Table 2.1.1.** Effect of nitrogen placement in dibenzocyclooctynes. Activation parameters (kcal/mol) were calculated at the M06-2X/6-311++G(d,p) employing the IEFPCM solvation model (water). Preferred regioisomers are indicated with energies in bold typeface.

		Me-NH-C(=O)-CH <sub>2</sub> -N <sub>3</sub> <b>1</b>		Me-NH-C(=O)-CH=N <sub>2</sub> <b>2</b>	
		<i>syn</i> TS	<i>anti</i> TS	<i>syn</i> TS	<i>anti</i> TS
<b>DIBO</b>		$\Delta E^\ddagger$ : 10.3	—	10.6	—
	CH <sub>2</sub> →NH	$\Delta G^\ddagger$ : 23.7	—	23.7	—
<b>DIBAC</b>		$\Delta E^\ddagger$ : 9.6	<b>9.1</b>	10.1	<b>8.9</b>
	constitutional isomers	$\Delta G^\ddagger$ : 23.3	<b>22.9</b>	23.3	<b>22.1</b>
<b>2-ABC</b>		$\Delta E^\ddagger$ : <b>8.3</b>	10.5	<b>6.2</b>	10.6
		$\Delta G^\ddagger$ : <b>21.9</b>	23.8	<b>19.5</b>	23.7
<b>3-ABC</b>		$\Delta E^\ddagger$ : 10.0	<b>9.7</b>	10.0	<b>9.8</b>
		$\Delta G^\ddagger$ : 23.5	<b>23.2</b>	22.8	<b>22.8</b>
<b>4-ABC</b>		$\Delta E^\ddagger$ : 9.8	<b>9.6</b>	9.9	<b>9.8</b>
		$\Delta G^\ddagger$ : 23.3	<b>22.9</b>	22.7	<b>22.9</b>
<b>5-ABC</b>		$\Delta E^\ddagger$ : 10.1	<b>9.7</b>	10.3	<b>10.0</b>
		$\Delta G^\ddagger$ : 23.5	<b>23.1</b>	23.2	<b>23.2</b>
<b>6-ABC</b>		$\Delta E^\ddagger$ : 8.6	<b>7.7</b>	7.1	<b>6.8</b>
		$\Delta G^\ddagger$ : 22.1	<b>21.3</b>	22.7	<b>19.7</b>

Comparing optimized geometries and NBO charges on each alkyne carbon of DIBO, DIBAC, 2-ABC, and 6-ABC illustrates the effects of a direct  $\pi_{CC} \rightarrow \sigma^*_{C-N}$  interactions between the alkyne and propargylic acceptors (Figure 2.1.2). Both 2-ABC and 6-ABC display greater asymmetry and polarization as a result of the proximal C–N bonds. In 2-ABC, the syn-periplanar orientation of the C–N acceptor (relative to the obtuse lobe of the bent alkyne) provides 5.7 kcal/mol of  $\pi_{CC} \rightarrow \sigma^*_{C-N}$  stabilization, whereas the anti-periplanar orientation in 6-ABC provides 6.6 kcal/mol, quantified via the second-order perturbation of NBO analysis from NBO 7.0 software (Figure 2.1.2 B).<sup>243</sup> The relatively minor difference in interaction energies, despite the formal charge on the nitrogen in 6-ABC, is in agreement with previous computational studies in which the syn-periplanar geometry was found to offset the energy cost of symmetric bending nearly as efficiently as the anti-periplanar geometry in 1-fluoro-2-butyne.<sup>218</sup> These direct

interactions between the alkyne  $\pi$ -bond and the propargylic C–N bonds in 2-ABC and 6-ABC account for the asymmetry and alkyne polarization.

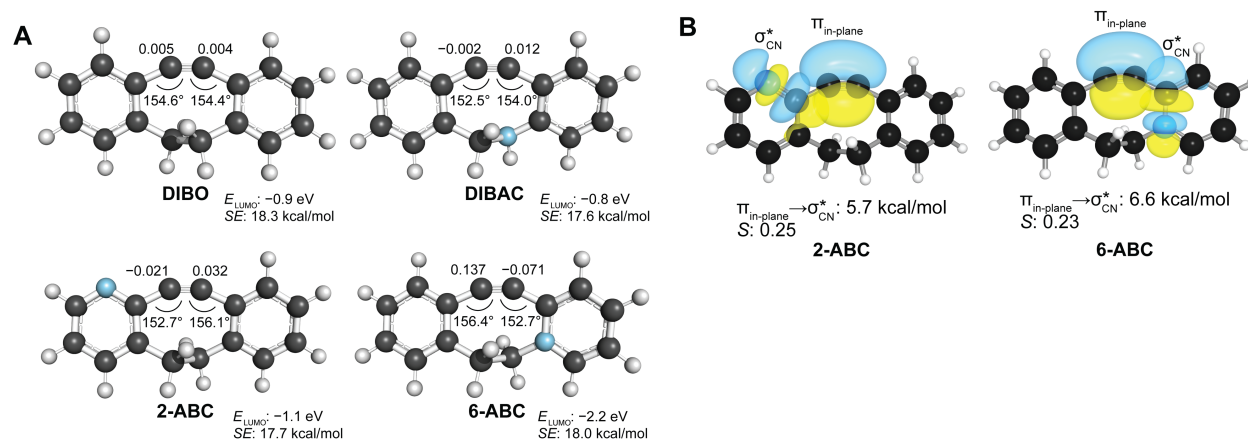


**Figure 2.1.2.** Combining increased strain with electronic activation. (A) Optimized geometries and NBO charge on the alkynyl carbons of DIBO, DIBAC, 2-ABC, and 6-ABC calculated at the M06-2X/6-311++G(d,p) employing the IEFPCM solvation model (water). (B) Interactions of the distorted alkyne with the syn-periplanar C–N bond in 2-ABC and the anti-periplanar C–N bond in 6-ABC. Shown are natural bonding orbitals depicting  $\pi_{\text{CC}} \rightarrow \sigma_{\text{CN}}^*$  interactions, second-order perturbations energies, and PNBO overlap integrals ( $S$ ). Strain energies ( $SE$ ) were calculated with the isodesmic equation in Figure 2.1.S3.<sup>216</sup>

Although the propargylic C–N bonds 2-ABC and 6-ABC lower the barriers to cycloaddition with azide **1** and diazo compound **2**, the two dipoles are affected differentially. For instance, the barrier for the reaction of azide **1** with 2-ABC is  $\sim 0.6$  kcal/mol higher in energy than is its reaction with 6-ABC (21.9 versus 21.3 kcal/mol), whereas the same comparison with diazo compound **2** shows a decrease of 0.2 kcal/mol (19.5 for 2-ABC versus 19.7 kcal/mol for 6-ABC).<sup>244</sup> Such differences can be exploited to develop chemoselective reactions between similar dipoles that are mutually orthogonal.<sup>225, 245, 246</sup>

To understand the reactivity of 2-ABC with the intent of exploiting differential reactivity toward different dipoles, we employed distortion/interaction (strain–activation) analysis.<sup>212, 214, 247-249</sup> In particular, we sought to compare the reactivity of 2-ABC to that of DIBO and DIBAC (Figure 2.1.3, Tables 2.1.S3–4). We found that the transition states for the reaction of each dipole with 2-ABC displayed the strongest interactions (–10.9 and –14.3 kcal/mol for **1**–2-ABC-TS and **2**–2-ABC-TS, respectively). Diazoacetamide **2** also provides a decrease in distortion energies for both the dipole (16.8 kcal/mol) and the cyclooctyne (3.7 kcal/mol) in **2**–2-ABC-TS relative to both **2**–DIBO-TS and **2**–DIBAC-TS. Meanwhile, azidoacetamide **1** displays its highest dipole distortion energy in **1**–2-ABC-TS (18.9 kcal/mol),<sup>250</sup> whereas the alkyne distortion energy (3.4 kcal/mol) is between that of **1**–DIBO-TS and **1**–DIBAC-TS. The transition state for the reaction of azide **1** and 2-ABC has a high distortion energy (18.9 kcal/mol; Figure 2.1.3). This energy arises from torsion of the acetamide group relative to that in **1**–DIBO-TS and **1**–DIBAC-TS (18.7 and 17.6 kcal/mol, respectively). This torsion sacrifices interactions between the acetamide carbonyl and the azido group ( $n_{\text{O}} \rightarrow \pi^*_{\text{NN}}$ : 0.7 kcal/mol); however, the loss of stabilization within azide **1** allows for the formation of a hydrogen bond in **1**–2-ABC-TS. An N $\cdots$ H distance of 2.05 Å was found between the aryl nitrogen of 2-ABC and the N–H hydrogen of azide **1** (Figures 2.1.3 A and 2.1.4). In **2**–2-ABC-TS, an N $\cdots$ H distance of 2.17 Å was observed, and that transition state resembles **2**–DIBO-TS and **2**–DIBAC-TS. Meanwhile, azidoacetamide **1** displays both a dipole distortion energy (16.6 kcal/mol) and an alkyne distortion energy (2.6 kcal/mol) in **1**–2-ABC-TS that are similar to those in **1**–DIBAC-TS.



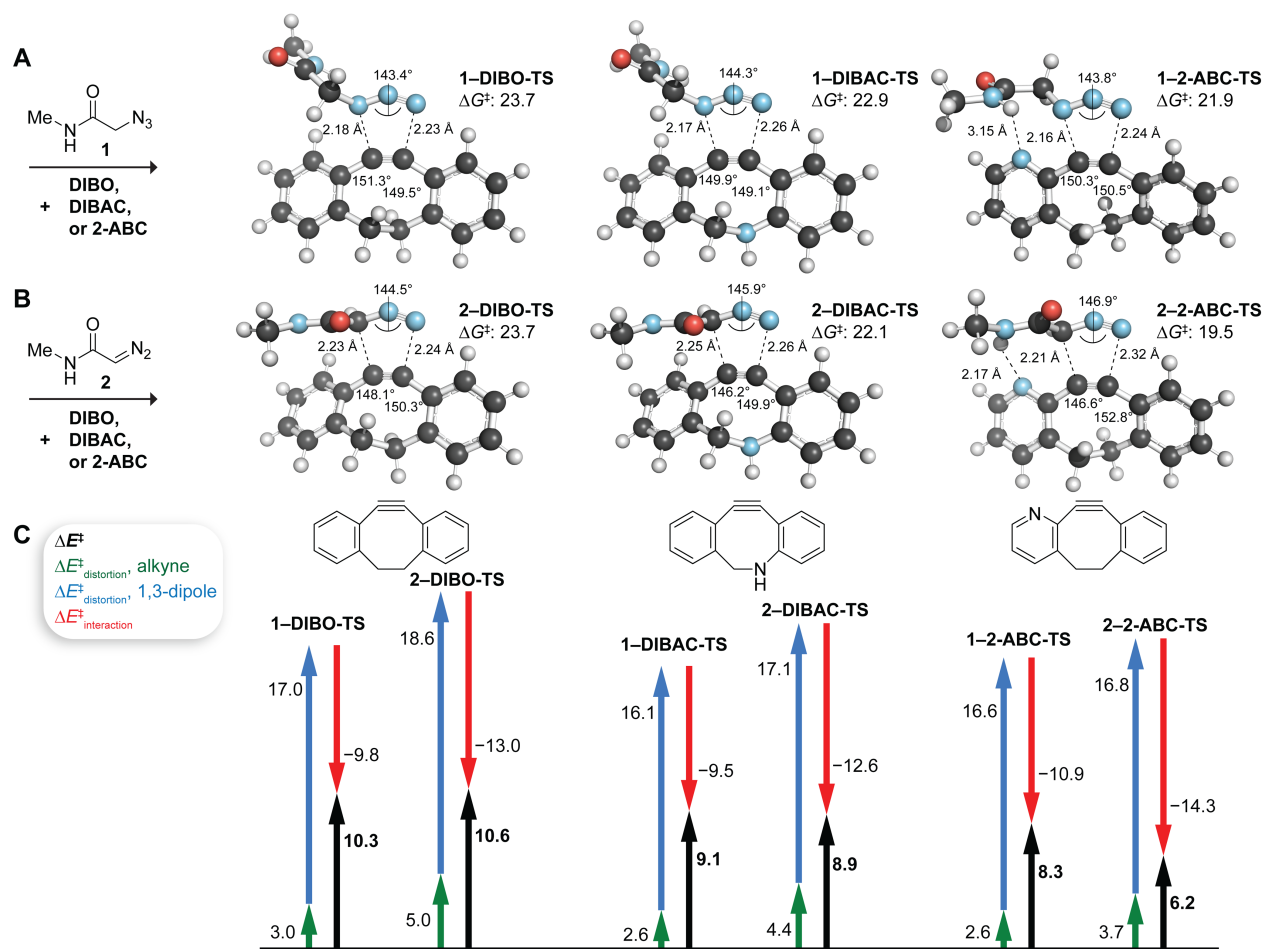


**Figure 2.1.3.** Computational analysis of cycloadditions with *N*-methylazidoacetamide (1) and *N*-methyl diazoacetamide (2). (A,B) Optimized transition state geometries and free energies of activation (kcal/mol) calculated at the M06-2X/6-311++G(d,p) level employing the IEFPCM solvation model (water). (C) Distortion/Interaction (Strain–Activation) analysis.

The origins of the favorable distortion and interaction energies for both 2-ABC transition states became apparent upon inspection of optimized geometries (Figures 2.1.3 and 2.1.4). The propargylic C–N bond within 2-ABC facilitates bond formation,<sup>219</sup> resulting in shortened incipient bonds at the internal N/C within the 2-ABC-TS relative to the corresponding DIBO-TS and DIBAC-TS, for each 1,3-dipole.

Interactions between the aryl nitrogen in 2-ABC and the acetamide in both dipoles **1** and **2** are evident from large interaction energies in optimized transition state geometries. In addition, 2-

ABC is the sole constitutional isomer in which the *syn* approach of substituents on the incoming dipole relative to the azabenzene ring is favored for both azide **1** and diazo compound **2** (Scheme 1). Having found that interactions in both **1**–2-ABC-TS and **2**–2-ABC-TS enable each dipole to overcome alkyne polarization in 2-ABC (Figure 2.1.2), we next examined the nature of the interactions that enhance cycloaddition reactivity.

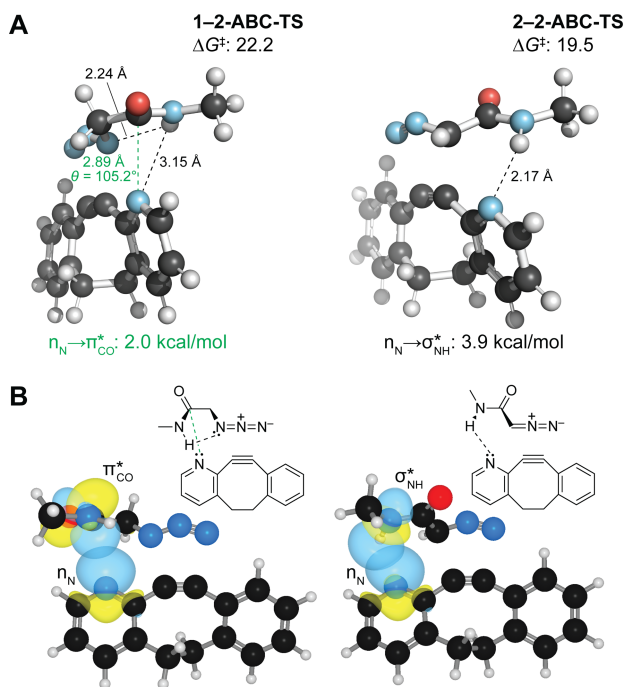


**Figure 2.1.4.** Comparison of interactions in 2-ABC cycloadditions with *N*-methylazidoacetamide (**1**) and *N*-methyldiazoacetamide (**2**). (A) Second-order perturbations (black) and steric repulsion (red) obtained from the NBO analysis. (B) Key stabilizing orbital interactions:  $N \cdots C=O$   $n \rightarrow \pi^*$  interaction with azide **1** and  $N \cdots H-N$  hydrogen bond with diazo compound **2**.

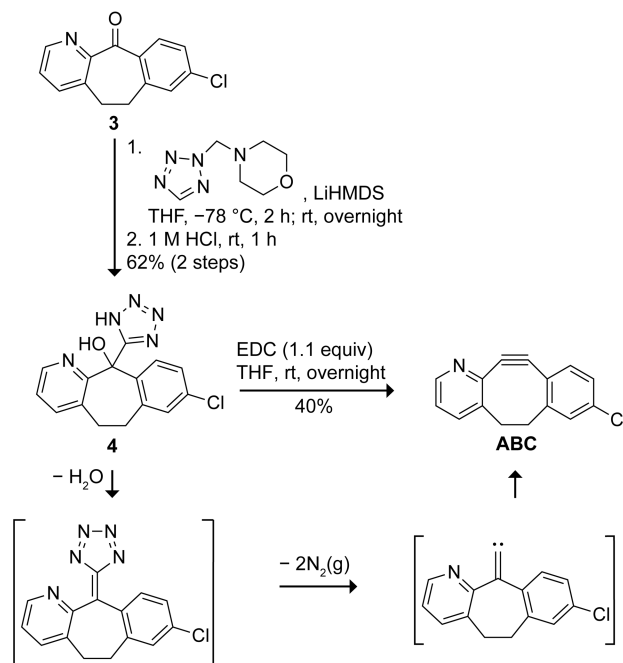
We found that azide **1** adopts a conformation containing an intramolecular  $N \cdots H-N$  hydrogen bond within a 5-membered ring. That hydrogen bond is retained in **1**–2-ABC-TS (Figure 2.1.4). There, significant stabilization via an  $n_N \rightarrow \pi_{C=O}^*$  interaction from the aryl nitrogen to the acetamide carbonyl of azide **1** is apparent from an  $N \cdots C=O$  distance of 2.89 Å,  $N \cdots C=O$  angle of  $105.2^\circ$ , and energy of 2.0 kcal/mol (Figure 2.1.4). Such an  $n \rightarrow \pi^*$  interaction<sup>251</sup> is unprecedented

in an SPAAC. In contrast to azide **1**, diazo compound **2** does not form an intramolecular hydrogen bond. Instead, we found an intermolecular hydrogen bond with N $\cdots$ H–N distance of 2.17 Å and energy of 3.9 kcal/mol in **2**–**2**-ABC-TS. That strong hydrogen bond leads to a lower activation barrier for diazoacetamide **2** than azide **1**.

#### 2.1.4 Synthesis of ABC

When considering the available synthetic methods to access strained alkynes, we were challenged by the inherent limitations posed by an azabenzene group. Common routes to cyclooctynes rely on the synthesis of parent alkenes, dibromination, and subsequent elimination of HBr (2 $\times$ ), often require extended synthetic routes.<sup>230, 235, 236</sup> A possible circumvention is the Friedel–Crafts reaction of electron-rich benzyl phenyl ethers with tetrachlorocyclopropene, followed by hydrolysis to generate a biaryl cyclopropenone and UV irradiation to form a cycloalkyne.<sup>226</sup> Unfortunately, an azabenzene group is not compatible with Friedel–Crafts reactions. To overcome these challenges, we reasoned that we could harness the high energy inherent in an alkylidene carbene to accomplish a [1,2]-rearrangement that yields a strained alkyne (Scheme 1). Analogous to the Fritsch–Buttenberg–Wiechell rearrangement<sup>252-254</sup> (which is the second step of the Corey–Fuchs reaction<sup>255</sup>), we report the dehydrative fragmentation of 5-hydroxyalkyl-1*H*-tetrazoles, accessed via a strategy employing *N*-morpholinomethyl-5-lithiotetrazole that is generated *in situ*.<sup>256, 257</sup> Nucleophilic addition of *N*-morpholinomethyl-5-lithiotetrazole to commercially available ketone **3**, which is a precursor to the antihistamine loratadine (Claritin<sup>®</sup>),<sup>258</sup> proceeded smoothly in THF and afforded the corresponding 5-hydroxyalkyl-1*H*-tetrazole (**4**) in 62% yield after acid hydrolysis. Tetrazole adduct **4** was dehydrated with EDC in THF to give the tetraazafulvene intermediate, which expels dinitrogen rapidly to generate an unstable alkylidene carbene.<sup>259</sup> Its [1,2]-rearrangement<sup>260</sup> affords the desired cyclooctyne in 40% yield. Adventitiously, this opportunistic route to ABC affords a chloro group that is an ideal handle for functionalization through well-established aryl chloride coupling chemistry.<sup>261, 262</sup> We also applied

the alkylidene carbene ring-expansion strategy for the expedient synthesis of DIBO, and we anticipate its utility in the synthesis of other cycloalkynes as well.



**Scheme 1.** Synthesis of ABC and Putative Mechanism for the Alkylidene Carbene Ring-Expansion of the Intermediate.

### 2.1.5 Reactivity of ABC

With ABC in hand, we examined its 1,3-dipolar cycloaddition with common dipoles. We focused on *N*-benzylazidoacetamide (**5**) and *N*-benzyl diazoacetamide (**6**).<sup>245, 246, 250, 263, 264</sup> Notably, the acetamide NH in **5** and **6** could enable formation of a hydrogen bond with the nitrogen of ABC. We measured the rates for the reaction of dipoles **5** and **6** with ABC in both aprotic (CH<sub>2</sub>Cl<sub>2</sub>) and protic solvents (MeOH and PBS containing 2% v/v DMSO).<sup>265</sup> We assessed the depletion of ABC by using HPLC and calculated second-order rate constants from the slope of a plot of [ABC]<sup>-1</sup> versus time. As a benchmark, we also measured the rate of the reaction of DIBO with each dipole. We found the reaction rates with ABC were exceptionally high (Figure 2.1.5). In all solvent conditions, each acetamide dipole displayed rate constants with ABC that exceed those attainable with commercially available cyclooctyne reagents. In CH<sub>2</sub>Cl<sub>2</sub>, the rate constants are among the

highest reported for both SPAAC and the analogous diazoacetamide reaction. The strategic CH→N substitution that converts DIBO to ABC, leads to 1,200 and 30-fold rate increases with *N*-benzyl diazoacetamide (**5**) and *N*-benzylazidoacetamide (**6**), respectively.

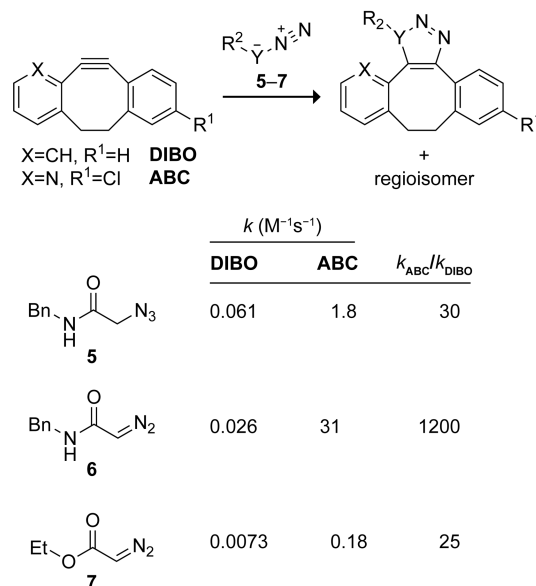


**Figure 2.1.5.** Second-order rate constants for the 1,3-dipolar cycloaddition of DIBO or ABC with dipoles **5–7** in  $CH_2Cl_2$ . Values are the mean from triplicate experiments.

A significantly larger rate constant for diazoacetamide **6** over the azidoacetamide **5** provides experimental corroboration of the computational predictions (Scheme 2.1.1 and Figure 2.1.4). With DIBO, the *N*-azidoacetamide reacts 2- to 3-fold faster than does the *N*-diazoacetamide, consistent with reactions of DIBAC<sup>245, 266</sup> and DIBONE.<sup>264</sup> Thus, the ~20-fold rate increase of *N*-benzyl diazoacetamide over *N*-benzyl azidoacetamide with ABC exceeds the difference observed with both DIBAC and DIBONE as well as with SNO-OCTs.<sup>223, 225</sup>

To assess the effect of the putative hydrogen bond, we tested the reactivity of ABC and DIBO with ethyl diazoacetate (**7**), which lacks a hydrogen bond donor. We found that the rate constant for the reaction of ABC with ester **7** was nearly 200-fold lower than that with amide **5**.

This decrease is substantially greater than the 4-fold decrease in rate constant for the reaction of these same dipoles with DIBO (Figure 2.1.5).

We also corroborated the existence of the hydrogen bond by comparing the regiochemistry of cycloadducts. To do so, we compared  $^1\text{H-NMR}$  spectra of the products of the cycloadditions of **5** and **6** with ABC to the  $^1\text{H-NMR}$  of the cycloaddition products of *N*-methylated derivatives of **5** and **6** with 2-ABC. Methylation of the amide in **5** and **6** impedes the formation of hydrogen bonds, allowing for direct comparison of its importance through their regioselectivity. As expected,  $^1\text{H-NMR}$  studies revealed that regioselectivity is attained only when a hydrogen bond is made in the transition state (Figure 2.1.6 A, Figure 2.1.S7).

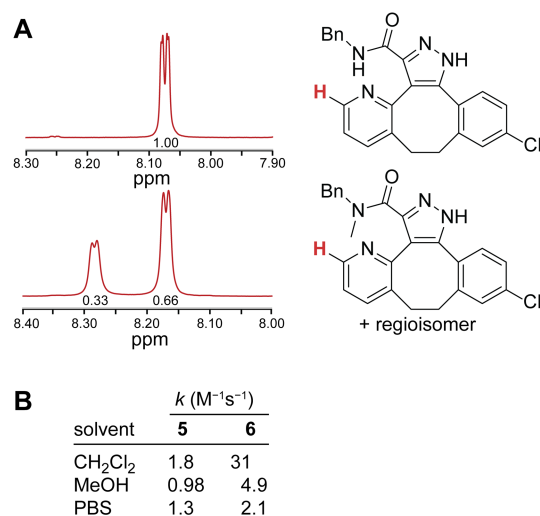


**Figure 2.1.6.** Effect of hydrogen bonding on the 1,3-dipolar cycloaddition of ABC with *N*-benzyl diazoacetamide (**6**). (A)  $^1\text{H-NMR}$  shifts of the C3-H (red) proton in the product of the cycloaddition of ABC with dipole **6** or its *N*-methyl derivative in  $\text{CH}_2\text{Cl}_2$ . (B) Second-order rate constants for the reaction of ABC with dipoles **5** and **6** in  $\text{CH}_2\text{Cl}_2$  (as in Figure 2.1.5), MeOH, and PBS containing DMSO (2% v/v). Values are the mean from triplicate experiments.

The use of protic solvents has little effect on the rate constant for the reaction of ABC with azide **5** but lowers the rate constant for the reaction with diazo compound **6** (Figure 2.1.6B). These

data are consistent with reports that protic solvents both strengthen and weaken aspects of  $n \rightarrow \pi^*$  interactions,<sup>267, 268</sup> like that in **1**-2-ABC-TS (Figure 2.1.4B), but weaken hydrogen bonding,<sup>269</sup> like that in **2**-2-ABC-TS (Figure 2.1.4B). Still, the reaction rates observed in protic solvents are among the highest reported for 1,3-dipolar cycloadditions.

We also corroborated the existence of an intramolecular hydrogen bond in an  $\alpha$ -azidoacetamide (Figure 2.1.4). Specifically, we found that azide **5** adopts a conformation containing an  $N \cdots H-N$  hydrogen bond within a 5-membered ring. That hydrogen bond is evident from the downfield chemical shift of the donor proton (6.60 ppm) compared with *N*-methyl acetamide (6.47 ppm).

To provide a benchmark for the general use of ABC in SPAAC, we performed a competition experiment. Specifically, we mixed 1 equiv of ABC with 1 equiv of both azide **5** and benzyl azide. The product ratios indicated preferential reaction with azide **5** (71:29 in  $CH_2Cl_2$  and 65:35 in MeOH), consistent with a favorable  $n \rightarrow \pi^*$  interaction in its TS (Figure 2.1.4) that is not accessible by benzyl azide. We conclude that  $\alpha$ -azidoacetamides (like azide **5**) are ideal for SPAAC with ABC but that other azides can react rapidly as well.

### 2.1.6 Stability of ABC

Finally, we sought to determine the stability of ABC in the presence of biological nucleophiles. To do so, we used a biomimetic concentration of glutathione,<sup>270</sup> which contains amino, carboxyl, and sulfhydryl groups. As a comparator, we used DIBAC. ABC and DIBAC were incubated in a solution of reduced glutathione (1 mM) and oxidized glutathione (0.2 mM) in PBS at 37 °C (Figure 2.1.S8). The rates of degradation of ABC and DIBAC under these conditions were comparable, with  $t_{1/2} = 1.9$  h and  $t_{1/2} = 3.8$  h, respectively.

### 2.1.7 Conclusion

### 2.1.7 Conclusion

In summary, computations were successful in guiding the design of ABC, which is the first known heterobiarylcylooctyne. Its combination of alkynyl strain and electronic tuning provides rate constants that are among the highest reported for an SPAAC. Moreover, the reaction of ABC with a diazo compound can be >10-fold faster than that with its azido analog, further expanding utility.

Our three-step synthetic route to ABC and DIBO is the first example of using an alkylidene carbene-mediated ring expansion to afford a strained alkyne. This expeditious route is shorter than that for accessing any other cyclooctyne used for SPAAC.<sup>230</sup>

ABC is the first iteration of a heterobiarylcylooctyne. Its desirable attributes encourage future iterations, including the incorporation of an azabenzene group into other cyclooctyne frameworks.

### 2.1.8 Computational Details

**Computational Details.** Geometry optimizations were performed with Gaussian 16 software<sup>S1</sup> at the M06-2X level of theory<sup>S2</sup> (including the IEFPCM dielectric continuum solvent model for either CH<sub>2</sub>Cl<sub>2</sub> or water, with UFF radii<sup>S3</sup>) or the B97D/6-311+G(d,p) level of theory<sup>S3</sup> (including the CPCM solvation model for either CH<sub>2</sub>Cl<sub>2</sub> or water<sup>S4,S5</sup>). Frequency calculations were performed to confirm stationary points as minima or first-order saddle points. All  $\Delta E$  and  $\Delta E^\ddagger$  values include zero-point corrections. For previous reports benchmarking the methods utilized, see ref. S6 and S7. Coordinates, total energies, and imaginary frequencies (transition states) are provided in the XYZ files.

**Conformational Search.** Due to conformational constraints, the cyclooctynes and 1,3-dipoles display relatively few degrees of freedom, allowing for manual conformational searches at the levels of theory specified above. Conformational searches were performed at both levels of theory, employing the specified solvation models for water. Low energy structures were re-



optimized in dichloromethane. For simplicity and brevity, tables contain the activation energies and free energies corresponding to located minima which display the most favorable free energy of activation. Figures S1 and S2 contain representative, low lying transition states located for 2-ABC and ABC.

**Starting materials:** In all cyclooctynes (other than DIBAC), rotation about the ethylene bridge gives an enantiomer and conformational analysis is unnecessary. For DIBAC, nitrogen inversion was considered. For diazoacetamides, the *s-cis* and *s-trans* conformers of the diazo group relative to the carbonyl were optimized. For azidoacetamides, rotation about the  $\psi$  ( $\text{NC}-\text{C}_\alpha\text{N}_3$  dihedral) and  $\phi$  ( $\text{CC}_\alpha-\text{NN}_2$ ) dihedral angles were examined via input geometries that varied in  $60^\circ$  increments. These input geometries converged on 2–3 structures, dependent upon the level of theory and solvation model, that were within  $\sim 0.5$ – $2.0$  kcal/mol.

**Azidoacetamide transition states:** Modes of approach considered the  $\psi$  and  $\phi$  dihedral angles described above and rotation about the dihedral angle about the azido group ( $\text{NN}-\text{NC}_\omega$ ). The cyclooctyne ring limits the latter to a potential range of  $\sim 180^\circ$  in the TS. For non-symmetric cyclooctynes (DIBAC and ABCs) both the *syn* and *anti* approach of the 1,3-dipole substituents relative to the aza-/azabenzene-ring were considered. For DIBAC, all of the above was considered, along with nitrogen inversion. Low energy transition states are included.

**Diazoacetamide transition states:** The above modes of approach were chosen as input geometries for each diazoacetamide conformation (*i.e.*, the *s-cis* and *s-trans* conformers). Minima were located for each transition state. Low energy transition states are included.

### 2.1.9 Acknowledgments

This work was supported by Grant R01 GM044783 (NIH). High-performance calculations made use of resources at the UNM Center for Advanced Research Computing, which is supported in part by the National Science Foundation. We would like to thank Brian J. Graham (Massachusetts Institute of Technology) and Matthew R. Aronoff (ETH–Zürich) for helpful

discussions. N.S.A. was supported by a Graduate Research Fellowship from the NSF (grant no. 1745302). Work at UNM was performed on the traditional homelands of the Pueblo of Sandia; for more information, see: <https://diverse.unm.edu/about/land-acknowledgement.html>

### 2.1.10 Experimental Procedure

#### General

All chemicals were from commercial sources and were used without further purification. NMR spectra were acquired with an Avance Neo 400 spectrometer or Avance Neo 500 spectrometer from Bruker (Billerica, MA, USA). Mass spectra were acquired by using positive ionization with an AccuTOF-DART 4G instrument from JEOL (Tokyo, Japan). HPLC experiments were carried out on a 1200 series HPLC from Agilent Technologies (Santa Clara, CA, USA) equipped with a Varian Microsorb-MV 100-5 C18 250 × 4.6 mm column. Gradients were run with water containing TFA (0.1% v/v) and ACN containing TFA (0.1% v/v). Absorbance was measured at 280 nm. Column chromatography was performed with an Isolera automated purification system from Biotage (Uppsala, Sweden) using prepacked SNAP KP silica gel columns. Thermostability was assessed with a Stanford Research Systems Optimelt automated melting point system.

The phrase “concentrated under reduced pressure” refers to the removal of solvents and other volatile materials using a rotary evaporator at water aspirator pressure (<20 Torr) while maintaining the water-bath temperature of 40 °C. Residual solvent was removed from samples by the vacuum (<0.1 Torr) achieved by a mechanical belt-drive oil pump.

All procedures were performed in air at ambient temperature (~22 °C) and pressure (1.0 atm) unless indicated otherwise.

#### Synthetic Methods

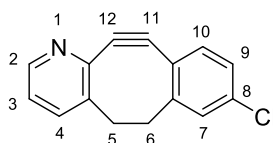
*N*-Benzylazidoacetamide (5) and *N*-benzyldiazoacetamide (6). These compounds were synthesized as reported previously.<sup>S264</sup>

*4-((N-Tetrazolyl)methyl)morpholine (8)*. To a cold (0 °C), stirred solution of tetrazole (0.70 g, 10.0 mmol, 1.0 equiv) in methanol (10 mL) was added morpholine (0.957 g, 0.95 mL, 11.0 mmol, 1.1 equiv), and the mixture was stirred for 15 min. An aqueous solution of 37% v/v formaldehyde (0.98 mL, 12.0 mmol, 1.2 equiv) was added dropwise, and the mixture was stirred overnight at room temperature. The reaction mixture was then concentrated under reduced pressure, and the residue was recrystallized from a 1:2 v/v mixture of CH<sub>2</sub>Cl<sub>2</sub> and hexanes to give compound **8** as a mixture of *N* tautomers, as white crystals (1.48 g, 8.74 mmol, 88 %). All spectral data matches published data.<sup>256</sup> **<sup>1</sup>H NMR** (400 MHz, CDCl<sub>3</sub>, δ): 8.67 (s, 0.2H), 8.56 (s, 0.8H), 5.53 (s, 1.6H), 5.31 (s, 0.4H), 3.82–3.61 (m, 4H), 2.69–2.65 (m, 3.2H), 2.62 (t, *J* = 4.7 Hz, 0.8H). **<sup>13</sup>C NMR** (101 MHz, CDCl<sub>3</sub>, δ): 152.69, 74.00, 66.64, 66.44, 49.85, 49.76. **HRMS** *m/z* calcd for C<sub>6</sub>H<sub>12</sub>N<sub>5</sub>O [M + H]<sup>+</sup>, 170.10364; found, 170.10408.

*8-Chloro-11-(1H-tetrazol-5-yl)-6,11-dihydro-5H-benzo[5,6]cyclohepta[1,2-b]pyridin-11-ol (4)*. To a stirred solution of 4-((*N*-tetrazolyl)methyl)morpholine (**8**) (0.70 g, 8.24 mmol, 2.0 equiv) and 8-chloro-5*H*-benzo[5,6]cyclohepta[1,2-*b*]pyridin-11(6*H*)-one (**3**) (0.5 g, 4.12 mmol, 1.0 equiv) in THF (10 mL), under N<sub>2</sub>(g) at –78 °C (acetone/CO<sub>2</sub>), was added 1 M LiHMDS in THF (4.33 mL, 4.33 mmol, 2.1 equiv) dropwise via a syringe. The reaction mixture was stirred for 2 h at –78 °C then allowed to warm to room temperature overnight. The reaction mixture was concentrated under reduced pressure, and the remaining residue was treated with aqueous HCl (1 M, 25 mL) and stirred at room temperature for 1 h. The solution was then extracted with EtOAc (3 × 50 mL), and the combined organic extracts were dried over Na<sub>2</sub>SO<sub>4</sub>(s), filtered, and concentrated under reduced pressure. The residue was purified by flash column chromatography on silica gel (hexanes/EtOAc 85:15→25:75) to provide compound **4** (672 mg, 2.14 mmol, 52%) as a white solid. **<sup>1</sup>H NMR** (500 MHz, chloroform-*d*, δ): 8.78 (s, 1H), 8.46 (s, 1H), 8.09 (dd, *J* = 8.4, 4.0 Hz, 1H), 7.64 (d, *J* = 7.6 Hz, 1H), 7.37 (d, *J* = 6.6 Hz, 1H), 7.25 (d, *J* = 8.9 Hz, 1H), 7.17 (s, 1H), 3.40–3.32 (m, 1H), 3.05–2.93 (m, 3H), 2.74–2.67 (m, 1H). **<sup>13</sup>C NMR** (126 MHz,

chloroform-*d*,  $\delta$ ): 161.98, 152.43, 143.57, 142.67, 141.72, 140.09, 138.54, 134.70, 134.38, 129.45, 127.21, 126.36, 124.64, 30.81, 29.95. **HRMS**  $m/z$  calcd for  $C_{15}H_{13}ON_5Cl$   $[M + H]^+$ , 314.08086; found, 314.08960.

*2-Azabenzot-8-chlorobenzocyclooctyne (ABC)*. To a stirred solution of compound **4** (0.514 g, 1.64 mmol, 1.0 equiv) in THF (5.0 mL), was treated with EDC (0.345 mg, 1.80  $\mu$ mol, 1.1 equiv) and allowed to react overnight. The reaction mixture was concentrated under reduced pressure, and the residue was purified by flash column chromatography on silica gel (hexanes/EtOAc 85:15 $\rightarrow$ 25:75) to provide ABC (157 mg, 0.66 mmol, 40%) as a pale yellow solid. mp: decomposition observed at  $\geq 80$  °C. **<sup>1</sup>H NMR** (500 MHz, chloroform-*d*,  $\delta$ ): 8.44 (dd,  $J = 5.0, 1.6$  Hz, 1H), 7.51 (dd,  $J = 7.6, 1.6$  Hz, 1H), 7.30–7.20 (m, 3H), 7.12 (dd,  $J = 7.7, 4.9$  Hz, 1H), 3.30–3.18 (m, 2H), 2.36 (ddq,  $J = 15.1, 8.5, 3.7$  Hz, 2H). **<sup>13</sup>C NMR** (126 MHz, chloroform-*d*,  $\delta$ ): 155.00, 148.55, 147.75, 144.65, 136.34, 134.52, 129.74, 127.45, 126.88, 121.97, 121.20, 113.31, 109.88, 35.62, 34.79. **HRMS**  $m/z$  calcd for  $C_{15}H_{11}NCl$   $[M + H]^+$ , 240.05800; found, 240.06485. The atom-numbering and IUPAC name of ABC is as follows:



8-chloro-5,6-dihydro-11,12-didehydrobenzo[5,6]cycloocta[1,2-*b*]pyridine

*5-(1H-Tetrazol-5-yl)-10,11-dihydro-5H-dibenzo[*a,d*][7]annulen-5-ol (9)*. To a stirred solution of compound **8** (0.70 g, 8.24 mmol, 2.0 equiv) and dibenzosuberone (0.25 g, 1.22 mmol, 1.0 equiv) in THF (5 mL), under  $N_2(g)$  at  $-78$  °C (acetone/ $CO_2$ ), was added 1 M LiHMDS in THF (2.56 mmol, 2.56 mL, 2.1 equiv) dropwise via a syringe. The reaction mixture was stirred for 2 h at  $-78$  °C then allowed to warm to room temperature overnight. The reaction mixture was concentrated under reduced pressure, and the remaining residue was treated with aqueous HCl (1 M, 25 mL) and stirred at room temperature for 1 h. The solution was then extracted with EtOAc (3  $\times$  50 mL), and the combined organic extracts were dried over  $Na_2SO_4(s)$ , filtered, and

concentrated under reduced pressure. The residue was purified by flash column chromatography on silica gel (2% v/v MeOH in CH<sub>2</sub>Cl<sub>2</sub>) to provide compound **9** (0.3596 g) as a white solid with some impurities but was used in the next step without further purification. <sup>1</sup>H NMR (400 MHz, MeOD, δ): 8.09–7.99 (m, 2H), 7.31–7.25 (m, 4H), 7.18–7.12 (m, 2H), 2.83 (s, 4H). <sup>13</sup>C NMR (101 MHz, MeOD, δ): 162.16, 141.12, 137.93, 130.25, 128.05, 125.83, 125.22, 71.82, 32.05. HRMS *m/z* calcd for C<sub>16</sub>H<sub>15</sub>ON<sub>4</sub> [M + H]<sup>+</sup>, 279.12458; found, 279.12665.

*Dibenzocyclooctyne (DIBO)*. A stirred solution of compound **9** (0.200 g, 0.72 mmol, 1.0 equiv) in CH<sub>2</sub>Cl<sub>2</sub> (4 mL) was treated with DIC (0.109 g, 0.86 mmol, 1.2 equiv) and allowed to react overnight. The reaction mixture was concentrated under reduced pressure and purified by flash column chromatography on silica gel (hexanes) to provide DIBO (0.072 g, 0.373 mmol, 51%) as a white solid. <sup>1</sup>H NMR (500 MHz, CDCl<sub>3</sub>, δ): 7.38–7.31 (m, 4H), 7.31–7.26 (m, 4aH), 3.38–3.29 (m, 2H), 2.50–2.40 (m, 2H). <sup>13</sup>C NMR (126 MHz, CDCl<sub>3</sub>, δ): 153.62, 129.41, 127.69, 126.52, 126.12, 123.95, 111.55, 36.47. HRMS *m/z* calcd for C<sub>16</sub>H<sub>13</sub> [M + H]<sup>+</sup>, 205.10172; found, 205.10245.

*N-Methyl-N-benzyl-2-bromoacetamide (10)*. To a stirred solution of *N*-methylbenzylamine (606 mg, 5 mmol, 1.0 equiv) and triethylamine (0.7 mL, 5 mmol, 1.0 equiv) in anhydrous CH<sub>2</sub>Cl<sub>2</sub> (10 mL) was added a solution of bromoacetyl bromide (1.06 g, 5.25 mmol, 1.05 equiv) in CH<sub>2</sub>Cl<sub>2</sub> (2 mL) dropwise at 0 °C. The resulting mixture was allowed to react for 4 h at room temperature. The reaction was quenched with saturated NaHCO<sub>3</sub> (10 mL) at 0 °C, extracted with diethyl ether (3 × 25 mL), washed with brine, dried over Na<sub>2</sub>SO<sub>4</sub>(s), filtered and concentrated under reduced pressure. The resultant crude material was used in subsequent steps without further purification.

*2-Azido-N-methyl-N-(phenylmethyl)acetamide (11)*. To a stirred solution of compound **10** (1.34 g, 5.53 mmol, 1 equiv) in DMF (25 mL), was added sodium azide (0.719 g, 11.06 mmol, 2.0 equiv) and the resulting mixture was allowed to react overnight at room temperature. A mixture of H<sub>2</sub>O/Et<sub>2</sub>O 1:1 was added to the reaction mixture, and the aqueous phase was extracted with Et<sub>2</sub>O

(3 × 25 mL), the organic extract was then washed with water (8 × 20 mL) and brine, and dried over Na<sub>2</sub>SO<sub>4</sub>(s). The resulting mixture was concentrated under reduced pressure, and the residue was purified by flash column chromatography on silica gel (hexanes/EtOAc 85:15→25:75) to provide compound **11** (0.351 g, 31%) as a colorless oil. <sup>1</sup>H NMR (500 MHz, chloroform-*d*, δ): 7.31 (ddd, *J* = 34.5, 19.6, 7.7 Hz, 5H), 7.15 (d, *J* = 7.5 Hz, 1H), 4.61 (s, 1H), 4.45 (s, 1H), 3.96 (d, *J* = 11.2 Hz, 2H), 3.01 (s, 1H), 2.86 (s, 2H). <sup>13</sup>C NMR (126 MHz, chloroform-*d*, δ): 167.29, 136.47, 135.57, 129.15, 128.73, 128.24, 128.00, 127.70, 126.21, 52.76, 51.25, 50.64, 50.51, 34.38, 33.88. HRMS *m/z* calcd for C<sub>10</sub>H<sub>13</sub>ON<sub>4</sub> [M + H]<sup>+</sup>, 205.10894; found, 205.11737.

*2-Diazo-N-methyl-N-(phenylmethyl)acetamide* (**12**). Compound **11** (0.120 g, 0.586 mmol, 1.0 equiv) was dissolved in H<sub>2</sub>O/THF 1:9 (20 mL). To this solution was added 2,5-dioxopyrrolidin-1-yl 3-(diphenylphosphanyl)propanoate (0.219 g, 0.615 mmol, 1.05 equiv), and the reaction mixture was stirred for 4 h at room temperature before a saturated aqueous solution of NaHCO<sub>3</sub> (15 mL) was added. The reaction mixture was then stirred vigorously for 3 h. The reaction mixture was diluted with brine and extracted with CH<sub>2</sub>Cl<sub>2</sub> (3×). The combined organic extracts were dried over Na<sub>2</sub>SO<sub>4</sub>(s), filtered, and concentrated under reduced pressure, and the residue was purified with silica gel chromatography (hexanes/EtOAc 50:50) to give (**12**) (33.3 mg, 29%). <sup>1</sup>H NMR (400 MHz, chloroform-*d*, δ): 7.40–7.21 (m, 5H), 5.01 (s, 1H), 4.65–4.38 (m, 2H), 2.89 (s, 3H). <sup>13</sup>C NMR (101 MHz, chloroform-*d*, δ): 166.14, 128.78, 127.55, 46.53, 34.33, 33.98, 25.64, 24.97. HRMS *m/z* calcd for C<sub>10</sub>H<sub>12</sub>ON<sub>3</sub> [M + H]<sup>+</sup>, 190.09804; found, 190.10475.

### Cycloaddition General Procedure A

Azides or diazo compounds were dissolved in anhydrous CH<sub>2</sub>Cl<sub>2</sub> (0.5 mL) in a scintillation vial at room temperature with stirring. To this solution was added a solution of cyclooctyne in anhydrous CH<sub>2</sub>Cl<sub>2</sub> (0.5 mL), and the reaction mixture was stirred overnight. The reaction mixture was concentrated under reduced pressure, and the residue was purified by flash column chromatography on silica gel (hexanes/EtOAc 85:15→25:75) to provide the desired product.

*ABC-N-Benzylazidoacetamide Cycloadduct (13)*. Following Cycloaddition General Procedure A, a solution of azide **5** (7.989 mg, 0.042 mmol) dissolved in anhydrous CH<sub>2</sub>Cl<sub>2</sub> was treated with ABC (10 mg, 0.042 mmol) to provide compound **13**. <sup>1</sup>H NMR (500 MHz, chloroform-*d*, δ): 8.27 (dd, *J* = 4.7, 1.6 Hz, 1H), 7.65 (dd, *J* = 7.9, 1.6 Hz, 1H), 7.53 (d, *J* = 8.2 Hz, 1H), 7.49 (t, *J* = 5.9 Hz, 1H), 7.35–7.18 (m, 8H), 5.26 (s, 2H), 4.47 (d, *J* = 5.7 Hz, 2H), 3.22 (dd, *J* = 8.3, 5.0 Hz, 2H), 3.13 (dd, *J* = 8.3, 5.0 Hz, 2H). <sup>13</sup>C NMR (126 MHz, chloroform-*d*, δ): 171.19, 165.82, 147.31, 144.97, 144.36, 140.34, 139.83, 137.80, 136.56, 134.59, 134.46, 132.25, 129.71, 128.70, 128.36, 127.68, 127.56, 126.93, 123.85, 52.64, 43.62, 34.24, 33.31. HRMS *m/z* calcd for C<sub>24</sub>H<sub>21</sub>ON<sub>5</sub>Cl [M + H]<sup>+</sup>, 430.14346; found, 430.16281.

*ABC-N-Benzyl diazoacetamide Cycloadduct (14)*. Following Cycloaddition General Procedure A, a solution of diazo compound **6** (7.358 mg, 0.042 mmol) dissolved in anhydrous CH<sub>2</sub>Cl<sub>2</sub> was treated with ABC (10 mg, 0.042 mmol) to provide compound **14**. <sup>1</sup>H NMR (500 MHz, chloroform-*d*, δ): 9.77 (s, 1H), 8.10 (dd, *J* = 4.8, 1.7 Hz, 1H), 7.66 (dd, *J* = 7.8, 1.7 Hz, 1H), 7.37–7.12 (m, 3H), 7.25 (m, 3H), 7.19 (d, *J* = 2.2 Hz, 1H), 7.15 (m, 2H), 4.58 (d, *J* = 5.2 Hz, 2H), 3.34–3.22 (m, 2H), 3.11 (d, *J* = 7.1 Hz, 2H). <sup>13</sup>C NMR (126 MHz, chloroform-*d*, δ): 159.67, 146.36, 139.54, 138.91, 137.34, 136.84, 134.22, 134.01, 130.07, 128.67, 127.81, 127.51, 126.46, 123.01, 43.92, 35.45, 32.34. HRMS *m/z* calcd for C<sub>24</sub>H<sub>20</sub>ON<sub>4</sub>Cl [M + H]<sup>+</sup>, 415.13256; found, 415.14917.

*ABC-2-Azido-N-methyl-N-(phenylmethyl)acetamide Cycloadduct (15)*. Following Cycloaddition General Procedure A, a solution of compound **11** (8.578 mg, 0.042 mmol) dissolved in anhydrous CH<sub>2</sub>Cl<sub>2</sub> was treated with 2-ABC (10 mg, 0.042 mmol) to provide compound **15** as regioisomers. <sup>1</sup>H NMR (500 MHz, chloroform-*d*, δ): 8.45 (dd, *J* = 4.7, 1.7 Hz, 1H), 8.37 (dd, *J* = 4.8, 1.6 Hz, 0.5H), 7.66 (ddd, *J* = 7.5, 5.6, 1.7 Hz, 2H), 7.55 (d, *J* = 8.3 Hz, 1H), 7.53 (d, *J* = 8.3 Hz, 1H), 7.41–7.33 (m, 2H), 7.25 (m, 8H), 7.13–7.07 (m, 1H), 6.94–6.86 (m, 2H), 5.73 (s, 3H), 4.58 (s, 1H), 4.46 (s, 2H), 3.35–3.30 (m, 3H), 3.27 (dd, *J* = 8.1, 4.7 Hz, 3H), 2.96 (s, 3H), 2.87 (s, 2H). <sup>13</sup>C NMR (126 MHz, chloroform-*d*, δ): 165.51, 165.25, 147.08, 146.98, 146.16, 146.03,

144.96, 144.93, 140.61, 139.37, 139.32, 136.84, 136.73, 136.29, 135.41, 134.77, 134.62, 134.16, 134.14, 132.42, 129.81, 129.78, 129.18, 128.88, 128.86, 128.62, 128.04, 127.75, 127.54, 126.68, 126.67, 126.29, 123.37, 123.31, 52.70, 51.28, 50.32, 50.11, 34.49, 34.02, 33.98, 33.88. **HRMS**  $m/z$  calcd for  $C_{25}H_{23}ON_5Cl$   $[M + H]^+$ , 444.15911; found, 444.18030.

*2-ABC-2-Diazo-N-methyl-N-(phenylmethyl)acetamide Cycloadduct (16)*. Following Cycloaddition General Procedure A, a solution of compound **12** (8.136 mg, 0.042 mmol) dissolved in anhydrous  $CH_2Cl_2$  was treated with 2-ABC (10 mg, 0.042 mmol) to provide compound **16** as regioisomers.  **$^1H$  NMR** (500 MHz, chloroform-*d*,  $\delta$ ): 8.43 (d,  $J = 4.7$  Hz, 1H), 8.34–8.27 (m, 0.59H), 7.51 (d,  $J = 7.5$  Hz, 2H), 7.35–7.20 (m, 12H), 7.16–7.03 (m, 3H), 4.69 (s, 3H), 3.25–3.19 (m, 2H), 3.19–3.09 (m, 5H), 2.89 (s, 2H), 2.87 (s, 3H).  **$^{13}C$  NMR** (126 MHz, chloroform-*d*,  $\delta$ ): 164.85, 164.36, 149.68, 149.43, 146.90, 143.64, 143.39, 141.45, 139.26, 136.76, 136.51, 134.97, 134.83, 133.86, 131.49, 129.94, 129.81, 128.56, 128.49, 128.23, 128.14, 127.59, 127.39, 127.32, 126.76, 122.05, 121.92, 121.07, 54.84, 50.94, 36.07, 34.66, 34.45, 33.61, 33.53, 32.82. **HRMS**  $m/z$  calcd for  $C_{25}H_{22}ON_4Cl$   $[M + H]^+$ , 429.14821; found, 429.16635.

*ABC-Ethyl diazoacetate Cycloadduct (17)*. Following Cycloaddition General Procedure A, a solution of compound **7** (4.792 mg, 0.042 mmol) dissolved in anhydrous  $CH_2Cl_2$  was treated with ABC (10 mg, 0.042 mmol) to provide (**17**).  **$^1H$  NMR** (500 MHz, chloroform-*d*,  $\delta$ ): 8.46 (dd,  $J = 4.7, 1.7$  Hz, 1H), 7.56 (d,  $J = 7.8$  Hz, 1H), 7.26 (d,  $J = 8.3$  Hz, 1H), 7.20 (d,  $J = 2.2$  Hz, 1H), 7.17–7.12 (m, 2H), 4.27 (q,  $J = 7.1$  Hz, 2H), 3.14 (q,  $J = 4.0$  Hz, 4H), 1.19 (t,  $J = 7.1$  Hz, 3H).  **$^{13}C$  NMR** (126 MHz, chloroform-*d*,  $\delta$ ): 159.93, 147.02, 140.57, 137.99, 134.84, 134.63, 132.06, 130.18, 129.21, 126.63, 122.63, 61.27, 34.65, 33.07, 13.95. **HRMS**  $m/z$  calcd for  $C_{19}H_{17}O_2N_3Cl$   $[M + H]^+$ , 354.10093; found, 354.11700.

*DIBO-N-Benzylazidoacetamide Cycloadduct (18)*. Following Cycloaddition General Procedure A, a solution of azide **5** (7.989 mg, 0.042 mmol) dissolved in anhydrous  $CH_2Cl_2$  was treated with DIBO (10 mg, 0.042 mmol) to provide compound **18**.  **$^1H$  NMR** (500 MHz,



chloroform-*d*,  $\delta$ ): 7.55–7.48 (m, 1H), 7.41–7.17 (m, 12H), 7.14 (dd,  $J = 7.4, 1.2$  Hz, 1H), 5.16 (d,  $J = 16.4$  Hz, 1H), 5.03 (d,  $J = 16.6$  Hz, 1H), 4.53 (dd,  $J = 14.7, 6.0$  Hz, 1H), 4.43 (dd,  $J = 14.9, 5.4$  Hz, 1H), 3.35 (td,  $J = 12.1, 10.3, 4.5$  Hz, 1H), 3.15–3.03 (m, 2H), 2.92–2.81 (m, 1H).  $^{13}\text{C}$  NMR (126 MHz, chloroform-*d*,  $\delta$ ): 165.43, 147.01, 141.71, 137.85, 137.27, 135.18, 131.70, 130.92, 130.46, 130.25, 129.23, 129.01, 128.81, 128.41, 127.77, 127.72, 126.80, 126.13, 125.14, 51.32, 43.75, 36.34, 33.02. **HRMS**  $m/z$  calcd for  $\text{C}_{25}\text{H}_{23}\text{N}_4\text{O}$   $[\text{M} + \text{H}]^+$ , 395.18718; found, 395.19003.

*DIBO-N-Benzyl diazoacetamide Cycloadduct (19)*. Following Cycloaddition General Procedure A, a solution of diazo compound **6** (7.350 mg, 0.042 mmol) dissolved in anhydrous  $\text{CH}_2\text{Cl}_2$  was treated with DIBO (10 mg, 0.042 mmol) to provide compound **19**.  $^1\text{H}$  NMR (500 MHz, chloroform-*d*,  $\delta$ ): 11.58 (s, 1H), 7.34–7.08 (m, 13H), 6.84 (s, 1H), 4.73–4.57 (m, 1H), 4.50–4.39 (m, 1H), 3.44–2.87 (m, 4H).  $^{13}\text{C}$  NMR (126 MHz, chloroform-*d*,  $\delta$ ): 171.21, 160.59, 140.56, 139.01, 137.82, 131.05, 130.95, 130.91, 130.88, 129.85, 128.68, 128.64, 128.30, 127.69, 127.45, 126.09, 126.07, 120.39, 43.26, 36.30, 33.18. **HRMS**  $m/z$  calcd for  $\text{C}_{25}\text{H}_{22}\text{ON}_3$   $[\text{M} + \text{H}]^+$ , 380.17629; found, 380.185730.

*DIBO-Ethyl diazoacetate Cycloadduct (20)*. Following Cycloaddition General Procedure A, a solution of compound **7** (4.792 mg, 0.042 mmol) dissolved in anhydrous  $\text{CH}_2\text{Cl}_2$  was treated with DIBO (10 mg, 0.042 mmol) to provide compound **20**.  $^1\text{H}$  NMR (500 MHz, chloroform-*d*,  $\delta$ ): 7.70–7.35 (m, 1H), 7.35 (s, 0H), 7.34–7.08 (m, 8H), 4.33 (d,  $J = 49.5$  Hz, 2H), 3.48–2.81 (m, 4H), 1.28 (t,  $J = 7.7$  Hz, 3H).  $^{13}\text{C}$  NMR (126 MHz, chloroform-*d*,  $\delta$ ): 160.55, 139.83, 139.11, 131.55, 131.12, 131.06, 130.76, 129.69, 129.07, 128.83, 128.02, 126.06, 125.33, 123.61, 61.20, 36.44, 32.95, 31.60, 14.21, 14.13, 14.09. **HRMS**  $m/z$  calcd for  $\text{C}_{20}\text{H}_{19}\text{N}_2\text{O}_2$   $[\text{M} + \text{H}]^+$ , 319.14465; found, 319.14713.

### Cyclooctyne Stability Experiments

A solution of ABC (25  $\mu\text{M}$ ) or DIBAC (25  $\mu\text{M}$ ) was prepared in phosphate-buffered saline containing reduced glutathione (1.0 mM), oxidized glutathione (0.2 mM), and DMSO (2% v/v).

The solutions were incubated at 37 °C, and HPLC analyses were carried out every hour to determine the remaining concentration of dipolarophile. Subsequently, plots of  $\ln(\text{concentration})$  versus time were prepared to calculate values of  $k_{\text{obs}}$  for the degradation. These values were divided by the concentration of reduced glutathione to obtain second-order rate constants for the degradation with respect to reduced glutathione.

### 2.1.11 Kinetic Analyses

#### Kinetics General Method A

Stock solutions at the specified concentrations in the specified solvents were prepared for each dipole and dipolarophile. Aliquots (0.5 mL) of dipole and dipolarophile were mixed, and reactions were monitored by HPLC with aliquots injected at the timepoints shown in the kinetic traces below. Each reaction was carried out in triplicate. The concentration of remaining dipolarophile was obtained from its corresponding peak in the chromatogram monitored at 280 nm. Second-order rate constants were calculated from the slope of the plot of  $[\text{dipolarophile}]^{-1}$  versus time.

#### Kinetics General Method B

Stock solutions of the specified dipoles and dipolarophiles were prepared in DMSO at 2.5 mM. An aliquot (10  $\mu\text{L}$ ) of each stock was added to 1 mL of PBS (final concentration: 25  $\mu\text{M}$ ), and reactions were monitored by HPLC with aliquots injected at the timepoints specified in Figure 2.1.S3. Each reaction was carried out in triplicate. The concentration of remaining dipolarophile was obtained from its corresponding peak in the chromatogram monitored at 280 nm. Second-order rate constants were calculated from the slope of the plot of  $[\text{dipolarophile}]^{-1}$  versus time.

*Reaction of Compound 5 with DIBO in  $\text{CH}_2\text{Cl}_2$ .* Kinetics General Method A was followed using stock solutions at 2 mM and resulting in final reaction concentrations of 1 mM compound **5** and 1 mM DIBO.

*Reaction of Compound 6 with DIBO in CH<sub>2</sub>Cl<sub>2</sub>.* Kinetics General Method A was followed using stock solutions at 2 mM and resulting in final reaction concentrations of 1 mM compound **6** and 1 mM DIBO.

*Reaction of Compound 5 with ABC in CH<sub>2</sub>Cl<sub>2</sub>.* Kinetics General Method A was followed using stock solutions at 20 μM and resulting in final reaction concentrations of 10 μM compound **5** and 10 μM ABC.

*Reaction of Compound 6 with ABC in CH<sub>2</sub>Cl<sub>2</sub>.* Kinetics General Method A was followed using stock solutions at 80 μM and resulting in final reaction concentrations of 40 μM compound **6** and 40 μM ABC.

*Reaction of Compound 7 with ABC in CH<sub>2</sub>Cl<sub>2</sub>.* Kinetics General Method A was followed using stock solutions at 400 μM and resulting in final reaction concentrations of 200 μM compound **7** and 200 μM ABC.

*Reaction of Compound 11 with ABC in CH<sub>2</sub>Cl<sub>2</sub>.* Kinetics General Method A was followed using stock solutions at 80 μM and resulting in final reaction concentrations of 40 μM compound **11** and 40 μM ABC.

*Reaction of Compound 12 with ABC in CH<sub>2</sub>Cl<sub>2</sub>.* Kinetics General Method A was followed using stock solutions at 80 μM and resulting in final reaction concentrations of 40 μM compound **12** and 40 μM ABC.

*Reaction of Compound 5 with ABC in MeOH.* Kinetics General Method A was followed using stock solutions at 20 μM and resulting in final reaction concentrations of 10 μM compound **5** and 10 μM ABC.

*Reaction of Compound 6 with ABC in MeOH.* Kinetics General Method A was followed using stock solutions at 80 μM and resulting in final reaction concentrations of 40 μM compound **6** and 40 μM ABC.

*Reaction of Compound 11 with ABC in MeOH.* Kinetics General Method A was followed using stock solutions at 80  $\mu\text{M}$  and resulting in final reaction concentrations of 40  $\mu\text{M}$  compound **11** and 40  $\mu\text{M}$  ABC.

*Reaction of Compound 12 with ABC in MeOH.* Kinetics General Method A was followed using stock solutions at 80  $\mu\text{M}$  and resulting in final reaction concentrations of 40  $\mu\text{M}$  compound **12** and 40  $\mu\text{M}$  ABC.

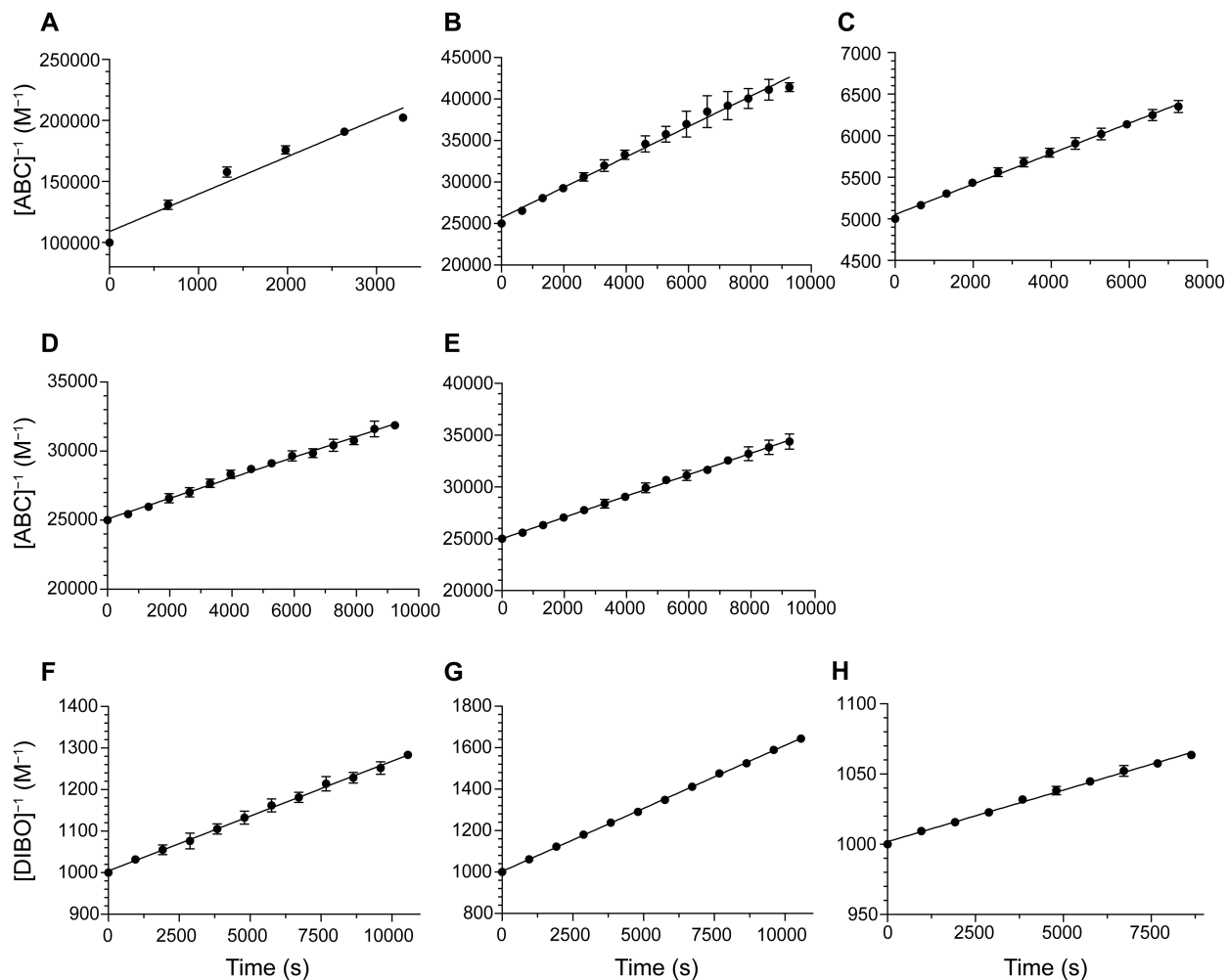
*Reaction of Compound 5 with ABC in PBS Containing DMSO (2% v/v).* Kinetics General Method B was followed.

*Reaction of Compound 6 with ABC in PBS Containing DMSO (2% v/v).* Kinetics General Method B was followed.

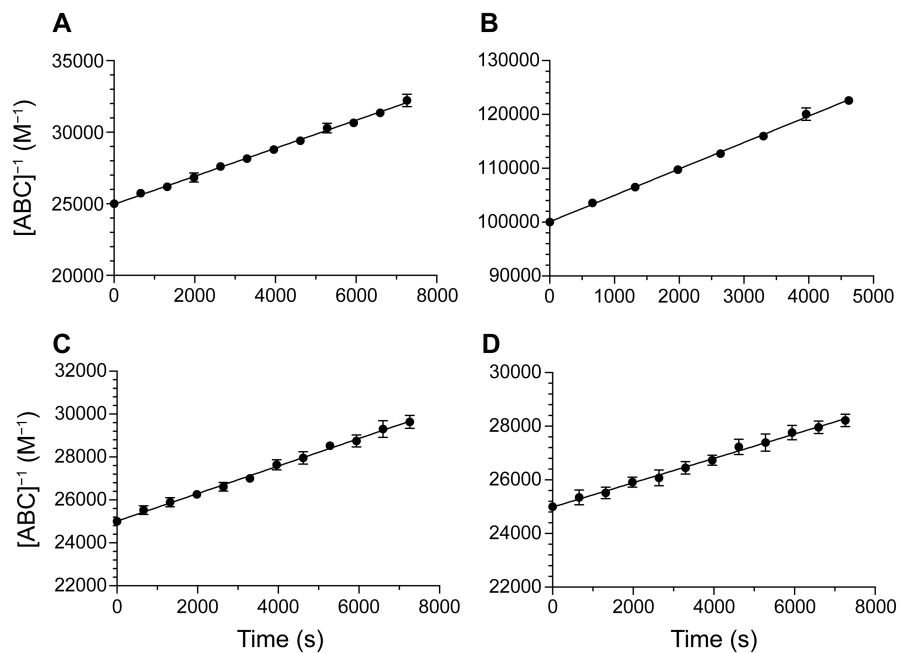
*Reaction of Compound 11 with ABC in PBS Containing DMSO (2% v/v).* Kinetics General Method B was followed.

*Reaction of Compound 12 with ABC in PBS Containing DMSO (2% v/v).* Kinetics General Method B was followed.

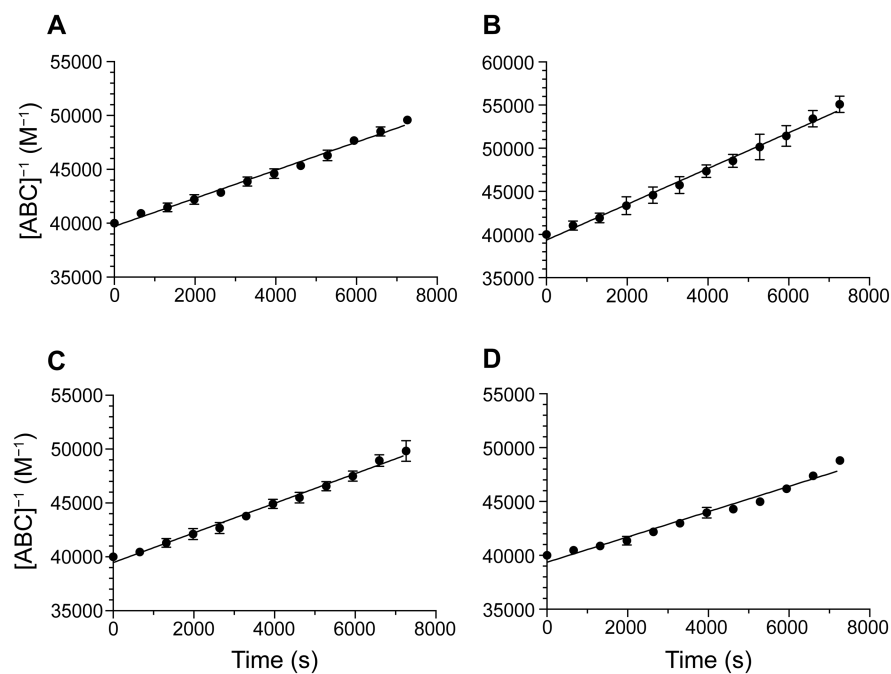
## 2.1.12 Kinetic Traces



**Figure 2.1.7.** Kinetic traces for the reactions of ABC with (A) azide **5**, (B) diazo compound **6**, (C) diazo compound **7**, (D) azide **11** ( $k = 1.0 \text{ M}^{-1}\text{s}^{-1}$ ), and (E) diazo compound **12** ( $k = 0.75 \text{ M}^{-1}\text{s}^{-1}$ ); and the reactions of DIBO with (F) azide **5**, (G) diazo compound **6**, and (H) diazo compound **7**. All reactions were carried out in  $\text{CH}_2\text{Cl}_2$  at  $26 \text{ }^\circ\text{C}$  and were monitored by HPLC. Values are the mean  $\pm$  SD for triplicate experiments.

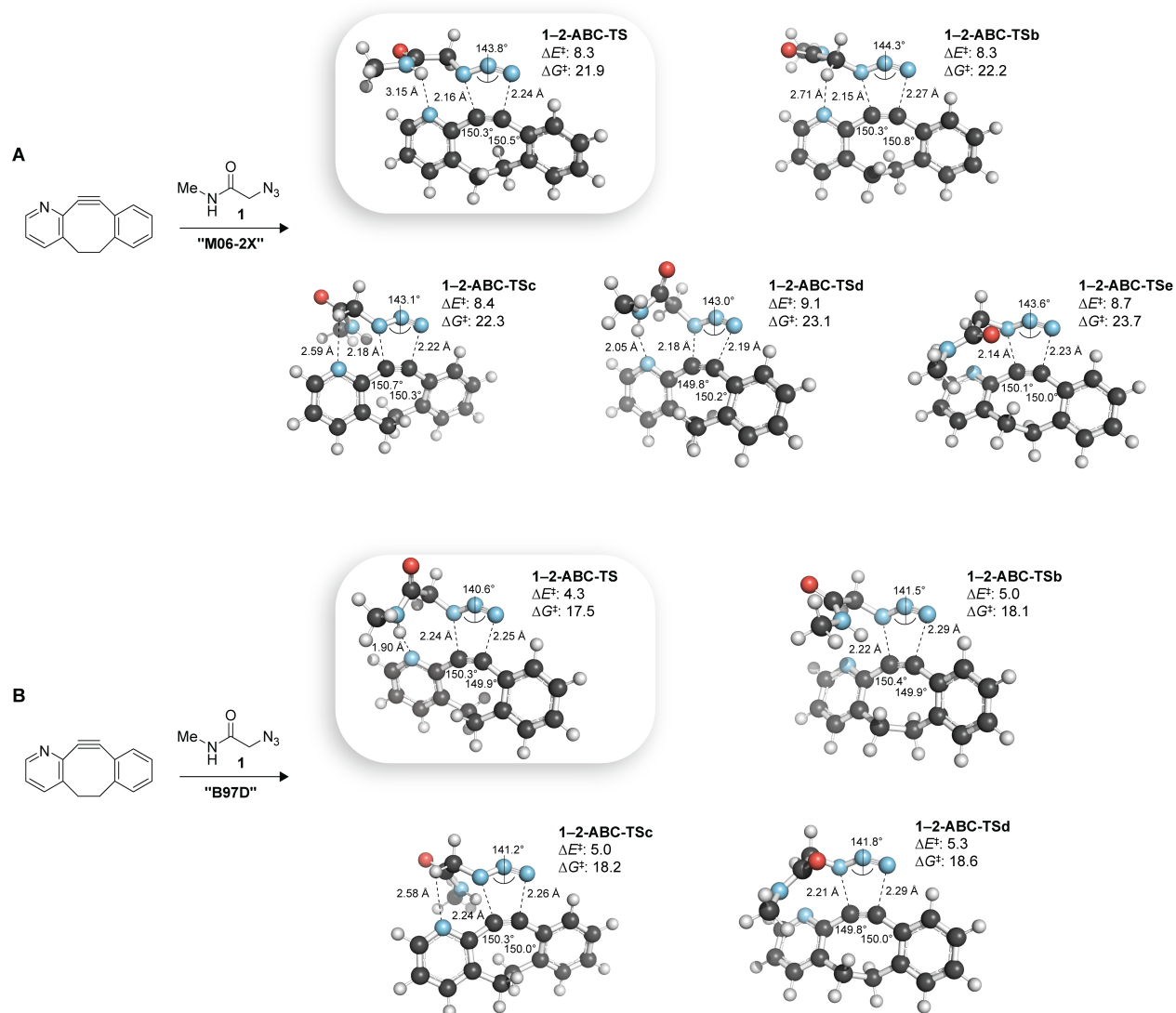


**Figure 2.1.8.** Kinetic traces for the reactions of ABC with (A) azide **5**, (B) diazo compound **6**, (C) azide **11**, and (D) diazo compound **12**. All reactions were carried out in MeOH at 26 °C and were monitored by HPLC. Values are the mean  $\pm$  SD for triplicate experiments.



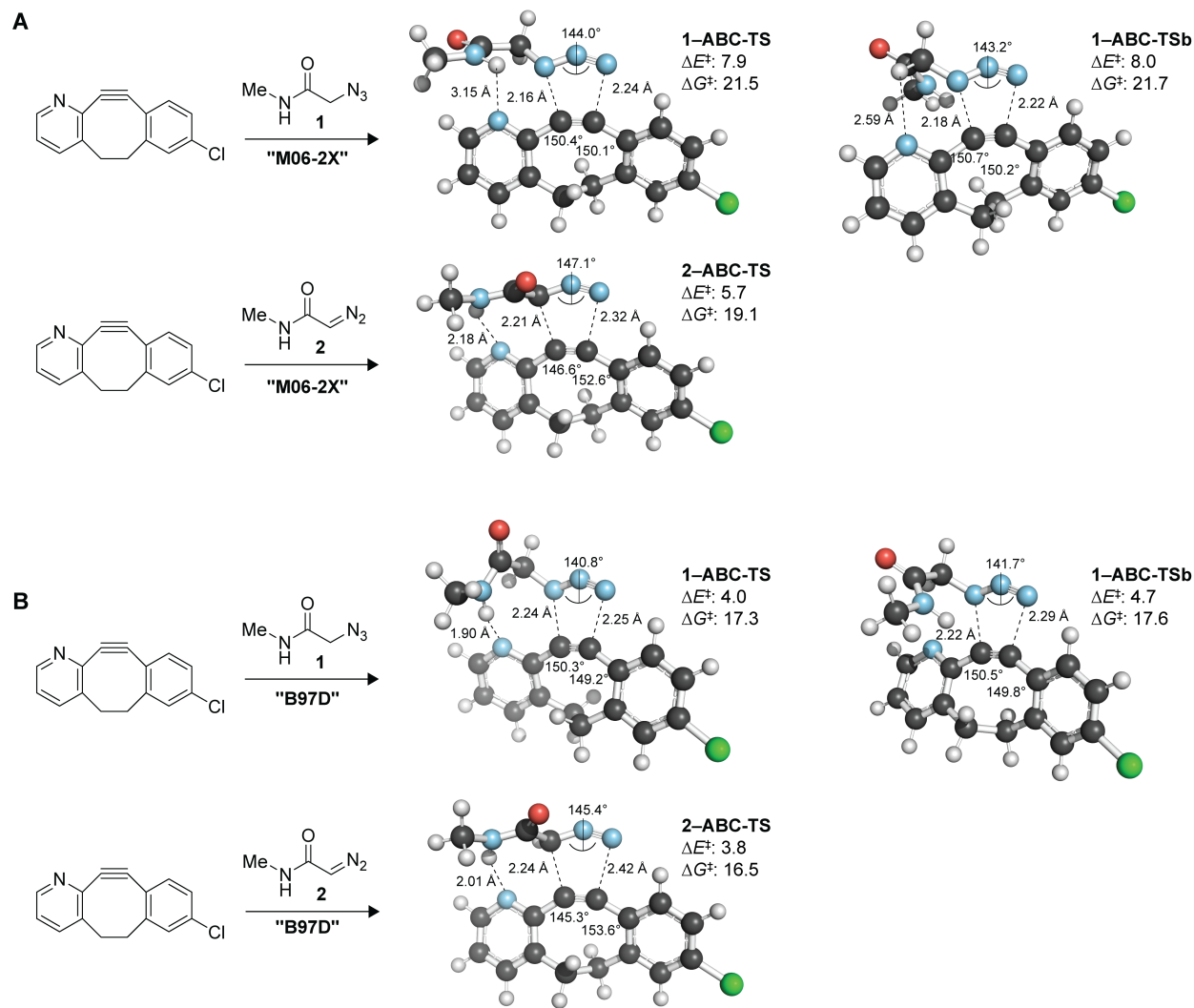
**Figure 2.1.9.** Kinetic traces for the reactions of ABC with (A) azide **5**, (B) diazo compound **6**, (C) azide **11**, and (D) diazo compound **12**. All reactions were carried out in PBS containing DMSO (2% v/v) at 26 °C and were monitored by HPLC. Values are the mean  $\pm$  SD for triplicate experiments.

## 2.1.13 Supporting Information Figures:

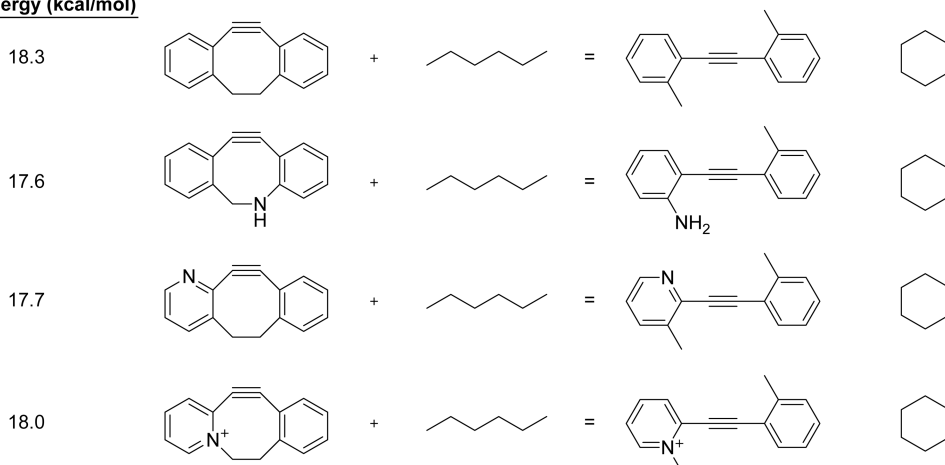


**Figure 2.1.S1.** Optimized transition state geometries for the *syn* reaction of *N*-methylazidoacetamide **1** with 2-ABC at (A) the M06-2X/6-311++G(d,p) employing the IEFPCM solvation model for water, and (B) the B97D/6-311+G(d,p) employing the CPCM solvation model for water.





**Figure 2.1.S2.** Optimized transition state geometries for the reaction of *N*-methylazidoacetamide **1** and *N*-methyldiazoacetamide **2** with ABC at the M06-2X/6-311++G(d,p) employing the IEFPCM solvation model for water (A), and the B97D/6-311++G(d,p) employing the CPCM solvation model for water (B).

**Strain Energy (kcal/mol)**

**Figure 2.1.S3.** Isodesmic equations used to calculate strain energies of dibenzocyclooctyne (DIBO), dibenzoazacyclooctyne (DIBAC), 2-azabenzobenzocyclooctyne (2-ABC), and 6-azabenzobenzocyclooctyne (6-ABC) calculated at the M06-2X/6-311++G(d,p) employing the IEFPCM solvation model (water). A correction of 2.2 kcal/mol was used to account for the nonzero strain energy of cyclohexane.<sup>S216</sup>

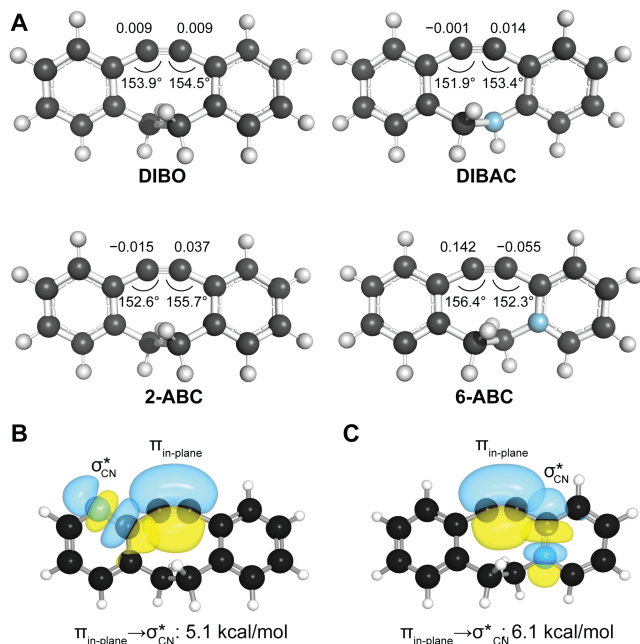


**Figure 2.1.S4.** Combining increased strain with electronic activation. (A) Optimized geometries and NBO charge on each alkyne carbon of dibenzocyclooctyne (DIBO), dibenzoazacyclooctyne

(DIBAC), 2-azabenzobenzocyclooctyne (2-ABC), and 6-azabenzobenzocyclooctyne (6-ABC) calculated at the B97D/6-311+G(d,p) employing the CPCM solvation model (water). (B,C) Natural bonding orbitals depicting  $\pi_{CC} \rightarrow \sigma^*_{CN}$  interactions with the the *syn*-periplanar C–N bond in 2-ABC (B) and *anti*-periplanar C–N bond in 6-ABC (C).

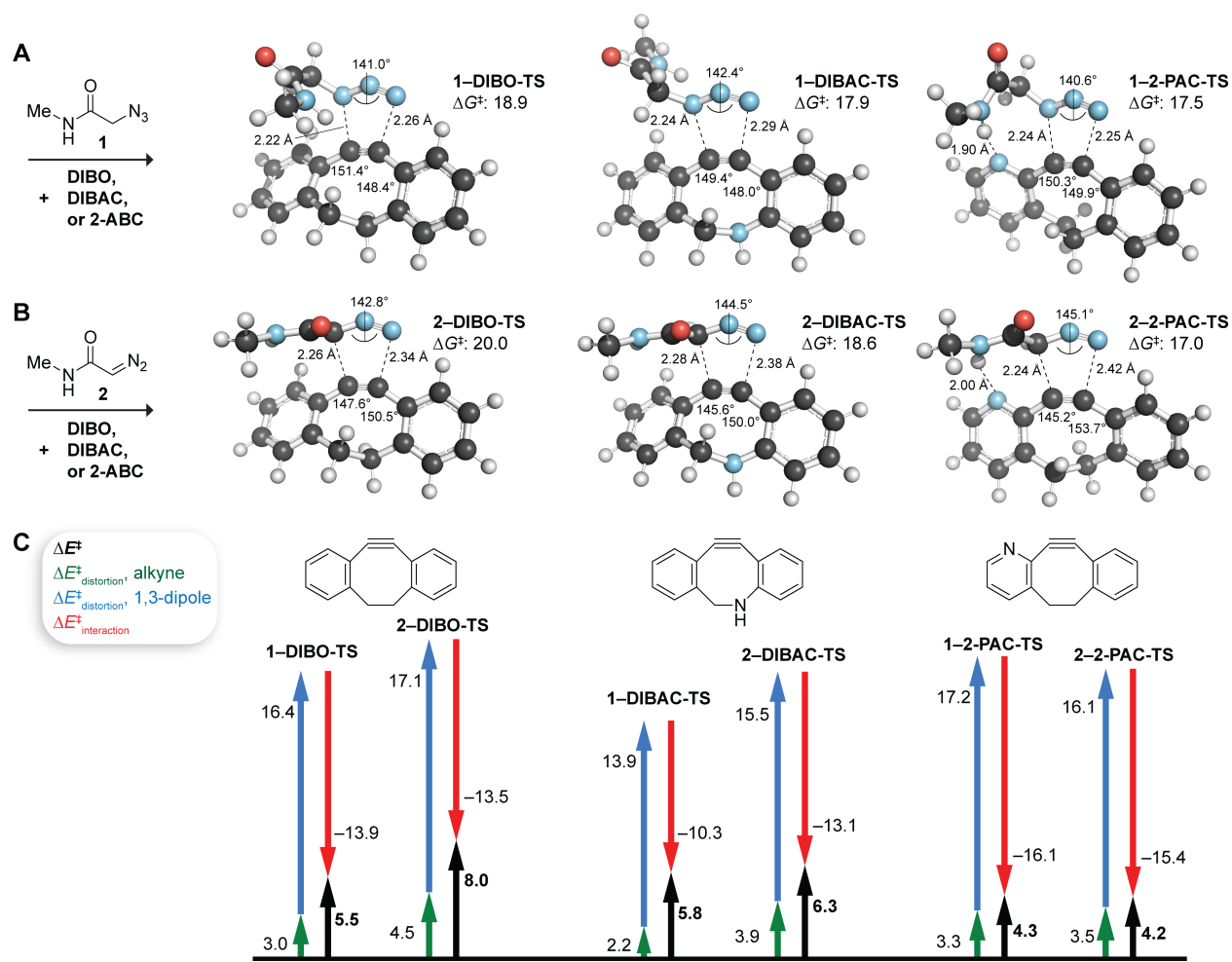


**Figure 2.1.S5.** Computational analysis of cycloadditions with *N*-methylazidoacetamide **1** and *N*-methyldiazoacetamide **2**. (A,B) Optimized transition state geometries and free energies of activation (kcal/mol) calculated at the B97D/6-311+G(d,p) level employing the CPCM solvation model (water). (C) Distortion/Interaction (Strain–Activation) analysis.

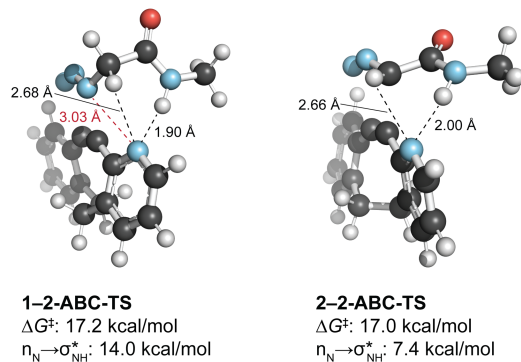


**Figure 2.1.S6.** Comparison of hydrogen bonding interactions in 2-ABC cycloadditions with *N*-methylazidoacetamide **1** (left) and *N*-methyldiazoacetamide **2** (right). The  $\text{N} \cdots \text{N}$  distance (red) is the basis for steric repulsion. Second-order perturbations obtained from the NBO analysis provide a measure of relative hydrogen bond strengths. Optimized transition state geometries are from Figure S5.

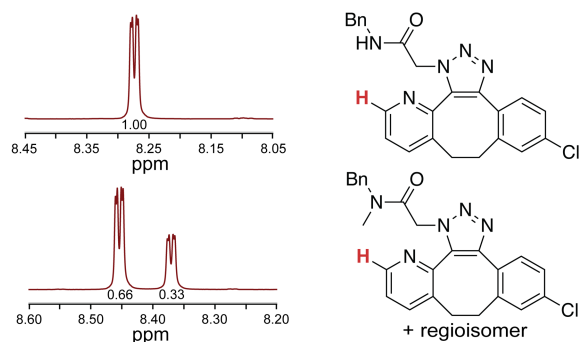


**Figure 2.1.S7.** Effect of hydrogen bonding on the 1,3-dipolar cycloaddition of ABC with *N*-benzylazidoacetamide (**5**) and its *N*-methylated derivative.  $^1\text{H}$  NMR shifts of the C3-H (red) proton in the product of the cycloaddition of ABC with dipole **5** or its *N*-methyl derivative in  $\text{CH}_2\text{Cl}_2$ . A single regioisomer is observed with dipole **5** whereas two regioisomers are observed for the *N*-methylated derivative.

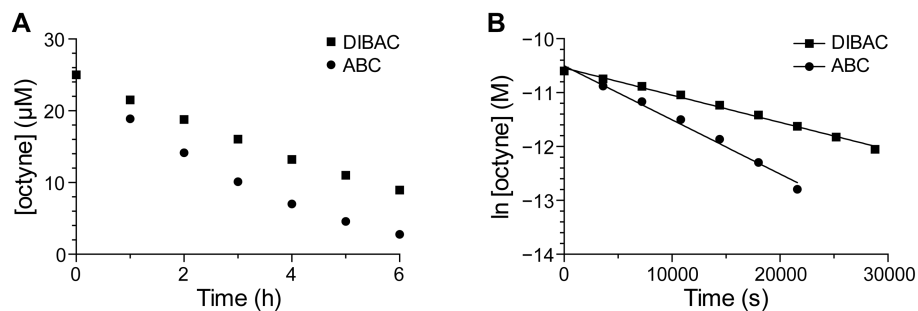
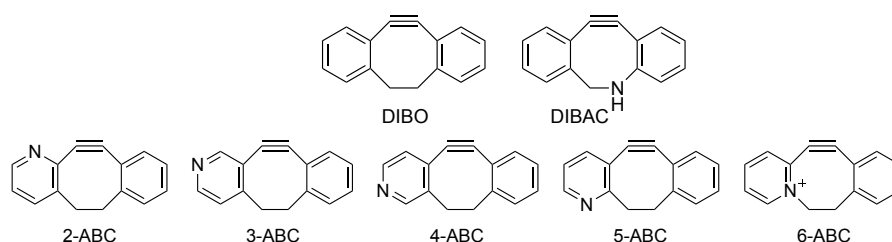


**Figure 2.1.S8.** Stability of DIBAC and ABC in the presence of 1 mM reduced glutathione and 0.2 mM oxidized glutathione in PBS containing DMSO (2% v/v) at 37 °C. (A) Concentration of remaining DIBAC and ABC as determined by HPLC. (B) Natural logarithm of the concentration of DIBAC and ABC over time in order to determine second order rate constants of degradation. With respect to reduced glutathione, the second-order rate constants were  $0.05 \text{ M}^{-1}\text{s}^{-1}$  and  $0.10 \text{ M}^{-1}\text{s}^{-1}$  for DIBAC and ABC, respectively. Values are the mean  $\pm$  SD for triplicate experiments. (Error bars are smaller than the data points.)

## 2.1.14 Supporting Information Tables:

**Table 2.1.S1.** Energies and free energies of activation (kcal/mol) for cycloadditions of *N*-methyl diazoacetamide and *N*-methyl azidoacetamide with constitutional isomers of dibenzoazacyclooctyne (DIBAC). Geometries were optimized at both M06-2X/6-311++G(d,p) employing the IEFPCM solvation model and B97D/6-311+G(d,p) employing the CPCM solvation model for either CH<sub>2</sub>Cl<sub>2</sub> or water.<sup>a</sup> Energies for the preferred regioisomer are in bold typeface.



Method	Solvent	Compound	<i>N</i> -Me-azidoacetamide				<i>N</i> -Me-diazoacetamide			
			<i>syn</i> TS		<i>anti</i> TS		<i>syn</i> TS		<i>anti</i> TS	
			$\Delta E^\ddagger$	$\Delta G^\ddagger$	$\Delta E^\ddagger$	$\Delta G^\ddagger$	$\Delta E^\ddagger$	$\Delta G^\ddagger$	$\Delta E^\ddagger$	$\Delta G^\ddagger$
M06-2X	CH <sub>2</sub> Cl <sub>2</sub>	DIBO	9.6	23.5	—	—	10.6	23.7	—	—
		DIBAC	8.9	<b>22.2</b>	8.9	22.4	10.1	23.2	<b>8.8</b>	<b>21.6</b>
		2-ABC	<b>6.1</b>	<b>19.5</b>	10.4	23.9	<b>5.5</b>	<b>18.8</b>	10.7	23.7
		3-ABC	9.8	<b>23.0</b>	<b>9.5</b>	23.1	9.9	22.9	<b>9.8</b>	<b>22.7</b>
		4-ABC	9.5	<b>22.2</b>	<b>9.5</b>	23.0	10.0	22.9	<b>9.7</b>	<b>22.5</b>
		5-ABC	9.8	<b>22.7</b>	<b>9.6</b>	23.1	11.6	24.6	<b>9.7</b>	<b>21.1</b>
		6-ABC	8.6	22.5	<b>7.5</b>	<b>21.0</b>	7.0	20.7	<b>6.1</b>	<b>19.3</b>
M06-2X	H <sub>2</sub> O	DIBO	10.3	23.7	—	—	10.6	23.7	—	—
		DIBAC	9.6	23.3	<b>9.1</b>	<b>22.9</b>	10.1	23.3	<b>8.9</b>	<b>22.1</b>
		2-ABC	<b>8.3</b>	<b>21.9</b>	10.5	23.8	<b>6.2</b>	<b>19.5</b>	10.6	23.7
		3-ABC	10.0	23.5	<b>9.7</b>	<b>23.2</b>	10.0	22.8	9.8	22.8
		4-ABC	9.8	23.3	<b>9.6</b>	<b>22.9</b>	9.9	<b>22.7</b>	<b>9.8</b>	22.9
		5-ABC	10.1	23.5	<b>9.7</b>	<b>23.1</b>	10.3	23.2	<b>10.0</b>	<b>23.2</b>
		6-ABC	8.6	22.1	<b>7.7</b>	<b>21.3</b>	7.1	20.5	<b>6.8</b>	<b>19.7</b>
B97D	CH <sub>2</sub> Cl <sub>2</sub>	DIBO	5.2	19.6	—	—	7.8	20.0	—	—
		DIBAC	4.7	18.9	5.5	<b>18.5</b>	7.0	19.4	<b>6.1</b>	<b>18.5</b>
		2-ABC	<b>3.9</b>	<b>18.2</b>	6.2	20.4	<b>3.6</b>	<b>16.4</b>	8.4	20.8
		3-ABC	5.0	19.2	<b>4.8</b>	<b>19.2</b>	7.1	<b>19.1</b>	7.1	19.3
		4-ABC	5.2	19.5	<b>4.8</b>	<b>19.2</b>	7.2	19.4	<b>7.1</b>	19.4
		5-ABC	5.2	19.6	<b>4.9</b>	<b>19.4</b>	7.8	19.8	<b>7.3</b>	<b>19.4</b>
		6-ABC	5.3	19.3	<b>4.9</b>	<b>18.7</b>	4.7	16.9	<b>4.0</b>	<b>16.0</b>
B97D	H <sub>2</sub> O	DIBO	5.5	18.9	—	—	8.0	20.0	—	—
		DIBAC	5.2	18.2	<b>5.8</b>	<b>17.9</b>	7.1	19.6	<b>6.3</b>	<b>18.6</b>
		2-ABC	<b>4.3</b>	<b>17.5</b>	6.4	19.8	<b>4.2</b>	<b>17.0</b>	8.4	20.8
		3-ABC	5.4	18.6	<b>5.1</b>	<b>18.4</b>	7.5	19.5	<b>7.2</b>	<b>19.3</b>
		4-ABC	5.5	18.7	<b>5.1</b>	<b>18.4</b>	7.3	<b>19.2</b>	7.3	19.6
		5-ABC	5.6	18.8	<b>5.3</b>	<b>18.6</b>	7.8	<b>19.3</b>	<b>7.5</b>	19.5
		6-ABC	5.3	18.6	<b>5.3</b>	<b>18.0</b>	4.8	17.0	<b>4.7</b>	<b>16.6</b>

<sup>a</sup>Energies given for conformers favored by  $\Delta G^\ddagger$ . See Figure S1 and the computational details.

**Table 2.1.S2.** Distortion/Interaction (Activation–Strain) analysis of energies (kcal/mol) for cycloadditions of *N*-methyl azidoacetamide **1** with constitutional isomers of dibenzoazacyclooctyne (DIBAC). Geometries optimized at both M06-2X/6-311++G(d,p) employing the IEFPCM solvation model for either CH<sub>2</sub>Cl<sub>2</sub> or water, and B97D/6-311+G(d,p) employing the CPCM solvation model for either CH<sub>2</sub>Cl<sub>2</sub> or water. Energies for the preferred regioisomer are in bold typeface.

Method	Solvent	Compound	<i>syn</i> TS				<i>anti</i> TS			
			$\Delta E^{\ddagger}_{\text{distortion}}$			$\Delta E^{\ddagger}_{\text{interaction}}$	$\Delta E^{\ddagger}_{\text{distortion}}$			$\Delta E^{\ddagger}_{\text{interaction}}$
			1,3-Dipole	Alkyne	Total		1,3-Dipole	Alkyne	Total	
M06-2X	CH <sub>2</sub> Cl <sub>2</sub>	DIBO	18.6	3.2	21.8	-12.1	—	—	—	—
		DIBAC	18.3	3.0	21.3	-12.5	16.1	2.5	18.6	-9.7
		2-ABC	<b>16.7</b>	<b>2.6</b>	<b>19.3</b>	<b>-13.2</b>	16.2	2.4	18.7	-10.9
		3-ABC	16.7	2.9	19.6	-9.9	<b>16.7</b>	<b>2.9</b>	<b>19.6</b>	<b>-10.1</b>
		4-ABC	16.8	3.0	19.8	-10.3	<b>16.7</b>	<b>2.9</b>	<b>19.6</b>	<b>-10.2</b>
		5-ABC	17.0	3.0	20.0	-10.2	<b>16.8</b>	<b>2.9</b>	<b>19.7</b>	<b>-10.1</b>
		6-ABC	16.7	3.7	20.4	-11.8	<b>16.0</b>	<b>3.8</b>	<b>19.7</b>	<b>-12.2</b>
M06-2X	H <sub>2</sub> O	DIBO	17.0	3.0	20.1	-9.8	—	—	—	—
		DIBAC	18.3	3.1	22.1	-11.8	<b>16.1</b>	<b>2.6</b>	<b>18.7</b>	<b>-9.5</b>
		2-ABC	<b>16.6</b>	<b>2.6</b>	<b>19.2</b>	<b>-10.9</b>	16.8	3.0	19.8	-9.3
		3-ABC	16.7	3.0	19.7	-9.7	<b>16.6</b>	<b>3.0</b>	<b>19.6</b>	<b>-9.9</b>
		4-ABC	16.7	3.1	19.8	-10.0	<b>16.7</b>	<b>2.9</b>	<b>19.6</b>	<b>-10.0</b>
		5-ABC	16.9	3.0	19.9	-9.8	<b>16.8</b>	<b>2.9</b>	<b>19.7</b>	<b>-10.0</b>
		6-ABC	16.5	3.6	20.1	-11.5	<b>15.9</b>	<b>3.7</b>	<b>19.6</b>	<b>-11.9</b>
B97D	CH <sub>2</sub> Cl <sub>2</sub>	DIBO	16.3	3.0	19.4	-14.2	—	—	—	—
		DIBAC	16.2	2.9	19.1	-14.4	<b>13.7</b>	<b>2.2</b>	<b>15.9</b>	<b>-10.4</b>
		2-ABC	<b>17.1</b>	<b>3.3</b>	<b>20.5</b>	<b>-16.6</b>	16.0	3.1	19.1	-13.0
		3-ABC	16.0	3.0	19.0	-14.0	15.8	3.0	18.8	-14.0
		4-ABC	16.0	3.2	19.1	-13.9	<b>15.9</b>	<b>2.9</b>	<b>18.8</b>	<b>-13.9</b>
		5-ABC	16.2	3.0	19.2	-14.0	<b>16.1</b>	<b>2.9</b>	<b>19.0</b>	<b>-14.1</b>
		6-ABC	15.4	3.9	19.2	-13.5	<b>14.0</b>	<b>3.6</b>	<b>17.5</b>	<b>-12.6</b>
B97D	H <sub>2</sub> O	DIBO	16.4	3.0	19.4	-13.9	—	—	—	—
		DIBAC	16.3	2.9	19.2	-14.0	<b>13.9</b>	<b>2.2</b>	<b>16.1</b>	<b>-10.3</b>
		2-ABC	<b>17.1</b>	<b>3.3</b>	<b>20.4</b>	<b>-16.1</b>	16.1	3.1	19.2	-12.8
		3-ABC	16.1	3.0	19.1	-13.7	<b>15.9</b>	<b>2.9</b>	<b>18.8</b>	<b>-13.8</b>
		4-ABC	16.1	3.2	19.3	-13.8	<b>16.0</b>	<b>2.9</b>	<b>18.9</b>	<b>-13.7</b>
		5-ABC	<b>16.3</b>	<b>3.0</b>	<b>19.3</b>	<b>-13.8</b>	<b>16.2</b>	<b>2.9</b>	<b>19.1</b>	<b>-13.9</b>
		6-ABC	<b>15.5</b>	<b>3.8</b>	<b>19.3</b>	<b>-14.0</b>	<b>14.1</b>	<b>3.5</b>	<b>17.6</b>	<b>-12.3</b>

**Table 2.1.S3.** Distortion/Interaction (Activation–Strain) analysis of energies (kcal/mol) for cycloadditions of *N*-methyl diazoacetamide **2** with constitutional isomers of dibenzoazacyclooctyne (DIBAC). Geometries optimized at both M06-2X/6-311++G(d,p) employing the IEFPCM solvation model for either CH<sub>2</sub>Cl<sub>2</sub> or water, and B97D/6-311+G(d,p)

employing the CPCM solvation model for either CH<sub>2</sub>Cl<sub>2</sub> or water. Energies for the preferred regioisomer are in bold typeface.

Method	Solvent	Compound	<i>syn</i> TS				<i>anti</i> TS			
			$\Delta E^\ddagger_{\text{distortion}}$			$\Delta E^\ddagger_{\text{interaction}}$	$\Delta E^\ddagger_{\text{distortion}}$			$\Delta E^\ddagger_{\text{interaction}}$
			1,3-Dipole	Alkyne	Total		1,3-Dipole	Alkyne	Total	
M06-2X	CH <sub>2</sub> Cl <sub>2</sub>	DIBO	18.6	5.0	23.7	-13.0	—	—	—	—
		DIBAC	17.5	4.3	21.8	-11.7	<b>17.5</b>	<b>4.4</b>	<b>21.9</b>	<b>-13.1</b>
		2-ABC	<b>16.8</b>	<b>3.8</b>	<b>20.6</b>	<b>-15.1</b>	18.5	5.2	23.6	-12.9
		3-ABC	18.0	4.8	22.8	-12.9	<b>18.1</b>	<b>5.0</b>	<b>23.1</b>	<b>-13.3</b>
		4-ABC	17.9	5.0	22.9	-13.0	<b>18.2</b>	<b>5.0</b>	<b>23.1</b>	<b>-13.4</b>
		5-ABC	18.2	4.9	23.1	-11.5	<b>18.3</b>	<b>4.9</b>	<b>23.2</b>	<b>-13.4</b>
		6-ABC	17.4	5.6	23.0	-15.9	<b>16.6</b>	<b>5.7</b>	<b>22.3</b>	<b>-16.2</b>
M06-2X	H <sub>2</sub> O	DIBO	18.6	5.0	23.6	-13.0	—	—	—	—
		DIBAC	17.6	4.2	21.9	-11.7	<b>17.1</b>	<b>4.4</b>	<b>21.5</b>	<b>-12.6</b>
		2-ABC	<b>16.8</b>	<b>3.7</b>	<b>20.5</b>	<b>-14.3</b>	18.3	5.1	23.4	-12.8
		3-ABC	18.1	4.8	22.9	-12.9	<b>18.0</b>	<b>5.0</b>	<b>23.0</b>	<b>-13.2</b>
		4-ABC	18.0	5.0	23.0	-13.1	18.2	4.9	23.1	-13.3
		5-ABC	18.3	4.9	23.2	-12.9	<b>18.1</b>	<b>4.8</b>	<b>23.0</b>	<b>-12.9</b>
		6-ABC	17.2	5.4	22.6	-15.5	<b>16.7</b>	<b>5.6</b>	<b>22.3</b>	<b>-15.5</b>
B97D	CH <sub>2</sub> Cl <sub>2</sub>	DIBO	17.2	4.5	21.7	-13.9	—	—	—	—
		DIBAC	15.9	3.7	19.6	-12.6	<b>15.5</b>	<b>3.9</b>	<b>19.4</b>	<b>-13.3</b>
		2-ABC	<b>16.1</b>	<b>3.5</b>	<b>19.6</b>	<b>-16.0</b>	17.0	4.6	21.6	-13.2
		3-ABC	16.5	4.4	20.8	-13.7	16.5	4.4	20.9	-13.8
		4-ABC	16.5	4.4	20.9	-13.7	16.7	4.3	21.0	-13.9
		5-ABC	16.8	4.5	21.3	-13.5	<b>16.9</b>	<b>4.3</b>	<b>21.1</b>	<b>-13.9</b>
		6-ABC	<b>15.8</b>	<b>5.1</b>	<b>20.9</b>	<b>-16.3</b>	<b>15.1</b>	<b>5.4</b>	<b>20.5</b>	<b>-16.4</b>
B97D	H <sub>2</sub> O	DIBO	17.1	4.5	21.6	-13.5	—	—	—	—
		DIBAC	15.9	3.6	19.5	-12.4	<b>15.5</b>	<b>3.9</b>	<b>19.2</b>	<b>-13.1</b>
		2-ABC	<b>16.1</b>	<b>3.5</b>	<b>19.6</b>	<b>-15.4</b>	16.9	4.6	21.5	-13.1
		3-ABC	16.3	4.3	20.6	-13.2	<b>16.4</b>	<b>4.4</b>	<b>20.8</b>	<b>-13.6</b>
		4-ABC	16.4	4.4	20.8	-13.5	16.6	4.3	20.9	-13.4
		5-ABC	16.7	4.5	21.2	-13.4	16.8	4.2	21.0	13.6
		6-ABC	15.7	5.1	20.7	-15.9	<b>15.1</b>	<b>5.4</b>	<b>20.4</b>	<b>-15.8</b>

<sup>a</sup>Energies given for alternative conformations as shown in Figure S1.

**Table 2.1.S4.** Distortion/Interaction (Activation–Strain) analysis of energies (kcal/mol) for cycloadditions of *N*-methyl diazoacetamide **2** with constitutional isomers of dibenzoazacyclooctyne (DIBAC). Geometries optimized at both M06-2X/6-311++G(d,p) employing the IEFPCM solvation model for either CH<sub>2</sub>Cl<sub>2</sub> or water, and B97D/6-311+G(d,p) employing the CPCM solvation model for either CH<sub>2</sub>Cl<sub>2</sub> or water. Energies for the preferred regioisomer are in bold typeface.

Method	Solvent	R	<i>N</i> -Me- <i>N</i> -R-azidoacetamide				<i>N</i> -Me- <i>N</i> -R-diazoacetamide			
			<i>syn</i> TS		<i>anti</i> TS		<i>syn</i> TS		<i>anti</i> TS	
			$\Delta E^\ddagger$	$\Delta G^\ddagger$	$\Delta E^\ddagger$	$\Delta G^\ddagger$	$\Delta E^\ddagger$	$\Delta G^\ddagger$	$\Delta E^\ddagger$	$\Delta G^\ddagger$
M06-2X	CH <sub>2</sub> Cl <sub>2</sub>	H	<b>7.3</b>	<b>20.5</b>	10.1	23.1	<b>5.0</b>	<b>18.4</b>	10.3	23.2
		H <sub>2</sub> O	<b>7.9</b>	<b>21.5</b>	10.2	23.3	<b>5.7</b>	<b>19.1</b>	10.2	23.2
	H <sub>2</sub> O	Me	<b>8.1</b>	<b>20.5</b>	9.8	24.3	<b>6.8</b>	<b>20.0</b>	10.7	24.1
		Me	<b>8.6</b>	<b>21.3</b>	9.8	24.3	<b>7.2</b>	<b>19.9</b>	10.6	23.9

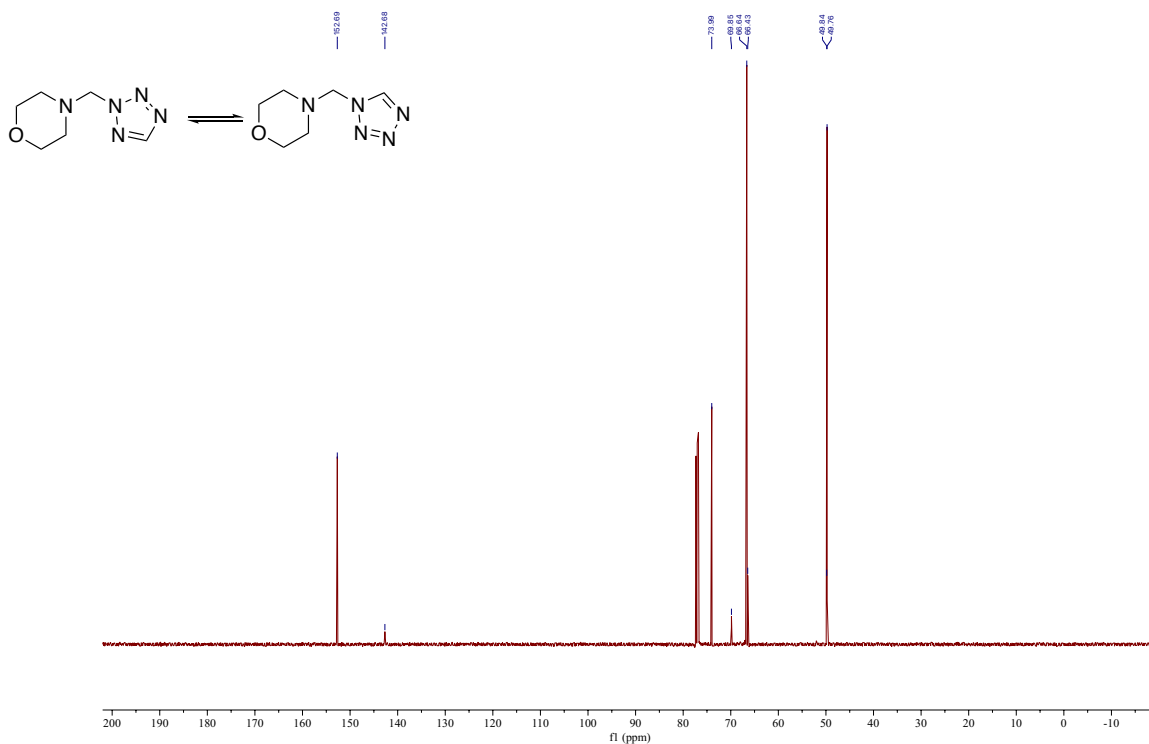
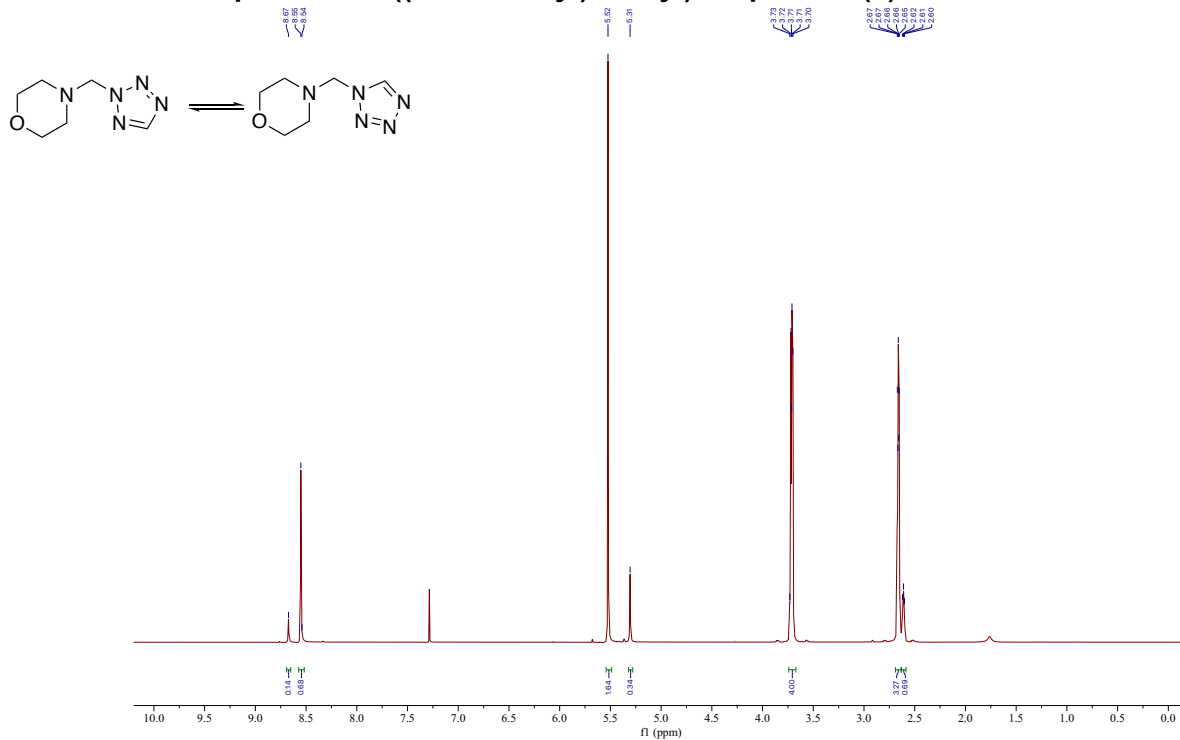


B97D	CH <sub>2</sub> Cl <sub>2</sub>	H	<b>3.6</b>	<b>18.1</b>	6.1	20.5	<b>3.3</b>	<b>16.0</b>	8.0	20.2
	H <sub>2</sub> O	H	<b>4.0</b>	<b>17.3</b>	6.3	19.6	<b>3.8</b>	<b>16.5</b>	8.1	20.3
	CH <sub>2</sub> Cl <sub>2</sub>	Me	<b>5.1</b>	<b>18.6</b>	6.3	21.0	<b>4.9</b>	<b>16.9</b>	7.8	20.0
	H <sub>2</sub> O	Me	<b>5.8</b>	<b>18.5</b>	6.8	21.2	<b>5.3</b>	<b>17.3</b>	7.9	20.1

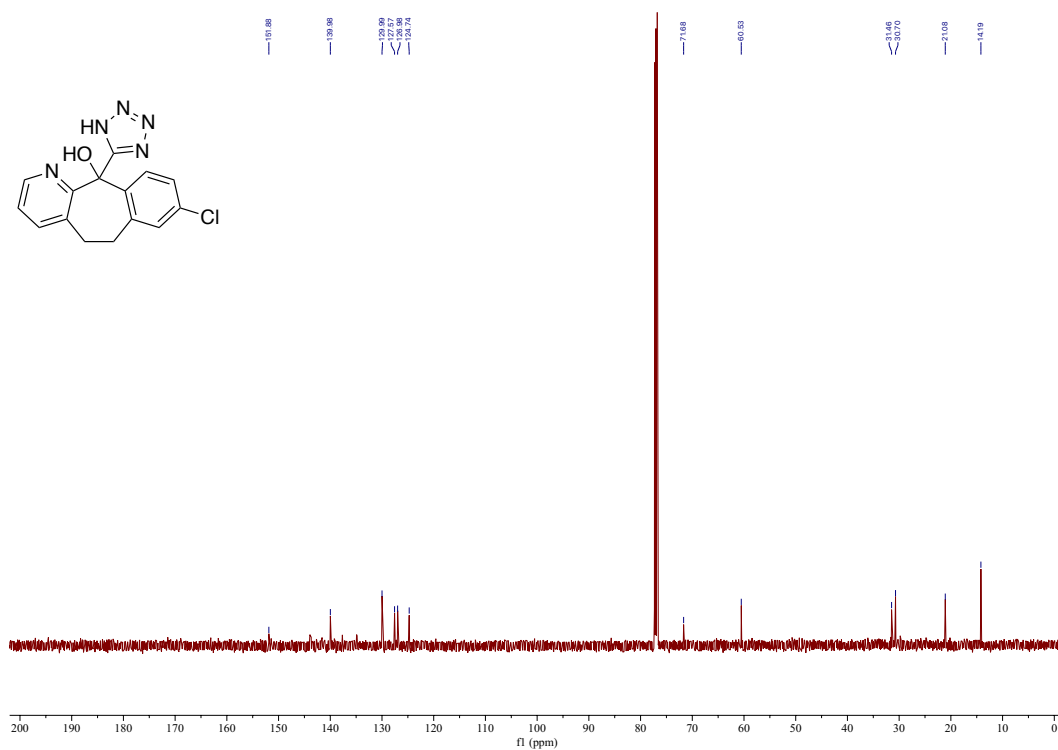
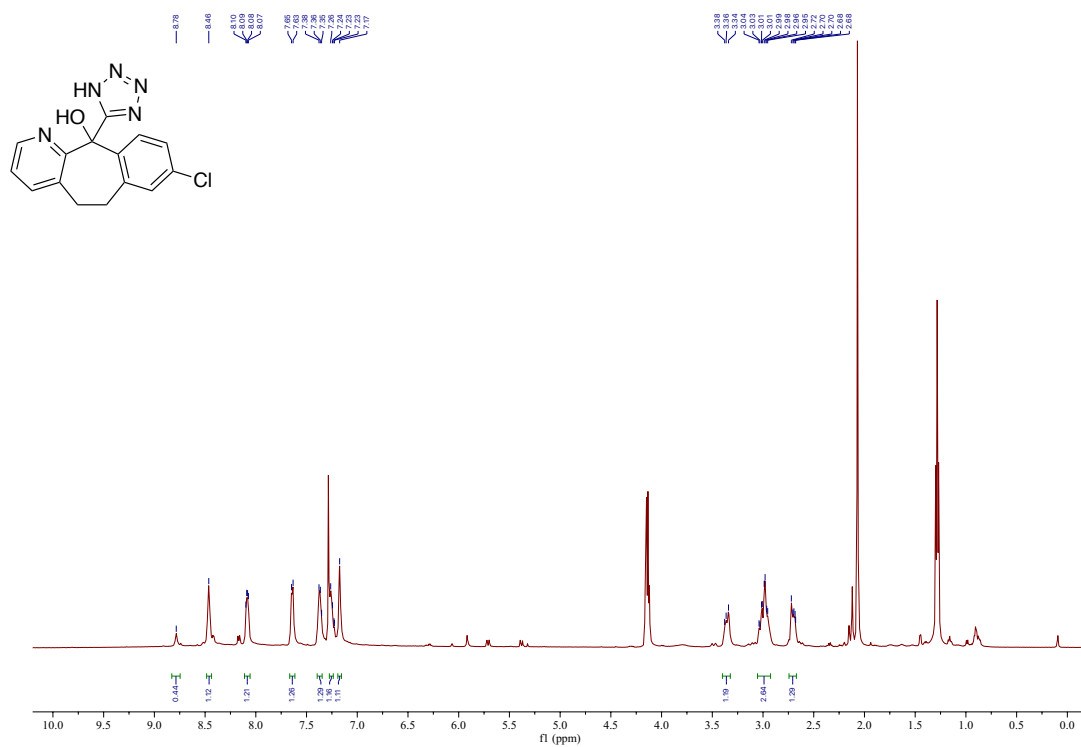
## 2.1.14 NMR Spectra

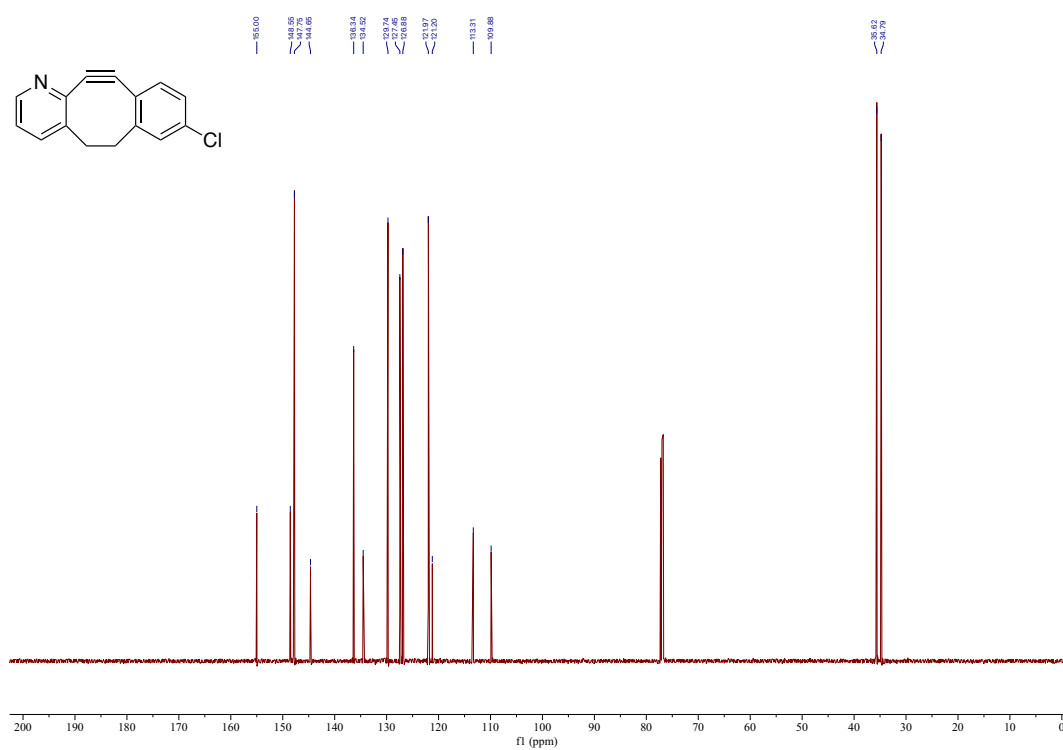
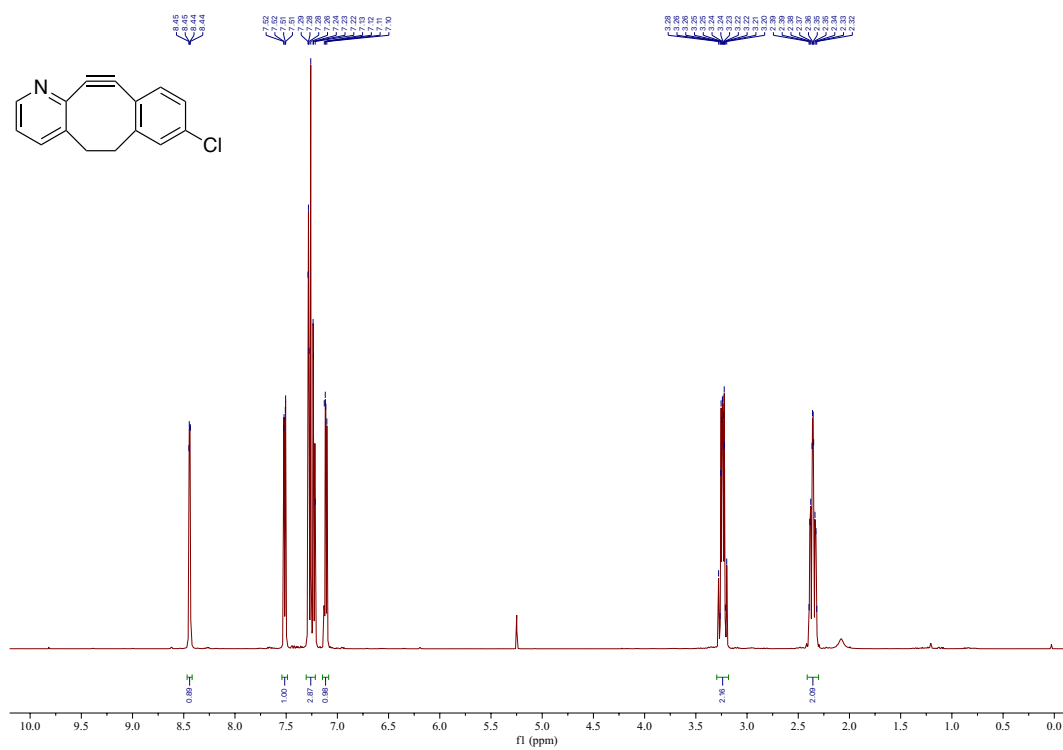
**NMR Spectra** (All compounds were dissolved in  $\text{CDCl}_3$  unless indicated otherwise.)

**$^1\text{H}$  and  $^{13}\text{C}$  NMR Spectra of 4-((*N*-Tetrazolyl)methyl)morpholine (**8**)**

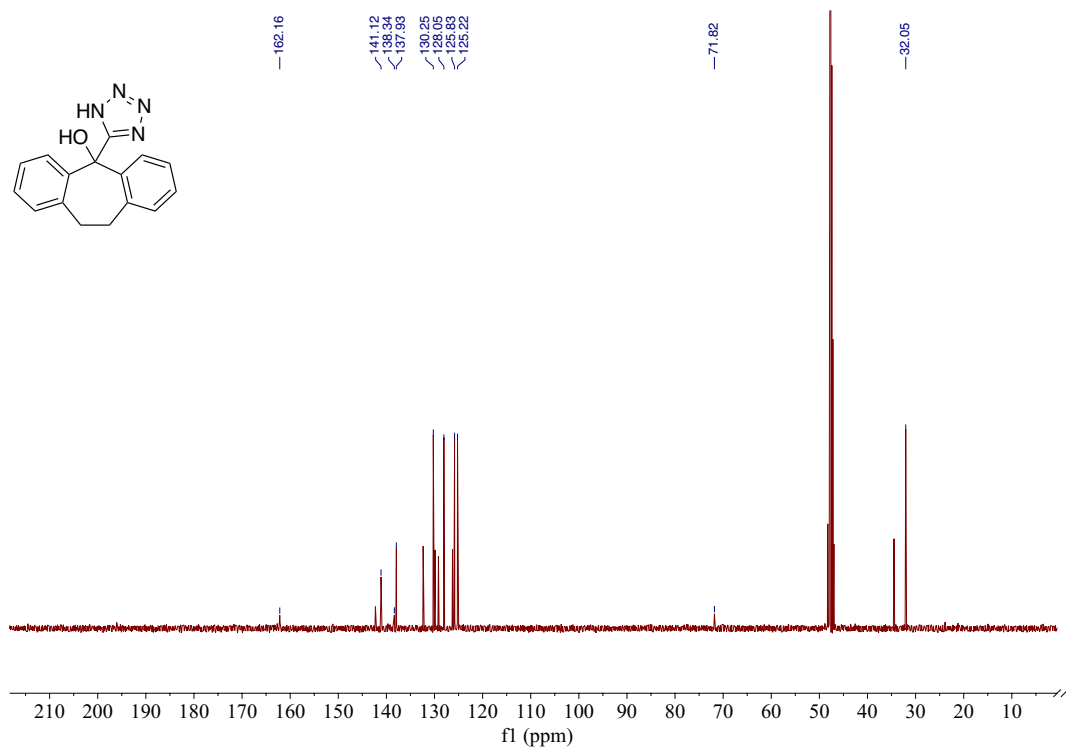
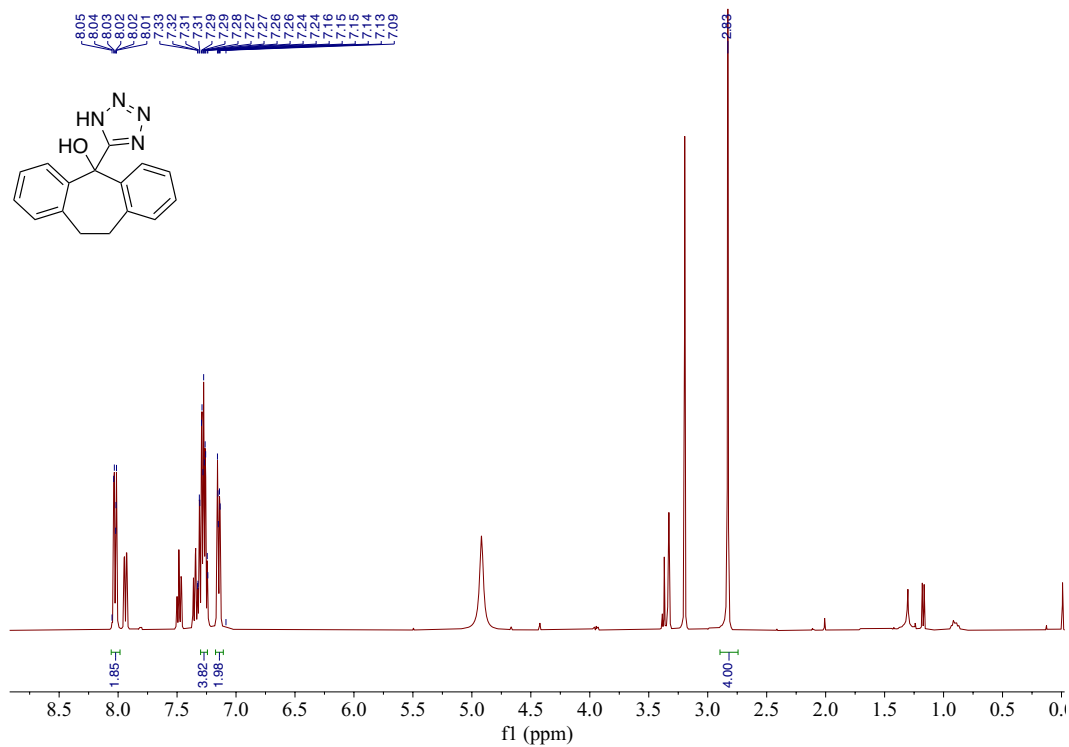


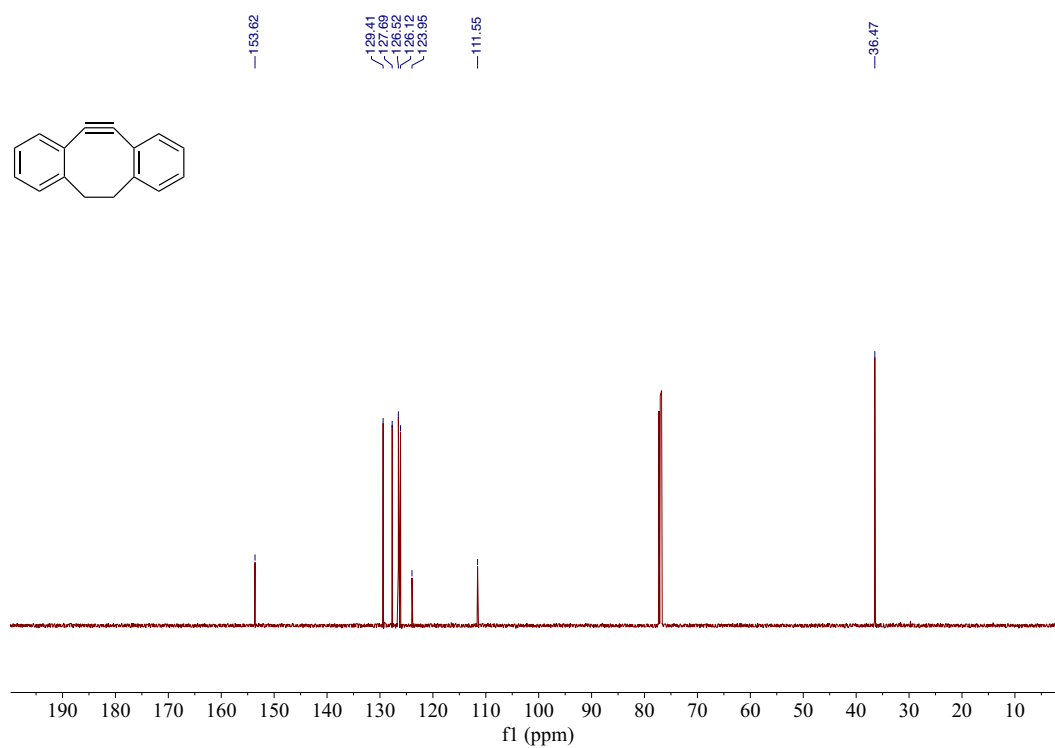
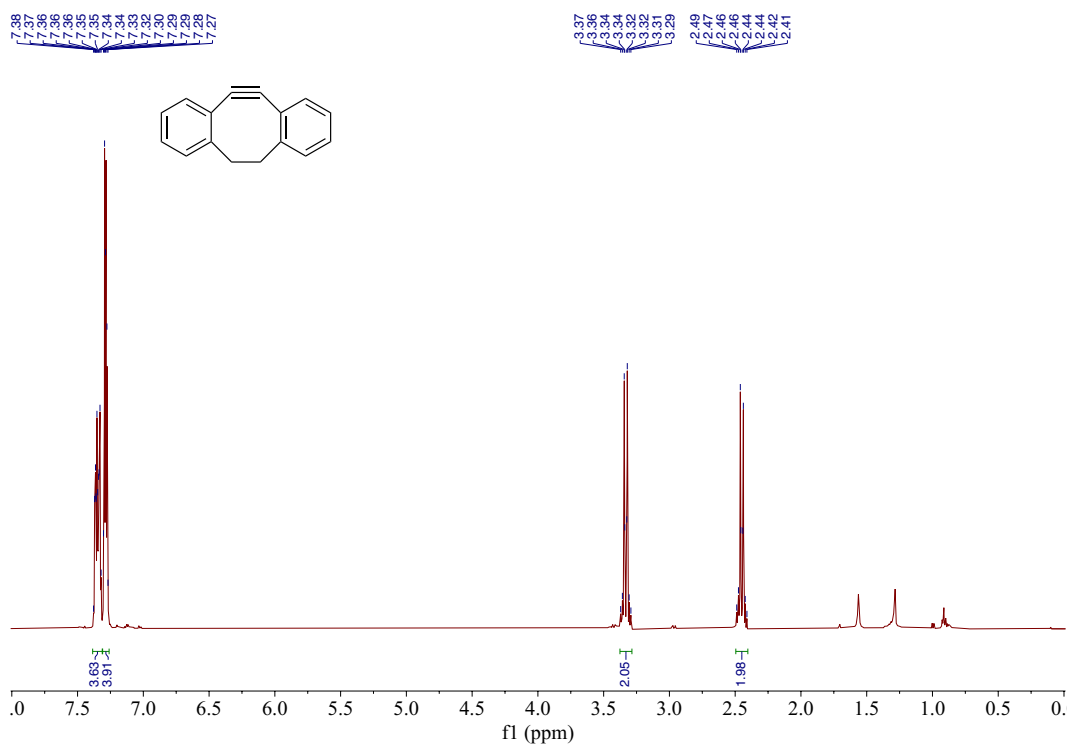
**<sup>1</sup>H and <sup>13</sup>C NMR Spectra of 8-Chloro-11-(1*H*-tetrazol-5-yl)-6,11-dihydro-5*H*-benzo[5,6]cyclohepta[1,2-*b*]pyridin-11-ol (4)**

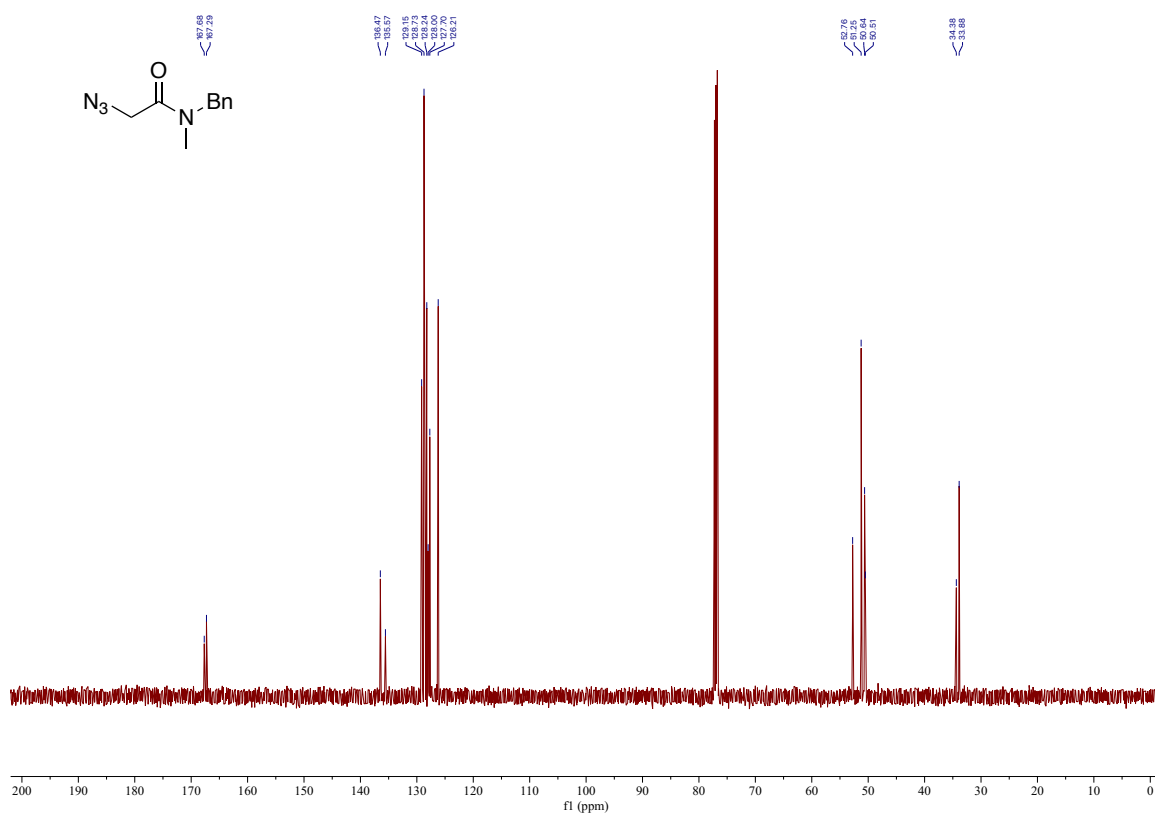
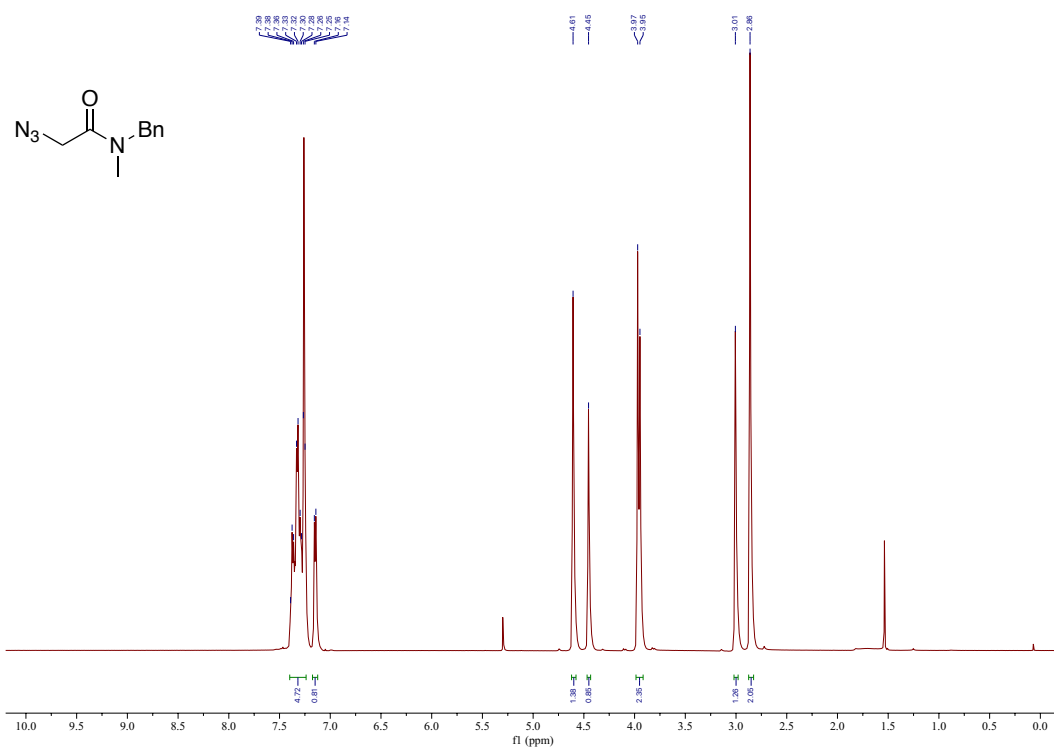


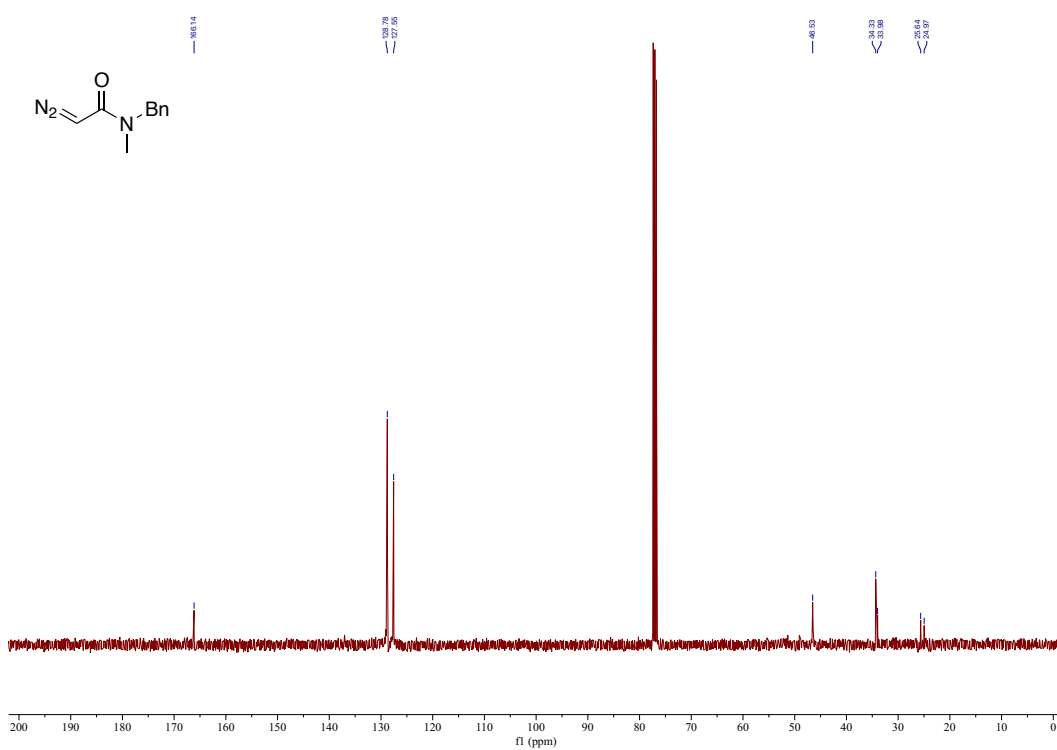
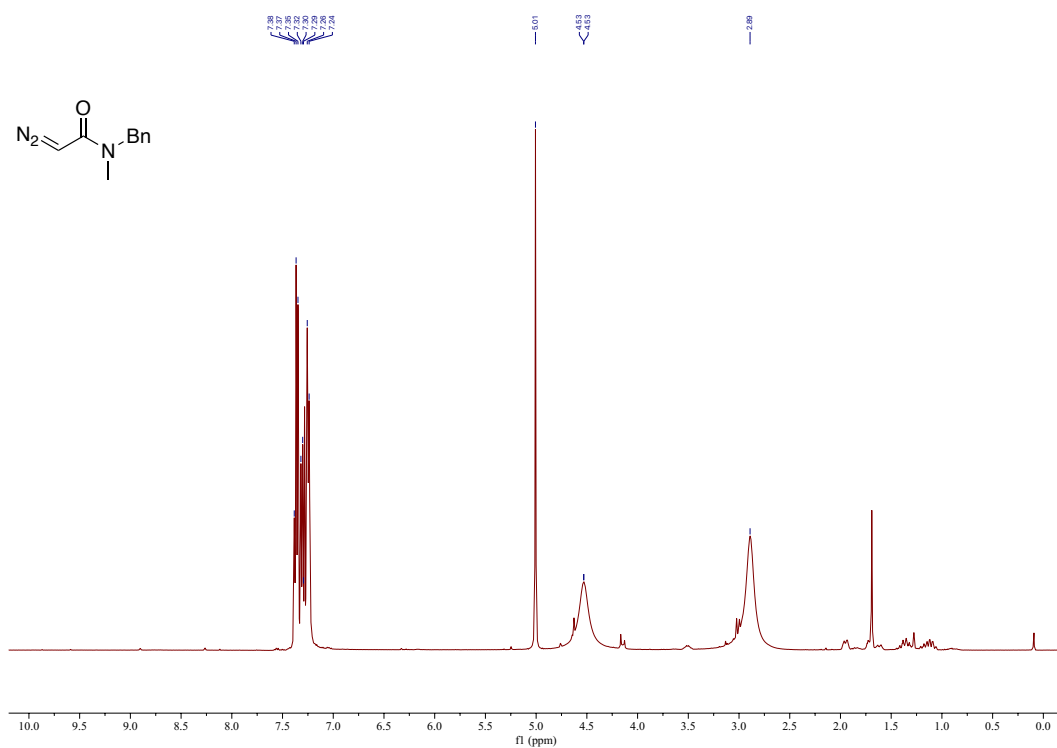
**$^1\text{H}$  and  $^{13}\text{C}$  NMR Spectra of 2-Azabenzocyclooctyne (ABC)**

**<sup>1</sup>H and <sup>13</sup>C NMR Spectra of 5-(1*H*-Tetrazol-5-yl)-10,11-dihydro-5*H*-dibenzo[*a,d*][7]annulen-5-ol (9).** Both spectra were obtained in CD<sub>3</sub>OD.

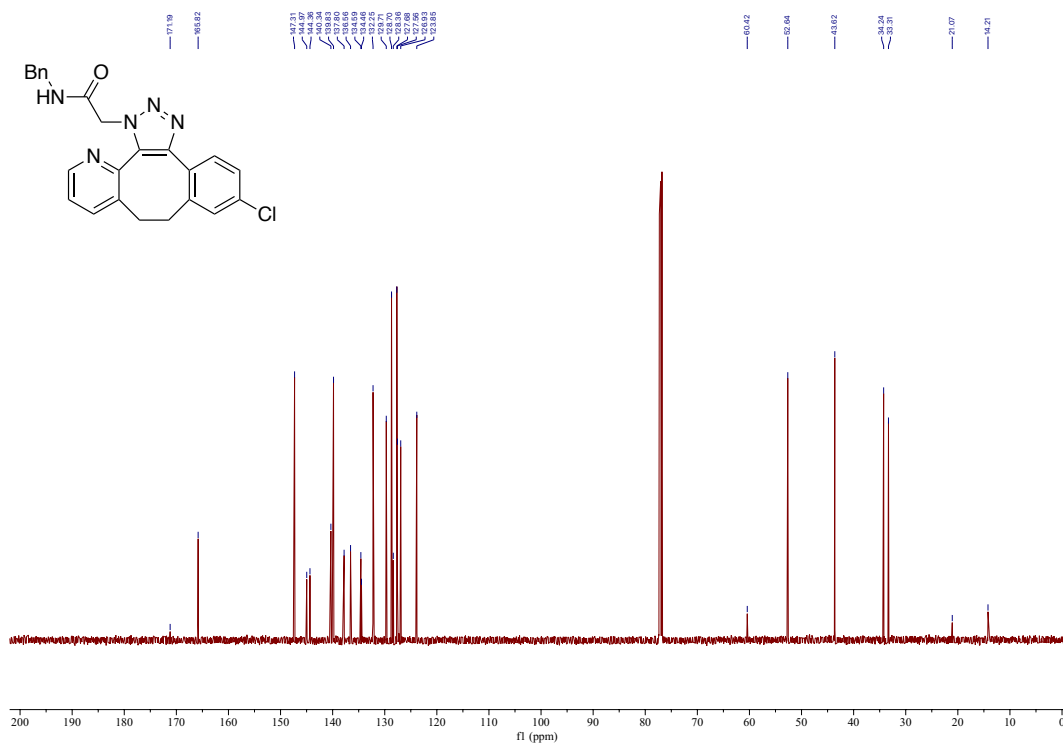
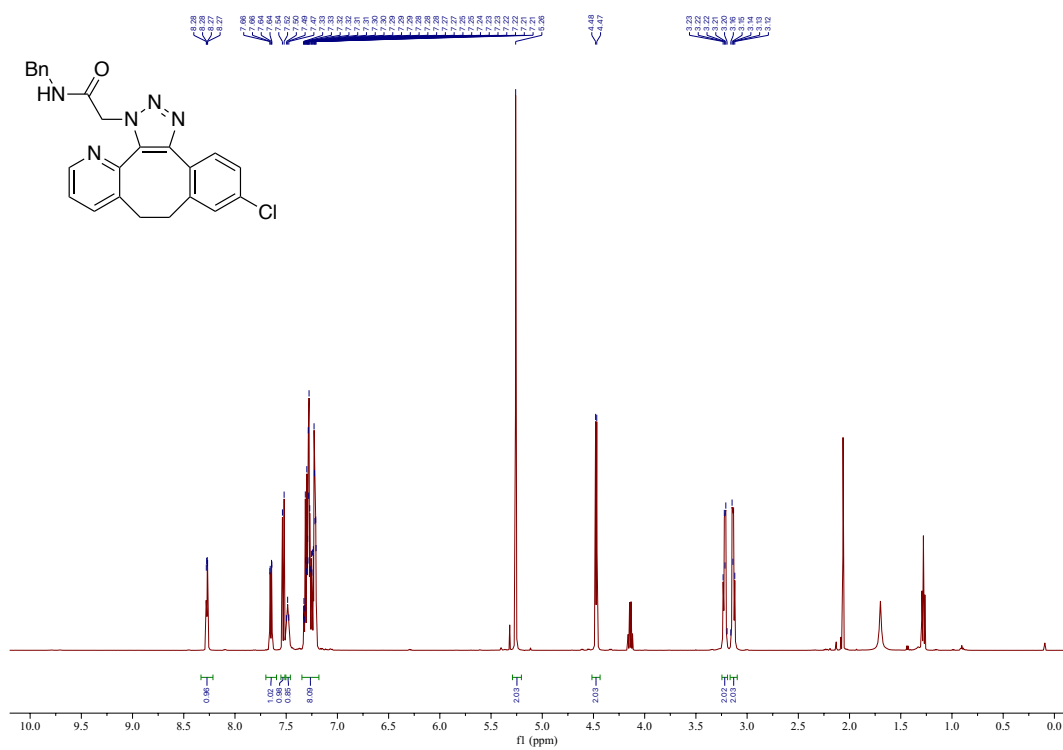


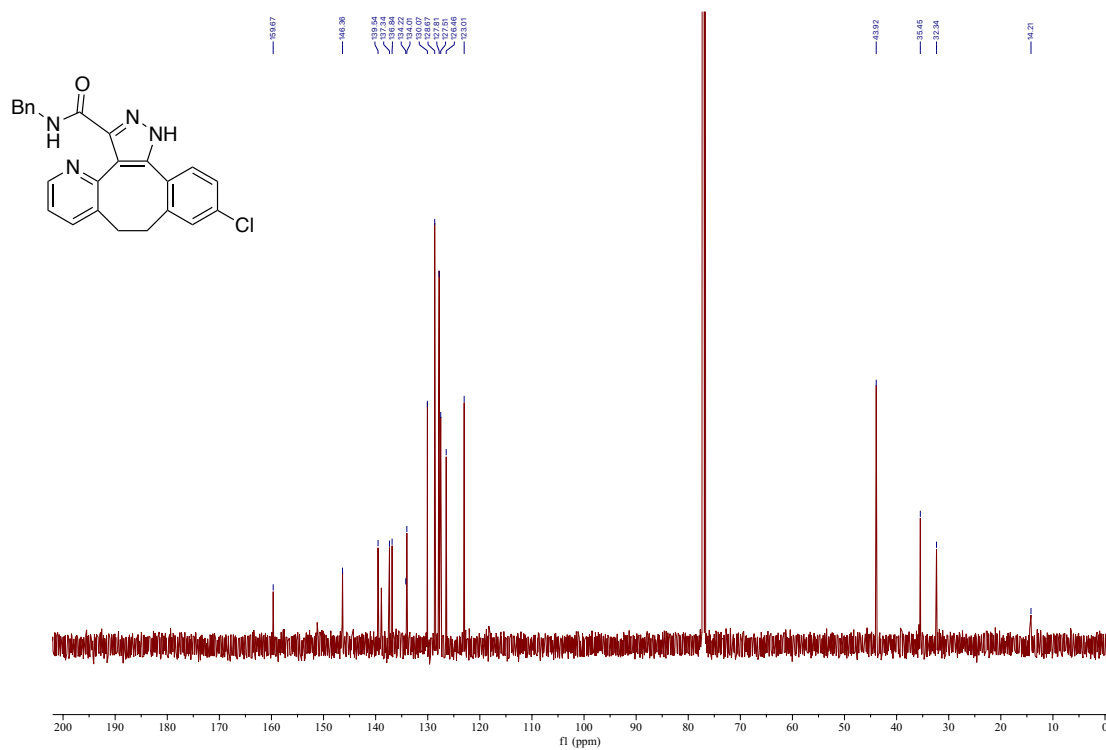
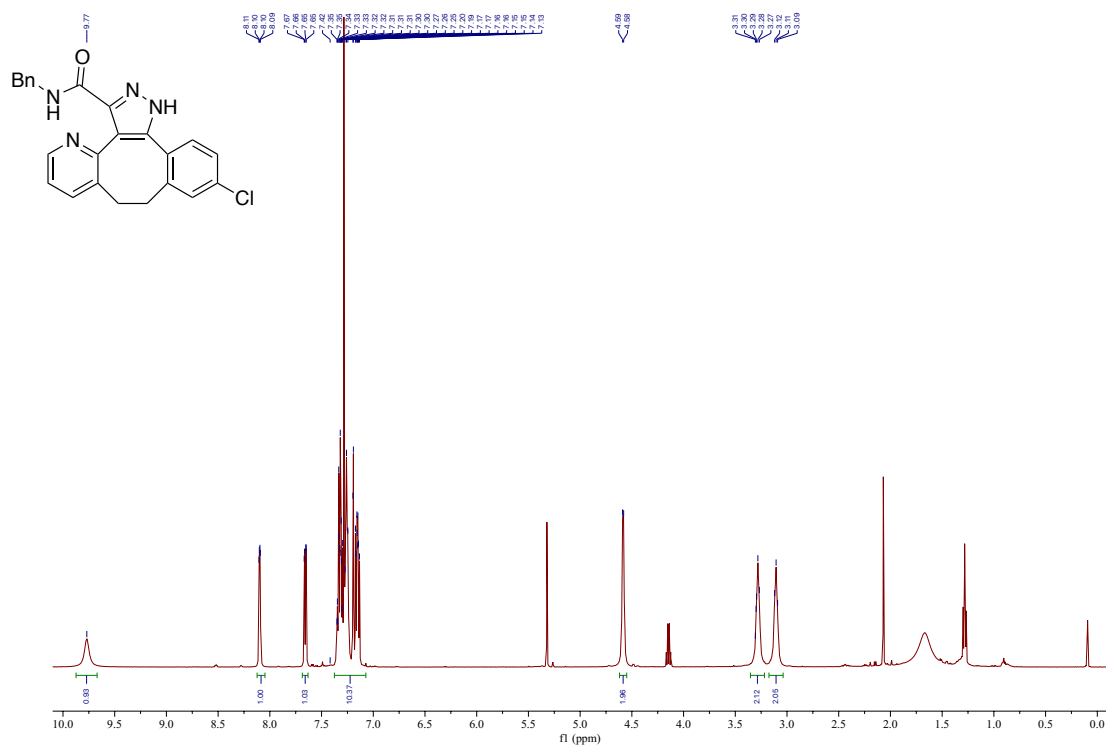
**$^1\text{H}$  and  $^{13}\text{C}$  NMR Spectra of Dibenzocyclooctyne (DIBO)**

**$^1\text{H}$  and  $^{13}\text{C}$  NMR Spectra of 2-Azido-*N*-methyl-*N*-(phenylmethyl)acetamide (11)**

**$^1\text{H}$  and  $^{13}\text{C}$  NMR Spectra of 2-Diazo-*N*-methyl-*N*-(phenylmethyl)acetamide (12)**

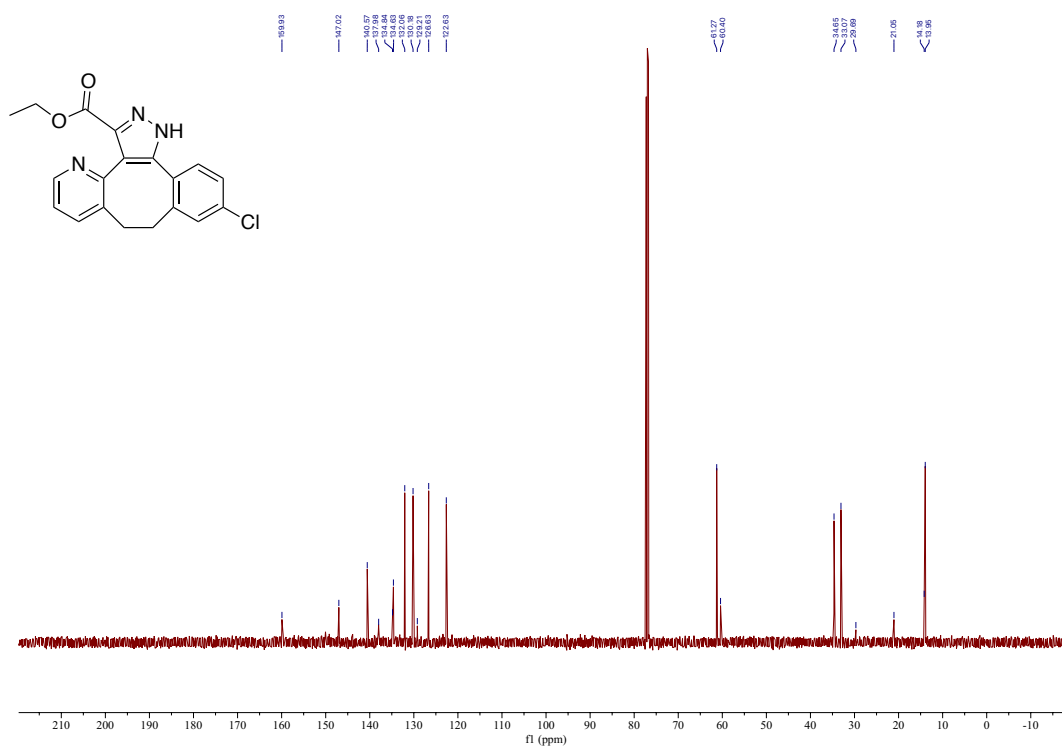
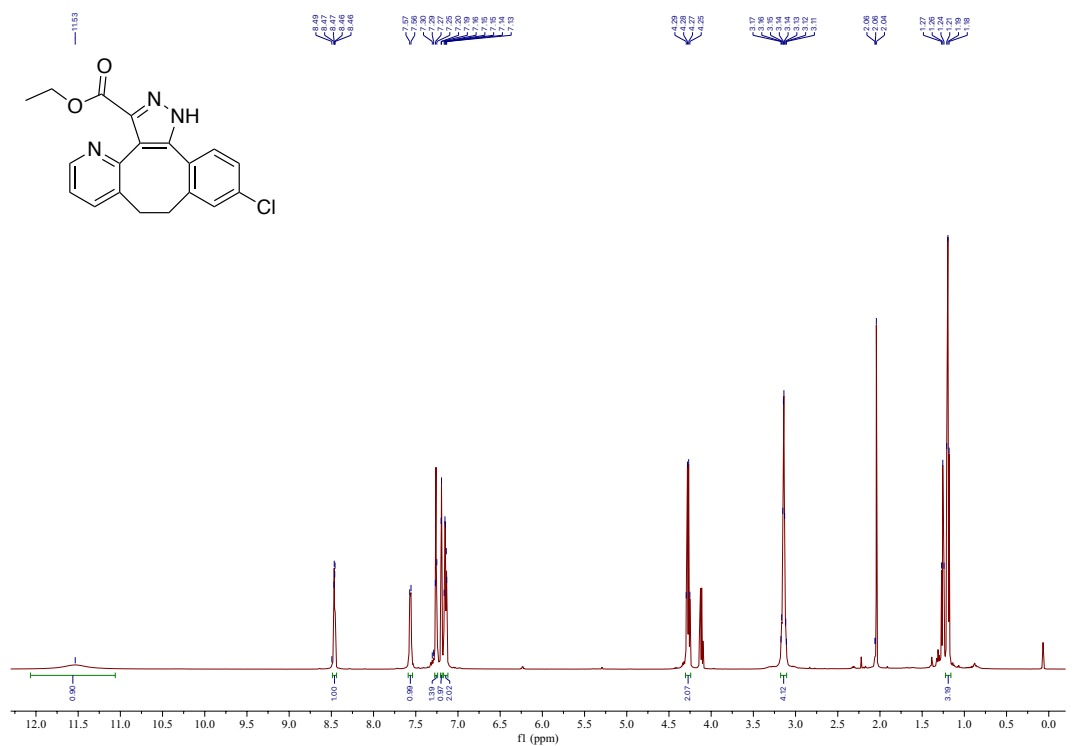


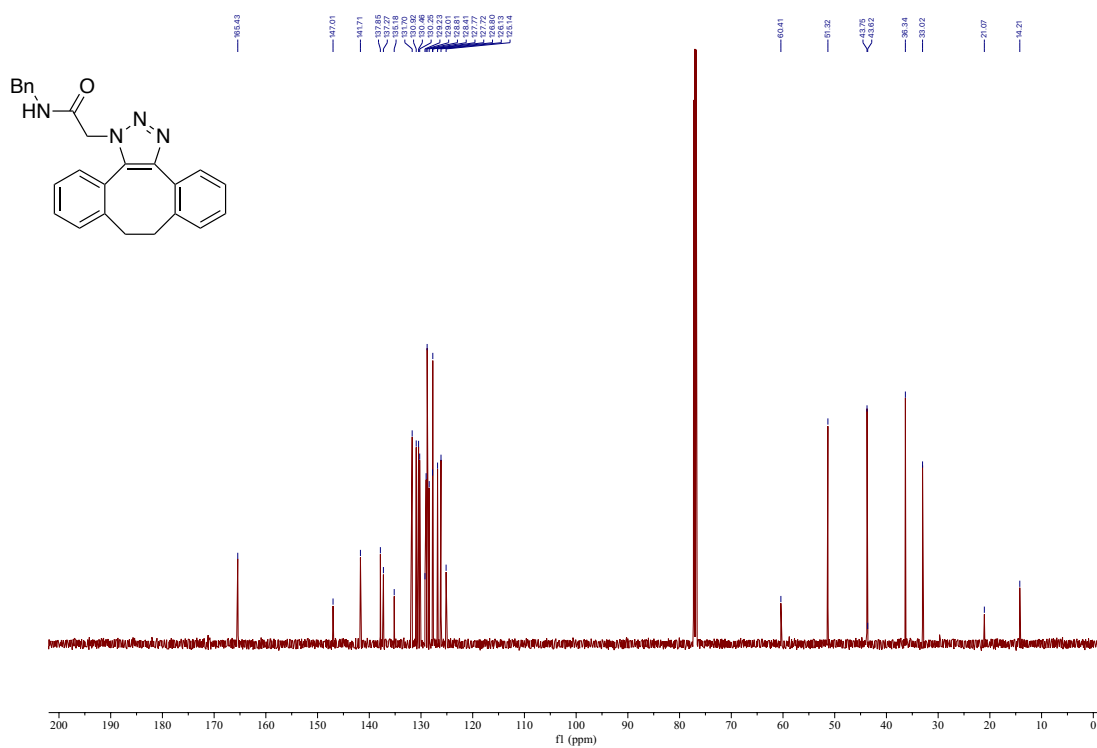
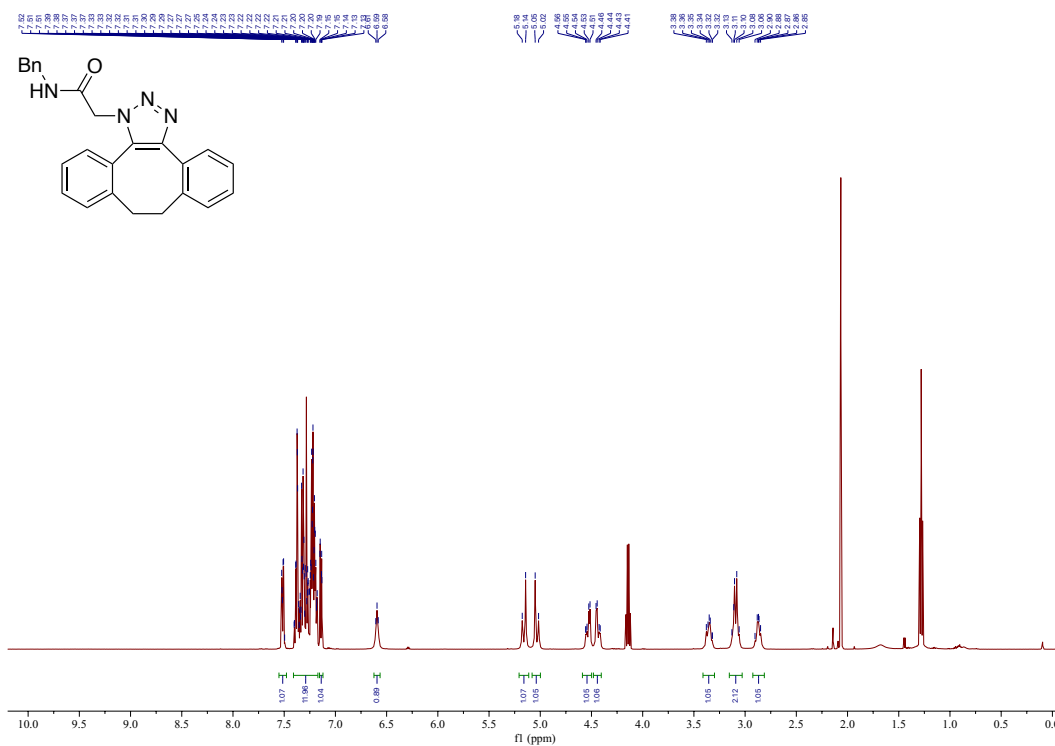
**$^1\text{H}$  and  $^{13}\text{C}$  NMR Spectra of ABC-N-Benzyl diazoacetamide Cycloadduct (13)**

**$^1\text{H}$  and  $^{13}\text{C}$  NMR Spectra of ABC–N-Benzylazidoacetamide Cycloadduct (14)**

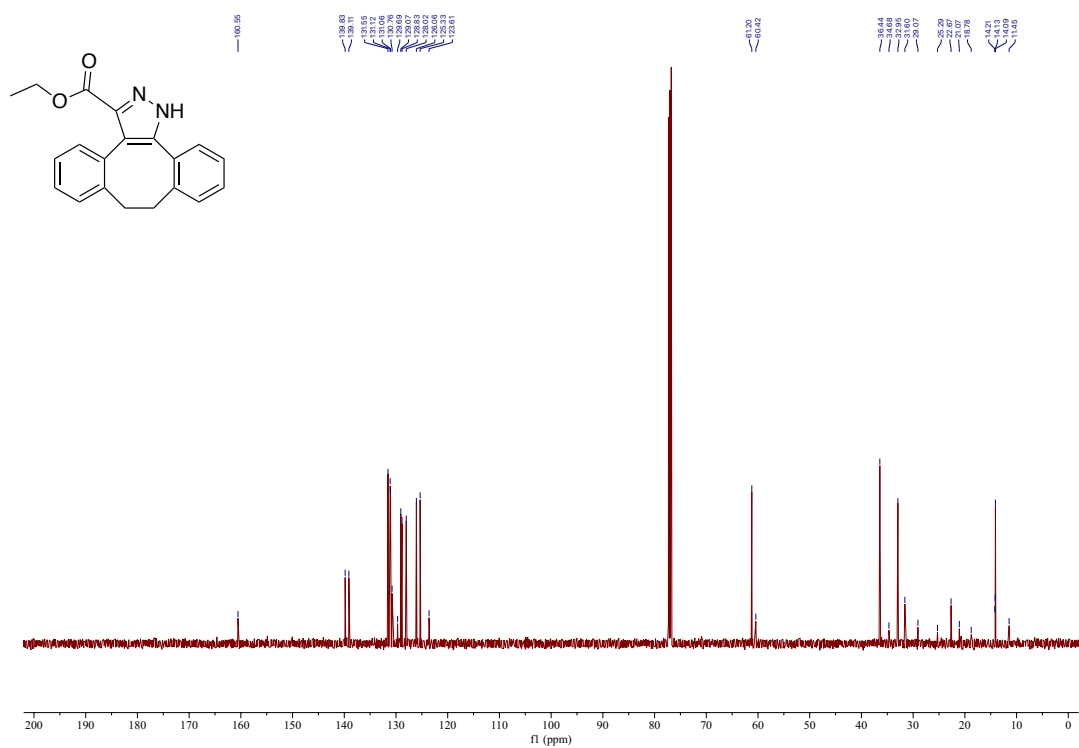
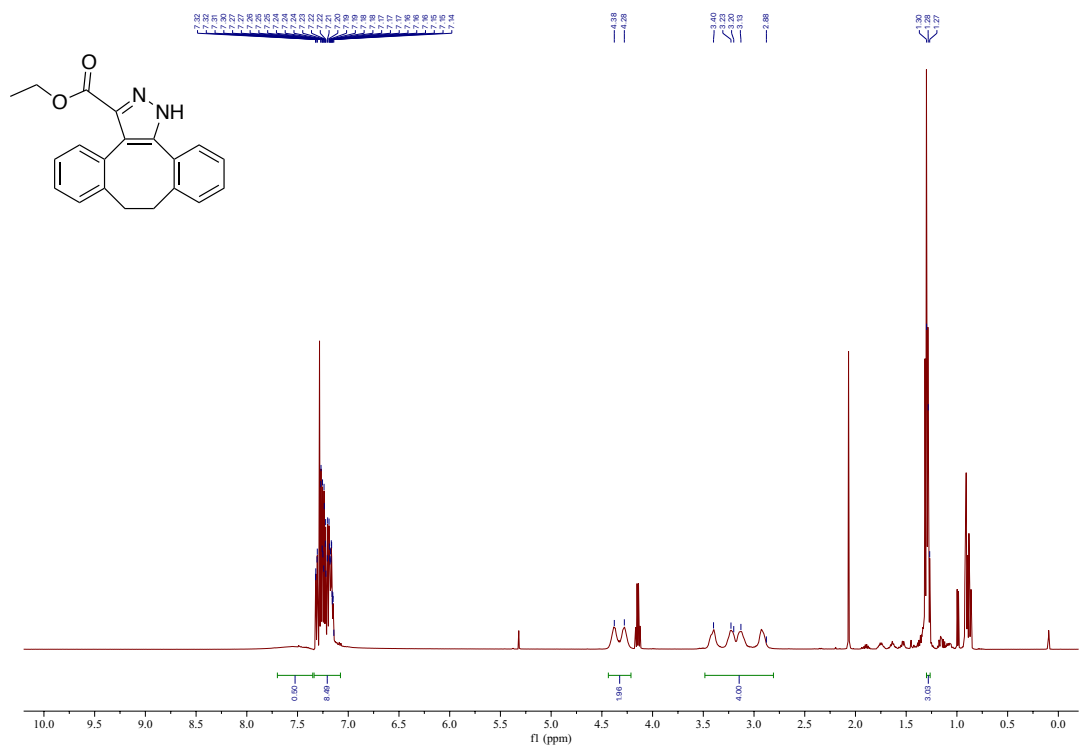




**$^1\text{H}$  and  $^{13}\text{C}$  NMR Spectra of ABC-Ethyl diazoacetate Cycloadduct (17)**

**$^1\text{H}$  and  $^{13}\text{C}$  NMR Spectra of DIBO-*N*-Benzylazidoacetamide Cycloadduct (18)**



**$^1\text{H}$  and  $^{13}\text{C}$  NMR Spectra of DIBO–Ethyl diazoacetate Cycloadduct (20)**



## References

1. Shoulders, M. D.; Raines, R. T., Collagen structure and stability. *Annu. Rev. Biochem.* **2009**, *78*, 929-958.
2. Adzhubei, A. A.; Sternberg, M. J. E.; Makarov, A. A., Polyproline-II Helix in Proteins: Structure and Function. *J Mol Biol* **2013**, *425* (12), 2100-2132.
3. Ramshaw, J. A. M.; Shah, N. K.; Brodsky, B., Gly-X-Y tripeptide frequencies in collagen: A context for host-guest triple-helical peptides. *J. Struct. Biol.* **1998**, *122*, 86-91.
4. Theocharis, A. D.; Skandalis, S. S.; Gialeli, C.; Karamanos, N. K., Extracellular matrix structure. *Adv. Drug Delivery Rev.* **2016**, *97*, 4-27.
5. Brazel, D.; Oberbäumer, I.; Dieringer, H.; Babel, W.; Glanville, R. W.; Deutzmann, R.; Kuhn, K., Completion of the amino acid sequence of the  $\alpha 1$  chain of human basement membrane collagen (type IV) reveals 21 non-triplet interruptions located within the collagenous domain. *Eur. J. Biochem.* **1987**, *168*, 529-536.
6. Bella, J.; Eaton, M.; Brodsky, B.; Berman, H. M., Crystal and molecular structure of a collagen-like peptide at 1.9 Å resolution. *Science* **1994**, *266*, 75-81.
7. Bella, J.; Brodsky, B.; Berman, H. M., Disrupted collagen architecture in the crystal structure of a triple-helical peptide with a Gly $\rightarrow$ Ala substitution. *Connect. Tissue Res.* **1996**, *35*, 401-406.
8. Bretscher, L. E.; Jenkins, C. L.; Taylor, K. M.; DeRider, M. L.; Raines, R. T., Conformational stability of collagen relies on a stereoelectronic effect. *J. Am. Chem. Soc.* **2001**, *123*, 777-778.
9. Hinderaker, M. P.; Raines, R. T., An electronic effect on protein structure. *Protein Sci.* **2003**, *12*, 1188-1194.
10. Berg, R. A.; Prockop, D. J., The thermal transition of a non-hydroxylated form of collagen. Evidence for a role for hydroxyproline in stabilizing the triple helix of collagen. *Biochem. Biophys. Res. Commun.* **1973**, *52*, 115-120.
11. Suzuki, E.; Fraser, R. D. B.; MacRae, T. P., Role of hydroxyproline in the stabilization of the collagen molecule via water molecules. *Int. J. Biol. Macromol.* **1980**, *2*, 54-56.
12. Vitagliano, L.; Berisio, R.; Mazzarella, L.; Zagari, A., Structural bases of collagen stabilization induced by proline hydroxylation. *Biopolymers* **2001**, *58*, 459-464.
13. Eberhardt, E. S.; Panasik, N., Jr.; Raines, R. T., Inductive effects on the energetics of prolyl peptide bond isomerization: Implications for collagen folding and stability. *J. Am. Chem. Soc.* **1996**, *118*, 12261-12266.
14. Shoulders, M. D.; Hodges, J. A.; Raines, R. T., Reciprocity of steric and stereoelectronic effects in the collagen triple helix. *J. Am. Chem. Soc.* **2006**, *128*, 8112-8113.
15. DeRider, M. L.; Wilkens, S. J.; Waddell, M. J.; Bretscher, L. E.; Weinhold, F.; Raines, R. T.; Markley, J. L., Collagen stability: Insights from NMR spectroscopic and hybrid density functional computational investigations of the effect of electronegative substituents on prolyl ring conformations. *J. Am. Chem. Soc.* **2002**, *124*, 2497-2505.
16. Newberry, R. W.; Raines, R. T., 4-Fluoroproline: Conformational analysis and effects on the stability and folding of peptides and proteins. *Top. Heterocycl. Chem.* **2017**, *48*, 1-26.
17. Zhang, Y.; Malamakal, R. M.; Chenoweth, D. M., Aza-Glycine Induces Collagen Hyperstability. *Journal of the American Chemical Society* **2015**, *137* (39), 12422-12425.
18. Zhang, Y.; Herling, M.; Chenoweth, D. M., General Solution for Stabilizing Triple Helical Collagen. *J. Am. Chem. Soc.* **2016**, *138* (31), 9751-9754.
19. Kasznel, A. J.; Zhang, Y.; Hai, Y.; Chenoweth, D. M., Structural Basis for Aza-Glycine Stabilization of Collagen. *J. Am. Chem. Soc.* **2017**, *139* (28), 9427-9430.

20. Van Der Rest, M.; Garrone, R., Collagen family of proteins. *The FASEB Journal* **1991**, *5* (13), 2814-2823.
21. Long, C. G.; Thomas, M.; Brodsky, B., Atypical Gly-X-Y sequences surround interruptions in the repeating tripeptide pattern of basement membrane collagen. *Biopolymers* **1995**, *35*, 621-628.
22. Leikina, E.; Merts, M. V.; Kuznetsova, N.; Leikin, S., Type I collagen is thermally unstable at body temperature. *Proc. Natl. Acad. Sci. U.S.A.* **2002**, *99*, 1314-1318.
23. Wang, A. Y.; Mo, X.; Chen, C. S.; Yu, S. M., Facile modification of collagen directed by collagen mimetic peptides. *J. Am. Chem. Soc.* **2005**, *127*, 4130-4131.
24. Hwang, J.; Huang, Y.; Burwell, T. J.; Peterson, N. C.; Connor, J.; Weiss, S. J.; Yu, S. M.; Li, Y., In situ imaging of tissue remodeling with collagen hybridizing peptides. *ACS Nano* **2017**, *11* (10), 9825-9835.
25. Beck, K.; Chan, V. C.; Shenoy, N.; Kirkpatrick, A.; Ramshaw, J. A. M.; Brodsky, B., Destabilization of osteogenesis imperfecta collagen-like model peptides correlates with the identity of the residue replacing glycine. *Proc. Natl. Acad. Sci. U.S.A.* **2000**, *97*, 4273-4278.
26. Bodian, D. L.; Madhan, B.; Brodsky, B.; Klein, T. E., Predicting the Clinical Lethality of Osteogenesis Imperfecta from Collagen Glycine Mutations. *Biochemistry* **2008**, *47* (19), 5424-5432.
27. Myllyharju, J., Prolyl 4-hydroxylases, key enzymes in the synthesis of collagens and regulation of the response to hypoxia, and their roles as treatment targets. *Ann. Med.* **2008**, *40*, 402-417.
28. Gilkes, D. M.; Chaturvedi, P.; Bajpai, S.; Wong, C. C.; Wei, H.; Pitcairn, S.; Hubbi, M. E.; Wirtz, D.; Semenza, G. L., Collagen Prolyl Hydroxylases Are Essential for Breast Cancer Metastasis. *Cancer Research* **2013**, *73* (11), 3285.
29. Kersteen, E. A.; Raines, R. T., Contribution of tertiary amides to the conformational stability of collagen triple helices. *Biopolymers* **2001**, *59*, 24-28.
30. Hodges, J. A.; Raines, R. T., Stereoelectronic and steric effects in the collagen triple helix: Toward a code for strand association. *J. Am. Chem. Soc.* **2005**, *127*, 15923-15932.
31. Chattopadhyay, S.; Raines, R. T., Collagen-based biomaterials for wound healing. *Biopolymers* **2014**, *101* (8), 821-833.
32. Seo, N.; Russell, B. H.; Rivera, J. J.; Liang, X.; Xu, X.; Afshar-Kharghan, V.; Höök, M., An engineered  $\alpha_1$  integrin-binding collagenous sequence. *J. Biol. Chem.* **2010**, *285*, 31046-31054.
33. An, B.; DesRochers, T. M.; Qin, G.; Xia, X.; Thiagarajan, G.; Brodsky, B.; Kaplan, D. L., The influence of specific binding of collagen-silk chimeras to silk biomaterials on hMSC behavior. *Biomaterials* **2013**, *34* (2), 402-412.
34. Peng, Y. Y.; Stoichevska, V.; Schacht, K.; Werkmeister, J. A.; Ramshaw, J. A. M., Engineering multiple biological functional motifs into a blank collagen-like protein template from *Streptococcus pyogenes*. *J. Biomed. Mater. Res. Part A* **2014**, *102* (7), 2189-2196.
35. Yu, Z.; Visse, R.; Inouye, M.; Nagase, H.; Brodsky, B., Defining requirements for collagenase cleavage in collagen type III using a bacterial collagen system. *J. Biol. Chem.* **2012**, *287* (27), 22988-22997.
36. Versteegen, R. M.; Rossin, R.; ten Hoeve, W.; Janssen, H. M.; Robillard, M. S., Click to Release: Instantaneous Doxorubicin Elimination upon Tetrazine Ligation. *Angew. Chem. Int. Ed.* **2013**, *52* (52), 14112-14116.
37. Devaraj, N. K., The Future of Bioorthogonal Chemistry. *ACS Cent. Sci.* **2018**, *4* (8), 952-959.
38. Klemperer, P., The concept of collagen diseases. *Am. J. Pathol.* **1950**, *26* (4), 505-519.

39. Coelho, N. M.; McCulloch, C. A., Contribution of collagen adhesion receptors to tissue fibrosis. *Cell Tissue Res.* **2016**, *365* (3), 521-538.
40. Conklin, M. W.; Eickhoff, J. C.; Riching, K. M.; Pehlke, C. A.; Eliceiri, K. W.; Provenzano, P. P.; Friedl, A.; Keely, P. J., Aligned collagen is a prognostic signature for survival in human breast carcinoma. *Am. J. Pathol.* **2011**, *178* (3), 1221-1232.
41. Provenzano, P. P.; Eliceiri, K. W.; Campbell, J. M.; Inman, D. R.; Shite, J. G.; Keely, P. J., Collagen reorganization at the tumor-stromal interface facilitates local invasion. *BMC Med.* **2006**, *4*, 38.
42. Hollander, A. P.; Heathfield, T. F.; Webber, C.; Iwata, Y.; Bourne, R.; Rorabeck, C.; Poole, A. R., Increased damage to type II collagen in osteoarthritic articular cartilage detected by a new immunoassay. *J. Clin. Invest.* **1994**, *93* (4), 1722-1732.
43. Xu, S.; Xu, H.; Wang, W.; Li, S.; Li, H.; Li, T.; Zhang, W.; Yu, X.; Liu, L., The role of collagen in cancer: from bench to bedside. *J. Transl. Med.* **2019**, *17* (1), 309.
44. Balu, M.; Mazhar, A.; Hayakawa, Carole K.; Mittal, R.; Krasieva, Tatiana B.; König, K.; Venugopalan, V.; Tromberg, Bruce J., In Vivo Multiphoton NADH Fluorescence Reveals Depth-Dependent Keratinocyte Metabolism in Human Skin. *Biophys. J.* **2013**, *104* (1), 258-267.
45. Kretschmer, S.; Pieper, M.; Hüttmann, G.; Bölke, T.; Wollenberg, B.; Marsh, L. M.; Garn, H.; König, P., Autofluorescence multiphoton microscopy for visualization of tissue morphology and cellular dynamics in murine and human airways. *Lab. Invest.* **2016**, *96* (8), 918-931.
46. Skala, M. C.; Riching, K. M.; Gendron-Fitzpatrick, A.; Eickhoff, J.; Eliceiri, K. W.; White, J. G.; Ramanujam, N., *In vivo* multiphoton microscopy of NADH and FAD redox states, fluorescence lifetimes, and cellular morphology in precancerous epithelia. *Proc. Natl. Acad. Sci.* **2007**, *104* (49), 19494.
47. Freund, I.; Deutsch, M.; Sprecher, A., Connective tissue polarity. Optical second-harmonic microscopy, crossed-beam summation, and small-angle scattering in rat-tail tendon. *Biophys. J.* **1986**, *50* (4), 693-712.
48. Campagnola, P. J.; Dong, C. Y., Second harmonic generation microscopy: principles and applications to disease diagnosis. *Laser Photonics Rev.* **2011**, *5* (1), 13-26.
49. Campagnola, P., Second Harmonic Generation Imaging Microscopy: Applications to Diseases Diagnostics. *Anal. Chem.* **2011**, *83* (9), 3224-3231.
50. Chen, X.; Nadiarynkh, O.; Plotnikov, S.; Campagnola, P. J., Second harmonic generation microscopy for quantitative analysis of collagen fibrillar structure. *Nat. Protoc.* **2012**, *7* (4), 654-669.
51. Conklin, M. W.; Eickhoff, J. C.; Riching, K. M.; Pehlke, C. A.; Eliceiri, K. W.; Provenzano, P. P.; Friedl, A.; Keely, P. J., Aligned Collagen Is a Prognostic Signature for Survival in Human Breast Carcinoma. *Am. J. Pathol.* **2011**, *178* (3), 1221-1232.
52. Sung-Jan, L.; Chih-Jung, H.; Ruei-Jr, W.; Chien-Jui, K.; Jau-Shiuh, C.; Jung-Yi, C.; Wei-Chou, L.; Shiou-Hwa, J.; Chen-Yuan, D. In *Quantitative multiphoton imaging for guiding basal-cell carcinoma removal*, Proc.SPIE, 2007.
53. Mumtaz, S.; Schomaker, N.; Von Roenn, N., Pro: Noninvasive Imaging Has Replaced Biopsy as the Gold Standard in the Evaluation of Nonalcoholic Fatty Liver Disease. *Clin. Liver Dis.* **2019**, *13* (4), 111-113.
54. Darian, S. J.; Alexander, N. J.; Hsin-Yu, C.; Zachary, A.; Karissa, B. T.; Nathan, K. S.; Paul, J. C., Probing ECM remodeling in idiopathic pulmonary fibrosis via second harmonic generation microscopy analysis of macro/supramolecular collagen structure. *J. Biomed. Opt.* **2019**, *25* (1), 1-13.

55. Wanxin, S.; Shi, C.; Dean, C. S. T.; Nancy, T.; Guangfa, X.; Huihuan, T.; Hanry, Y., Nonlinear optical microscopy: use of second harmonic generation and two-photon microscopy for automated quantitative liver fibrosis studies. *J. Biomed. Opt.* **2008**, *13* (6), 1-7.
56. Organization, W. H. Burn Fact Sheets. (accessed April 1, 2021).
57. Paul, D. W.; Ghassemi, P.; Ramella-Roman, J. C.; Prindeze, N. J.; Moffatt, L. T.; Alkhalil, A.; Shupp, J. W., Noninvasive imaging technologies for cutaneous wound assessment: A review. *Wound Repair Regen.* **2015**, *23* (2), 149-162.
58. Tanaka, R.; Fukushima, S.; Sasaki, K.; Tanaka, Y.; Murota, H.; Matsumoto, T.; Araki, T.; Yasui, T., In vivo visualization of dermal collagen fiber in skin burn by collagen-sensitive second-harmonic-generation microscopy. *J. Biomed. Opt.* **2013**, *18* (6), 8.
59. Tilbury, K.; Campagnola, P. J., Applications of Second-Harmonic Generation Imaging Microscopy in Ovarian and Breast Cancer. *Perspect. Medicin. Chem.* **2015**, *7*, PMC.S13214.
60. Lu, P.; Takai, K.; Weaver, V. M.; Werb, Z., Extracellular matrix degradation and remodeling in development and disease. *Cold Spring Harb. Perspect. Biol.* **2011**, *3* (12), a005058.
61. Kirkpatrick, N. D.; Brewer, M. A.; Utzinger, U., Endogenous optical biomarkers of ovarian cancer evaluated with multiphoton microscopy. *Cancer Epidemiol. Biomarkers Prev.* **2007**, *16* (10), 2048-2057.
62. Lin, S. J.; Jee, S. H.; Kuo, C. J.; Wu, R. J.; Lin, W. C.; Chen, J. S.; Liao, Y. H.; Hsu, C. J.; Tsai, T. F.; Chen, Y. F.; Dong, C. Y., Discrimination of basal cell carcinoma from normal dermal stroma by quantitative multiphoton imaging. *Opt. Lett.* **2006**, *31* (18), 2756-2758.
63. Dimitrow, E.; Ziemer, M.; Koehler, M. J.; Norgauer, J.; Konig, K.; Elsner, P.; Kaatz, M., Sensitivity and specificity of multiphoton laser tomography for *in vivo* and *ex vivo* diagnosis of malignant melanoma. *J. Invest. Dermatol.* **2009**, *129* (7), 1752-1758.
64. Skala, M. C.; Squirrell, J. M.; Vrotsos, K. M.; Eickhoff, J. C.; Gendron-Fitzpatrick, A.; Eliceiri, K. W.; Ramanujam, N., Multiphoton microscopy of endogenous fluorescence differentiates normal, precancerous, and cancerous squamous epithelial tissues. *Cancer Res.* **2005**, *65* (4), 1180-1186.
65. Okuyama, K.; Hongo, C.; Fukushima, R.; Wu, G.; Narita, H.; Noguchi, K.; Tanaka, Y.; Nishino, N., Crystal structures of collagen model peptides with Pro-Hyp-Gly repeating sequence at 1.26 Å resolution: Implications for proline ring puckering. *Biopolymers: Pept. Sci.* **2004**, *76*, 367-377.
66. Shoulders, M. D.; Raines, R. T., Modulating collagen triple-helix stability with 4-chloro, 4-fluoro, and 4-methylprolines. *Adv. Exp. Med. Biol.* **2009**, *611*, 251-252.
67. Hodges, J. A.; Raines, R. T., Stereoelectronic effects on collagen stability: The dichotomy of 4-fluoroproline diastereomers. *J. Am. Chem. Soc.* **2003**, *125*, 9262-9263.
68. Chattopadhyay, S.; Raines, R. T., Collagen-based biomaterials for wound healing. *Biopolymers* **2014**, *101*, 821-833.
69. Wahyudi, H.; Reynolds, A. A.; Li, Y.; Owen, S. C.; Yu, S. M., Targeting collagen for diagnostic imaging and therapeutic delivery. *J. Control. Release* **2016**, *240*, 323-331.
70. Siebler, C.; Erdmann, R. S.; Wennemers, H., From azidoproline to functionalizable collagen. *Chimia* **2013**, *67*, 891-895.
71. Shekhter, A. B.; Fayzullin, A. L.; Vukolova, M. N.; Rudenko, T. G.; Osipycheva, V. D.; Litvitsky, P. F., Medical applications of collagen and collagen-based materials. *Curr. Med. Chem.* **2019**, *26*, 506-516.
72. Chattopadhyay, S.; Murphy, C. J.; McAnulty, J. F.; Raines, R. T., Peptides that anneal to natural collagen *in vitro* and *ex vivo*. *Org. Biomol. Chem.* **2012**, *10*, 5892-5897.
73. Ellison, A. J.; Raines, R. T., A pendant peptide endows a sunscreen with water-resistance. *Org. Biomol. Chem.* **2018**, *16*, 7139-7142.

74. Chattopadhyay, S.; Guthrie, K. M.; Teixeira, L.; Murphy, C. J.; Dubielzig, R. R.; McAnulty, J. F.; Raines, R. T., Anchoring a cytoactive factor in a wound bed promotes healing. *J. Tissue. Eng. Regen. Med.* **2016**, *10* (12), 1012-1020.
75. Kerns, E. H.; Di, L., *Drug Like Properties: Concept, Structure, Design and Methods, from ADME to Toxicity Optimization*. Elsevier: Boston, MA, 2008.
76. Li, Y.; Foss, C. A.; Pomper, M. G.; Yu, S. M., Imaging denatured collagen strands *in vivo* and *ex vivo* via photo-triggered hybridization of caged collagen mimetic peptides. *J. Vis. Exp.* **2014**, e51052.
77. Li, Y.; Foss, C. A.; Summerfield, D. D.; Doyle, J. J.; Torok, C. M.; Dietz, H. C.; Pomper, M. G.; Yu, S. M., Targeting collagen strands by photo-triggered triple-helix hybridization. *Proc. Natl. Acad. Sci. USA* **2012**, *109*, 14767-14772.
78. Berisio, R.; Vitagliano, L.; Mazzarella, L.; Zagari, A., Crystal structure of the collagen triple helix model [(Pro-Pro-Gly)<sub>10</sub>]<sub>3</sub>. *Protein. Sci.* **2002**, *11* (2), 262-270.
79. Mayo, S. L.; Olafson, B. D.; Goddard, W. A., DREIDING: A generic force field for molecular simulations. *J. Phys. Chem.* **1990**, *94* (26), 8897-8909.
80. MacKerell, A. D., Jr.; Bashford, D.; Bellott, M.; Dunbrack, R. L., Jr.; Evanseck, J. D.; Field, M. J.; Fischer, S.; Gao, J.; Guo, H.; Ha, S.; Joseph-McCarthy, D.; Kuchnir, L.; Kuczera, K.; Lau, F. T.; Mattos, C.; Michnick, S.; Ngo, T.; Nguyen, D. T.; Prodhom, B.; Reiher, W. E.; Roux, B.; Schlenkrich, M.; Smith, J. C.; Stote, R.; Straub, J.; Watanabe, M.; Wiórkiewicz-Kuczera, J.; Yin, D.; Karplus, M., All-atom empirical potential for molecular modeling and dynamics studies of proteins. *J. Phys. Chem.* **1998**, *B102* (18), 3586-3616.
81. Shoulders, M. D.; Guzei, I. A.; Raines, R. T., 4-Chloroprolines: Synthesis, conformational analysis, and incorporation in collagen triple helices. *Biopolymers* **2008**, *89*, 443-454.
82. Chorghade, M. S.; Mohapatra, D. K.; Sahoo, G.; Gurjar, M. K.; Mandlecha, M. V.; Bhoite, N.; Moghe, S.; Raines, R. T., Practical syntheses of 4-fluoroprolines. *J. Fluorine Chem.* **2008**, *129*, 781-784.
83. Bennink, L. L.; Li, Y.; Kim, B.; Shin, I. J.; San, B. H.; Zangari, M.; Yoon, D.; Yu, S. M., Visualizing collagen proteolysis by peptide hybridization: From 3D cell culture to *in vivo* imaging. *Biomaterials* **2018**, *183*, 67-76.
84. Barth, D.; Milbradt, A. G.; Renner, C.; Moroder, L., A (4*R*)- or a (4*S*)-fluoroproline residue in position Xaa of the (Xaa-Yaa-Gly) collagen repeat severely affects triple-helix formation. *ChemBioChem* **2004**, *5*, 79-86.
85. Lopes, J. L.; Miles, A. J.; Whitmore, L.; Wallace, B. A., Distinct circular dichroism spectroscopic signatures of polyproline II and unordered secondary structures: Applications in secondary structure analyses. *Protein Sci.* **2014**, *23* (12), 1765-1772.
86. Inouye, K.; Kobayashi, Y.; Kyogoku, Y.; Kishida, Y.; Sakakibara, S.; Prockop, D. J., Synthesis and physical properties of (Hydroxyproline-Proline-Glycine)<sub>10</sub>. Hydroxyproline in the X-position decreases the melting temperature of the collagen triple helix. *Arch. Biochem. Biophys.* **1982**, *219*, 198-203.
87. Zhang, H.; Li, Y.; Jiang, Z.-X., Fluorine is flourishing in pharmaceuticals. *J. Biomol. Res. Ther.* **2012**, *1*, e107.
88. Cory, A. H.; Owen, T. C.; Barltrop, J. A.; Cory, J. G., Use of an aqueous soluble tetrazolium/formazan assay for cell growth assays in culture. *Cancer Commun.* **1991**, *3*, 207-212.
89. Roth, S.; Freund, I., Second harmonic generation in collagen. *J. Chem. Phys.* **1979**, *70*, 1637-1643.
90. Rajan, N.; Habermehl, J.; Cote, M. F.; Doillon, C. J.; Mantovani, D., Preparation of ready-to-use, storable and reconstituted type I collagen from rat tail tendon for tissue engineering applications. *Nat. Protoc.* **2006**, *1* (6), 2753-2758.

91. Waggoner, A.; Kenneth, S., Covalent labeling of proteins and nucleic acids with fluorophores. *Methods Enzymol.* **1995**, *246*, 362-373.
92. Mostaçõ-Guidolin, L.; Rosin, N. L.; Hackett, T. L., Imaging collagen in scar tissue: Developments in second harmonic generation microscopy for biomedical applications. *Int. J. Mol. Sci.* **2017**, *18*, E1772.
93. Tran, R. J.; Sly, K. L.; Conboy, J. C., Applications of surface second harmonic generation in biological sensing. *Annu. Rev. Anal. Chem.* **2017**, *10*, 387-414.
94. Keikhosravi, A.; Bredfeldt, J. S.; Sagar, A. K.; Eliceiri, K. W., Second-harmonic generation imaging of cancer. *Methods Cell Biol.* **2014**, *123*, 531-546.
95. Rueden, C. T.; Schindelin, J.; Hiner, M. C.; DeZonia, B. E.; Walter, A. E.; Arena, E. T.; Eliceiri, K. W., ImageJ2: ImageJ for the next generation of scientific image data. *BMC Bioinformatics* **2017**, *18* (1), 529.
96. Rybarczyk, M. M.; Schafer, J. M.; Elm, C. M.; Sarvepalli, S.; Vaswani, P. I.; Balhara, K. S.; Carlson, L. C.; Jacquet, G. A., A systematic review of burn injuries in low- and middle-income countries: Epidemiology in the WHO-defined African Region. *Afr. J. Emerg. Med.* **2017**, *7*, 30-37.
97. Karim, A. S.; Yan, A.; Ocotl, E.; Bennett, D. D.; Wang, Z.; Kendzioriski, C.; Gibson, A. L. F., *Wound Repair Regen.* **2018**, *27*, 150-161.
98. Thatcher, J. E.; Squiers, J. J.; Kanick, S. C.; King, D. R.; Lu, Y.; Wang, Y.; Mohan, R.; Sellke, E. W.; DiMaio, J. M., *Adv. Wound Care* **2016**, *5*, 360-378.
99. Shoulders, M. D.; Satyshur, K. A.; Forest, K. T.; Raines, R. T., Stereoelectronic and steric effects in side chains preorganize a protein main chain. *Proc. Natl. Acad. Sci. USA* **2010**, *107* (2), 559-64.
100. Word, J. M.; Lovell, S. C.; LaBean, T. H.; Taylor, H. C.; Zalis, M. E.; Presley, B. K.; Richardson, J. S.; Richardson, D. C., Visualizing and quantifying molecular goodness-of-fit: Small-probe contact dots with explicit hydrogen atoms. *J. Mol. Biol.* **1999**, *285* (4), 1711-1733.
101. Lim, K.-T.; Brunett, S.; Iotov, M.; McClurg, R. B.; Vaidehi, N.; Dasgupta, S.; Taylor, S.; Goddard, W., Molecular dynamics for very large systems on massively parallel computers: The MPSim program. *J. Comput. Chem.* **1997**, *18*, 501-521.
102. Wahyudi, H.; Reynolds, A. A.; Li, Y.; Owen, S. C.; Yu, S. M., Targeting collagen for diagnostic imaging and therapeutic delivery. *J. Controlled Release* **2016**, *240*, 323-331.
103. Dones, J. M.; Tanrikulu, I. C.; Chacko, J. V.; Schroeder, A. B.; Hoang, T. T.; Gibson, A. L. F.; Eliceiri, K. W.; Raines, R. T., Optimization of interstrand interactions enables burn detection with a collagen-mimetic peptide. *Org. Biomol. Chem.* **2019**, *17*, 9906-9912.
104. Chattopadhyay, S.; Murphy, C. J.; McAnulty, J. F.; Raines, R. T., Peptides that anneal to natural collagen *in vitro* and *ex vivo*. *Organic & biomolecular chemistry* **2012**, *10* (30), 5892-5897.
105. Song, J. Y.; Pineault, K. M.; Dones, J. M.; Raines, R. T.; Wellik, D. M., *Hox* genes maintain critical roles in the adult skeleton. *Proc. Natl. Acad. Sci. USA* **2020**, *117*, xxx-xxx.
106. Chattopadhyay, S.; Guthrie, K. M.; Teixeira, L.; Murphy, C. J.; Dubielzig, R. R.; McAnulty, J. F.; Raines, R. T., Anchoring a cytoactive factor in a wound bed promotes healing. *J. Tissue Eng. Regen. Med.* **2014**, *10* (12), 1012-1020.
107. Tanrikulu, I. C.; Raines, R. T., Optimal interstrand bridges for collagen-like biomaterials. *J. Am. Chem. Soc.* **2014**, *136* (39), 13490-13493.
108. Delsuc, N.; Uchinomiya, S.; Ojida, A.; Hamachi, I., A host-guest system based on collagen-like triple-helix hybridization. *Chem. Commun.* **2017**, *53* (51), 6856-6859.
109. Kotch, F. W.; Raines, R. T., Self-assembly of synthetic collagen triple helices. *Proc. Natl. Acad. Sci. USA* **2006**, *103*, 3028-3033.

110. Koide, T.; Homma, D. L.; Asada, S.; Kitagawa, K., Self-complementary peptides for the formation of collagen-like triple helical supramolecules. *Bioorg. Med. Chem. Lett.* **2005**, *15*, 5230-5233.
111. Yamazaki, C. M.; Asada, S.; Kitagawa, K.; Koide, T., Artificial collagen gels via self-assembly of *de novo* designed peptides. *Biopolymers* **2008**, *90*, 816-823.
112. Yamazaki, C. M.; Kadoya, Y.; Hozumi, K.; Okano-Kosugi, H.; Asada, S.; Kitagawa, K.; Nomizu, M.; Koide, T., A collagen-mimetic triple helical supramolecule that evokes integrin-dependent cell responses. *Biomaterials* **2010**, *31*, 1925-1934.
113. Sardi, F.; Manta, B.; Portillo-Ledesma, S.; Knoop, B.; Comini, M. A.; Ferrer-Sueta, G., Determination of acidity and nucleophilicity in thiols by reaction with monobromobimane and fluorescence detection. *Anal. Biochem.* **2013**, *435*, 74-82.
114. Kim, J.-S.; Raines, R. T., Dibromobimane as a fluorescent crosslinking reagent. *Anal. Biochem.* **1995**, *225*, 174-176.
115. Takita, K. K.; Fujii, K. K.; Ishii, K.; Koide, T., Structural optimization of cyclic peptides that efficiently detect denatured collagen. *Org. Biomol. Chem.* **2019**, *17*, 7380-7387.
116. Takita, K. K.; Fujii, K. K.; Kadonosono, T.; Masuda, R.; Koide, T., Cyclic peptides for efficient detection of collagen. *ChemBioChem* **2018**, *19*, 1613-1617.
117. Blackwell, H. E.; Clemons, P. A.; Schreiber, S. L., Exploiting site-site interactions on solid support to generate dimeric molecules. *Org. Lett.* **2001**, *3* (8), 1185-1188.
118. Blackwell, H. E.; Sadowsky, J. D.; Howard, R. J.; Sampson, J. N.; Chao, J. A.; Steinmetz, W. E.; O'Leary, D. J.; Grubbs, R. H., Ring-closing metathesis of olefinic peptides: Design, synthesis, and structural characterization of macrocyclic helical peptides. *J. Org. Chem.* **2001**, *66*, 5291-5302.
119. Fields, G. B.; Prockop, D. J., Perspective on the synthesis and application of triple-helical collagen-model peptides. *Biopolymers* **1996**, *40* (4), 345-357.
120. Hodges, J. A.; Raines, R. T., Stereoelectronic effects on collagen stability: The dichotomy of 4-fluoroproline diastereomers. *J. Am. Chem. Soc.* **2003**, *125*, 9263-9264.
121. Tamburro, A. M.; Guantieri, V.; Cabrol, D.; Broch, H.; Vasilescu, D., Experimental and theoretical conformational studies on polypeptide models of collagen. *Int. J. Pept. Protein Res.* **1984**, *24* (6), 627-635.
122. Persikov, A. V.; Ramshaw, J. A. M.; Kirkpatrick, A.; Brodsky, B., Amino acid propensities for the collagen triple-helix. *Biochemistry* **2000**, *29*, 14960-14967.
123. Hwang, J.; Huang, Y.; Burwell, T. J.; Peterson, N. C.; Connor, J.; Weiss, S. J.; Yu, S. M.; Li, Y., *In situ* imaging of tissue remodeling with collagen hybridizing peptides. *ACS Nano* **2017**, *11*, 9825-9835.
124. Tanrikulu, I. C.; Westler, W. M.; Ellison, A. J.; Markley, J. L.; Raines, R. T., Templated collagen "double helices" maintain their structure. *J. Am. Chem. Soc.* **2020**, *142*, 1137-1141.
125. Hintersteiner, M.; Buehler, C.; Auer, M., On-bead screens sample narrower affinity ranges of protein-ligand interactions compared to equivalent solution assays. *Chem. Phys. Chem.* **2012**, *13*, 3472-3480.
126. Daniel, C.; Roupioz, Y.; Gasparutto, D.; Livache, T.; Buhot, A., Solution-phase vs surface-phase aptamer-protein affinity from a label-free kinetic biosensor. *PLoS One* **2013**, *8*, e75419.
127. Holmgren, S.; Bretscher, L. E.; Taylor, K. M.; Raines, R. T., A hyperstable collagen mimic. *Chem. Biol.* **1999**, *6* (2), 67-70.
128. Holmgren, S.; Taylor, K.; Bretscher, L.; Raines, R. T., Code for collagen's stability deciphered. *Nature* **1998**, *392*, 666-667.
129. Bretscher, L.; Jenkins, C. L.; Taylor, K. M.; Raines, R. T., Conformational stability of collagen relies on a stereoelectronic effect. *J. Am. Chem. Soc.* **2001**, *123*, 777-778.

130. Davis, J. M.; Bächinger, H. P., Hysteresis in the triple helix-coil transition of type III collagen. *J. Biol. Chem.* **1993**, *268*, 25965-25972.
131. Mizuno, K.; Boudko, S. P.; Engel, J.; Bächinger, H. P., Kinetic hysteresis in collagen folding. *Biophys. J.* **2010**, *98*, 3004-3014.
132. Fischer, G., Chemical aspects of peptide bond isomerisation. *Chem. Soc. Rev.* **2000**, *29*, 119-127.
133. Egli, J.; Siebler, C.; Köhler, M.; Zenobi, R.; Wennemers, H., Hydrophobic moieties bestow fast-folding and hyperstability on collagen triple helices. *J. Am. Chem. Soc.* **2019**, *141*, 5607-5611.
134. Sweeney, S. M.; DiLullo, G.; Slater, S. J.; Martinez, J.; Iozzo, R. V.; Lauer-Fields, J. L.; Fields, G. B.; San Antonio, J. D., Angiogenesis in collagen I requires  $\alpha_2\beta_1$  ligation of a GFP\*GER sequence and possibly p38 MAPK activation and focal adhesion disassembly. *J. Biol. Chem.* **2003**, *278*, 30516-30523.
135. Knight, C. G.; Morton, L. F.; Onley, D. J.; Peachey, A. R.; Messent, A.; Smethurst, P. A.; Tuckwell, D. S.; Farndale, R. W.; Barnes, M. J., Identification in collagen type I of an integrin  $\alpha_2\beta_1$ -binding site containing an essential GER sequence. *J. Biol. Chem.* **1998**, *273*, 33287-33294.
136. Sipilä, K. H.; Drushinin, K.; Rappu, P.; Jokinen, J.; Salminen, T. A.; Salo, A. M.; Käpylä, J.; Myllyharju, J.; Heino, J., Proline hydroxylation in collagen supports integrin binding by two distinct mechanisms. *J. Biol. Chem.* **2018**, *293*, 7645-7658.
137. Scholl, M.; Ding, S.; Lee, C. W.; Grubbs, R. H., Synthesis and activity of a new generation of ruthenium-based olefin metathesis catalysts coordinated with 1,3-dimesityl-4,5-dihydroimidazol-2-ylidene ligands. *Organic letters* **1999**, *1*, 953-956.
138. Jida, M.; Betti, C.; Schiller, P. W.; Tourwe, D.; Ballet, S., One-pot isomerization-cross metathesis-reduction (ICMR) synthesis of lipophilic tetrapeptides. *ACS Comb. Sci.* **2014**, *16* (7), 342-351.
139. Durchschlag, H.; Zipper, P., Calculation of the partial volume of organic compounds and polymers. *Ultracentrifugation* **1994**, *94*, 20-39.
140. Karim, A. S.; Yan, A.; Ocotl, E.; Bennett, D. D.; Wang, Z.; Kendziorski, C.; Gibson, A. L. F., Discordance between histologic and visual assessment of tissue viability in excised burn wound tissue. *Wound Repair Regen.* **2019**, *27* (2), 150-161.
141. Kowalske, K. J., Burn Wound Care. *Phys. Med. Rehabil. Clin. N. Am.* **2011**, *22* (2), 213-227.
142. Hernandez, P.; Buller, D.; Mitchell, T.; Wright, J.; Liang, H.; Manchanda, K.; Welch, T.; Huebinger, R. M.; Carlson, D. L.; Wolf, S. E.; Song, J., Severe Burn-Induced Inflammation and Remodeling of Achilles Tendon in a Rat Model. *Shock* **2018**, *50* (3).
143. Zhai, Q.; Zhou, F.; Ibrahim, M. M.; Zhao, J.; Liu, X.; Wu, J.; Chen, L.; Qi, S., An immune-competent rat split thickness skin graft model: useful tools to develop new therapies to improve skin graft survival. *Am. J. Transl. Res.* **2018**, *10* (6), 1600-1610.
144. Van Goethem, E.; Poincloux, R.; Gauffre, F.; Maridonneau-Parini, I.; Le Cabec, V., Matrix Architecture Dictates Three-Dimensional Migration Modes of Human Macrophages: Differential Involvement of Proteases and Podosome-Like Structures. *J. Immunol.* **2010**, *184* (2), 1049.
145. Morris, J. L.; Cross, S. J.; Lu, Y.; Kadler, K. E.; Lu, Y.; Dallas, S. L.; Martin, P., Live imaging of collagen deposition during skin development and repair in a collagen I – GFP fusion transgenic zebrafish line. *Dev. Biol.* **2018**, *441* (1), 4-11.
146. Chvapil, M.; Speer, D. P.; Owen, J. A.; Chvapil, T. A., Identification of the Depth of Burn Injury by Collagen Stainability. *Plast. Reconstr. Surg.* **1984**, *73* (3).



147. Jaskille, A. D.; Ramella-Roman, J. C.; Shupp, J. W.; Jordan, M. H.; Jeng, J. C., Critical Review of Burn Depth Assessment Techniques: Part II. Review of Laser Doppler Technology. *J. Burn. Care. Res.* **2010**, *31* (1), 151-157.
148. Heimbach, D.; Engrav, L.; Grube, B.; Marvin, J., Burn depth: A review. *World. J. Surg.* **1992**, *16* (1), 10-15.
149. Monstrey, S.; Hoeksema, H.; Verbelen, J.; Pirayesh, A.; Blondeel, P., Assessment of burn depth and burn wound healing potential. *Burns* **2008**, *34* (6), 761-769.
150. Khatib, M.; Jabir, S.; Fitzgerald O'Connor, E.; Philp, B., A Systematic Review of the Evolution of Laser Doppler Techniques in Burn Depth Assessment. *Plast. Surg. Int.* **2014**, *2014*, 621792.
151. Israel, J. S.; Greenhalgh, D. G.; Gibson, A. L., Variations in Burn Excision and Grafting: A Survey of the American Burn Association. *J. Burn. Care. Res.* **2017**, *38* (1), e125-e132.
152. Sharma, V. P.; O'Boyle, C. P.; Jeffery, S. L. A., Man or Machine? The Clinimetric Properties of Laser Doppler Imaging in Burn Depth Assessment. *J. Burn. Care. Res.* **2011**, *32* (1), 143-149.
153. Thatcher, J. E.; Li, W.; Rodriguez-Vaqueiro, Y.; Squiers, J. J.; Mo, W.; Lu, Y.; Plant, K. D.; Sellke, E.; King, D. R.; Fan, W.; Martinez-Lorenzo, J. A.; DiMaio, J. M., Multispectral and Photoplethysmography Optical Imaging Techniques Identify Important Tissue Characteristics in an Animal Model of Tangential Burn Excision. *J. Burn. Care. Res.* **2016**, *37* (1), 38-52.
154. McUmbler, H.; Dabek, R. J.; Bojovic, B.; Driscoll, D. N., Burn Depth Analysis Using Indocyanine Green Fluorescence: A Review. *J. Burn. Care. Res.* **2019**, *40* (4), 513-516.
155. Kaiser, M.; Yafi, A.; Cinat, M.; Choi, B.; Durkin, A. J., Noninvasive assessment of burn wound severity using optical technology: A review of current and future modalities. *Burns* **2011**, *37* (3), 377-386.
156. Megens, R. T. A.; Egbrink, M. G. A. o.; Cleutjens, J. P. M.; Kuijpers, M. J. E.; Schiffers, P. H. M.; Merckx, M.; Slaaf, D. W.; van Zandvoort, M. A. M. J., Imaging Collagen in Intact Viable Healthy and Atherosclerotic Arteries Using Fluorescently Labeled CNA35 and Two-Photon Laser Scanning Microscopy. *Mol. Imag.* **2007**, *6* (4), 7290.2007.00021.
157. Barth, D.; Milbradt, A. G.; Renner, C.; Moroder, L., A (4R)- or a (4S)-Fluoroproline Residue in Position Xaa of the (Xaa-Yaa-Gly) Collagen Repeat Severely Affects Triple-Helix Formation. *Chem. Bio. Chem.* **2004**, *5* (1), 79-86.
158. Dones, J. M.; Tanrikulu, I. C.; Chacko, J. V.; Schroeder, A. B.; Hoang, T. T.; Gibson, A. L. F.; Eliceiri, K. W.; Raines, R. T., Optimization of interstrand interactions enables burn detection with a collagen-mimetic peptide. *Org. Biomol. Chem.* **2019**, *17* (46), 9906-9912.
159. Schindelin, J.; Arganda-Carreras, I.; Frise, E.; Kaynig, V.; Longair, M.; Pietzsch, T.; Preibisch, S.; Rueden, C.; Saalfeld, S.; Schmid, B.; Tinevez, J.-Y.; White, D. J.; Hartenstein, V.; Eliceiri, K.; Tomancak, P.; Cardona, A., Fiji: an open-source platform for biological-image analysis. *Nat. Methods* **2012**, *9* (7), 676-682.
160. Pierce, M. C.; Sheridan, R. L.; Hyle Park, B.; Cense, B.; de Boer, J. F., Collagen denaturation can be quantified in burned human skin using polarization-sensitive optical coherence tomography. *Burns* **2004**, *30* (6), 511-517.
161. Zhang, R. R.; Schroeder, A. B.; Grudzinski, J. J.; Rosenthal, E. L.; Warram, J. M.; Pinchuk, A. N.; Eliceiri, K. W.; Kuo, J. S.; Weichert, J. P., Beyond the margins: real-time detection of cancer using targeted fluorophores. *Nat. Revi. Clin. Oncol.* **2017**, *14* (6), 347-364.
162. Mallo, M.; Wellik, D. M.; Deschamps, J., Hox genes and regional patterning of the vertebrate body plan. *Dev. Biol.* **2010**, *344* (1), 7-15.
163. Fromental-Ramain, C.; Warot, X.; Messadecq, N.; LeMeur, M.; Dolle, P.; Chambon, P., Hoxa-13 and Hoxd-13 play a crucial role in the patterning of the limb autopod. *Development* **1996**, *122* (10), 2997.

164. Fromental-Ramain, C.; Warot, X.; Lakkaraju, S.; Favier, B.; Haack, H.; Birling, C.; Dierich, A.; Dollé, P.; Chambon, P., Specific and redundant functions of the paralogous Hoxa-9 and Hoxd-9 genes in forelimb and axial skeleton patterning. *Development* **1996**, *122* (2), 461.
165. Wellik, D. M.; Capecchi, M. R., *Hox10* and *Hox11* Genes Are Required to Globally Pattern the Mammalian Skeleton. *Science* **2003**, *301* (5631), 363.
166. Davis, A. P.; Witte, D. P.; Hsieh-Li, H. M.; Potter, S. S.; Capecchi, M. R., Absence of radius and ulna in mice lacking *hoxa-11* and *hoxd-11*. *Nature* **1995**, *375* (6534), 791-795.
167. Nelson, L. T.; Rakshit, S.; Sun, H.; Wellik, D. M., Generation and expression of a Hoxa11eGFP targeted allele in mice. *Dev. Dyn.* **2008**, *237* (11), 3410-3416.
168. Swinehart, I. T.; Schlientz, A. J.; Quintanilla, C. A.; Mortlock, D. P.; Wellik, D. M., Hox11 genes are required for regional patterning and integration of muscle, tendon and bone. *Development (Cambridge, England)* **2013**, *140* (22), 4574-4582.
169. Pineault, K.; Swinehart, I.; Garthus, K.; Ho, E.; Yao, Q.; Schipani, E.; Kozloff, K.; Wellik, D., Hox11 genes regulate postnatal longitudinal bone growth and growth plate proliferation. *Biology open* **2015**, *4*.
170. Rux, D. R.; Song, J. Y.; Swinehart, I. T.; Pineault, K. M.; Schlientz, A. J.; Trulick, K. G.; Goldstein, S. A.; Kozloff, K. M.; Lucas, D.; Wellik, D. M., Regionally Restricted Hox Function in Adult Bone Marrow Multipotent Mesenchymal Stem/Stromal Cells. *Developmental cell* **2016**, *39* (6), 653-666.
171. Rux, D. R.; Song, J. Y.; Pineault, K. M.; Mandair, G. S.; Swinehart, I. T.; Schlientz, A. J.; Garthus, K. N.; Goldstein, S. A.; Kozloff, K. M.; Wellik, D. M., Hox11 Function Is Required for Region-Specific Fracture Repair. *J. Bone. Miner. Res.* **2017**, *32* (8), 1750-1760.
172. Pineault, K. M.; Song, J. Y.; Kozloff, K. M.; Lucas, D.; Wellik, D. M., Hox11 expressing regional skeletal stem cells are progenitors for osteoblasts, chondrocytes and adipocytes throughout life. *Nat. Commun.* **2019**, *10* (1), 3168.
173. Leucht, P.; Kim, J.-B.; Amasha, R.; James, A. W.; Girod, S.; Helms, J. A., Embryonic origin and Hox status determine progenitor cell fate during adult bone regeneration. *Development* **2008**, *135* (17), 2845.
174. Ackema, K.; Charité, J., Mesenchymal stem cells from different organs are characterized by distinct topographic Hox codes. *Stem Cells and Development* **2008**, *17* (5), 979-991.
175. Wu, Y.; Liang, D.; Wang, Y.; Bai, M.; Tang, W.; Bao, S.; Yan, Z.; Li, D.; Li, J., Correction of a Genetic Disease in Mouse via Use of CRISPR-Cas9. *Cell. Stem. Cell.* **2013**, *13* (6), 659-662.
176. McKee, M. D.; Cole, W. G., Chapter 2 - Bone Matrix and Mineralization. In *Pediatric Bone (Second Edition)*, Glorieux, F. H.; Pettifor, J. M.; Jüppner, H., Eds. Academic Press: San Diego, 2012; pp 9-37.
177. van Oers, R. F. M.; Wang, H.; Bacabac, R. G., Osteocyte shape and mechanical loading. *Curr. Osteoporos. Rep.* **2015**, *13* (2), 61-66.
178. Lattouf, R.; Younes, R.; Lutomski, D.; Naaman, N.; Godeau, G.; Senni, K.; Changotade, S., Picrosirius Red Staining: A Useful Tool to Appraise Collagen Networks in Normal and Pathological Tissues. *J. Histochem. Cytochem.* **2014**, *62* (10), 751-758.
179. Junqueira, L. C. U.; Bignolas, G.; Brentani, R. R., Picrosirius staining plus polarization microscopy, a specific method for collagen detection in tissue sections. *Histochem. J.* **1979**, *11* (4), 447-455.
180. Ljusberg, J.; Wang, Y.; Lång, P.; Norgård, M.; Dodds, R.; Hultenby, K.; Ek-Rylander, B.; Andersson, G., Proteolytic Excision of a Repressive Loop Domain in Tartrate-resistant Acid Phosphatase by Cathepsin K in Osteoclasts \*. *J. Biol. Chem.* **2005**, *280* (31), 28370-28381.

181. Blumer, M. J. F.; Hausott, B.; Schwarzer, C.; Hayman, A. R.; Stempel, J.; Fritsch, H., Role of tartrate-resistant acid phosphatase (TRAP) in long bone development. *Mechanisms of Development* **2012**, *129* (5), 162-176.
182. Gradin, P.; Hollberg, K.; Cassady, A. I.; Lång, P.; Andersson, G., Transgenic Overexpression of Tartrate-Resistant Acid Phosphatase Is Associated with Induction of Osteoblast Gene Expression and Increased Cortical Bone Mineral Content and Density. *Cells Tissues Organs* **2012**, *196* (1), 68-81.
183. Rutkovskiy, A.; Stensløkken, K.-O.; Vaage, I. J., Osteoblast Differentiation at a Glance. *Med. Sci. Monit.* **2016**, *22*, 95-106.
184. Lian, J. B.; Stein, G. S., CHAPTER 6 - Osteoblast Biology. In *Osteoporosis (Third Edition)*, Marcus, R.; Feldman, D.; Nelson, D. A.; Rosen, C. J., Eds. Academic Press: San Diego, 2008; pp 93-150.
185. Klein-Nulend, J.; Bacabac, R. G.; Mullender, M. G., Mechanobiology of bone tissue. *Pathol. Biol.* **2005**, *53* (10), 576-580.
186. Pavalko, F. M.; Norvell, S. M.; Burr, D. B.; Turner, C. H.; Duncan, R. L.; Bidwell, J. P., A Model for mechanotransduction in bone cells: The load-bearing mechanosomes. *J. Cell. Biochem.* **2003**, *88* (1), 104-112.
187. Bonewald, L. F., Generation and function of osteocyte dendritic processes. *J. Musculoskelet Neuronal Interact.* **2005**, *5* (4), 321-324.
188. Turner, C. H.; Robling, A. G.; Duncan, R. L.; Burr, D. B., Do Bone Cells Behave Like a Neuronal Network? *Calcif. Tissue. Int.* **2002**, *70* (6), 435-442.
189. Asnaghi, M. A.; Aerts, J.-M.; Alakpa, E. V.; Alexander, M. R.; Alini, M.; Alm, J. J.; Atala, A.; Badylak, S. F.; Groot, F. B.-d.; Black, C.; Brittberg, M.; Cha, C.; Cohen, S.; Dalby, M. J.; Dalton, P. D.; Davison, N. L.; Dawson, J. I.; de Boer, J.; DeRuiter, M. C.; Engler, A. J.; Geris, L.; Gibbs, S.; Gibbs, D.; Gittenberger-de Groot, A. C.; Grijpma, D. W.; Han, C.; Harvey, A. R.; Herrmann, M.; Hierck, B. P.; Hook, A. L.; Hubbell, J. A.; Hutmacher, D. W.; Joly, J.; Kanczler, J.; Karperien, M.; Kerr, C.; Khademhosseini, A.; Labuz, J. M.; Lambrechts, T.; LaPointe, V. L. S.; Laschke, M. W.; Le Blanc, K.; Levenberg, S.; Lindahl, A.; Londono, R.; Luyten, F. P.; Mantalaris, A.; Martin, I.; Martino, M. M.; McNamara, L. E.; Meijer, D.; Moroni, L.; Myers, S.; Navsaria, H.; Ojeh, N.; Oreffo, R. O. C.; Oudega, M.; Papantoniou, I.; Park, J.; Piraino, F.; Pittenger, M. F.; Plant, G. W.; Poelmann, R. E.; Qian, H.; Reischl, I.; Rice, J. J.; Roelen, B. A. J.; Rouwkema, J.; Ruvinov, E.; Sandberg, J. M.; Scherberich, A.; Schrooten, J.; Scott, E. A.; Shandalov, Y.; Sicari, B. M.; Smith, T.; Sohler, J.; Sonnaert, M.; Takayama, S.; Tare, R.; Truckenmüller, R.; Tsimbouri, P. M.; Turner, L.-A.; Van Assche, D.; van Blitterswijk, C. A.; Vanlauwe, J.; Verrier, S.; Welin, S.; Wendt, D.; Winkler, D. A.; Woodfield, T. B. F., Contributors. In *Tissue Engineering (Second Edition)*, Blitterswijk, C. A. V.; De Boer, J., Eds. Academic Press: Oxford, 2015; pp xxv-xxx.
190. Reznikov, N.; Shahar, R.; Weiner, S., Bone hierarchical structure in three dimensions. *Acta Biomaterialia* **2014**, *10* (9), 3815-3826.
191. Shapiro, F.; Wu, J. Y., Woven bone overview: structural classification based on its integral role in developmental, repair and pathological bone formation throughout vertebrate groups. 2019; Vol. 38, pp 137-167.
192. Gross, S.; Krause, Y.; Wuelling, M.; Vortkamp, A., Hoxa11 and Hoxd11 regulate chondrocyte differentiation upstream of Runx2 and Shox2 in mice. *PloS one* **2012**, *7* (8), e43553-e43553.
193. Zhao, W.; Byrne, M. H.; Wang, Y.; Krane, S. M., Osteocyte and osteoblast apoptosis and excessive bone deposition accompany failure of collagenase cleavage of collagen. *J. Clin. Investig.* **2000**, *106* (8), 941-949.

194. Bradaschia-Correa, V.; Leclerc, K.; Josephson, A. M.; Lee, S.; Palma, L.; Litwa, H. P.; Neibart, S. S.; Huo, J. C.; Leucht, P., Hox gene expression determines cell fate of adult periosteal stem/progenitor cells. *Sci. Rep.* **2019**, *9* (1), 5043.
195. Kalajzic, Z.; Liu, P.; Kalajzic, I.; Du, Z.; Braut, A.; Mina, M.; Canalis, E.; Rowe, D. W., Directing the expression of a green fluorescent protein transgene in differentiated osteoblasts: comparison between rat type I collagen and rat osteocalcin promoters. *Bone* **2002**, *31* (6), 654-660.
196. Bachmanov, A. A.; Reed, D. R.; Beauchamp, G. K.; Tordoff, M. G., Food intake, water intake, and drinking spout side preference of 28 mouse strains. *Behav. Genet.* **2002**, *32* (6), 435-443.
197. Kawamoto, T.; Shimizu, M., A method for preparing 2- to 50- $\mu$ m-thick fresh-frozen sections of large samples and undecalcified hard tissues. *Histochem. Cell Biol.* **2000**, *113* (5), 331-339.
198. Mangiavini, L.; Merceron, C.; Schipani, E., Analysis of Mouse Growth Plate Development. *Curr. Protoc. Mouse Biol.* **2016**, *6* (1), 67-130.
199. Jáuregui, E. J.; Akil, O.; Acevedo, C.; Hall-Glenn, F.; Tsai, B. S.; Bale, H. A.; Liebenberg, E.; Humphrey, M. B.; Ritchie, R. O.; Lustig, L. R.; Alliston, T., Parallel mechanisms suppress cochlear bone remodeling to protect hearing. *Bone* **2016**, *89*, 7-15.
200. Kolb, H. C.; Finn, M. G.; Sharpless, K. B., Click Chemistry: Diverse Chemical Function from a Few Good Reactions. *Angew. Chem., Int. Ed.* **2001**, *40* (11), 2004-2021.
201. Huisgen, R., 1,3-Dipolar cycloadditions. Past and future. *Angew. Chem., Int. Ed.* **1963**, *41*, 2596-2599.
202. Blomquist, A. T.; Liu, L. H., Many-Membered Carbon Rings. VII. Cycloöctyne. *J. Am. Chem. Soc.* **1953**, *75* (9), 2153-2154.
203. Wittig, G.; Krebs, A., Zur Existenz niedergliedriger Cycloalkine, I. *Chem. Ber.* **1961**, *94*, 3260-3275.
204. Banert, K.; Köhler, F., Synthesis of 1,4-diazidobuta-1,3-dienes by electrocyclic ring opening: Precursors for bi-2*H*-azirin-2-yls and their valence isomerization to diazabenzene. *Angew. Chem., Int. Ed.* **2001**, *40*, 174-177.
205. Agard, N. J.; Baskin, J. M.; Prescher, J. A.; Lo, A.; Bertozzi, C. R., A Comparative Study of Bioorthogonal Reactions with Azides. *ACS Chem. Biol.* **2006**, *1* (10), 644-648.
206. Agard, N. J.; Prescher, J. A.; Bertozzi, C. R., A Strain-Promoted [3 + 2] Azide-Alkyne Cycloaddition for Covalent Modification of Biomolecules in Living Systems. *J. Am. Chem. Soc.* **2004**, *126* (46), 15046-15047.
207. Note1, 2021.
208. Hill, R. K.; Rabinovitz, M., Stereochemistry of "No-Mechanism" Reactions: Transfer of Asymmetry in the Reaction of Olefins with Dienophiles. *J. Am. Chem. Soc.* **1964**, *86* (5), 965-966.
209. Doering, W. v. E.; Roth, W. R., The Overlap of Two Allyl Radicals or a Four-Centered Transition State in the Cope Rearrangement. *Tetrahedron* **1962**, *18* (1), 67-74.
210. Sletten, E. M.; Bertozzi, C. R., Bioorthogonal Chemistry: Fishing for Selectivity in a Sea of Functionality. *Angew. Chem., Int. Ed.* **2009**, *48*, 6974-6998.
211. Patterson, D. M.; Nazarova, L. A.; Prescher, J. A., Finding the Right (Bioorthogonal) Chemistry. *ACS Chem. Biol.* **2014**, *9*, 592-605.
212. Ess, D. H.; Houk, K. N., Distortion/Interaction Energy Control of 1,3-Dipolar Cycloaddition Reactivity. *J. Am. Chem. Soc.* **2007**, *129* (35), 10646-10647.
213. Schoenebeck, F.; Ess, D. H.; Jones, G. O.; Houk, K. N., Reactivity and Regioselectivity in 1,3-Dipolar Cycloadditions of Azides to Strained Alkynes and Alkenes: A Computational Study. *J. Am. Chem. Soc.* **2009**, *131* (23), 8121-8133.

214. Ess, D. H.; Houk, K. N., Theory of 1,3-Dipolar Cycloadditions: Distortion/Interaction and Frontier Molecular Orbital Models. *J. Am. Chem. Soc.* **2008**, *130* (31), 10187-10198.
215. Ess, D. H.; Jones, G. O.; Houk, K. N., Transition States of Strain-Promoted Metal-Free Click Chemistry: 1,3-Dipolar Cycloadditions of Phenyl Azide and Cyclooctynes. *Org. Lett.* **2008**, *10* (8), 1633-1636.
216. Bach, R. D., Ring Strain Energy in the Cyclooctyl System. The Effect of Strain Energy on [3 + 2] Cycloaddition Reactions with Azides. *J. Am. Chem. Soc.* **2009**, *131* (14), 5233-5243.
217. Chenoweth, K.; Chenoweth, D.; Goddard, W. A., III, Cyclooctyne-Based Reagents for Uncatalyzed Click Chemistry: A Computational Survey. *Org. Biomol. Chem.* **2009**, *7* (24), 5255-5258.
218. Gold, B.; Shevchenko, N. E.; Bonus, N.; Dudley, G. B.; Alabugin, I. V., Selective Transition State Stabilization via Hyperconjugative and Conjugative Assistance: Stereoelectronic Concept for Copper-Free Click Chemistry. *J. Org. Chem.* **2012**, *77* (1), 75-89.
219. Gold, B.; Dudley, G. B.; Alabugin, I. V., Moderating Strain without Sacrificing Reactivity: Design of Fast and Tunable Noncatalyzed Alkyne–Azide Cycloadditions via Stereoelectronically Controlled Transition State Stabilization. *J. Am. Chem. Soc.* **2013**, *135* (4), 1558-1569.
220. Fernández, I.; Cossío, F. P.; Bickelhaupt, F. M., Aromaticity and Activation Strain Analysis of [3 + 2] Cycloaddition Reactions between Group 14 Heteroallenes and Triple Bonds. *J. Org. Chem.* **2011**, *76* (7), 2310-2314.
221. Garcia-Hartjes, J.; Dommerholt, J.; Wennekes, T.; van Delft, F. L.; Zuilhof, H., Electronic Effects versus Distortion Energies During Strain-Promoted Alkyne–Azide Cycloadditions: A Theoretical Tool to Predict Reaction Kinetics. *Eur. J. Org. Chem.* **2013**, *2013* (18), 3712-3720.
222. Baskin, J. M.; Prescher, J. A.; Laughlin, S. T.; Agard, N. J.; Chang, P. V.; Miller, I. A.; Lo, A.; Codelli, J. A.; Bertozzi, C. R., Copper-Free Click Chemistry for Dynamic *in vivo* Imaging. *Proc. Natl. Acad. Sci. USA* **2007**, *104* (43), 16793-16797.
223. Burke, E. G.; Gold, B.; Hoang, T. T.; Raines, R. T.; Schomaker, J. M., Fine-Tuning Strain and Electronic Activation of Strain-Promoted 1,3-Dipolar Cycloadditions with Endocyclic Sulfamates in SNO-OCTs. *J. Am. Chem. Soc.* **2017**, *139* (23), 8029-8037.
224. Dommerholt, J.; Schmidt, S.; Temming, R.; Hendriks, L. J. A.; Rutjes, F. P. J. T.; van Hest, J. C. M.; Lefeber, D. J.; Friedl, P.; van Delft, F. L., Readily Accessible Bicyclononynes for Bioorthogonal Labeling and Three-Dimensional Imaging of Living Cells. *Angew. Chem., Int. Ed.* **2010**, *49* (49), 9422-9425.
225. Hu, Y.; Roberts, J. M.; Kilgore, H. R.; Mat Lani, A. S.; Raines, R. T.; Schomaker, J. M., Triple, Mutually Orthogonal Bioorthogonal Pairs through the Design of Electronically Activated Sulfamate-Containing Cycloalkynes. *J. Am. Chem. Soc.* **2020**, *142* (44), 18826-18835.
226. McNitt, C. D.; Popik, V. V., Photochemical Generation of oxa-Dibenzocyclooctyne (ODIBO) for Metal-Free Click Ligations. *Org. Biomol. Chem.* **2012**, *10* (41), 8200-8202.
227. Ni, R.; Mitsuda, N.; Kashiwagi, T.; Igawa, K.; Tomooka, K., Heteroatom-Embedded Medium-Sized Cycloalkynes: Concise Synthesis, Structural Analysis, and Reactions. *Angew. Chem., Int. Ed.* **2015**, *54* (4), 1190-1194.
228. Deb, T.; Tu, J.; Franzini, R. M., Mechanisms and Substituent Effects of Metal-Free Bioorthogonal Reactions. *Chem. Rev.* **2021**.
229. Harris, T.; Alabugin, I. V., Strain and stereoelectronics in cycloalkyne click chemistry. *Mendeleev Commun.* **2019**, *29* (3), 237-248.
230. Dommerholt, J.; Rutjes, F. P. J. T.; van Delft, F. L., Strain-Promoted 1,3-Dipolar Cycloaddition of Cycloalkynes and Organic Azides. *Top Curr Chem (Cham)* **2016**, *374*, 16.
231. Kim, E. J.; Kang, D. W.; Leuck, H. F.; Bond, M. R.; Ghosh, S.; Love, D. C.; Ahn, J.-S.; Kang, D.-O.; Hanover, J. A., Optimizing the Selectivity of DIFO-based Reagents for Intracellular Bioorthogonal Applications. *Carbohydr. Res.* **2013**, *377*, 18-27.

232. Gold, B.; Batsomboon, P.; Dudley, G. B.; Alabugin, I. V., Alkynyl Crown Ethers as a Scaffold for Hyperconjugative Assistance in Noncatalyzed Azide–Alkyne Click Reactions: Ion Sensing through Enhanced Transition-State Stabilization. *J. Org. Chem.* **2014**, *79* (13), 6221-6232.
233. Harris, T.; Gomes, G. d. P.; Ayad, S.; Clark, R. J.; Lobodin, V. V.; Tuscan, M.; Hanson, K.; Alabugin, I. V., Twisted Cycloalkynes and Remote Activation of “Click” Reactivity. *Chem* **2017**, *3* (4), 629-640.
234. Ning, X.; Guo, J.; Wolfert, M. A.; Boons, G.-J., Visualizing Metabolically-Labeled Glycoconjugates of Living Cells by Copper-Free and Fast Huisgen Cycloadditions. *Angew. Chem., Int. Ed.* **2008**, *47*, 2253-2255.
235. Debets, M. F.; van Berkel, S. S.; Schoffelen, S.; Rutjes, F. P. J. T.; van Hest, J. C. M.; van Delft, F. L., Aza-Dibenzocyclooctynes for Fast and Efficient Enzyme PEGylation via Copper-Free (3+2) Cycloaddition. *Chem. Commun.* **2010**, *46* (1), 97-99.
236. Kuzmin, A.; Poloukhine, A.; Wolfert, M. A.; Popik, V. V., Surface Functionalization Using Catalyst-Free Azide–Alkyne Cycloaddition. *Bioconjugate Chem.* **2010**, *21* (11), 2076-2085.
237. Gordon, C. G.; Mackey, J. L.; Jewett, J. C.; Sletten, E. M.; Houk, K. N.; Bertozzi, C. R., Reactivity of Biarylazacyclooctynones in Copper-Free Click Chemistry. *J. Am. Chem. Soc.* **2012**, *134* (22), 9199-9208.
238. Sletten, E. M.; Nakamura, H.; Jewett, J. C.; Bertozzi, C. R., Difluorobenzocyclooctyne: Synthesis, Reactivity, and Stabilization by  $\beta$ -Cyclodextrin. *J. Am. Chem. Soc.* **2010**, *132* (33), 11799-11805.
239. Escorihuela, J.; Das, A.; Looijen, W. J. E.; van Delft, F. L.; Aquino, A. J. A.; Lischka, H.; Zuilhof, H., Kinetics of the Strain-Promoted Oxidation-Controlled Cycloalkyne–1,2-Quinone Cycloaddition: Experimental and Theoretical Studies. *J. Org. Chem.* **2018**, *83* (1), 244-252.
240. Frisch, M. J.; Trucks, G. W.; Schlegel, H. B.; Scuseria, G. E.; Robb, M. A.; Cheeseman, J. R.; Scalmani, G.; Barone, V.; Petersson, G. A.; Nakatsuji, H.; Li, X.; Caricato, M.; Marenich, A. V.; Bloino, J.; Janesko, B. G.; Gomperts, R.; Mennucci, B.; Hratchian, H. P.; Ortiz, J. V.; Izmaylov, A. F.; Sonnenberg, J. L.; Williams; Ding, F.; Lipparini, F.; Egidi, F.; Goings, J.; Peng, B.; Petrone, A.; Henderson, T.; Ranasinghe, D.; Zakrzewski, V. G.; Gao, J.; Rega, N.; Zheng, G.; Liang, W.; Hada, M.; Ehara, M.; Toyota, K.; Fukuda, R.; Hasegawa, J.; Ishida, M.; Nakajima, T.; Honda, Y.; Kitao, O.; Nakai, H.; Vreven, T.; Throssell, K.; Montgomery Jr., J. A.; Peralta, J. E.; Ogliaro, F.; Bearpark, M. J.; Heyd, J. J.; Brothers, E. N.; Kudin, K. N.; Staroverov, V. N.; Keith, T. A.; Kobayashi, R.; Normand, J.; Raghavachari, K.; Rendell, A. P.; Burant, J. C.; Iyengar, S. S.; Tomasi, J.; Cossi, M.; Millam, J. M.; Klene, M.; Adamo, C.; Cammi, R.; Ochterski, J. W.; Martin, R. L.; Morokuma, K.; Farkas, O.; Foresman, J. B.; Fox, D. J. *Gaussian 16 Rev. C.01*, Wallingford, CT, 2016.
241. Zhao, Y.; Truhlar, D. G., The M06 Suite of Density Functionals for Main Group Thermochemistry, Thermochemical Kinetics, Noncovalent Interactions, Excited States, and Transition Elements: Two New Functionals and Systematic Testing of Four M06-Class Functionals and 12 Other functionals. *Theor Chem Account* **2008**, *120* (1), 215-241.
242. Grimme, S., Semiempirical GGA-Type Density Functional Constructed with a Long-Range Dispersion Correction. *J. Comput. Chem.* **2006**, *27* (15), 1787-1799.
243. Glendening, E.; Badenhoop, J.; Reed, A.; E., C.; Bohmann, J.; Morales, C.; Karafiloglou, P.; Landis, C.; Weinhold, F., NBO 7.0: Natural Bond Orbital Analysis Program. *Theoretical Chemistry Institute, University of Wisconsin, Madison* (2018).
244. Note2, 2012.
245. Aronoff, M. R.; Gold, B.; Raines, R. T., 1,3-Dipolar Cycloadditions of Diazo Compounds in the Presence of Azides. *Org. Lett.* **2016**, *18* (7), 1538-1541.
246. Aronoff, M. R.; Gold, B.; Raines, R. T., Rapid Cycloaddition of a Diazo Group with an Unstrained Dipolarophile. *Tetrahedron Lett.* **2016**, *57* (22), 2347-2350.

247. Bickelhaupt, F. M., Understanding Reactivity with Kohn–Sham Molecular Orbital Theory: E2–S<sub>N</sub>2 Mechanistic Spectrum and Other Concepts. *J. Comput. Chem.* **1999**, *20* (1), 114-128.
248. Fernández, I.; Bickelhaupt, F. M., The activation strain model and molecular orbital theory: understanding and designing chemical reactions. *Chem. Soc. Rev.* **2014**, *43* (14), 4953-4967.
249. Bickelhaupt, F. M.; Houk, K. N., Analyzing Reaction Rates with the Distortion/Interaction–Activation Strain Model. *Angew. Chem., Int. Ed.* **2017**, *56*, 10070-10086.
250. Gold, B.; Aronoff, M. R.; Raines, R. T., Decreasing Distortion Energies without Strain: Diazo-Selective 1,3-Dipolar Cycloadditions. *J. Org. Chem.* **2016**, *81* (14), 5998-6006.
251. Newberry, R. W.; Raines, R. T., The n→π\* Interaction. *Acc. Chem. Res.* **2017**, *50*, 1838-1846.
252. Fritsch, P., IV. Ueber die Darstellung von Diphenylacetaldehyd und eine neue Synthese von Tolanderivaten. *Liebigs Ann.* **1894**, *279*, 319-323.
253. Buttenberg, W. P., Condensation des Dichloracetals mit Phenol und Toluol. *Liebigs Ann.* **1894**, *279*, 324-337.
254. Wiechell, H., Condensation des Dichloracetals mit Anisol und Phenetol. *Liebigs Ann.* **1894**, *279*, 337-344.
255. Corey, E. J.; Fuchs, P. L., A Synthetic Method for Formyl→Ethyne Conversion (RCHO→RC≡CH or RC≡CR'). *Tetrahedron Lett.* **1972**, 3769-3772.
256. Alexakos, P. D.; Wardrop, D. J., N-Morpholinomethyl-5-lithiotetrazole: A Reagent for the One-Pot Synthesis of 5-(1-Hydroxyalkyl)tetrazoles. *J. Org. Chem.* **2019**, *84* (19), 12430-12436.
257. Note3, 2021.
258. Liu, W.; Zhou, J.; Zhang, T.; Zhu, H.; Qian, H.; Zhang, H.; Huang, W.; Gust, R., Design and Synthesis of Thiourea Derivatives Containing a Benzo[5,6]cyclohepta[1,2-*b*]pyridine Moiety as Potential Antitumor and Anti-Inflammatory Agents. *Bioorg. Med. Chem. Lett.* **2012**, *22* (8), 2701-2704.
259. Wardrop, D. J.; Komenda, J. P., Dehydrative Fragmentation of 5-Hydroxyalkyl-1*H*-tetrazoles: A Mild Route to Alkylidenecarbenes. *Org. Lett.* **2012**, *14* (6), 1548-1551.
260. Dale, H. J. A.; Nottingham, C.; Poree, C.; Lloyd-Jones, G. C., Systematic Evaluation of 1,2-Migratory Aptitude in Alkylidene Carbenes. *J. Am. Chem. Soc.* **2021**, *143*, 2097-2107.
261. Littke, A. F.; Fu, G. C., Palladium-Catalyzed Coupling Reactions of Aryl Chlorides. *Angew. Chem., Int. Ed.* **2002**, *41*, 4176-4311.
262. Hu, Z.; Wei, X.-J.; Hangelmann, J.; Seitz, A.-K.; Rodstein, I.; Gessner, V. H.; Goosen, L. J., Coupling of Reformatsky Reagents with Aryl Chlorides Enabled by Ylide-Functionalized Phosphine Ligands. *Angew. Chem., Int. Ed.* **2021**, *60*, xxx-xxx.
263. Mix, K. A.; Aronoff, M. R.; Raines, R. T., Diazo Compounds: Versatile Tools for Chemical Biology. *ACS Chem. Biol.* **2016**, *11* (12), 3233-3244.
264. McGrath, N. A.; Raines, R. T., Diazo Compounds as Highly Tunable Reactants in 1,3-Dipolar Cycloaddition Reactions with Cycloalkynes. *Chem. Sci.* **2012**, *3* (11), 3237-3240.
265. Note4, 2021.
266. Andersen, K. A.; Aronoff, M. R.; McGrath, N. A.; Raines, R. T., Diazo Groups Endure Metabolism and Enable Chemoselectivity in Cellulo. *J. Am. Chem. Soc.* **2015**, *137* (7), 2412-2415.
267. Zheng, H.; Ye, H.; Yu, X.; You, L., Interplay Between n→π\* Interactions and Dynamic Covalent Bonds: Quantification and Modulation by Solvent Effects. *J. Am. Chem. Soc.* **2019**, *141*, 8825-8833.
268. Siebler, C.; Maryasin, B.; Kuemin, M.; Erdmann, R. S.; Rigling, C.; Grünenfelder, C.; Ochsenfeld, C.; Wennemers, H., Importance of Dipole Moments and Ambient Polarity for the Conformation of Xaa–Pro Moieties—A Combined Experimental and Theoretical Study. *Chem. Sci.* **2015**, *6*, 6725-6730.

269. Reichardt, C.; Welton, T., *Solvents and Solvent Effects in Organic Chemistry*, 4th ed. Wiley–VCH: Weinheim, Germany, 2011.
270. Lyles, M. M.; Gilbert, H. F., Catalysis of the Oxidative Folding of Ribonuclease A by Protein Disulfide Isomerase: Dependence of the Rate on the Composition of the Redox Buffer. *Biochemistry* **1991**, *30* (3), 613-619.
271. Scalmani, G.; Frisch, M. J., Continuous surface charge polarizable continuum models of solvation. I. General formalism. *J. Chem. Phys.* **2010**, *132* (11), 114110.
272. Barone, V.; Cossi, M., Quantum Calculation of Molecular Energies and Energy Gradients in Solution by a Conductor Solvent Model. *J. Phys. Chem. A* **1998**, *102* (11), 1995-2001.
273. Cossi, M.; Rega, N.; Scalmani, G.; Barone, V., Energies, structures, and electronic properties of molecules in solution with the C-PCM solvation model. *Journal of Computational Chemistry* **2003**, *24* (6), 669-681.
274. Garcia-Hartjes, J.; Dommerholt, J.; Wennekes, T.; van Delft, F. L.; Zuilhof, H., Electronic Effects versus Distortion Energies During Strain-Promoted Alkyne-Azide Cycloadditions: A Theoretical Tool to Predict Reaction Kinetics. *Eur. J. Org. Chem.* **2013**, *2013* (18), 3712-3720.
275. Escorihuela, J.; Das, A.; Looijen, W. J. E.; van Delft, F. L.; Aquino, A. J. A.; Lischka, H.; Zuilhof, H., Kinetics of the Strain-Promoted Oxidation-Controlled Cycloalkyne-1,2-Quinone Cycloaddition: Experimental and Theoretical Studies. *J. Org. Chem.* **2018**, *83* (1), 244-252.